



**Numerical and experimental modelling of
tidal range structures with focus on
conservation of momentum through
hydraulic structures**

By

Nejc Čož

A thesis submitted to Cardiff University in candidature for the degree of
Doctor of Philosophy (PhD)

School of Engineering

Cardiff University

2019

To Sara

You always believed in me and encouraged me to pursue my dreams. Thanks for being there on every step of this journey.

Abstract

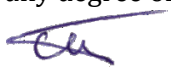
Hydrodynamic modelling has an important role in the development of Tidal Range energy Structures (TRS). The aim of this research study was to develop a methodology for the simulation of TRS with Delft3D software. The study has focused on two key issues of the regional-scale hydrodynamic models. Firstly, the majority of studies before the year 2016 have ignored the conservation of momentum of the flow through the hydraulic structures. Secondly, 3D hydrostatic models have been largely underused in TRS simulations to date. The first key objective was to develop a TRS module for Delft3D software. The case study of Severn Barrage was used for validation. Direct comparisons with the past studies showed good agreement between the results, confirming the appropriateness of the developed model. The second key objective was to introduce a novel approach for the treatment of momentum transfer through hydraulic structures. This was achieved by representing the momentum of the discharged water as an additional external force in the momentum equation. The final key objectives were (i) to validate the developed method through a series of physical experiments and (ii) to use it in the regional-scale model with the Swansea Bay tidal lagoon. A good match between measurements and simulation results confirmed that momentum conservation is required for accurately predicting the velocity of the discharged jets. The results without the momentum conservation achieved only 50 per cent of the measured velocity. Extending the 2D model to 3D was found to be more important for the estimation of local bed shear stress, than for predicting the velocity field. The 3D simulations did slightly improve the accuracy of the velocity field, but more importantly, they have produced a more realistic vertical velocity profile. The 3D model can capture the attachment of the jets to the bottom surface, distorting the standard logarithmic profile assumed in depth-averaged shallow water flows. As a result, the bed shear stress increased by 75 per cent from 2D to 3D simulation. The Swansea Bay lagoon case study showed that momentum conservation only affected the area close to the structure. The results were found to be sensitive to the vertical velocity profile of the jet. The simplified velocity distribution had

Abstract

a bigger impact on the hydrodynamics and power output estimation than the realistic distribution. In general, the 2D model with momentum conservation was found to be sufficient for analysing hydrodynamics in most cases. However, the 3D model has proved to be indispensable for accurate predictions of local-scale impacts, especially in an around the lagoon.

Declaration

This work has not been submitted in substance for any other degree or award at this or any other university or place of learning, nor is being submitted concurrently in candidature for any degree or other award.

Signed 

Date 20/5/2019

Statement 1

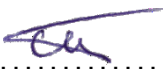
This thesis is being submitted in partial fulfilment of the requirements for the degree of PhD.

Signed 

Date 20/5/2019

Statement 2

This thesis is the result of my own independent work/investigation, except where otherwise stated. Other sources are acknowledged by explicit references. The views expressed are my own.

Signed 

Date 20/5/2019

Statement 3

I hereby give consent for my thesis, if accepted, to be available for photocopying and for inter-library loan, and for the title and summary to be made available to outside organisations.

Signed 

Date 20/5/2019

Acknowledgements

This work was funded as part of the Water Informatics, Science and Engineering Centre for Doctoral Training (WISE CDT) under a grant from the Engineering and Physical Sciences Research Council (EPSRC), grant number EP/L016214/1.

I would like to thank my supervisors, Dr Reza Ahmadian and Professor Roger A. Falconer, for their help and guidance during my PhD.

I greatly appreciate Professor Binliang Lin from Tsinghua University for hosting me in a research visit and everyone at the hydraulic laboratory for making me feel at home. In particular, I would like to thank Yaling Chen for her help with setting up the experiment and Bing Yuan for helping me navigate around Tsinghua and Beijing.

I would especially like to thank all my colleagues at WISE CDT and Hydro-environmental Research Centre for their assistance throughout my PhD. In particular, I am very grateful to David Glover and Jonathan King for helping me accommodate to life in Cardiff and to my dear friend Giovanni Musolino for always offering the moral support when needed. I would also like to thank Sam Bray and Athanasios Angeloudis for their kindness and support during my first year of the research.

Finally, I would like to express my gratitude to my partner Sara Peterlin, my mother Irena Modic-Čož and my sister Sinja Čož for their unconditional support during my PhD.

Table of contents

Abstract.....	III
Declaration.....	V
Acknowledgements	VII
Table of contents	IX
List of figures.....	XV
List of tables	XXVII
Nomenclature	XXXI
Chapter 1 Introduction	1
1.1 Research background.....	1
1.2 Research objectives	6
1.3 Thesis outline	7
Chapter 2 Literature review	9
2.1 Introduction	9
2.2 Renewable energy	10
2.2.1 Tidal power.....	12
2.2.2 Review papers of tidal power technology.....	14
2.2.3 Existing projects	16
2.2.4 Tidal resource and future proposals	23
2.2.5 Advantages and disadvantages of TRS	33
2.3 Tidal hydrodynamics.....	34
2.4 Numerical modelling of tidal range structures	38
2.4.1 The multi-scale modelling approach.....	38
2.4.2 Evolution of numerical modelling of the Severn barrage.....	41
2.4.3 Evolution of numerical modelling of the Swansea Bay lagoon	46
2.4.4 3D models.....	48
2.4.5 Momentum conservation.....	50

Table of contents

2.5	Summary	52
Chapter 3 Numerical model		55
3.1	Introduction	55
3.2	Governing equations	56
3.2.1	Continuity equation.....	56
3.2.2	Momentum equations.....	56
3.3	Numerical methods.....	58
3.3.1	Spatial discretisation.....	58
3.3.2	Temporal discretisation	60
3.4	Delft3D-FLOW numerical model	62
3.4.1	Hydrodynamic equations.....	62
3.4.2	Numerical methods	74
3.5	Summary	84
Chapter 4 Modelling tidal range structures		85
4.1	Introduction	85
4.2	Conceptual approach.....	86
4.3	Operational sequence.....	88
4.3.1	One-way operational sequence	88
4.3.2	Two-way operational sequence	90
4.3.3	Numerical algorithm	92
4.4	Turbines and sluice gates	98
4.4.1	Turbines	98
4.4.2	Sluice gates.....	102
4.4.3	Implementation into the numerical model.....	104
4.5	Momentum conservation.....	106
4.5.1	Implementation into the numerical model.....	109
4.6	Summary	110

Table of contents

Chapter 5 Development model: Severn Barrage.....	111
5.1 Introduction.....	111
5.2 Methodology.....	112
5.2.1 Severn Barrage scheme description.....	113
5.2.2 Numerical model.....	115
5.3 Model validation.....	118
5.4 Results.....	130
5.4.1 Barrage operation.....	130
5.4.2 Continental Shelf model results.....	134
5.4.3 Severn Estuary model results.....	142
5.5 Summary.....	147
Chapter 6 Experimental model: barrage in a flume.....	149
6.1 Introduction.....	149
6.2 Methodology.....	151
6.3 Physical experiment.....	153
6.3.1 Experimental set-up.....	153
6.3.2 Case studies.....	156
6.3.3 Measurements.....	157
6.4 Numerical model set-up.....	163
6.5 Results.....	166
6.5.1 Water levels.....	166
6.5.2 Contribution of momentum conservation.....	168
6.5.3 Depth-averaged velocity.....	173
6.5.4 Velocity vectors 2D vs 3D.....	179
6.5.5 Vertical variation of velocity.....	184
6.5.6 Bed shear stress.....	199
6.6 Summary.....	206

Table of contents

Chapter 7 Model application: Swansea Bay tidal lagoon	209
7.1 Introduction	209
7.2 Methodology	210
7.2.1 Tidal lagoon scheme description	213
7.2.2 Numerical model set-up	215
7.2.3 Far-field impacts.....	218
7.3 Calibration and validation.....	220
7.3.1 Calibration.....	221
7.3.2 Validation.....	223
7.4 Results	226
7.4.1 Lagoon operation	226
7.4.2 Velocity field.....	229
7.4.3 Bed shear stress	237
7.4.4 Water levels.....	247
7.4.5 Power output.....	248
7.5 Summary	250
Chapter 8 Conclusion and future research	255
8.1 General conclusions.....	255
8.2 Recommendations for further study	262
References.....	265
Publication list.....	283
A Operational sequence flow charts.....	285
A.1 One-way ebb generation.....	285
A.2 Two-way generation.....	287

Table of contents

B	Additional CSM validation results.....	289
B.1	Severn Estuary and Bristol Channel	289
B.2	Irish Sea	297
B.3	Celtic Sea.....	301
C	Photos from Tsinghua hydraulic laboratory	309
D	Technical drawing - barrage model.....	313
E	Layout of the experiment - plan view	315
F	Validation results - Swansea Bay.....	316

List of figures

Figure 2.1: A diagram illustrating the overlap between marine energy and hydro-power.	13
Figure 2.2: Classification of tidal power technologies. Adapted from Adcock et al. (2015).	13
Figure 2.3: Drawing of a traditional tide mill with (1) retention basin, (2) dam, (3) mill, (4) miller's dwelling, (5) sluice leading to the hydraulic wheel, and (6) sluice gate (Charlier 2007).	17
Figure 2.4: An aerial image of the Rance Tidal Power Station located in the Rance River estuary in France. Image captured from Google Earth.....	18
Figure 2.5: An aerial image of the Sihwa Lake Tidal Power Station located in the on the western coast of the Korean Peninsula. Image captured from Google Earth.....	19
Figure 2.6: An aerial image of Kislaya the Guba Tidal Power Station located in the Kislaya Guba fjord in the Barents Sea, Russia. Image captured from Google Earth.	20
Figure 2.7: An aerial image of the Annapolis Royal Generating Station located on the Annapolis River in Nova Scotia, Canada. Image captured from Google Earth	21
Figure 2.8: An aerial image of the Jiangxia Tidal Power Station located in the in Jiangxia Harbour, Wenling City, China. Image captured from Google Earth.....	22
Figure 2.9: The global theoretical tidal range energy resource calculated as annual energy yield in kWh/m ² (Neill et al. 2018).	24

List of figures

Figure 2.10: The theoretical tidal range energy resource over the northwest European shelf seas, calculated as annual energy yield in kWh/m ² . Areas landward of the [blue, red, black] contour lines denote regions with water depths less than 30m and where energy density exceeds 84, 60, and 50 kWh/m ² , respectively (Neill et al. 2018).	26
Figure 2.11: Map of shortlisted schemes in the Severn Estuary (DECC 2010).....	27
Figure 2.12: Sites, identified by TLP viable for tidal range lagoon deployment in the UK; Red - Swansea Bay lagoon; Blue - TLP projects under development; Yellow - additional viable sites (Tidal Lagoon Power 2016).....	28
Figure 2.13: Severn Barrage designs: (a) Thomas Fulljames's own impression of his proposed barrage in 1849; (b) Cutaway view of turbine caisson with a bulb turbine. ..	29
Figure 2.14: Swansea Bay Lagoon layout overlaid on the Admiralty Chart background (Tidal Lagoon Plc 2017).....	31
Figure 2.15: (a) A bulb turbine designed specifically for tidal range schemes. (b) The design is based on the conventional bulb turbine (Tidal Lagoon Power 2016).	31
Figure 2.16: The effects of the Moon on the tidal range (Rourke et al. 2010).	34
Figure 2.17: Difference in tidal range of shallow waters between (a) the progressive and (b) standing waves, shown for an idealized frictionless tide (Parker 2007).	36
Figure 2.18: (a) Mean spring tidal range and (b) Co-tidal lines, drawn through locations of equal Mean High Water Interval in the Severn Estuary and English Channel (Uncles 2010).....	37
Figure 2.19: Bulb turbine cross-section (Wilhelm et al. 2016b)	51

List of figures

Figure 3.1: Arrangement of the unknowns for staggered grid (Rijkswaterstaat 2016).	63
Figure 3.2: Example of a curvilinear grid in Delft3D defined in OSGB 1936 coordinate system.....	64
Figure 3.3: Mapping of physical space Ω to computational space G_H . G_{mm} represents the locations of the unknown variables (Rijkswaterstaat 2016).....	65
Figure 3.4: Illustration of the fundamental differences between the σ -grid (a) and Z-grid (b) vertical coordinate systems available in Delft3D.	65
Figure 3.5: Definition of the σ coordinate system and characteristic parameters describing depth (d), water level (ζ) and total depth (H) (Deltares 2014).	67
Figure 3.6: Schematic definition of the vertical grid with layer interfaces (Rijkswaterstaat 2016).....	67
Figure 3.7: Distinguishable terms of the momentum equation (3.13).	77
Figure 4.1: Diagram of a one-way operating sequence with generation during ebb tide (i.e. ebb-generation). Adapted from Xia et al. (2010b).....	89
Figure 4.2: Diagram of a one-way operating sequence with generation during flood tide (i.e. flood-generation). Adapted from Xia et al. (2010b).....	90
Figure 4.3: Diagram of a two-way operating sequence with generation during both ebb and flood tides. Adapted from Xia et al. (2010b).	91
Figure 4.4: Cross-section of a bi-directional bulb turbine proposed for the Swansea Bay tidal lagoon (Tidal Lagoon Plc 2016).....	99

List of figures

Figure 4.5: A typical Andritz Hydro hill chart for a double-regulated bulb unit on which the Q-H relationships used in this study are based on (Aggidis and Feather 2012).....	100
Figure 4.6: Q-H and P-H relationships for bi-directional turbines used in this study..	102
Figure 4.7: An example of (a) a water passageway (Lee et al. 2010) and (b) a sliding gate (Tidal Lagoon Plc 2016) typically used in TRS designs.....	103
Figure 4.8: Cross-section of a sluice caisson proposed for the Swansea Bay tidal lagoon (Tidal Lagoon Plc 2016).....	104
Figure 5.1: Layout of the barrage wall and locations of turbines and sluice gates. Image courtesy of Severn Tidal Power Group (STPG 1989).....	114
Figure 5.2. Study area - showing open boundaries of the Continental Shelf domain (orange) and Severn Estuary model (yellow). Closed boundaries were characterized by the coastline (black).....	115
Figure 5.3: Computational domain of the CS model, showing the bathymetry data in Delft3D.....	117
Figure 5.4: Computational domain of the SE model, showing the bathymetry data in Delft3D.....	117
Figure 5.5: Locations of the observation sites used for validation of the tidal flow (yellow) and water levels (green).	119
Figure 5.6: Comparisons between Delft3D results, EFDC results and observed data for the validation site C1, located in the upper reaches of the Bristol Channel, near Gower.	123

List of figures

Figure 5.7: Comparisons between Delft3D results, EFDC results and observed data for the validation site C2, located in the middle reaches of the Bristol Channel, near Lynton.	124
Figure 5.8: Comparisons between Delft3D results, EFDC results and observed data for the validation site C3, located in the middle reaches of the Bristol Channel, near Gower.	125
Figure 5.9: Comparisons between Delft3D results, EFDC results and observed data for the validation site C4, located in the Celtic Sea.....	126
Figure 5.10: Comparisons between Delft3D results, EFDC results and observed data for the validation site C5, located in the Irish Sea.....	127
Figure 5.11: Water level results from Delft3D compared with the observed data from BODC in five locations in the Bristol Channel and Severn Estuary.	129
Figure 5.12: Location of the points used to calculate the mean head difference on the SE computational grid, showing the bathymetry and location of the barrage.	130
Figure 5.13: Predicted water levels on either side of the Severn Barrage and the corresponding power output over a typical neap-spring tidal cycle.....	132
Figure 5.14: Predicted water levels either side of the barrage and operation stages showing the operation of the Severn Barrage during a typical spring tidal cycle. Operational sequences: (1) holding stage - high water, (2) generating stage, (3) holding stage - low water, (4) filling stage.....	133
Figure 5.15: Predicted water levels either side of the barrage and operation stages showing the operation of the Severn Barrage during a typical neap tidal cycle.	

List of figures

Operational sequences: (1) holding stage - high water, (2) generating stage, (3) holding stage - low water, (4) filling stage.	133
Figure 5.16: Maximum water elevation changes due to the barrage operation. Positive differences denote an increase and negative a decrease in water elevations after including the barrage in the simulation.	135
Figure 5.17: Locations of observation points for the analysis of water elevation changes due to the barrage operation.	136
Figure 5.18: Time series of water level change between CS0 (without barrage) and CS1 (with barrage) over two typical neap tidal cycles at the observation site P1 in the Irish Sea.	138
Figure 5.19: Time series of water level change between CS0 (without barrage) and CS1 (with barrage) over two typical neap tidal cycles at the observation site P2 in the Celtic Sea.	138
Figure 5.20: Time series of water level change between CS0 (without barrage) and CS1 (with barrage) over two typical neap tidal cycles at the observation site P3 at the location of the SE open boundary.	139
Figure 5.21: Time series of water level change between CS0 (without barrage) and CS1 (with barrage) over two typical neap tidal cycles at the observation site P4 in the Swansea Bay.	140
Figure 5.22: Time series of water level change between CS0 (without barrage) and CS1 (with barrage) over two typical neap tidal cycles at the observation site P5 in the middle of Bristol Channel, downstream of the barrage.	140

List of figures

Figure 5.23: Time series of water level change between CS0 (without barrage) and CS1 (with barrage) over two typical neap tidal cycles at the observation site P6 upstream of the barrage, close to Newport.....	141
Figure 5.24: Maximum water levels (a) without and (b) with the barrage and (c) the differences between the two.	143
Figure 5.25: Minimum water depths (a) without and (b) with the barrage and (c) the differences between the two.	144
Figure 5.26: Maximum tidal currents (a) without and (b) with the barrage and (c) a close-up of the differences between the two around in the vicinity of the barrage.....	146
Figure 6.1: A diagram of the experimental setup in the flume (the drawing is not to scale).	154
Figure 6.2: Experimental ADV locations on a cross-section with the locations of the ducts visible in the background.....	155
Figure 6.3: Locations of the pressure sensor in the flume (not to scale). Some labels are hidden to prevent overcrowding of the image.....	155
Figure 6.4: ADV measurements for THU 1 presented as 3D velocity vectors and axial velocity contours at 5 locations downstream of the barrage.	159
Figure 6.5: ADV measurements for THU 2 presented as 3D velocity vectors and axial velocity contours at 5 locations downstream of the barrage.	160
Figure 6.6: ADV measurements for THU 3 presented as 3D velocity vectors and axial velocity contours at 5 locations downstream of the barrage.	161

List of figures

- Figure 6.7: Average water elevation in the flume obtained from pressure sensors measurements for (a) THU 1 with 41 l/s and 16 cm weir and (b) THU 2 and THU 3 with 18 l/s and 17 cm. 162
- Figure 6.8: Example of (a) Water Levels and (b) Depth-Averaged Velocity time-series for THU 1 case in 2D mode. After 5 minutes the oscillations stop when the steady flow state was reached. 164
- Figure 6.9: Example of: (a) Water Levels and (b) Depth-Averaged Velocities time-series for THU 1 case in 3D mode. After 5 minutes the oscillations stop when the steady flow state was reached. 164
- Figure 6.10: Velocity magnitude for THU 1; (top) results of a depth-averaged simulation with the addition of momentum; (bottom) result without the addition of momentum. 170
- Figure 6.11: Velocity magnitude for THU 2; (top) results of a depth-averaged simulation with the addition of momentum; (bottom) result without the addition of momentum. 171
- Figure 6.12: Velocity magnitude for THU 3; (top) results of a depth-averaged simulation with the addition of momentum; (bottom) result without the addition of momentum. 172
- Figure 6.13: Depth-averaged axial (left) and lateral (right) velocities at 5 observational cross-sections downstream of the barrage for the THU 1 case, comparing the experimental measurements with the 2D and 3D model results. 176
- Figure 6.14: Depth-averaged axial (left) and lateral (right) velocities at 5 observational cross-sections downstream of the barrage for the THU 2 case, comparing the experimental measurements with the 2D and 3D model results. 177

List of figures

Figure 6.15: Depth-averaged axial (left) and lateral (right) velocities at 5 observational cross-sections downstream of the barrage for the THU 3 case, comparing the experimental measurements with the 2D and 3D model results.....178

Figure 6.16: Delft3D depth-averaged velocity vectors comparison between 2D (top) and 3D (bottom) simulations for THU 1.....181

Figure 6.17: Delft3D depth-averaged velocity vectors comparison between 2D (top) and 3D (bottom) simulations for THU 2.....182

Figure 6.18: Delft3D depth-averaged velocity vectors comparison between 2D (top) and 3D (bottom) simulations for THU 3.....183

Figure 6.19: Comparison of the velocity profile for THU 1 between laboratory observations and numerical 3D simulation at four depths: (a) 0.04 m, (b) 0.08 m, (c) 0.12 m, and (d) 0.16 m.185

Figure 6.20: Comparison of the velocity profile for THU 2 between laboratory observations and numerical 3D simulation at four depths: (a) 0.04 m, (b) 0.08 m, (c) 0.12 m, and (d) 0.16 m.190

Figure 6.21: Comparison of the velocity profile for THU 3 between laboratory observations and numerical 3D simulation at four depths: (a) 0.04 m, (b) 0.08 m, (c) 0.12 m, and (d) 0.16 m.195

Figure 6.22: Ratio of local bed stress to reference bed stress, “mass-only” simulation, THU 1.....201

Figure 6.23: Ratio of local bed stress to reference bed stress, 2D with momentum, THU 1.201

List of figures

Figure 6.24: Ratio of local bed stress to reference bed stress, 3D with momentum, THU 1.	201
Figure 6.25: Ratio of local bed stress to reference bed stress, “mass-only” simulation, THU 2.....	203
Figure 6.26: Ratio of local bed stress to reference bed stress, 2D with momentum, THU 2.	203
Figure 6.27: Ratio of local bed stress to reference bed stress, 3D with momentum, THU 2.	203
Figure 6.28: Ratio of local bed stress to reference bed stress, “mass-only” simulation, THU 3.....	205
Figure 6.29: Ratio of local bed stress to reference bed stress, 2D with momentum, THU 3.	205
Figure 6.30: Ratio of local bed stress to reference bed stress, 3D with momentum, THU 3.	205
Figure 7.1: Turbine cross-section – the flow-through area at the duct entrance and exit is rectangular and it transitions to a smaller circular shape in the middle at the location of the turbine runner.	211
Figure 7.2: Representation of velocity distribution in the numerical model for a 2D and 3D configuration.	212
Figure 7.3: The distinctive horseshoe shape of the current lagoon proposal and its location in the Swansea Bay (image courtesy of Tidal Lagoon Plc).	214

List of figures

Figure 7.4: Domain of the model, overlaid with the computational grid.....	216
Figure 7.5: Water elevation time-series at the open boundary for a full neap-spring tidal cycle.....	217
Figure 7.6: Bathymetry of the numerical model, showing the lagoon and domain boundaries.....	217
Figure 7.7: Impact of the lagoon on maximum water levels under a two-way operation.	219
Figure 7.8: Computational domain for the assessment, with the outline of the proposed tidal lagoon in Swansea Bay and with cyan diamonds showing calibration sites and magenta dots showing validation sites (background map from Google Maps service).	220
Figure 7.9: Sensitivity analysis of roughness coefficient at locations four observation sites in the Severn Estuary and Bristol Channel	223
Figure 7.10: Validation results showing water levels and flow velocity at location L3 and L5.	224
Figure 7.11: Location of points for determining the head difference across the lagoons.	227
Figure 7.12: Two-way operation of the Swansea Bay lagoon during a typical spring tidal cycle. Showing water levels on both sides of the lagoon and the corresponding operational stages.....	228

List of figures

Figure 7.13: A comparison of velocity fields during the flood generation for a typical spring tidal cycle – (a) without lagoon, (b) SBL 1, (c) SBL 2, (d) SBL 3, (e) SBL 4, and (f) SBL 5.....	231
Figure 7.14: A comparison of velocity fields during the ebb generation for a typical spring tidal cycle – (a) without lagoon, (b) SBL 1, (c) SBL 2, (d) SBL 3, (e) SBL 4, and (f) SBL 5.	234
Figure 7.15: Representative 3D velocity profiles for SBL4 and SBL5 during the ebb generation in four locations downstream of the turbine.	237
Figure 7.16: Prediction of bed shear stress in Swansea Bay prior to construction of the lagoon.....	238
Figure 7.17: Bed shear stress during the flood generation – (a) without lagoon, (b) SBL 1, (c) SBL 2, (d) SBL 3, (e) SBL 4, and (f) SBL 5.....	241
Figure 7.18: Bed shear stress during the ebb generation – (a) without lagoon, (b) SBL 1, (c) SBL 2, (d) SBL 3, (e) SBL 4, and (f) SBL 5.	244
Figure 7.19: Comparison of water elevations inside the lagoon for the five different cases.	248
Figure 7.20: Predicted water levels on either side of the Severn Barrage and the corresponding power output over a typical neap-spring tidal cycle for the SBL 1 case.	249

List of tables

Table 2.1: UK's annual electricity production from renewable sources in 2017 (BEIS 2018b).	11
Table 2.2: Overview of the operational tidal range projects as of 2018.....	17
Table 2.3: UK Tidal range resource by region (DECC 2010).	25
Table 2.4: Estimated annual energy output for Swansea Bay tidal lagoon as predicted across different studies.	48
Table 4.1: Numerical values of operational stages for ebb generation.....	93
Table 4.2: Numerical values of operational stages for two-way generation	95
Table 5.1: Specifications of the Severn Barrage scheme used in this study.	114
Table 5.2: Validation results for current speed at five observation locations C1 to C5.	122
Table 5.3: Validation results for spring tide speed at five observation locations C1 to C5.	122
Table 5.4: Validation results for neap tide speed at five observation locations C1 to C5.	122
Table 5.5: Validation results for water levels at five observation locations W1 to W5.	128

List of tables

Table 6.1: Three different barrage configurations for the experimental setup....	157
Table 6.2: Recorded and computed water levels for THU 1 at four locations downstream of the barrage (R07-R10).....	166
Table 6.3: Recorded and computed water levels for THU 2 at four locations downstream of the barrage (R07-R10).....	167
Table 6.4: Recorded and computed water levels for THU 3 at four locations downstream of the barrage (R07-R10).....	167
Table 7.1: Summary of the five different scenarios investigated in this study.....	212
Table 7.2: Specifications of the Swansea Bay lagoon scheme used in this study.....	215
Table 7.3: Sensitivity analysis of roughness coefficient (Hinkley Point).	222
Table 7.4: Sensitivity analysis of roughness coefficient (Ilfracombe).....	222
Table 7.5: Sensitivity analysis of roughness coefficient (Mumbles).	222
Table 7.6: Sensitivity analysis of roughness coefficient (Newport).....	222
Table 7.7: Validation results for water levels at five observation locations.....	225
Table 7.8: Validation results for current speed at five observation locations.	225
Table 7.9: Validation results for velocity direction at five observation locations.....	225
Table 7.10: Peak flow velocity (u_T) and instantaneous discharge (Q_T) just downstream of the turbine exit for a typical spring tidal cycle during flood power generation and the	

List of tables

corresponding head difference (H_T). Velocities for scenarios SBL4 and SBL5 are presented both with a depth-averaged value (u_T) for comparison with 2D models and with separate values for respective computational layers (u_{Tk}).....230

Table 7.11: Peak flow velocity (u_T) and instantaneous discharge (Q_T) just downstream of the turbine exit for a typical spring tidal cycle during ebb power generation and the corresponding head difference (H_T). Velocities for scenarios SBL4 and SBL5 are presented both with a depth-averaged value (u_T) for comparison with 2D models and with separate values for respective computational layers (u_{Tk}).....230

Table 7.12: Maximum water level values in meters recorded during a typical spring tide, illustrated in Figure 7.19.....247

Table 7.13: Minimum water level values in meters recorded during a typical spring tide, illustrated in Figure 7.19.....247

Table 7.14: Typical annual energy prediction extrapolated from a characteristic neap-spring tidal cycle for the five different cases.....250

Nomenclature

Abbreviations

1D	One-dimensional
2D	Two-dimensional
3D	Three-dimensional
ADI	alternating direction implicit (method)
ADP	acoustic Doppler profiler
ADV	acoustic Doppler velocimeter
AEM	algebraic eddy (viscosity) model
BEIS	Department for Business, Energy and Industrial Strategy
BODC	British Oceanic Data Centre
CD	chart datum
CF	capacity factor
CFD	computational fluid dynamics
CFL	Courant-Friedrichs-Lewy (condition)
CPU	central processing unit
CS	continental shelf (model)
CSM	continental shelf model
DCO	development consent order
DECC	Department of Energy and Climate Change
EFDC	Environmental Fluid Dynamics Code
FDM	finite difference method
FEM	finite element method
FVM	finite volume method
GMT	Greenwich mean time
HAT	highest astronomical tide
HPC	high-performance computing
HRC	Hydro-environmental Research Centre
HW	high water
LAT	lowest astronomical tide
LES	Large Eddy Simulation
LiDAR	Light Detection and Ranging
LW	low water

Nomenclature

MSL	mean sea level
NSE	Nash-Sutcliffe (model) efficiency
OD	ordnance datum
OSGB	Ordnance Survey of Great Britain
PC	personal computer
PDE	partial differential equations
PVC	polyvinyl chloride
RANS	Reynolds averaged Navier-Stokes (equations)
RMSE	root mean square error
SBL	Swansea Bay lagoon (model)
SE	Severn Estuary (model)
SGS	sub-grid scale
SI	scatter index
STPG	Severn Tidal Power Group
SWE	shallow water equations
THU	Name used for experiments in <u>Tsinghua</u> flume
TLP	Tidal Lagoon Power
TRS	tidal range structures
TVD	total variation diminishing
WL	water level

List of symbols

<i>Symbol</i>	<i>Units</i>	<i>Meaning</i>
A	m^2	area
A_S	m^2	sluice gate flow-through area
A_T	m^2	turbine flow-through area
B_k	m^2s^{-3}	buoyancy flux term for turbulent kinetic energy
B_ε	m^2s^{-4}	buoyancy flux term for the dissipation of turbulent kinetic energy
C_{2D}^2, C_{3D}^2	$m^{1/2}s^{-1}$	2D- and 3D-Chézy coefficients
$c_{2\varepsilon}$	-	calibration constant
C_d	-	discharge coefficient
C_{max}	-	dimensionless Courant number

Nomenclature

d	m	time-independent depth below the reference plane
D	m	turbine diameter
f	s ⁻¹	electricity grid frequency
f_x, f_y, f_z	ms ⁻²	external body forces
f_u, f_v	s ⁻¹	Coriolis parameters
$\overline{F_T}$	N	force of a jet entering a body of water
$F_{T\xi}$	N	force of a jet entering a body of water in scalar form
F_ξ, F_η	ms ⁻²	turbulent momentum flux
g	ms ⁻²	gravitational acceleration
G_p	-	number of generator poles
$\sqrt{G_{\xi\xi}}, \sqrt{G_{\eta\eta}}$	m	transformation coefficients between curvilinear and rectangular coordinate systems
h	m	head difference
H	m	total depth
H_{gen}	m	required head difference for start of power generation
H_{min}	m	minimum required head difference for efficient generation
H_{ref}	m	referential head difference
k	m ² s ²	energy dissipation
L	m	mixing length
m, n, k	-	indices denoting the position in the curvilinear grid
n	-	number of data points
M_ξ, M_η	ms ²	contributions due to external body forces
n_{11}	s ⁻¹	unit speed of a turbine
O_i	-	observed data points
\bar{O}	-	mean of the observed data
P	W	power
P_k	m ² s ⁻³	turbulent kinetic energy production
P_{kw}	m ² s ⁻³	turbulent energy production due to wave action
P_ε	m ² s ⁻⁴	dissipation of turbulent kinetic energy
$P_{\varepsilon w}$	m ² s ⁻⁴	dissipation of turbulent kinetic energy due to wave action
P_ξ, P_η	kg (ms) ⁻²	pressure gradient
P, E	ms ⁻¹	source term of precipitation and sink term of evaporation

Nomenclature

q_{in}, q_{out}	s^{-1}	local source and sink terms per unit volume
Q	ms^{-1}	global source or sink per unit area
Q_T	m^3s^{-1}	flow rate through turbine
Q_S	m^3s^{-1}	flow rate through sluice gate
Q_{11}	m^3s^{-1}	specific discharge of a turbine
r	-	Pearson's correlation factor
S_i	-	simulation results
\bar{S}	-	mean of simulation results
S_p	s^{-1}	speed of turbine
t	s	time
Δt	s	time-step
t_{hold}	s	maximum holding time
u, v, w	ms^{-1}	velocity components in main Cartesian directions
U, V	ms^{-1}	depth averaged velocities in x and y directions
\vec{v}_1, \vec{v}_2	ms^{-1}	velocities of the flow entering and exiting the control volume
\hat{u}, u	ms^{-1}	velocity of the incoming jet and background velocity
V_{cell}	m^3	volume of a computational cell
x, y, z	m	main Cartesian coordinates
Δx	m	spatial interval

List of Greek letter symbols

<i>Symbol</i>	<i>Units</i>	<i>Meaning</i>
ε	m^2s^{-3}	dissipation for turbulent kinetic energy
ζ	s	time-dependent free surface elevation
η	-	overall efficiency of a turbine
μ	$N\ sm^{-1}$	dynamic viscosity
ν	m^2s^{-1}	kinematic viscosity
ν_{3D}	m^2s^{-1}	contribution of a selected 3D-turbulence closure model
ν_H	m^2s^{-1}	horizontal eddy viscosity
ν_H^{back}	m^2s^{-1}	background horizontal viscosity

Nomenclature

ν_{mol}	m^2s^{-1}	kinematic viscosity of water
ν_V	m^2s^{-1}	vertical eddy viscosity
ν_V^{back}	m^2s^{-1}	background vertical viscosity
ν_{SGS}	m^2s^{-1}	sub-grid-scale turbulence
ξ, η	m	horizontal, curvilinear coordinates
ρ	$kg\ m^{-3}$	density
ρ_0	$kg\ m^{-3}$	density of water
σ	-	scaled vertical coordinate
σ_{mol}	-	Prandtl-Schmidt number for molecular mixing
$\overline{\tau}_b$	$N\ m^{-2}$	bed shear stress (depth averaged model)
$\overline{\tau}_{b3D}$	$N\ m^{-2}$	bed shear stress (3D model)
ω	ms^{-1}	vertical velocity related to the moving σ plane

Chapter 1

Introduction

1.1 Research background

With increasing concern over climate change and a rapid rise of carbon dioxide concentrations in the atmosphere, the move towards renewable energy has never been more relevant. Nowadays, the concern over the future of our planet is rapidly increasing, sparking serious debates amongst the general public, experts, industry stakeholders and governments on how to mitigate the effects of climate change. “Sustainable development”, “Carbon neutrality”, “Low-carbon economy”, “Life-cycle assessment”, “Carbon footprint” and “Renewable energy” are just some of the commonly used buzzwords that repeatedly emerge from such debates. Governments and industries have finally started to invest heavily in the development of renewable energy technologies to combat these issues (REN21 2018). The signing of the historical Paris Agreement in 2015 saw 174 states and the European Union committing to contesting the climate change by adopting mitigation strategies into their own national agendas (United Nations 2016b). To date, the number of signatories has risen to 195 Parties, that together represent more than 88 per cent of global greenhouse emissions (United Nations 2016a). In 2017, the renewable power generation saw its largest annual increase ever, raising total capacity by almost 9% globally over the previous year and thereby overtaking the combined additions in coal, natural gas and nuclear power in the same year (REN21 2018). The continuous advancements in the technology, that can be attributed to the intensive academic and commercial research studies are constantly increasing the efficiency and affordability of renewable energy solutions.

In the UK, the main use of renewable energy is for electricity generation; in 2017, renewables accounted for 29.3 per cent of domestic electricity production (BEIS 2018a). The number has been steadily rising over the past decade, with a 19 per cent annual increase in 2017 alone. The wind was by far the most utilised renewable source, accounting for 50 per cent of the annual electricity output from renewable resources (BEIS 2018b). Other major renewable sources include bioenergy, solar photovoltaics and hydropower. Ocean energy remains a largely untapped resource, with only a few small-scale waves and tidal stream projects currently in operation.

The UK has an enormous tidal energy resource that is largely unexploited, mainly because of doubts over the economic viability and concerns over impacts on the environment (Neill et al. 2018). In general, tidal energy is considered to be a promising technology with great potential for the production of clean power (Hendry 2016). In contrast to wind and solar, tidal energy conversion is entirely predictable and can be forecasted with high accuracy and far into the future (Ellabban et al. 2014). To make the projects more viable, the current development has to be focused on the reduction of construction costs, optimisation of electricity output and minimization of uncertainties on environmental impacts (Neill et al. 2018).

There are two main principles for the extraction of tidal power. Tidal stream technologies generate electricity by extracting kinetic energy from the tidal current, while tidal range technologies rely on the potential energy created by rising and falling of tides. Severn Estuary has the most significant tidal range in the UK, presenting a potential for deployment of both stream and range technologies. However, due to its exceptional tidal amplitude, it is considered the most important region for the development of tidal range technologies in the country. As a result, the region has attracted a lot of commercial interest and has been frequently used in academic research for case studying the deployment of the technology.

Conceptually, Tidal Range Structures (TRS) work on the principle of creating an artificial hydraulic head difference by impounding water, which is then used to drive the turbines

installed in the impoundment walls. Based on the layout of the walls, the structures can be split into barrages and lagoons. The barrages are generally very large structures that span the two banks of a large inlet or bay, creating an extensive impoundment basin on the upstream side of the wall (DECC 2010). Tidal lagoons are much smaller objects. They are created by constructing a circularly-shaped embankment that forms the impoundment basin. Due to their smaller size, they are thought to be a more environmentally friendly alternative to barrages (Angeloudis and Falconer 2017). With both types of technology being viable for deployment in the Severn Estuary, several different configurations of barrages and lagoons, including a combination of both, have been proposed so far. A proposal from Severn Tidal Power Group (STPG 1989) has been the most popular and most studied design proposal for a tidal barrage. With an embankment wall spanning between Cardiff and Weston-super-Mare, it was estimated that this scheme could generate around 17 TWh of electricity per year, supplying around 5 per cent of UK's energy requirements (Bray et al. 2016). However, due to its large size, high construction costs and uncertainties over environmental impacts, the scheme has gradually fallen out of favour. In its place, tidal lagoons have been progressively gaining more attention, which led to the formation of Tidal Lagoon Power, a company that put forward a plan for construction of six tidal lagoons in the UK (Hendry 2016). A tidal lagoon in Swansea Bay would be the first of the proposed schemes, powering around 150,000 households with a prospective 320 MW of installed capacity.

Environmental impacts are one of the main concerns regarding the TRS in the Severn Estuary (Kirby and Retière 2009). They include: (i) changes in maximum and minimum water levels, which can lead to reduction of intertidal habitats and increase in flood risk in some places Xia et al. (2010b); (ii) interruption to fish migration and injury from impact with turbines (Dadswell and Rulifson 1994); and (iii) changes in sediment transport patterns due to reduced velocity of the tidal current, which can affect the marine ecosystem through stronger light penetration due to lowered levels of turbidity and concentration of suspended sediment (Ahmadian et al. 2010a; Cornett et al. 2013; Neill et al. 2017). The physical presence of a tidal barrage or lagoon will also have an

impact on society, affecting activities occurring in the area and wellbeing of local residents. This may include increased difficulty to navigate for commercial and recreational vessels due to an obstruction; collision risk; noise pollution during both construction and operation; negative effect on tourism, recreation and activities in nature (Hooper and Austen 2013). However, not all impacts are necessarily negative; potential benefits, apart from clean energy, include potential road and rail links (in the case of a barrage), increased employment, improved conditions for recreation either upstream or inside the basin, and lowering flood risk. All these factors present a complex multi-objective system that requires a sophisticated decision-making tool for impact analysis and a reliable hydrodynamic model is one of the essential elements for such investigation.

Hydrodynamic models have an important role in the development of tidal energy schemes. They play a key part in the optimisation of the design and operating procedures and provide a good base for assessment of environmental impacts (Adcock et al. 2015). Consequently, there is an incentive for constant development and improvement of numerical modelling tools to enhance the accuracy and confidence in the hydrodynamic simulation (Angeloudis et al. 2016b). The numerical models extend from simple theoretical and 0D models to sophisticated multidimensional models that often require access to high-performance computing to make them feasible for practical use (Neill et al. 2018). The most commonly used are 2D hydro-environmental models – they are flexible and robust tools for modelling the flow at a regional scale. They have been applied to the analysis of tidal barrages and lagoons by a number of authors, utilizing several different software suites, such as DIVAST (Ahmadian et al. 2010a), EFDC (Zhou et al. 2014c; Bray et al. 2016), FV2D (Ahmadian et al. 2014b) and TELEMAC (Bourban et al. 2014).

Operation of a TRS is not by default included in conventional hydrodynamic models, hence, a particular TRS module has to be developed and retrofitted into the original source code. For the model to work properly it is essential that the implemented algorithms are based on a firm theoretical background and have to include at least: (i) a

method to physically separate the two subdomains (impoundment basin and seaward side); (ii) an algorithm that determines operational stages of the power plant, i.e. controlling the gates and turbines that allow transfer of the water between the two sub-basins; and (iii) procedures that accurately calculate the transfer of water through sluices and turbines. Based on the needs of an individual study, these algorithms can considerably vary in complexity from model to model. For example, a study focused on optimisation of electricity output will consider a more complex formulation of the way power generation is estimated, while a different study focusing on environmental impacts might completely ignore the power production, but would introduce a more sophisticated representation of water transfer through the hydraulic structures.

To increase accuracy of the hydrodynamic predictions, this study includes a newly developed method for transfer of momentum through hydraulic structures. Treatment of momentum is important for accurate predictions of the velocity field in the vicinity of the TRS (Angeloudis et al. 2016b). Conventional models often simplify the transfer through hydraulic structures and completely ignore the conservation of momentum. While that would be sufficient for preliminary analysis or prediction of assessment of far-field impacts, disregarding the momentum conservation generally leads to unrealistic predictions of the near-field conditions, particularly regarding the jets that form just downstream of the hydraulic structures. This can have a direct impact on phenomena associated with the velocity field, including water quality, sediment transport; and an indirect impact on predicted estimation of power production. The implementation of such procedures normally requires a full user-access to the source code, which is only possible with the academic research codes or open-sourced software.

One such modelling suite is Delft3D, an open source software, which was developed by Deltares, and is already widely used across industry and academia worldwide (Deltares 2014). It includes options for both 2D depth-averaged and 3D hydrostatic simulations. The curvilinear grid allows for a more natural fit of the computational mesh to the complex coastline and offers possibility for high resolution refinement of the grid around the areas of interest, such as around the barrage or lagoon. It integrates flow and

transport modelling systems, making it very attractive for hydro-environmental analysis of coastal and estuarine environments, such as the coastal waters around the UK. The software was selected to be used in this study with an aim to build a flexible and robust modelling tool that will be used for analysis of future tidal proposals in the Severn Estuary by the Hydro-environmental Research Centre (HRC) at Cardiff University. However, the open-source nature of Delft3D, and its wide-spread use across both academia and industry, means that the developed modifications will be available for use by any interested party.

In summary, the development of renewable energy projects is crucial for decreasing the carbon footprint and is a paramount factor in the transition towards the carbon-free economy. Tidal power presents one of the largest untapped renewable resources. The sheer scale of a tidal range power plant requires a significant initial investment and faces a lengthy construction period. Hence, any uncertainties on the efficiency of the power production and worries about the environmental impacts can discourage the stakeholders and lawmakers from supporting such schemes. The assessment of TRS relies heavily on the numerical modelling of their operation and simulation of the resulting hydrodynamic conditions.

1.2 Research objectives

The main aim of this research study is to improve the existing hydro-environmental modelling tools for tidal range energy projects. The model was developed to be specifically used for simulation of any future tidal proposals in the region, however, flexibility of the model should also allow its application to any other tidal range project worldwide. Furthermore, because of the open-source environment of Delft3D software, the modifications can be shared with any other parties already using the software. To achieve this, the following key objectives have been identified:

- Assess current methodology for simulation of tidal range structures (TRS) in hydrodynamic models and implement the numerical techniques into the Delft3D software.
- Develop an improved method for numerical modelling of the momentum transfer through a TRS that can be applied to the finite-difference numerical models, such as Delft3D.
- Validate the developed method through a physical experiment in a laboratory flume.
- Assess the impacts of the developed method on the performance of the model by applying it to an actual tidal range energy project, namely Swansea Bay lagoon.

Achieving these research objectives will improve the accuracy of hydro-environmental modelling of tidal range energy projects. It will provide a better understanding of the hydrodynamic processes related to the operation of TRSs and will contribute to a more informed decision making when designing future proposals.

1.3 Thesis outline

The thesis is organised into eight chapters, including:

Chapter 1: Introduction, which presents a wider research background and motivation for this research study.

Chapter 2: Literature review, which collates and overviews the main literature relevant for this research study.

Chapter 3: Numerical model, which presents the general governing equations and numerical methods used in hydrodynamic modelling and explains the numerical background of the model used in this research study, namely Delft3D.

Chapter 4: Modelling tidal range structures, which explains the numerical formulations of the procedures used for modelling the TRSs and their implementation into the Delft3D source code.

Chapter 5: Development model: Severn Barrage, which uses the Severn barrage continental shelf model as a development model for the implementation of the techniques described in Chapter 4.

Chapter 6: Experimental model: barrage in a flume, which describes the physical experimental model and provides validation analysis for the developed momentum transfer method using the experimental data.

Chapter 7: Model application: Swansea Bay tidal lagoon, which uses the Swansea Bay lagoon as a case study to demonstrate the improvements to the treatment of the momentum through the TRS.

Chapter 8: Conclusion and future research, which presents the summary of the work and the main findings of this research study, and provides suggestions for potential future research following from the conclusions of this study.

Chapter 2

Literature review

2.1 Introduction

This chapter presents an overview of the main literature relevant to the numerical modelling of tidal range energy projects. Tidal power technologies represent a large subgroup inside the field of renewable energy. The studies on tidal power cover a wide spectrum of knowledge, ranging from purely engineering point of view (focusing on the design, modelling, construction, optimisation, etc.) to ecological (health risks, impact on the animal habitats, etc.) and socioeconomic aspects. However, since the focus of this study is on hydro-environmental modelling of tidal range structures, the non-engineering aspects are not going to be reviewed in detail and will only be referred to as appropriate. The emphasis is on the technology of tidal range power, with special attention to the hydrodynamic modelling of such schemes.

The chapter is divided into three subsequent sections. Section 2.2 gives a general insight into the renewable energy sector, describing its history and defining the role of tidal power in the progression towards a carbon-neutral economy. Section 2.3 explains the physics of the tides in relation to the Severn Estuary. Section 2.4 provides a detailed summary of existing numerical models for hydrodynamic simulation of tidal power. First, the multi-scale approach to TRS modelling is addressed. It is followed by a comprehensive report on previous numerical models of the Severn Barrage and Swansea Bay Lagoon projects. And finally, a quick assessment is given on the use of 3D modelling and momentum conservation techniques in TRS studies.

2.2 Renewable energy

By definition, renewable energy is energy produced from natural sources - such as sun, wind and water - that are continually replenished on a human timescale (Ellabban et al. 2014). Renewable sources represent one of the main drivers of sustainable development and are fundamental for a transition towards a carbon-neutral economy (Dincer 2000). The extraction technologies have been already known and successfully deployed for decades, however, the accelerated development and a rapid increase in capacity have exposed a number of challenges related to renewable energy. One of the biggest drawbacks is the stochastic nature of the sources; oftentimes they are weather dependent and geographically diffused, which means that their output can be predicted, but not controlled (Uqaili and Harijan 2012). There are also questions over environmental and ecological impacts; for example, projects involving wind and tidal turbines have raised concerns over an increase in animal mortality rate as well as loss of important natural habitats (Wolf et al. 2009). Nevertheless, the positives still significantly outweigh the negatives, if compared to the traditional fossil fuel based technologies.

Renewable resources provided 29.3 per cent of the electricity generated in the UK in 2017, an increase of 4.8 percentage points from the previous year (BEIS 2018b). Table 2.1 classifies the UK's annual electricity production by a renewable resource. With a 39 per cent increase from the previous year, wind extraction has now become the primary source of renewable electricity in the country. The 50 TWh of output was achieved by an extensive increase in capacity and favourable wind conditions in 2017. Tidal energy finds itself on the other end of the spectrum – together with wave technology it produced only 4 GWh of output in 2017, making it almost negligible source in the country's renewables portfolio. Alternatively, the viability of the technology can be represented by the capacity factor (CF), an indicator that measures the economic (not physical) efficiency of power production. The CF metric is primarily used for cost calculations of power generation schemes and can be indirectly used for illustrating the overall achievement of carbon

reduction objectives (Boccard 2009). It is defined as a ratio between the net electricity generated in a selected time interval to the energy that could have been generated at continuous full-power operation during the same period. The Digest of UK Energy Statistics (BEIS 2018b) has presented the CFs for the UK’s renewable energy sector for the year 2017 as a ratio between the net generated electricity and the total generating capacity, as presented in Table 2.1. The main reason for a low CF factor of the wave and tidal source is that the deployed technologies is still in its initial stage and is expected to increase with further development of the technology. For example, a study from (Clarke et al. 2006) showed how the CF of tidal stream turbines can be significantly increased solely by regulating and limiting the power delivered from a turbine by using a lower capacity generator. This enabled the turbines to operate at their rated capacity for longer periods of time, raising the CF from the initial 14.7 per cent to 32.5 percent, which is already much closer to ratios achieved by wind and hydropower (see Table 2.1).

Table 2.1: UK’s annual electricity production from renewable sources in 2017 (BEIS 2018b).

Renewable source	% increase from 2016	Output capacity (TWh)	% of total output	Capacity factor (%)
Wind	39	50	50	31.7
Bioenergy	6	31.9	32	61.5
Solar PV	11	11.5	12	10.7
Hydropower	10	5.9	6	36.5
Wave and tidal	100	0.004	< 0.01	3.0

Despite decades of development efforts, the ocean energy remains a largely untapped energy resource in the UK and worldwide. At the end of 2017, there was 529 MW of installed capacity in operation globally, of which more than 90 per cent came from only two tidal barrage facilities – Rance Tidal Power Station in France and Sihwa in South Korea (REN21 2018). The other 10 per cent are wave and tidal-stream resources. The successful deployment of MeyGen (Atlantis Resources Limited 2018) and Nova Innovation (Nova Innovation 2019) tidal stream, located off Caithness and Shetland respectively (Scotland, UK), have presented a breakthrough in commercial viability of the tidal stream technology. Both schemes are connected to the national grid, are fully-operational, and have already received a full consent and necessary permissions for

construction of additional turbines that will further increase their capacity. Although there has recently been more progress in the tidal stream energy, tidal range represents a more established technology, with the first successful tidal range project deployed more than 50 years ago.

2.2.1 Tidal power

In literature, the terms 'Marine power', 'Ocean energy' and 'Hydropower' are often used interchangeably when referring to tidal power. Diagram in Figure 2.1 illustrates the relationship of tidal power with these expressions. Adjectives 'marine' and 'ocean' are synonyms that refer to the energy carried by the ocean's body of water; i.e. waves, tides, salinity gradients and temperature gradients (IRENA 2018b). Offshore wind and offshore solar farms are sometimes erroneously included in this group because they are both constructed in marine environments. However, their resource for power generation is stored in the atmosphere and the sun respectively, and not in the ocean's body of water. Hydropower relies on the extraction of energy stored in flowing water by driving the water through a hydraulic turbine (IRENA 2018a). The hydroelectric power can be generated either from (i) the potential energy (dams, pumped-storage and tidal range) or from (ii) the kinetic energy (low-head hydro on rivers, ocean currents and tidal stream). Similarly, the terms 'energy' and 'power' are often used as synonyms, even though they technically mean different things. Energy is the capability to do work or generate power, while power represents the rate of extracted/consumed energy per unit time, most of the times in the form of electricity. The terms are interrelated and can, therefore, be used interchangeably when describing the technology; for example, tidal power and tidal energy both refer to the technology used for harnessing the energy stored in tides.

Chapter 2 Literature review

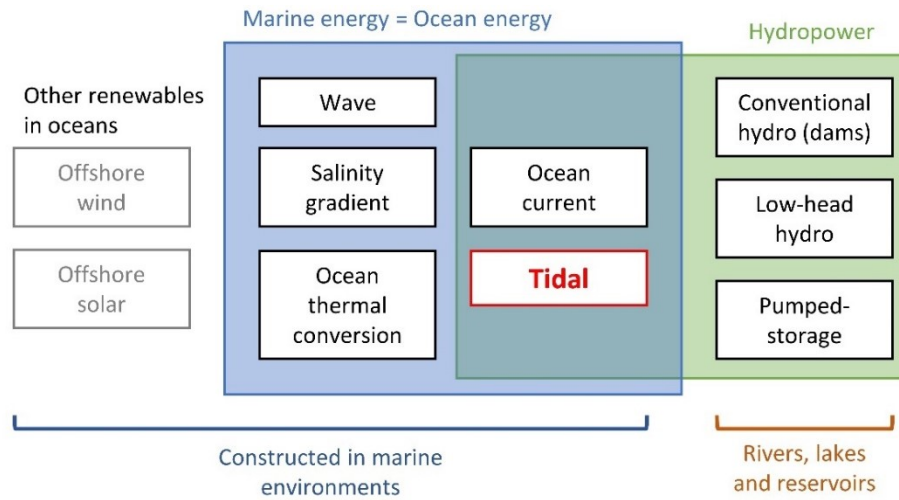


Figure 2.1: A diagram illustrating the overlap between marine energy and hydro-power.

Tidal power can be further divided into three sub-groups: tidal range, tidal stream and other innovative solutions (Figure 2.2). The latter represent embryonic technologies that could theoretically work but have not been yet seriously considered for practical deployment. They include proposals like tidal reefs and tidal fences – modified barrage designs that would lessen the impacts on the environment (DECC 2008), or Dynamic Tidal Power – a technology that uses a difference between the potential and kinetic energy of tides (Hulsbergen et al. 2008).

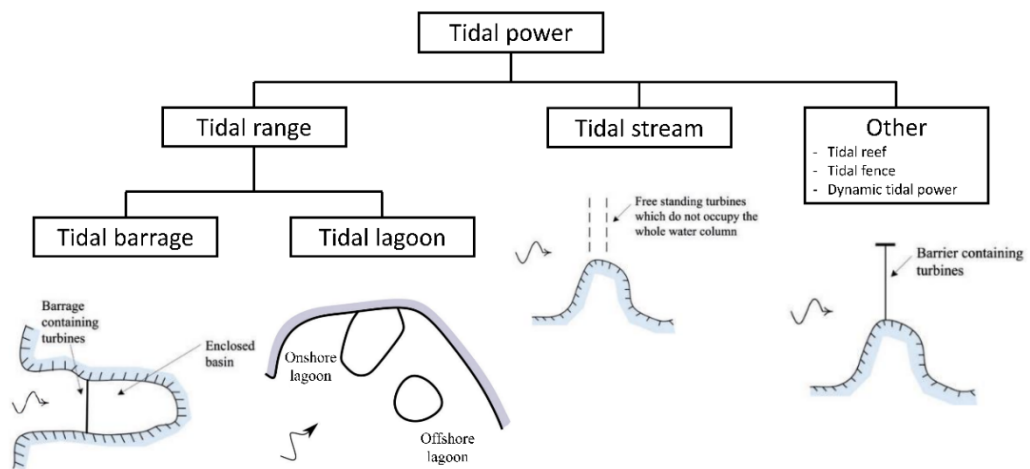


Figure 2.2: Classification of tidal power technologies. Adapted from Adcock et al. (2015).

Tidal range and tidal stream are the two main technological concepts for extracting energy from tides. Tidal stream takes advantage of kinetic energy stored in tidal currents. The energy is extracted through a tidal stream turbine – a device similar to a wind turbine but modified to work in an aquatic environment. Tidal range, on the other hand, relies on the potential energy stored in the tidal amplitude. This is achieved through the construction of a retention wall or an impoundment basin that is used to establish a hydraulic head difference, that drives the turbines installed in the structure's wall.

Based on the layout of the embankment, tidal range structures can be roughly split into two groups: (i) tidal barrages, and (ii) tidal lagoons (Figure 2.2). With tidal barrages, the embankment is constructed across an estuary or a large bay, creating a very large retention basin (DECC 2010). Tidal lagoons usually impound a much smaller area; most commonly they are constructed in the shape of a horseshoe and attached to the coastline (Waters and Aggidis 2016a). To avoid construction in the intertidal zone, the lagoon could be instead located offshore, usually taking a more circular shape to make the construction more economical (Adcock et al. 2015).

2.2.2 Review papers of tidal power technology

A number of review papers on the status of tidal range technology have been published over the last decade. They have provided an extensive database on the technology by collating the data from research studies spanning over the last 50 years and over a number of countries where tidal energy was successfully deployed. First such review was published by Rourke et al. (2010) with an aim to identify some of the key challenges that are holding back the development of the technology. It focused on tidal energy in general, explaining the theoretical background of the technology, listing the existing successful projects and identifying potential future projects worldwide. A review by Adcock et al. (2015) focused more on the advancements in hydraulic modelling of tidal power generation. The paper identifies the need for a multi-scale approach to numerical modelling of tidal energy projects; each scale cannot be fully uncoupled from the

adjacent scales and understanding these interactions is one of the key challenges faced by engineers. This is true for both tidal range and tidal stream technologies, where turbine-induced velocity patterns usually occur on a sub-grid scale and cannot be accounted for in conventional hydrodynamic models. A review by Waters and Aggidis (2016b) focused solely on the tidal range energy. The paper reviewed the possible alternative technologies and optimization techniques that could be introduced into the design of TRS to make them more attractive from the economic and ecological point of view. They include pumping and double-basin operating methods, as well as modified turbine designs and innovative solutions such as Archimedes screw and gyro turbines. However, many of the presented technologies were still at the theoretical stage at the time of the writing and could not realistically replace the conventional methods any time soon. This was followed by a review by Roberts et al. (2016) that focused on small-scale power generation in shallow-near-shore waters. Tidal stream turbines were identified as a preferable option for such deployment. The paper also investigated tidal lagoons which showed to be the least appropriate for deployment in near-shore environments, because they require significantly more investment to generate comparable levels of power at the small-scale level compared to tidal stream technologies. However, in 2016 an independent review of tidal lagoons, commissioned by the UK Government, provided unequivocal support for the development of UK's first tidal range structure – the Swansea Bay lagoon (Hendry 2016). The report identified the lagoon as a pilot project for further development of the tidal lagoon programme in the UK. If built, the project would provide valuable data on the full range of impacts on the environment – the biggest concern currently limiting the development of TRS – paving the way towards the larger-scale projects. Finally, a review by Neill et al. (2018) provided the most recent overview of the technology at the time of this writing. Tidal lagoons have been progressively generating commercial interest over recent times and were, therefore, the main focus of the review. The technology for building a lagoon is well known and has considerably improved since the deployment of the first TRS in the 1960s. However, high construction costs and uncertainty over environmental impacts still remain the main challenges preventing further deployment of the technology.

2.2.3 Existing projects

The history of harnessing tidal energy stretches all the way back to ancient times (Charlier and Menanteau 1997). The technology known as a tidal mill was already used by the ancient Greeks. Tidal mills were simple yet effective structures, using the water wheel to generate mechanical power by harnessing tidal energy, either directly from the tidal stream or through a construction of a dam with sluices, that formed a retention basin (Figure 2.3), from which the water was released during the low tides (Charlier 2007). The two concepts essentially represent the first prototypes of the modern-type tidal stream and tidal range power plants. The technology has been used continuously throughout history, however, it was not until the 1960s when tides were for the first time used to generate electricity instead of just mechanical power. The first such project was successfully built in France on the Rance River estuary in 1966. Similar smaller projects followed in Russia (Kislaya Guba), Canada (Annapolis Royal Generating Station) and China (Jiangxia) in 1968, 1984 and 1985 respectively (Table 2.2). After that, it was not until 2011 when the next larger project was constructed; on Lake Sihwa in South Korea, a tidal range power plant was installed into an existing barrage, transforming an artificial lake into a tidal basin, making it the largest tidal range scheme by installed capacity in the world. Even though there is still a lot of unused potential for tidal generation worldwide, no new tidal range energy projects have been initiated since.

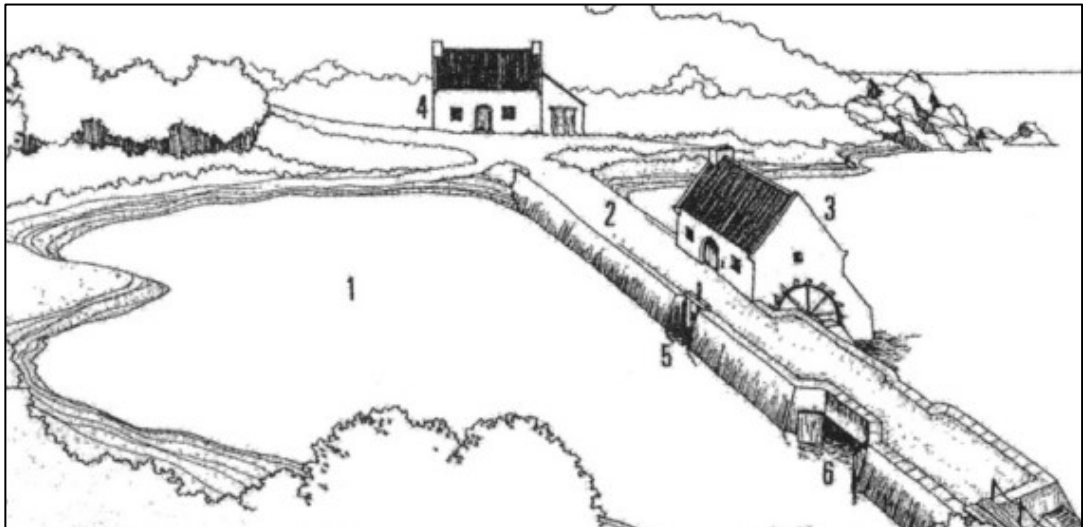


Figure 2.3: Drawing of a traditional tide mill with (1) retention basin, (2) dam, (3) mill, (4) miller's dwelling, (5) sluce leading to the hydraulic wheel, and (6) sluce gate (Charlier 2007).

Table 2.2: Overview of the operational tidal range projects as of 2018.

Power Plant	Country	Year	Capacity (MW)	Basin area (km ²)	Mean tidal range (m)
La Rance	France	1966	240	22	7.9
Kislaya Guba	Russia	1968	1.7	2	2.4
Annapolis Royal	Canada	1984	20	6	6.4
Jiangxia	China	1985	3.9	2	5.0
Lake Sihwa	South Korea	2011	254	42	7.8

Rance Tidal Power Station, France

The Rance Tidal Power Station is located on the estuary of the Rance River in Brittany, France (Figure 2.4). It is the first fully operational tidal range project in the world; opened in 1966, it has been reliably producing electricity for over 50 years (Charlier 2007). The barrage is 750 m long and extends down to a depth of 13 m, forming a 22 km² impoundment basin with a 184 million m³ storage capacity (Andre 1978). The barrage houses 24 identical 10 MW bulb units, which produce a total output of 240 MW and have an annual production capacity of around 480 GWh and a capacity factor of 24 per cent (Andre 1976; Neill et al. 2018). The turbines can only generate on an ebb tide, most efficiently under a head of 10 m, and between limits of 3.4 and 16.5 m (Andre 1976). The project is considered a success, however, the concerns about the associated environmental impacts have continually been raised since the beginning of its operation. Much of the damage has been caused by the construction, effectively destroying the local marine ecosystem (Retiere 1994). However, the majority of the species have since then returned; better understanding of the biological processes in the estuaries and continuous advancements in construction techniques mean that future projects should be able to avoid similar outcomes (Kirby and Retière 2009).

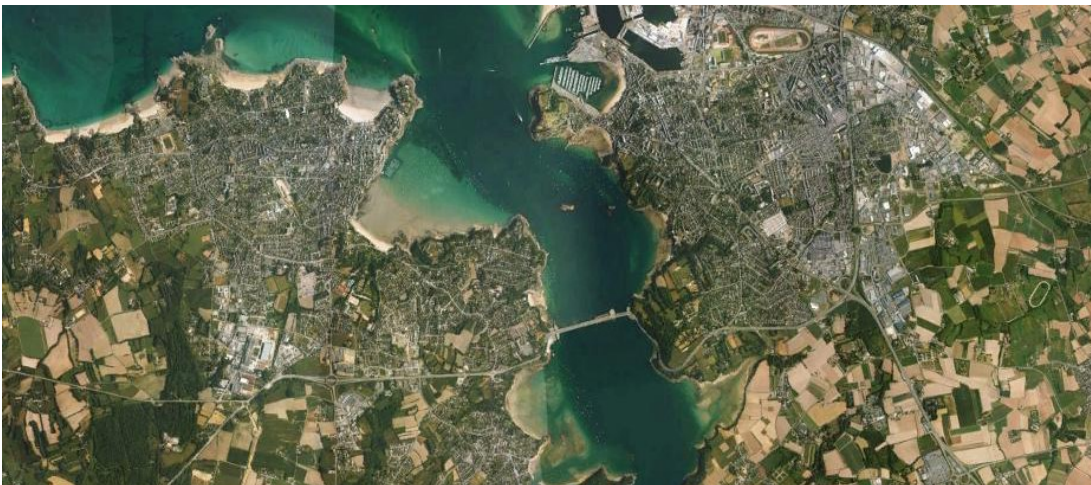


Figure 2.4: An aerial image of the Rance Tidal Power Station located in the Rance River estuary in France. Image captured from Google Earth.

Sihwa Lake Tidal Power Station, South Korea

Sihwa Lake Tidal Power Station is currently the world's largest (by capacity) and most recent tidal range structure. It is located on the western side of the Korean Peninsula (Figure 2.5), in the region experiencing the highest tides in the Yellow Sea (Lee 2011). The embankment, forming the Shiwa dam, was initially constructed to create a freshwater reservoir in the Kyeonggi Bay, creating a 56.5 km² lake, while also creating 173 km² of reclaimed land (Bae et al. 2010). Soon after construction, the lake was severely contaminated by the excessive inflow of polluted wastewater from the local industry. The only way to improve the water quality of the bay was to allow seawater exchange with the reservoir. The authorities saw an opportunity to turn this disaster into a positive; they constructed a tidal range power plant, that is simultaneously performing two functions: (i) seawater exchange for improved water quality and (ii) clean power generation. The power plant incorporates 10 bulb units with a total capacity of 254 MW and employs a flood-only operational scheme due to the limitations of the maximum water surface elevation in the lake (Cho et al. 2012). The project was considered a great success from a power generation, environmental and tourism points of view, so much so that it led South Korean government to explore further options for tidal range schemes in the region (Waters and Aggidis 2016b).



Figure 2.5: An aerial image of the Sihwa Lake Tidal Power Station located in the on the western coast of the Korean Peninsula. Image captured from Google Earth.

Kislaya Guba Tidal Power Station, Russia

Kislaya Guba Tidal Power Station was constructed in 1968 as a trial project by the Soviet government (Bernshtein 1972). Located in the Kislaya Guba fjord in the Barents Sea (Figure 2.6), it is the smallest of the existing tidal range schemes. Initially designed for just 400 kW, its installed capacity has recently grown to 1.7 MW (Neill et al. 2018). The power plant has recently celebrated 50 years of successful electricity generation, motivating the government to explore other viable sites in Russia – the White Sea reportedly holds a potential of 16 000 MW in its tidal range (Chaineux and Charlier 2008).

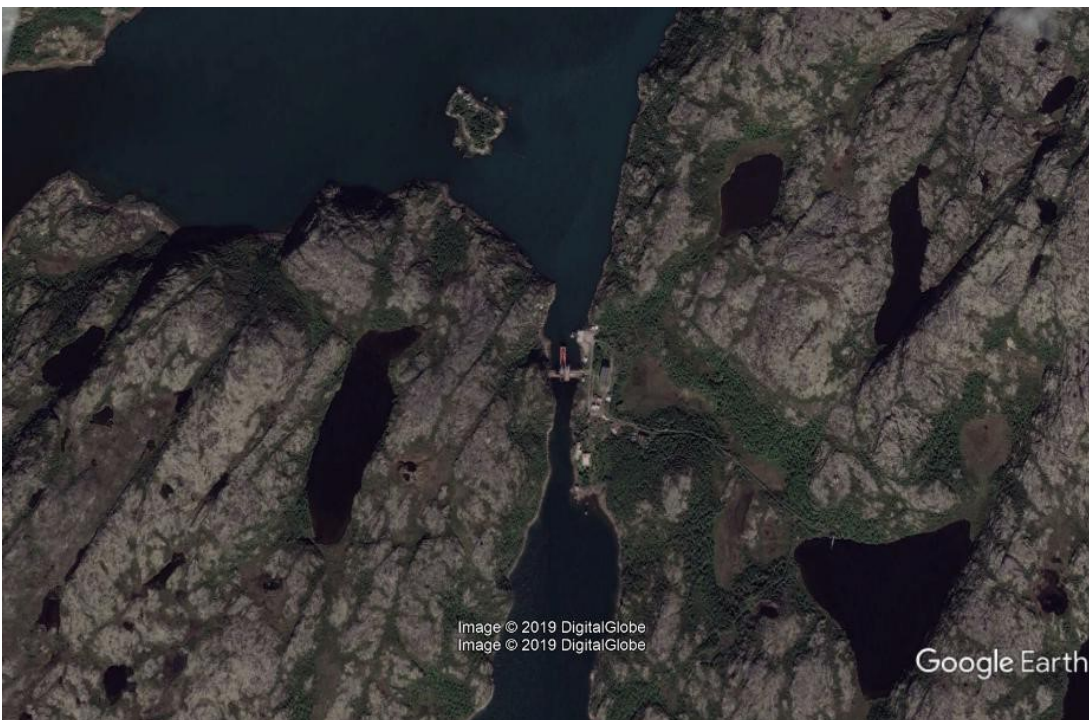


Figure 2.6: An aerial image of Kislaya the Guba Tidal Power Station located in the Kislaya Guba fjord in the Barents Sea, Russia. Image captured from Google Earth.

Annapolis Royal Generating Station, Canada

The Annapolis Royal Generating Station is a 20 MW tidal range power plant, located on the Annapolis River in Nova Scotia, Canada (Figure 2.7). Constructed in 1984, this scheme consists of a single Straflo turbine with a 20 MW of installed capacity, that produces 50 GWh of electricity per year. The powerplant is also used for flood defence, while the installed ship locks serve as an important transport link on the Annapolis River (Neill et al. 2018).



Figure 2.7: An aerial image of the Annapolis Royal Generating Station located on the Annapolis River in Nova Scotia, Canada. Image captured from Google Earth

Jiangxia Tidal Power Station, China

The Jiangxia Tidal Power Station was opened in 1985 and is located in Jiangxia Harbour, Wenling City, Zhejiang Province, China (Figure 2.8). The power plant operates bi-directionally and houses six bulb turbines, the last of which was installed in 2007, providing an installed capacity of 3.9MW (Wang et al. 2011). There have been several other tidal range proposals in Zhejiang Province that never became fully operational due to the issues with turbine construction and location-related problems (Du et al. 2017; Li and Pan 2017).



Figure 2.8: An aerial image of the Jiangxia Tidal Power Station located in the in Jiangxia Harbour, Wenling City, China. Image captured from Google Earth

2.2.4 Tidal resource and future proposals

There are many possible locations in the UK and worldwide, that are potentially feasible for the exploitation of tidal range for power generation. The Severn Estuary and Bristol Channel have been for decades considered as one of the key locations for the deployment of the technology in the UK (Roberts 1982). Other notable sites currently undergoing feasibility studies include Bay of Fundy in Canada (Cornett et al. 2013); White Sea in Russia (Bernshtein 1972); and Mersey Estuary (Aggidis and Benzon 2013), Soloway Firth (Aggidis and Feather 2012), Morecambe Bay (Burrows et al. 2009) and North Wales Coast (Evans et al. 2004) in the UK. In addition to these larger sites, there are numerous small-scale sites of interest in South Korea, India, Australia and Brazil (Rourke et al. 2010).

Worldwide

The analysis by Neill et al. (2018) estimated the global annual theoretical tidal range resource to be around 25 880 TWh. The resource characterization was based on annual sea surface elevations and water depths at $1/16^\circ \times 1/16^\circ$ global resolution and is presented on a contour map in Figure 2.9. The minimum acceptable annual energy yield was assumed to be 50 kWh/m² and maximum acceptable water depth of 30 m, constraining the potentially viable areas to coastal regions of only 11 countries (presented in the darker shades of red in Figure 2.9). Sorted in the order from having the most to having the least tidal range resource they include Australia, Canada, United Kingdom, France, USA, Brazil, South Korea, Argentina, Russia, India and China.

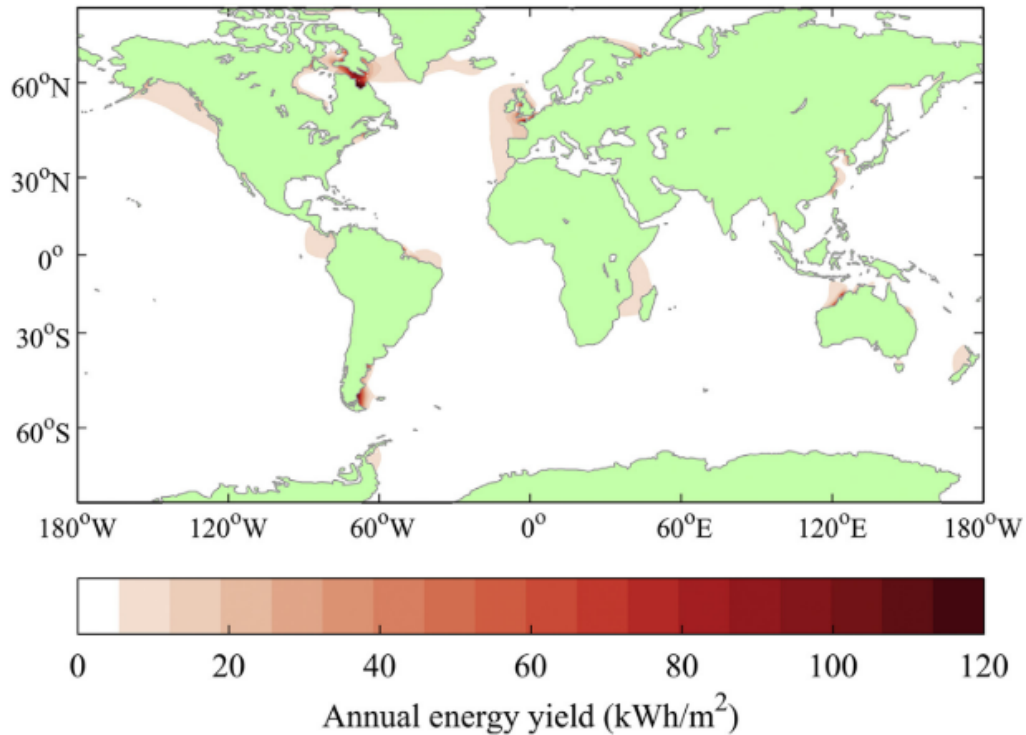


Figure 2.9: The global theoretical tidal range energy resource calculated as annual energy yield in kWh/m² (Neill et al. 2018).

However, in practice, the technical resource could be significantly lower than the estimated theoretical yield; according to some estimations the effective resource as low as 37 per cent (Prandle 1984). In addition, some areas could be impossible to exploit due to practical difficulties with development at larger scales, or due to the socio-economic, political and environmental constraints. Sea ice presents another obstacle for northern locations including Alaska, and Hudson Bay in Canada. Considering all these restrictions, the available global annual potential energy is reduced to 5792 TWh, with 90 per cent of the resource distributed across only five countries, including Australia, Canada, UK, France and USA. For a detailed list of locations, that were identified as technically feasible, the readers are referred to the publication by Neil et al. (2018).

United Kingdom

The review paper by Neill et al. (2018) has further focused on the northwest European shelf seas and including the entirety of the British Isles and French north coast (Figure 2.10). This region alone contains approximately one-quarter of the global theoretical resource. Based on the criteria for the exploitable area, 53 per cent of the resource was found in UK waters, with the remaining 47 per cent found off the north coast of France. In the UK it is concentrated along the coasts of Liverpool Bay, the Severn Estuary and Bristol Channel, Wash, and southeast England (Table 2.3). It has been estimated that the total UK tidal range potential could meet 10-15% of the UK's current electricity demand (DECC 2010). The most attractive region for the tidal range generation is the Severn Estuary (Table 2.3); with an exceptional tidal range of 14 m and a potential maximum installed capacity of 13.5 GW and a capacity factor of up to 20 per cent, it was estimated that it could deliver 19.7 TWh of electricity per year. For comparison, the proposed Hinkley Point C nuclear power station is expected to provide a similar annual output, however, due to a high capacity factor in the range of 90 per cent for modern day nuclear power technologies, this could be achieved through only 3.2 GW of electricity generation capacity (BEIS 2016).

Table 2.3: UK Tidal range resource by region (DECC 2010).

Location	Mean tidal range (m)	Estimated max. installed capacity (MW)	Predicted annual energy output (GWh)
Severn Estuary	11	13 500	19 700
Solway Firth	5.5	7200	10 250
Morecambe Bay	6.3	3000	4630
Wash	4.45	2400	3750
Humber	4.1	1080	1650
Thames	4.2	1120	1370
Mersey	6.45	700	1320
Dee	5.95	840	1160

Chapter 2

Literature review

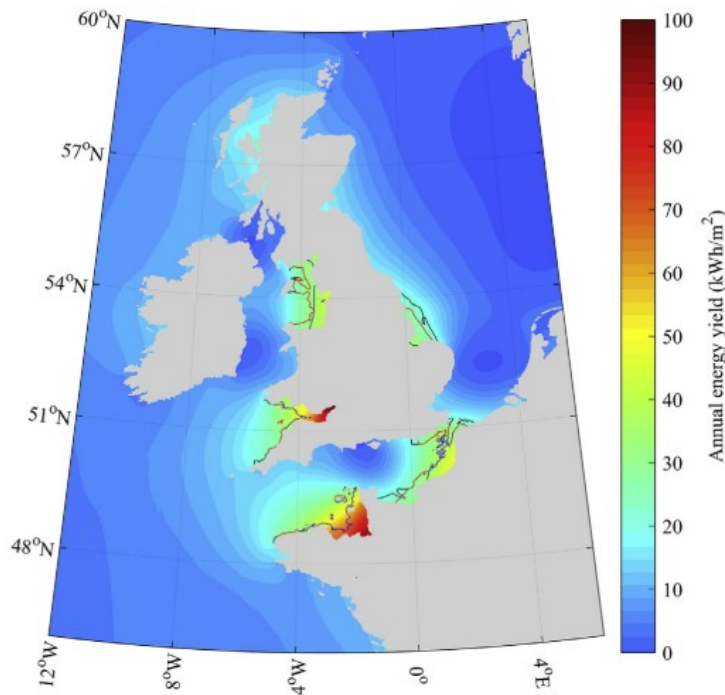


Figure 2.10: The theoretical tidal range energy resource over the northwest European shelf seas, calculated as annual energy yield in kWh/m². Areas landward of the [blue, red, black] contour lines denote regions with water depths less than 30m and where energy density exceeds 84, 60, and 50 kWh/m², respectively (Neill et al. 2018).

Following a public consultation in 2010, the Department of Energy and Climate Change (DECC) released a map of shortlisted tidal range schemes in the Severn Estuary, that are presented in Figure 2.11 (DECC 2010). The factors used to determine feasibility of the proposals were: (i) technical risk, (ii) cost of construction, (iii) cost of produced energy, (iv) how the costs fit into the energy and climate change goals, (v) affordability, (vi) environmental impact, and (vii) regional impact (ports, fishing and employment). The shortlisted schemes are all based on the technology that has been already tried and tested in tidal range schemes across the world.

Chapter 2 Literature review

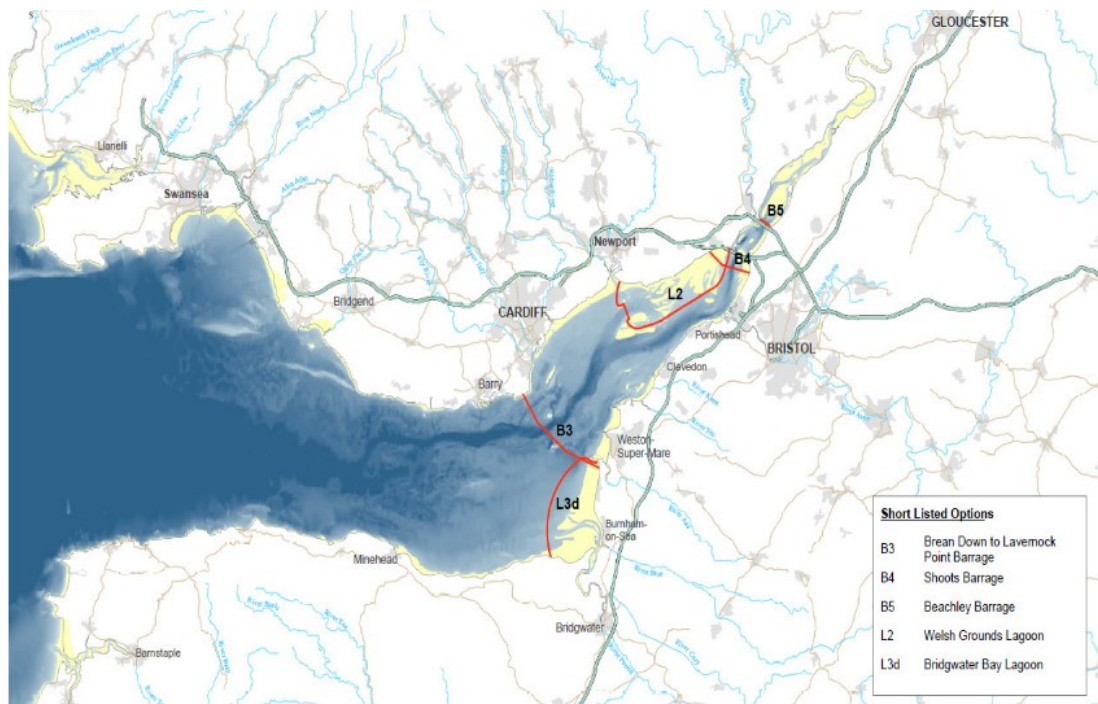


Figure 2.11: Map of shortlisted schemes in the Severn Estuary (DECC 2010).

The projects, shortlisted in Figure 2.11, included three tidal barrage alternatives, as well as two different tidal lagoon proposals. The barrage proposals have since fallen out of favour and the focus has shifted more towards the lagoons. Because lagoons are significantly smaller structures, they are viewed as a more environmentally-friendly alternative to the barrages, as well as more economical and technically feasible (Hinson 2018). In 2012, a report from Crown Estates (2016) concluded that there is potential for a significant quantity of tidal lagoons in the UK, particularly on the West Coast. This was soon followed by an ambitious plan from Tidal Lagoon Power Ltd (TLP) to develop proposals for a fleet of six tidal lagoons around the country (Figure 2.12), the first one being the Swansea Bay tidal lagoon (Cabr 2014).



Figure 2.12: Sites, identified by TLP viable for tidal range lagoon deployment in the UK; Red - Swansea Bay lagoon; Blue - TLP projects under development; Yellow - additional viable sites (Tidal Lagoon Power 2016).

Both Severn barrage and Swansea Bay lagoon were used as case studies in this thesis. The Severn barrage was selected as a development model for the TRS modifications to the Delft3D software as presented in Chapter 5. A more detailed case study featuring the Swansea Bay lagoon is presented in Chapter 7.

The Severn Barrage

The first proposal for a barrage in the Severn Estuary dates back to 1849 when Thomas Fulljames proposed building a barrage from Beachley to Aust (Figure 2.13a) with an aim to establish conditions for a large shipping harbour in the estuary (Carne 1995). The commercialization of the electricity production in the next century popularised the idea of a tidal barrage powerplant, that could harness a great capacity of electricity due to the

exceptional tidal range in the estuary. In search of the most feasible solution, the barrage design went through a number of proposals. The advancements in numerical simulations contributed to even more rapid development of the proposals in recent years. Several different locations along the Severn Estuary were considered, with the UK government shortlisting three possible layouts in a feasibility study in 2010 (DECC 2010). The possible layouts included Beachley Barrage, located just upstream of the Severn Bridge and the smallest of the selected alternatives (Figure 2.11-B5); Shoots Barrage, a smaller barrage located just downstream of the Second Severn Crossing (Figure 2.11-B4); and Brean Down to Lavernock Point Barrage, the same layout as first proposed by the Severn Tidal Power Group (STPG 1989).

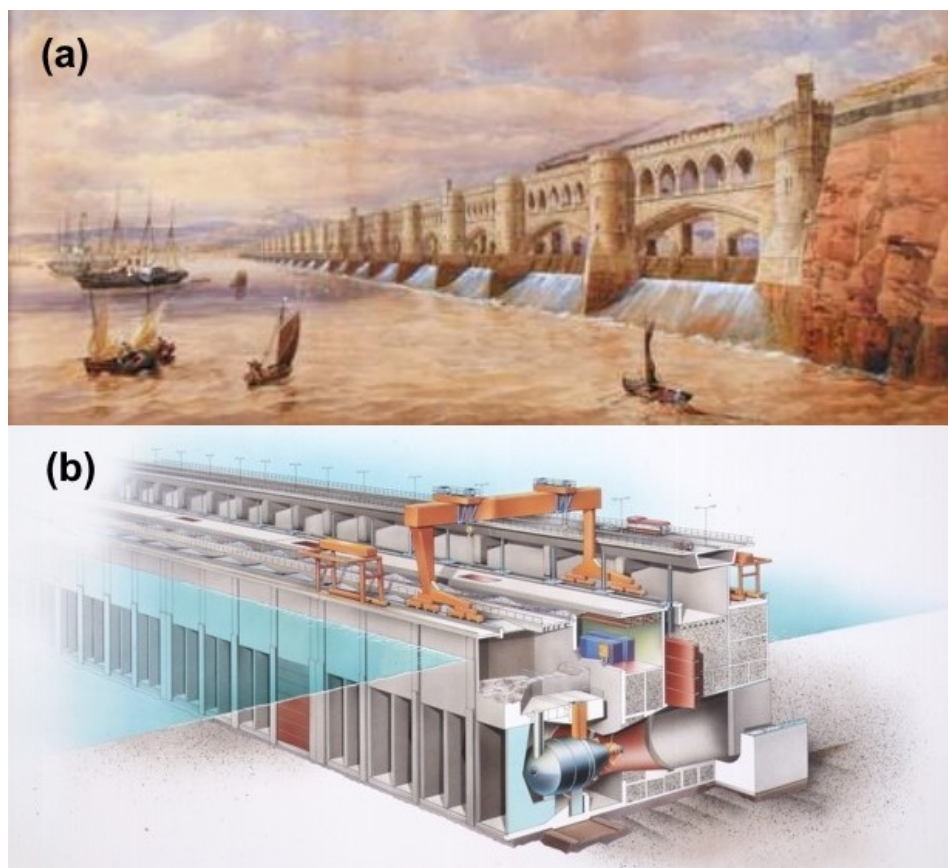


Figure 2.13: Severn Barrage designs: (a) Thomas Fulljames's own impression of his proposed barrage in 1849; (b) Cutaway view of turbine caisson with a bulb turbine.

The most popular and the most studied of the alternatives is the STPG design and is commonly referred to as the original Severn Barrage (Falconer et al. 2009). The proposal presented a 16.2 km long barrage (Figure 2.13b), housing 216 bulb turbines for a total installed capacity of 8640 MW, generating only during the ebb tide (STPG 1989). It was predicted that such a scheme should yield between 14 and 17 TWh of electricity per year, roughly equivalent to 5 per cent of the UK's electricity demand (Bray et al. 2016). The project has been viewed as somewhat controversial, mostly because of the inevitable environmental implications of such a large-scale project, including changes in tidal range regime, potential loss of intertidal zones and reduction of tidal currents, directly and indirectly affecting the turbidity, suspended sediment concentrations and the benthic ecosystem (Kadiri et al. 2012). However, there were also noteworthy benefits to the construction of a barrage, such as reduction of flood risk (Ahmadian et al. 2014a), opportunities for recreation and tourism, and bolstering of local industry. The Severn Barrage tidal range power plant has been considered economically unfeasible by the UK Government, however, the project has not been ruled out of future consideration, if the environmental implications could be mitigated (DTI 2003).

The Swansea Bay Lagoon

In 2011, the TLP was set up to develop, construct and operate tidal lagoon power stations, with the project in Swansea Bay being the first of the six proposed schemes in the UK (Hendry 2016). The project involves the construction of an artificial lagoon in a shape of a horseshoe, connected to the Swansea Bay coast Figure 2.14, creating an 11.6 km² impoundment for the purpose of tidal power generation (Waters and Aggidis 2016a). Even though it would be considerably smaller than the proposed Severn barrage, if constructed, it would become the world's largest tidal range power plant to date. The lagoon would incorporate 16 bulb turbines (pictured in Figure 2.15b) for a total installed capacity of 320 MW, generating an estimated annual output of 0.5 TWh. The TLP was planning to design a lagoon-specific type of bi-directional bulb turbine (pictured in Figure 2.15a), that could be standardised and easily scalable, reducing the turbine cost of future projects (Tidal Lagoon Power 2016).

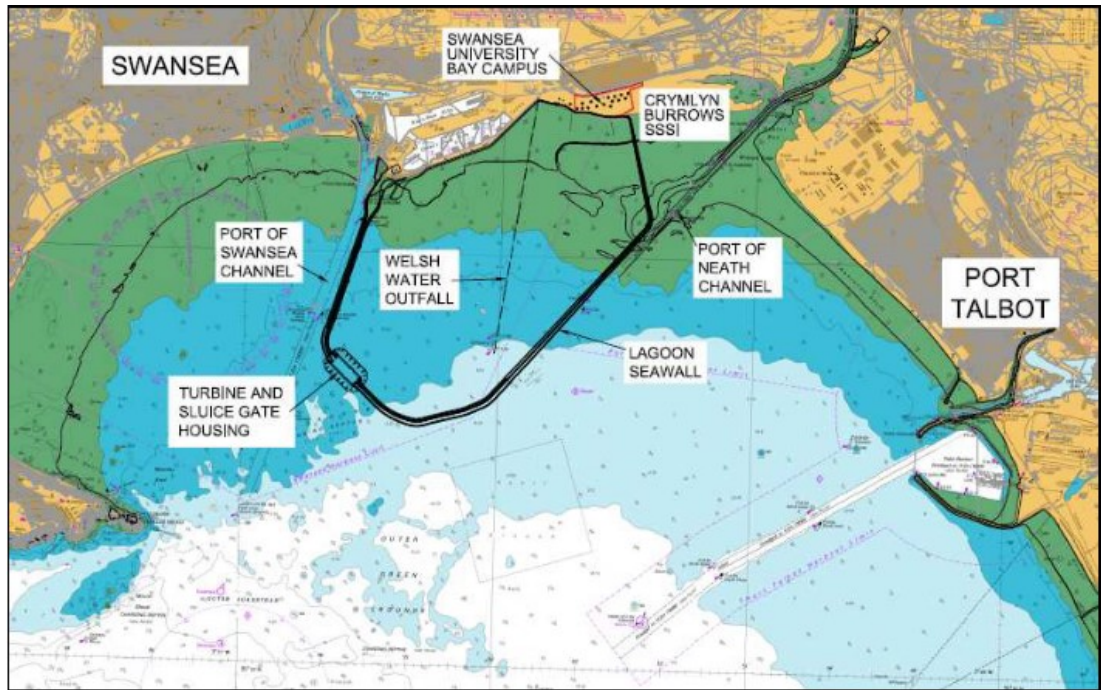


Figure 2.14: Swansea Bay Lagoon layout overlaid on the Admiralty Chart background (Tidal Lagoon Plc 2017).

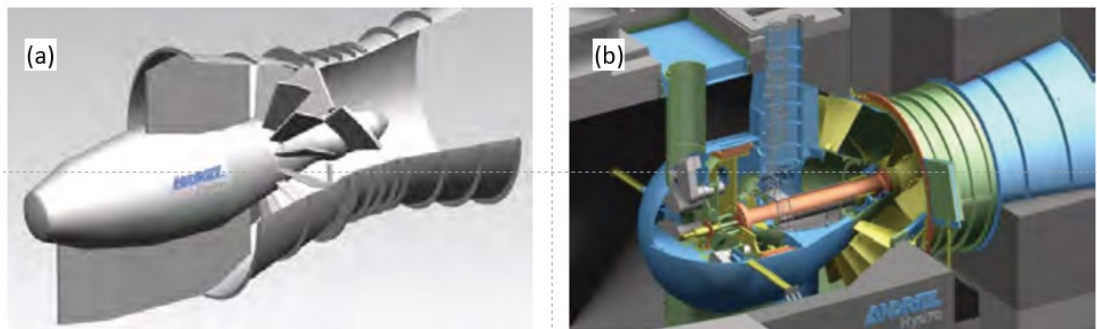


Figure 2.15: (a) A bulb turbine designed specifically for tidal range schemes. (b) The design is based on the conventional bulb turbine (Tidal Lagoon Power 2016).

One of the main environmental concerns associated with tidal lagoons is their impact on sediment dynamics (Neill et al. 2017). How the construction of a lagoon affects sediment dynamics is directly connected to the changes in the tidal hydrodynamics and will be significantly influenced by the operating mode and the design of the structure (Cornett

Chapter 2

Literature review

et al. 2013). It was shown that a counter-rotating eddy may form on the sides of the jet discharged from the turbines, significantly changing local sediment transport. Inside the impoundment, the reduced velocity can lead to increased accumulation of sediments which can lead to silting of the lagoon.

The project received development consent from the Secretary of State for Energy and Climate Change in 2015 and full support from the independent review, commissioned by the UK Government, entitled the Hendry Review of Tidal Lagoons (Hendry 2016). However, the UK government has recently withdrawn its support for the project and put the project indefinitely on hold, with the main concern being the cost of electricity compared to alternatives, such as wind farms and nuclear power (Guardian Media Group 2018).

2.2.5 Advantages and disadvantages of TRS

Advantages	Disadvantages
<p>Renewable source</p> <p>They do not depend on fossil fuels and do not produce CO₂ emissions. The source (tidal range) is renewed continuously by the gravitational pull of the Moon and Sun (Rourke et al. 2010).</p> <p>Reliable</p> <p>TRSs are designed for a very long lifespan; for example, the expected lifetime of the proposed Severn Barrage is 120 years, with turbine replacement occurring only every 40 years (Kelly et al. 2012).</p> <p>Efficient</p> <p>Bulb turbines used in TRSs are known to have high efficiency, with peak values above 90 per cent (Waters and Aggidis 2016b)</p> <p>Low operating costs</p> <p>They have low operating costs since they can virtually operate unattended (Hendry 2016).</p> <p>Flood protection</p> <p>TRSs can reduce the flood risk of the impounded coastal areas (Ahmadian et al. 2014b).</p> <p>Consistent and predictable</p> <p>Tides can be forecasted and are therefore predictable, which also means that power generation is predictable (Neill et al. 2018).</p>	<p>Location-specific</p> <p>Generation costs for TRSs are driven by the strength of the tidal range and the bathymetry of the site (Hendry 2016). Only 5 countries share 90 per cent of the resource (Neill et al. 2018).</p> <p>Environmental impacts</p> <p>Can change mean water elevations and reduce max. current velocity (Xia et al. 2010c). Impact on fish, marine mammals and birds (Dadswell and Rulifson 1994).</p> <p>Uncertainty</p> <p>Impacts are difficult to quantify, and so governments are hesitant to proceed with large-scale development (Neill et al. 2018).</p> <p>Distance from the grid</p> <p>Require construction close to the existing national grids to prevent excessive grid connection costs (Hendry 2016).</p> <p>High initial cost</p> <p>The estimated construction costs are substantial; £1bn for a lagoon in Swansea Bay and £34bn for the barrage across the Severn Estuary (Waters and Aggidis 2016a).</p>

2.3 Tidal hydrodynamics

Tidal energy is derived from the gravitational pull between the Earth's oceans and the heavenly bodies, particularly the Moon and the Sun, as well as from the centrifugal force produced by the rotation of the Earth and Moon about each other, as illustrated in Figure 2.16 (Rourke et al. 2010). This means that tidal phenomena are periodic, with the exact nature of periodic response varying according to the movement of the bodies and local geographical peculiarities (Hammons 1993).

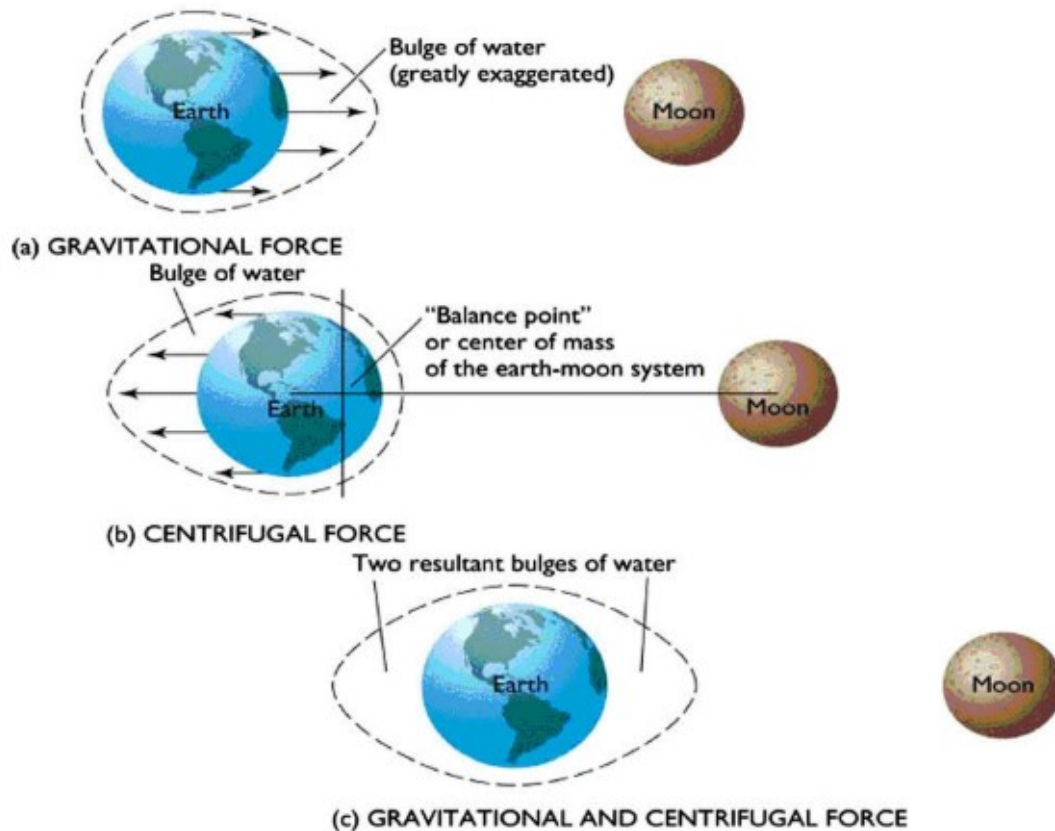


Figure 2.16: The effects of the Moon on the tidal range (Rourke et al. 2010).

The contribution to the tide by the energy at a particular frequency can be described by tidal harmonic constituent. Each constituent is represented by a cosine curve and holds

the information about its amplitude and phase lag. Summing up a set of various tidal constituents gives a harmonic tidal prediction that can be used by numerical models. The nomenclature for naming the constituents is a combination of a capital letter (or Greek letter in some cases) and a subscript number, which explain the source of the constituent and an approximate number of cycles per day respectively. For example, the most common constituents are M_2 and S_2 which present the influence of the Moon with 1.9323 tidal cycles per day and Sun with exactly 2 tidal cycles per day, both greatly contributing to the semidiurnal tidal activity (Parker 2007). Because of the elliptical orbit of the Moon and Earth the amplitude of the semidiurnal tide varies through the lunar month (29.5 days), with the tidal range being greatest at the full moon or new moon (spring tides) and lowest at half-moon (neap tides). Other major tidal constituents include N_2 and L_2 with a slightly higher and lower period than M_2 respectively, and diurnal constituents K_1 , O_1 , P_1 , Q_1 , and S_1 , with periods of 23.93, 25.82, 24.07, 26.87, and 24.00 hours (Wolanski and Elliott 2016).

Figure 2.17 illustrates two different extremes of an idealised tidal wave propagating in the shallow waters. If the wave enters an endless river, it will propagate up the river as a progressive wave (Figure 2.17a). Both crest and trough of the wave, i.e. high and low tide, move progressively up the reach, with the maximum flood current occurring at the same time as high water. If the width of the river was to decrease, moving upstream, the amplitude will increase due to the funnelling effect, as the same amount of water is being forced through a smaller cross-section. If this river is closed-off at exactly one quarter of a tidal wavelength, the tidal wave will be reflected at the closed end, superimposing the incoming and outgoing waves into a standing wave (Figure 2.17b). In this case, high water would occur at the same time everywhere on one side of the node and the tidal range would increase due to the superposition of the amplitude. If the tidal basin has the right combination of length and depth, where the natural period is exactly the same as the tidal period, its tidal range will be amplified even further due to the resonance of the tidal waves (Parker 2007).

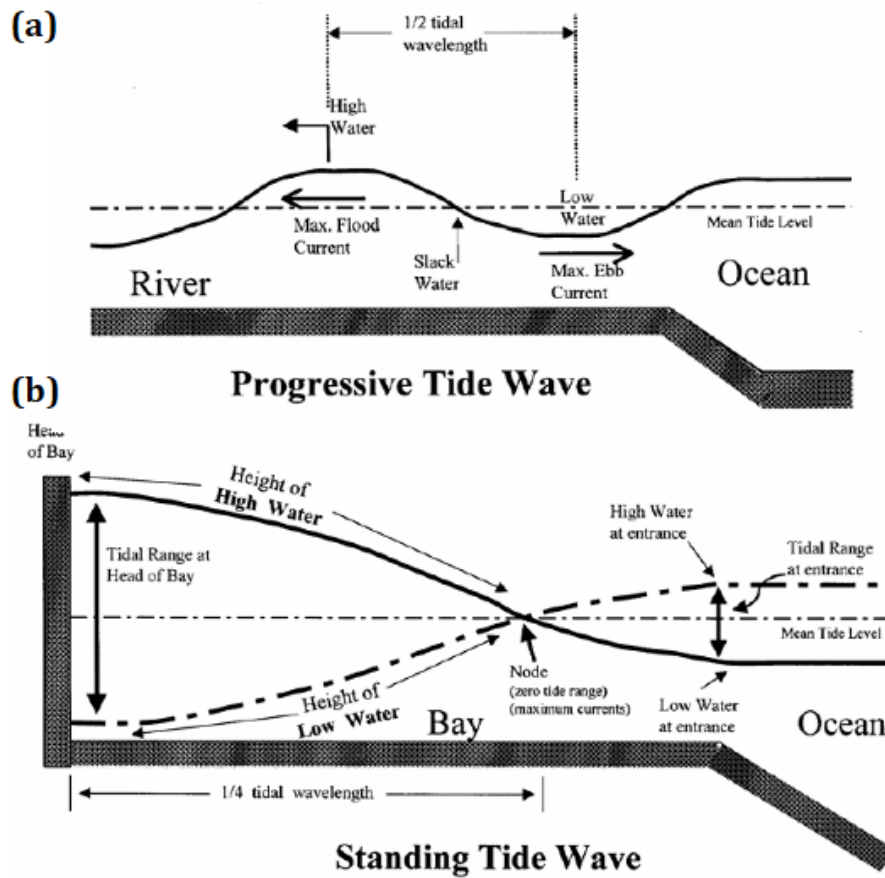


Figure 2.17: Difference in tidal range of shallow waters between (a) the progressive and (b) standing waves, shown for an idealized frictionless tide (Parker 2007).

This is also the case in Severn Estuary, where the tidal range is driven by two main mechanisms: (i) a funnelling effect at the upper reaches of the channel due to the wedge-shaped geometry and (ii) the quarter wavelength resonance of the channel with the incident North Atlantic tidal wave (Gao and Adcock 2015). Figure 2.18a shows the mean spring tidal range in the Bristol Channel and the Severn Estuary due to the combination of these effects, illustrating how tidal range increases with the distance upstream, varying significantly between the different points along the coastline (Hammons 1993). The typical mean spring tide at the mouth of Severn River is 12.2 m, with the high spring tidal range at approximately 14 m (Liang et al. 2014). The cotidal chart in Figure 2.18 shows locations that are in phase with one another (Neill and Hashemi 2018). As shown

on the chart, the entire Severn Estuary experiences a similar tidal phase, which means that water levels rise and fall almost uniformly across the whole domain. These unique characteristics can make the Severn Estuary challenging to represent in a hydrodynamic simulation; careful attention must be paid to the selection of appropriate boundary conditions, especially when including the tidal range energy devices (Adcock et al. 2011).

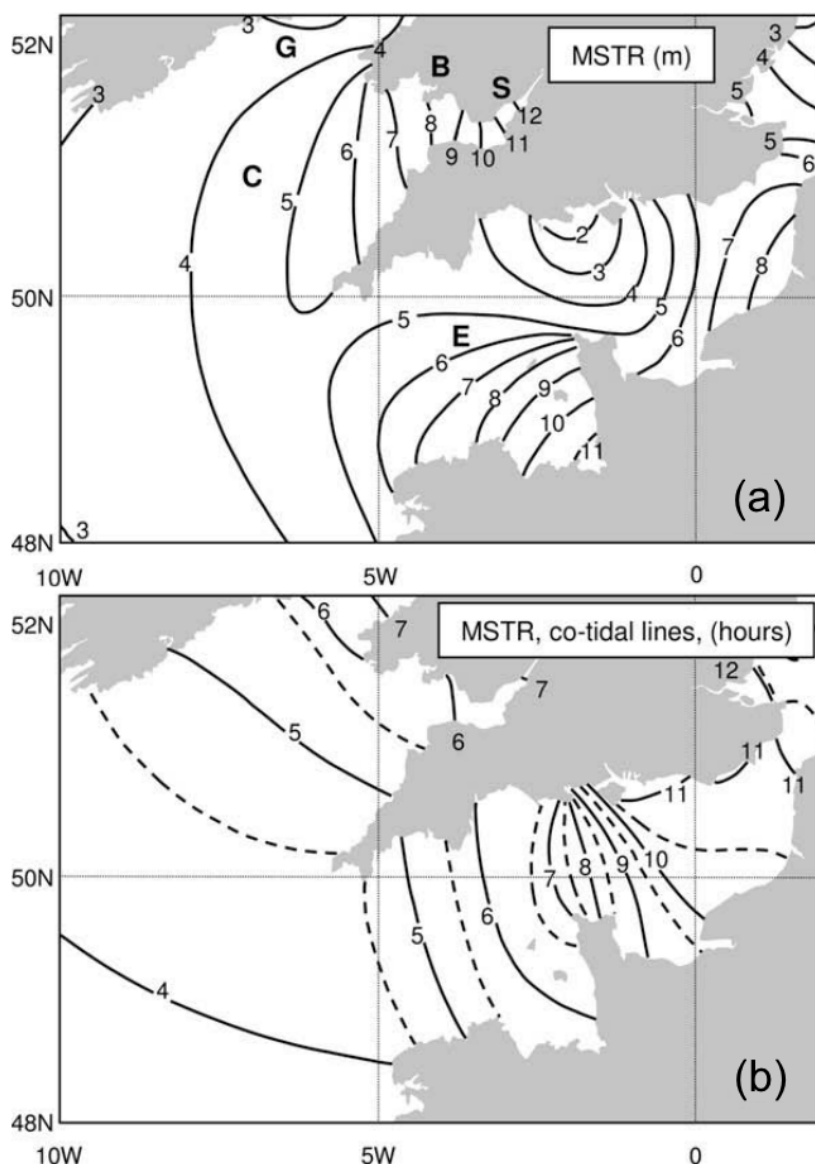


Figure 2.18: (a) Mean spring tidal range and (b) Co-tidal lines, drawn through locations of equal Mean High Water Interval in the Severn Estuary and English Channel (Uncles 2010).

2.4 Numerical modelling of tidal range structures

The main purpose of the hydrodynamic simulations is to provide valuable insight into resource assessment, the quantification of the potential impacts, and minimization of any detrimental effects through design optimisation (Neill et al. 2018). Hydrodynamic models provide time-series approximations of the state variables, such as water surface elevation and current velocity, which makes them useful tools for the study of potential impacts of the TRS. For the simulations to work properly and achieve a high level of reliability, a wide range of multi-scale processes must be included, either by simulating them directly or by providing parameterized approximations. This includes tidal, fluvial and wave dynamics, sediment transport and water quality, as well as the implementation of hydraulic structures, impoundment walls and operational algorithms of the tidal range power plants. The assessment of TRS schemes relies on the development of the numerical tools that can simulate their operation over time. A great number of computational studies on the design and performance has been published to-date. They range from simplified preliminary studies to more complex and detailed investigations of the technology, that often require high-performance computing capabilities for practical application.

2.4.1 The multi-scale modelling approach

A review paper by Adcock et al. (2015) presents the idea of the multi-scale nature of hydrodynamic models. Depending on the motivation and needs, different levels of sophistication are incorporated into the model, and often the scales of a model will overlap. An example of that can be seen in studies by Ahmadian et al. (2010a; 2014a) and Kadiri et al. (2012) where a coupled 1D-2D model is used to achieve higher efficiency and accuracy of sediment transport and water quality. Based on the scale and level of sophistication we can split the models roughly into four different groups: global-, regional-, local- and subgrid-scale models.

Regional-scale models

The majority of hydrodynamic studies of TRS are made on the regional scale. The flow complexities that occur on this level require us to use at least 2D if not 3D numerical models. They usually employ grids with the cell sizes ranging from as small as tens of meters to as large as several kilometres. A number of studies have applied 2D models to investigate the operation and environmental impacts of different TRS schemes. Falconer et al. (2009), Xia et al. (2010c), Kadiri et al. (2012), Ahmadian et al. (2014a) and Zhou et al. (2014b) have all used various numerical models for the analysis of the proposed Severn barrage in the Severn estuary. In all cases, the models have proved useful for a variety of studies, such as; investigation of regional hydrodynamics, sediment transport and water quality, optimisation of power generation efficiency and coastal flood risk assessment. Regional-scale models were also used on many tidal lagoon projects in the UK; Swansea Bay lagoon (Angeloudis et al. 2016b), North Wales lagoons (Ahmadian et al. 2010b; Angeloudis et al. 2016a) and Cardiff lagoon (Xia et al. 2010c; Angeloudis and Falconer 2017) to name just a few.

Global-scale and far-field models

Global-scale models usually refer to the atmospheric and ocean models that cover a large part or even the entire of the Earth's globe. In tidal range modelling, such models are used to assess the open boundary problem that can occur due to the operation of large schemes, e.g. a tidal barrage in an estuary (Adcock et al. 2011). The impacts on the flow conditions can be potentiality so far-reaching that they have a noticeable effect on the open boundary if the domain is too small (i.e. regional-scale). To evaluate far-field impacts in such cases, we need to expand regional models to a global scale. Such models employ a coarser numerical grid to cover an area where open boundary extends far away from the original location to a point where impacts of TRS on boundaries becomes negligible. In the case of the UK, it means going as far as the edge of the continental shelf, so they are commonly known as continental shelf models (CSM). Examples can be found in studies by Zhou et al. (2014a) and Bray et al. (2016) where the open-source EFDC

model was used to develop a CSM for the Severn barrage. A comprehensive study on the potential of renewable energy extraction in the UK has been conducted by Bourban et al. (2014). They have employed a two-dimensional TELEMAC code to model an area that covers all of UK coastal waters, the North Sea and extends offshore slightly beyond the northern European continental shelf.

Local-scale models

All the studies mentioned above are interested in large-scale hydrodynamic conditions but not so much on the local details. For studying flow on a local scale, i.e. in the vicinity of a barrage or a lagoon, a more detailed model with a denser mesh has to be employed. Typically, these models focus on the performance efficiency of the turbines or local scour due to the accelerated flow through a turbine. For example, an experimental study by Jeffcoate et al. (2013; 2017) assessed the shear stress of the bed downstream of a tidal barrage due to a three-dimensional nature of the flow conditions created by flow through turbines.

Subgrid-scale models

Studies on the subgrid-scale are looking at the representation of important small-scale physical processes that occur at length-scales that cannot be adequately resolved on a computational mesh. They are mostly concerned with the flow through the turbine itself and use more complex computational models, such as full 3D RANS simulation and large-eddy simulation (LES) (Wilhelm et al. 2016b).

The simulations presented in this thesis span over three different scales; (i) an extensive continental shelf model of the Severn barrage, (ii) a regional-scale model of the Severn Estuary for the Swansea Bay lagoon project, and (iii) a simulation of the laboratory experiment focusing on the near-field hydrodynamics. The developed methodology is robust enough to be applied to any case, regardless of the size of the domain and the resolution of the grid. At the same time, it is almost impossible to put one model into a

single category. Take the Swansea Bay lagoon model as an example - its domain is covering a relatively broad area of the Severn Estuary and Bristol Channel, but the flexibility of the curvilinear grid allows for a more refined resolution in the areas of interest (such as close to the structure). The inclusion of the lagoon and the focus on the treatment of the flow through the hydraulic structures causes the model overlap between the regional and local scale. This illustrates the challenges associated with TRS modelling, where the border between different scales often becomes fuzzy (Neill et al. 2018). The studies presented in this thesis try to address the significance of the multi-scale approach to the modelling and its appropriateness for the analysis of the TRS projects.

2.4.2 Evolution of numerical modelling of the Severn barrage

A great number of studies on hydrodynamical modelling of the Severn barrage have been published over the course of the last 10 years. In this section, when referring to the Severn barrage, we focus exclusively on the so-called Cardiff-Weston layout of the barrage (Figure 2.13c), which is the largest scheme considered to be potentially feasible by the Department of Energy and Climate Change (DECC 2010). During this period, we have seen the Severn barrage model evolve through a series of refinements and optimisations. The model was implemented into a number of software programmes, ranging from purely research codes such as DIVAST to more sophisticated open-source software suites such as EFDC and Delft3D.

A detailed study on the numerical modelling of the Severn barrage was first published by Xia et al. (2008; 2010a). The model employed a TVD finite volume scheme, based on a triangular unstructured grid, a method that is commonly used for simulation of estuarine hydrodynamics. The barrage was modelled through the domain decomposition technique with special treatment of the internal boundary in the location of turbines and sluice gates. This initial model used a simplified representation of the turbines; they were modelled using an orifice equation, which is inadequate for the

representation of turbines, as it provides inaccurate flow rates and consequently gives erroneous estimates of power production. With an ebb-only generation scheme, it predicted mean power output of 2 GW over a typical mean spring tidal cycle, a decrease of a maximum water level upstream of the barrage by 0.5-1.5 m, and a significant decrease of the maximum tidal currents in the main channel. The same model was also used in a study that investigated two alternative TRS projects in the Severn Estuary – the Fleming Lagoon and the Shoots Barrage (Xia et al. 2010c). Both alternatives were considered because of the smaller size, therefore reducing the ecological footprint of the project. The study concluded that the Fleming Lagoon would have little influence on the hydrodynamic processes in the estuary, while both barrages (Severn and Shoots) induced much more significant environmental impacts, such as a marked reduction in the water body exchange and the permanent flooding of some intertidal zones in the impounded basin area. The reported power output over a typical spring tidal cycle was 31.1 GWh, 5.6 GWh and 5.1 GWh for the Cardiff-Weston barrage, Shoots Barrage and Fleming lagoon respectively. In addition to a greater yield of produced power, the Severn barrage would also contribute to some positive hydrodynamic effects, especially with regard to the flood risk reduction. In a study by Falconer et al. (2009) the above model was refined by replacing the orifice equation with a hill chart. A hill chart is a manufacturing characteristic of a turbine and it relates the specific discharge and power production efficiency to the instantaneous head difference across the turbine, thereby more accurately predicting the turbine flow rate and power output. The refinements resulted in a reduction of the power output from 31.1 GWh to a more realistic 24.2 GWh over a mean spring tidal cycle. A further study by Xia et al. (2010b) used the same model to investigate the impact of different operating modes on water elevations and power output. Three different schemes were considered – ebb-only, flood-only and two-way generation. Flood generation produced the least electricity, while ebb and two-way predicted similar outputs. Two-way generation also raised concerns over increased flood risk and environmental impacts due to a reduced tidal range upstream of the barrage, making it less favourable of the two options. The estimation of power output was further improved by Xia et al. (2012), where the simulation was extended over a full

neap-spring tidal cycle, to include the neap-spring variation in tidal range. An extrapolation of the results over the whole year resulted in the estimated tidal energy output ranging between 13 and 16 TWh per annum, which is similar to 15.6 TWh per annum reported in DECC (2010). The study showed that more detailed information on the barrage and turbine parameters will result in more accurate predictions, indicating also that the power output from the Severn Barrage could be increased with technological advances in the sluice gate and turbine performance. The model was also used to investigate the role of the barrage in the future coastal flood risk in the estuary (Xia et al. 2011). Different seaward boundary scenarios were used, simulating the rise of the water surface elevation due to climate change. The results indicated that the construction of the barrage would help mitigate the impacts of the sea level rise by reducing the maximum water elevation upstream of the barrage. Similar conclusions were presented in another study that investigated the impacts of Severn barrage on the sea level rise (Ahmadian et al. 2014b). To reduce uncertainties arising from the treatment of the open boundary and increase the accuracy of the model, a cascade of three one-way nested models was employed to dynamically downscale the hydrodynamic processes from a global (ocean and atmospheric) model, through a regional (Irish Sea model), to a local coastal scale (Severn Estuary) model. The results showed that the barrage would reduce flood risk and showed no significant change in the electricity output due to the sea level rise.

The Severn barrage was also studied using DIVAST (Depth-Integrated Velocities and Solute Transport), a 2D hydro-environmental numerical model developed at Hydro-environmental Research Centre (HRC) in Cardiff University. In the study by Ahmadian et al. (2010a) DIVAST was dynamically linked with a 1D model, to Simulate the sediment transport and water quality indicator processes. 1D model covered the meandering upstream reach of the Severn Estuary, while the rest of the estuary together with the Bristol Channel fell into the 2D domain. Results showed that changes in tidal currents due to the construction of a barrage correspond to the reduction in suspended sediment levels, leading to a reduction in the concentration levels of faecal bacteria and increased

light penetration within the water column. This raised concerns from an ecological point of view, as the changes will also affect the benthic biodiversity of the estuary. The same model was later used to compare between ebb-only and two-way operational scheme (Ahmadian et al. 2014a). Results showed a larger decrease in the suspended sediment levels in the case of an ebb-only generation scheme, favouring the two-way operational scheme due to the smaller impacts on the environment.

EFDC (Environmental Fluid Dynamics Code) is another hydrodynamic modelling suite that was used to model the Severn barrage. EFDC is an open-source code developed and supported by the engineering company Dynamic Solutions-International. The model is based on the finite difference scheme, employed on an orthogonal curvilinear grid, and is widely used for modelling shallow water conditions in reservoirs and estuaries (Hamrick 1992). The code was first adapted for the simulation of TRS in a study by Zhou et al. (2014c), including the numerical implementation of hydraulic structures to represent turbines and sluice gates, the use of hill chart to calculate turbine flow rate and implementation of operational sequence algorithm for different operating modes. The barrage properties were based on the characteristics presented in a study by Falconer et al. (2009). An ebb-only generation scheme was used to investigate the impact of the barrage on hydrodynamics and salinity distribution in the estuary. Next, the model was used in a study that investigated the effects of the barrage on the open boundary (Zhou et al. 2014a). The seaward boundary of the Severn Estuary model was extended (i) to include the Irish Sea and (ii) reaching the continental shelf. Noticeable differences along the open boundary were observed when including the barrage in the simulation. The study demonstrated the need to consider a large computational domain when investigating large scale structures in the estuary, as the effects on the maximum sea level were observed far beyond the initial boundary condition. Next study by Zhou et al. (2014b) focused on the optimisation of the Severn barrage, as it considered different configurations of the turbines and sluice gates. With advances in technology, a new type of tidal turbines that were designed for high efficiency at very-low heads was investigated (Atkins and Rolls-Royce 2010). In addition to the conventional proposal

with 216 turbines and 166 sluices, two new designs with no sluices and 382 and 764 turbines respectively were included. The study concluded that new technology offers the best mitigating effects for the flood risks and significantly reduces the environmental impact of the barrage. The resulting flow patterns around the barrage were closest to the existing natural conditions because the barrage could operate at much lower heads. EFDC was again used in a study by Bray et al. (2016), where the continental shelf model was used to perform sensitivity analysis of the sluice gate discharge coefficient, which showed that performance of the barrage is not sensitive to the changes of the coefficient value and that any power losses due to uncertainty of its value can be easily mitigated by increasing the sluice gate capacity.

The long list of the collected literature above indicates the gradual progression from a simple conceptual model to a flexible and stable numerical model, that can be used for tidal energy analysis in the Severn estuary and investigation of hydrodynamic processes related to the operation of tidal range structures. The Severn barrage project proved to be an ideal case for the development and innovation of numerical modelling techniques related to TRSs. The combined outcome of the selected literature is a robust framework that has been so far implemented into several different hydrodynamic software suites, including DIVAST, EFDC and Delft3D. It has been so far used for: (i) hydrodynamic analysis, (ii) energy output estimation, (iii) optimisation of the barrage operation, (iv) sediment transport and water quality analysis, (v) flood risk analysis, (vi) far-field impacts on water levels beyond the open boundary, (vii) mitigation of flood risk due to climate change induced sea level rise, and (viii) informing on the design characteristics of the proposed projects (i.e. number of turbines and sluice gates, type of turbines, operation mode, etc.). Majority of the studies above were based on a 2D depth-averaged model of the estuary. While 2D models are generally accurate for predicting water elevation, they are unreliable for simulating more complex flow patterns due to the depth-averaging of the vertical velocity profile. Such flow properties are commonly present during the operation of TRSs, especially in the vicinity of the turbines where submerged high-velocity jets radically change the shape of the vertical velocity profile.

An expansion to 3D modelling of TRSs has been scarcely reported to date; 3D models would greatly contribute to the appreciation of the complex flow conditions generated by the hydraulic structure-induced water jets (Neill et al. 2018). This was the main motivation for the implementation of the TRS methodologies into the Delft3D software.

2.4.3 Evolution of numerical modelling of the Swansea Bay lagoon

Swansea Bay lagoon is the most recent TRS project that is currently being considered in the UK (Waters and Aggidis 2016a). It is considerably smaller than the proposed Severn barrage and is viewed as a pilot project for TRS deployment in the Severn Estuary and Bristol Channel region. A number of studies have emerged in recent years, that focused mainly on predicting and optimising the power output of the scheme. The initial estimation came from a study by Petley and Aggidis (2016), which employed a zero-dimensional (0D) computational model. 0D model is a simplified method for estimating the performance of a TRS (Aggidis and Benzon 2013). It works by accounting the changes of the water level inside the lagoon, assuming they are equivalent to the volume transferred in/out of the lagoon, divided by the surface area of the impoundment at that specific time. Because it is fast, simple to compose and computationally inexpensive, it can be particularly useful for the preliminary studies of the TRS performance in the design stage of a project. Utilizing a hill chart for tidal-range specific turbines (Andritz Hydro 2016), the study tested lagoon's efficiency under different operational modes, i.e. two-way generation, ebb-only generation, and ebb generation with pumping. The study predicted an annual power generation of 596.04 GWh for the ebb-only scheme, significantly more than a 479.8 GWh prediction for a two-way scheme. These predictions assumed a constant starting head difference throughout the simulation; the starting head has been carefully selected with an aim to achieve the most efficient power generation on average over a spring-neap tidal cycle. However, the generation could be further optimised by regulating the operational parameters in order to account for the variability of the tidal range. A methodology for such optimisation was presented in a study by Angeloudis et al. (2018), which considered a simultaneous operation of

Swansea Bay and Cardiff lagoons. The optimisation method resulted in a significant increase in annual power production. For the Swansea Bay lagoon with a two-way generation mode, it resulted in 463 GWh annually, rising to 569 GWh when including pumping. A similar study was performed by Xue et al. (2019), where a 10 per cent increase in efficiency was reported for the Swansea Bay lagoon with a two-way generation. These studies have illustrated the usefulness of the 0D method for the preliminary assessment and its contribution towards a more informed design process. However, there is a downside to the 0D modelling. For computational efficiency, the method sacrifices the information on local hydrodynamics. While this trade-off is acceptable for the needs of preliminary assessments, it falls short when performing more advanced studies, such as analysis of environmental impacts, which require a more complex and accurate hydrodynamic model. A 2D hydrodynamic simulation of Swansea Bay lagoon was first presented in a study by Angeloudis et al. (2016b). The study employed a 2D finite-volume model with an unstructured grid, including the methodology for the TRS operation that was already presented in Section 2.4.2 and was previously used in simulations of Severn barrage. The model included an additional refinement to the internal boundary condition to conserve the momentum on the incoming and outgoing flow through the structure. The results showed that the deviation on power predictions between the 0D and 2D methodologies depends on the manner the impoundment interferes with the existing flow and may vary on a case by case basis. For Swansea Bay lagoon the deviation was shown to be small enough to still consider 0D valid; 2D model predicted 490 GWh annually compared to 530 GWh annually predicted by the 0D model. A model with an optimised operational sequence in a later study (Angeloudis and Falconer 2017) increased the predicted power output to 586 GWh annually. The predicted annual power output estimates across the mentioned studies are collated in Table 2.4

Chapter 2
Literature review

Table 2.4: Estimated annual energy output for Swansea Bay tidal lagoon as predicted across different studies.

Study	Estimated output (GWh/yr.)	
	0D	2D
(Petley and Aggidis 2016)		
Two-way	479	-
Ebb-only	596	-
Ebb-only (optimised)	727	-
Ebb-only (w/ pumping, optimised)	732	-
(Angeloudis et al. 2016b)		
Two-way	530	490
(Angeloudis and Falconer 2017)		
Ebb-only	315	292
Two-way (conservative)	507	474
Two-way (optimised)	615	586
(Angeloudis et al. 2018)		
Two-way	-	417
Two-way (optimised)	-	463
Two-way (w/ pumping)	-	515
Two-way (w/ pumping, optimised)	-	569

So far, the studies involving numerical modelling of the Swansea Bay lagoon were mostly interested in the energy efficiency of the scheme. Little attention was given to the assessment of the environmental impacts. Angeloudis et al. (2016b) did investigate the effects of the refined momentum treatment on the local flow patterns, however, the main motivation behind this was to determine the extent of the 2D hydrodynamic effect on the energy extraction. A more detailed analysis of the environmental impacts is required to provide a more informed view of the appropriateness of the scheme.

2.4.4 3D models

As already mentioned before, regional scale 3D models of TRSs have been scarcely reported in the literature. This is mainly due to the expensive computational costs of the 3D models; due to the present limitations of computational resources, they are currently constrained to smaller scale hydraulic engineering applications, such as laboratory-scale

flows (Jeffcoate et al. 2013; Oh et al. 2016; Jeffcoate et al. 2017) and turbomachinery simulations (Wilhelm et al. 2016a; Wilhelm et al. 2016b).

The regional scale 3D models are usually based on a 2D grid that was extended in a vertical direction by the addition of several vertical layers. They are derived from the large-scale oceanic models and can employ hydrostatic or non-hydrostatic forms of Navier-Stokes equations (Marshall et al. 1997). At the time of writing, the use of a 3D hydrostatic model on a regional scale has been limited to the modelling of tidal stream extraction (Lin et al. 2015; Rahman and Venugopal 2015). Both studies employed a Delft3D model, where tidal stream turbines were modelled as an actuator disk – a methodology commonly used with wind turbines. In both studies, the 3D modelling resulted in increased accuracy of the results. However, even though the authors have not reported the required computational time, a concern was raised about the number of vertical layers. A full set of the PDEs has to be solved for each layer, meaning that the total computational time increases by the factor equivalent to the number of layers.

A study by Stansby et al. (2016) employed a 3D Telemac model to investigate the oscillatory flow around a headland. This study is not directly connected to the tidal range modelling, however, the recirculating flow conditions resulting from flow around a headland closely resemble the large eddies induced by the high-velocity jets from a TRS. The results showed marked differences between the 2D and 3D models, with the depth-averaged model considerably overpredicting the velocity magnitude. For TRS modelling this could have a notable impact on the local hydrodynamic conditions, directly affecting the water surface levels in the vicinity of the turbines, and indirectly affecting the estimation of generated energy that is governed by the head difference across the structure. In addition, a 2D depth-averaged model has been proved inadequate for predicting local scour and deposition (Jeffcoate et al. 2017). A 3D model will result in more accurate predictions of the bed shear stress downstream of the turbines, which is important from an environmental point of view - bed shear stress is instrumental for the sediment transport processes.

Therefore, the main reason for 3D modelling of TRS structures are: (i) appreciation of the 3D conditions generated by the TRS-induced water jets, (ii) increased accuracy of the hydrodynamic conditions in the vicinity of the hydraulic structures, and (iii) accurate prediction of the bed shear stress downstream of the hydraulic structures.

2.4.5 Momentum conservation

The flow through hydraulic structures, that represent turbines and sluice gates in a TRS hydrodynamic model, is calculated off the numerical grid and added to the simulation as a source/sink term or an internal boundary condition. A study by Angeloudis et al. (2016b) highlighted the importance of the correct momentum transfer through hydraulic structures of a TRS. The study showed that the velocity of the jet exiting a turbine could easily exceed 10 m/s. Such a magnitude would have a significant influence on the simulated velocity field, water quality, sediment transport, morphological and ecological processes due to the corresponding momentum of the jet. The paper tested certain formulations for their effect on the momentum flow through the depth-averaged model. The momentum conservation was applied to a finite-volume model by the way of a special internal boundary; the water depth across the boundary was artificially fixed to the value that forced the cell interface area to match the flow-through area of the turbine. The study found that the treatment of momentum can play a significant role in the prediction of the velocity field. Tests on TRSs of different sizes showed that the effect is particularly pronounced for the smaller schemes, such as lagoons, and less so for larger schemes; for the Severn Barrage, the results were largely independent of the momentum treatment.

The value of 10 m/s in (Angeloudis et al. 2016b) was obtained by dividing the discharge of a turbine with the minimum flow area at a turbine section (i.e. cross-sectional area at the location of the runner blade, the diameter of which also signifies the size of the turbine; denoted as D_M in Figure 2.19). This value is questionable, as it would mean that the flow through a turbine completely ignores any hydraulic losses due to the flow

through the diffuser-shaped draft tube. The main role of a draft tube is to increase the pressure of the exiting fluid at the expense of its velocity (Gubin 1973), which would imply that the draft tubes were either not designed properly or that their effect was ignored in the case above.

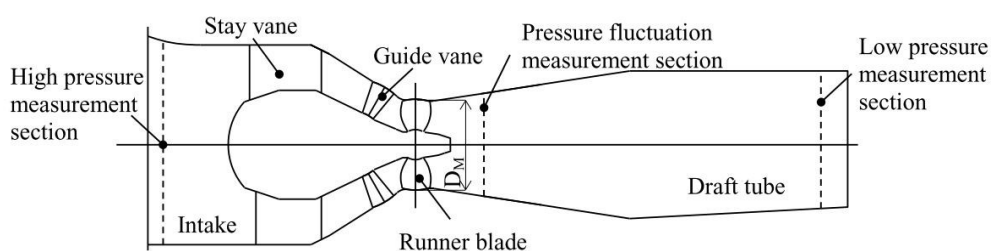


Figure 2.19: Bulb turbine cross-section (Wilhelm et al. 2016b)

The difference in the velocity profile at the turbine runner and at the draft tube exit was demonstrated in a study by Wilhelm et al. (2016b). The magnitude of the axial velocity at the draft tube exit was between 40 and 60 per cent of the magnitude at the runner and was relatively evenly distributed across the draft tube cross-section. Such a velocity distribution would have a significantly lesser impact on the hydrodynamic velocity field compared to the velocity profile assumed in the study by Angeloudis et al. (2016b).

To further investigate the impact of the momentum transfer through the hydraulic structures, a new methodology was developed and applied to the case studies presented in this thesis. The method is compatible with the Delft3D's finite-difference numerical scheme and can be applied to both 2D depth-averaged and 3D hydrostatic models. It was applied to the study of the Swansea Bay lagoon and to a numerical simulation of an experimental study involving a tidal barrage. A detailed description and formulation of the method are given in Chapter 4.

2.5 Summary

Tidal range technology has great potential for expanding UK's renewable energy portfolio, due to the enormous amounts of available capacity on the West Coast, particularly in the Severn Estuary and Bristol Channel. The technology has been proven successful by several projects worldwide, some of them operational for more than half of century. The technology is rapidly advancing, making the technology more efficient and resilient. Although there is a desire for the deployment of the technology in the UK, the projects are finding it hard to receive the support, mainly due to the high construction costs and uncertainties over environmental impacts.

The most recent proposal for a tidal lagoon in Swansea Bay has been rejected by the UK Government, even though it received unequivocal support from the experts. The technology, however, still represents a great potential to contribute towards the UK's renewable energy goals. To reduce the uncertainties and make the technology more worthwhile, significant investigations into the impacts of tidal power are required. This includes hydrodynamic modelling of the TRS structures, which requires a robust and flexible numerical model that can provide accurate and reliable predictions.

The overview of the existing numerical models has shown that a multi-scale approach has to be undertaken when simulating TRS operation. The models usually employ a relatively large domain, to assure that TRS operation does not interfere with the open boundary conditions. At the same time, special attention has to be given to local hydrodynamic effects deriving from the TRS operation, i.e. high-velocity jet exiting the turbines. Certain studies have identified the importance of the correct application of momentum transfer in regard to the turbine discharge, however, the implications of the method have not been thoroughly assessed, with a limited explanation of the theoretical background for the used methodology. To address these shortcomings, a novel method for momentum conservation is presented in this thesis, that was applied to the Delft3D model and tested on a laboratory-scale simulation and Swansea Bay lagoon model. The

thesis provides an assessment of how the novel method affects the hydrodynamic predictions, as well as its impacts on bed erosion and sediment transport.

The review has also identified a lack of 3D simulations in TRS studies. Because of the shallow water aspect, 3D models are often considered unnecessary for modelling estuarine hydrodynamics. However, due to the complexity of the high-velocity jets in the vicinity of the structures, 3D simulations could provide a more informed understanding of the flow patterns forming downstream of the turbines, which are essential for correct estimations of power output as well as for accurate predictions of the bed shear stress. Using the Delft3D software, the thesis also provides the comparison between the 2D and 3D simulations of the same case study, with an aim to evaluate the differences between the two and to assess the role of 3D simulations in TRS models.

Chapter 3

Numerical model

3.1 Introduction

This chapter presents the relevant governing equations and background of the numerical modelling associated with hydrodynamic simulations of TRS projects. The 2D Shallow Water Equations (SWE) are most commonly used for modelling the TRS on a regional scale. They are an efficient tool for resolving the hydrodynamics of tidal waves in estuaries or coastal regions and can be used for assessment of impacts on the natural environment deriving from extraction of tidal energy. The 3D numerical models present a more sophisticated alternative to 2D SWE models. They differ from 2D models in that they split the water column up into multiple layers. They are computationally more expensive and require adequate turbulence models for resolving horizontal mixing effect between the layers. Due to these limitations, 3D models are not commonly applied to modelling of TRS at a regional scale, and are more frequently used for modelling the flow at the local-scale, in the vicinity of the TRSs.

The chapter is further split into four sections. Section 3.2 presents an overview of the general governing equations that define the hydrodynamic properties of fluids in motion. Section 3.3 describes different numerical approaches available for solving the governing equations. Section 3.4 introduces the numerical model used in this study, namely Delft3D-FLOW, and provides the conceptual and numerical description of the model. Finally, section 3.5 provides a summary of the details presented in this chapter.

3.2 Governing equations

Any type of fluid flow can be simulated using a set of four Partial Differential Equations (PDE): (i) continuity of mass, (ii) conservation of momentum, (iii) equation of state, and (iv) conservation of energy. However, in most practical hydro-environmental engineering problems, only the continuity and momentum equations are required for accurate simulation of the fluid flow (Rajar 1997).

3.2.1 Continuity equation

The continuity equation governs the conservation of mass. By definition, it demands that the net fluid mass entering a control volume equals the amount by which the mass of the control volume changes in a specific time interval (Rajar 1997):

$$\frac{\partial \rho}{\partial t} + \frac{\partial \rho u}{\partial x} + \frac{\partial \rho v}{\partial y} + \frac{\partial \rho w}{\partial z} = 0 \quad (3.1)$$

where ρ is the density of the fluid and u , v and w are the velocity components in the main Cartesian directions x , y and z .

Considering the assumption of the incompressible flow, which can be applied in the majority of hydro-environmental engineering problems, the density of the fluid will stay constant over time and the Equation (3.1) can be rewritten as:

$$\frac{\partial u}{\partial x} + \frac{\partial v}{\partial y} + \frac{\partial w}{\partial z} = 0 \quad (3.2)$$

3.2.2 Momentum equations

The momentum equations describe the motion of viscous fluids. The equations are derived by applying Newton's second law of motion to an infinitesimal fluid element,

assuming the stress in the fluid is the sum of the viscous and pressure terms. The Momentum equations in the three cardinal directions of the Cartesian coordinate system in their general form are given as (Rajar 1997):

$$\begin{aligned} \frac{\partial u}{\partial t} + \frac{\partial u}{\partial x}u + \frac{\partial u}{\partial y}v + \frac{\partial u}{\partial z}w \\ = f_x - \frac{1}{\rho} \frac{\partial P}{\partial x} + \nu \left(\frac{\partial^2 u}{\partial x^2} + \frac{\partial^2 u}{\partial y^2} + \frac{\partial^2 u}{\partial z^2} \right) + \frac{\nu}{3} \frac{\partial}{\partial x} \left(\frac{\partial u}{\partial x} + \frac{\partial v}{\partial y} + \frac{\partial w}{\partial z} \right) \end{aligned} \quad (3.3)$$

$$\begin{aligned} \frac{\partial v}{\partial t} + \frac{\partial v}{\partial x}u + \frac{\partial v}{\partial y}v + \frac{\partial v}{\partial z}w \\ = f_y - \frac{1}{\rho} \frac{\partial P}{\partial y} + \nu \left(\frac{\partial^2 v}{\partial x^2} + \frac{\partial^2 v}{\partial y^2} + \frac{\partial^2 v}{\partial z^2} \right) + \frac{\nu}{3} \frac{\partial}{\partial y} \left(\frac{\partial u}{\partial x} + \frac{\partial v}{\partial y} + \frac{\partial w}{\partial z} \right) \end{aligned} \quad (3.4)$$

$$\begin{aligned} \frac{\partial w}{\partial t} + \frac{\partial w}{\partial x}u + \frac{\partial w}{\partial y}v + \frac{\partial w}{\partial z}w \\ = f_z - \frac{1}{\rho} \frac{\partial P}{\partial z} + \nu \left(\frac{\partial^2 w}{\partial x^2} + \frac{\partial^2 w}{\partial y^2} + \frac{\partial^2 w}{\partial z^2} \right) + \frac{\nu}{3} \frac{\partial}{\partial z} \left(\frac{\partial u}{\partial x} + \frac{\partial v}{\partial y} + \frac{\partial w}{\partial z} \right) \end{aligned} \quad (3.5)$$

where t is time, P is the pressure gradient, f_x , f_y and f_z are the external body forces and ν is the kinematic viscosity defined as:

$$\nu = \frac{\mu}{\rho} \quad (3.6)$$

with μ the dynamic viscosity of the fluid.

The continuity equation (3.2) and momentum equations (3.3) – (3.5) together form the fundamental system of equations for simulating fluids in motion, also commonly known as Navier-Stokes equations.

3.3 Numerical methods

Numerical methods are mathematical tools designed to solve complex numerical problems, e.g. solving a system of PDEs over large-scale spatial and temporal dimensions. As such, numerical methods are widely used for analysis of the underlying fluid dynamic behaviour governed by system of hydrodynamic equations (Rijkswaterstaat 2016). The numerical methods replace the complex PDEs with a set of algebraic equations, which calculate the system variables at discrete points in space and time domains (Neelz and Pender 2009). The process of obtaining these algebraic equations is called discretisation, and there are numerous methods available for the space-time discretisation of governing equations.

3.3.1 Spatial discretisation

Majority of the spatial discretisation methods used to solve hydrodynamic equations described in Section 3.2 are based on one of the three main discretisation strategies (Neelz and Pender 2009): (i) finite difference methods (FDM); (ii) finite element methods (FEM); and (iii) finite volume methods (FVM).

Finite difference method

This method solves the differential equations by replacing the derivatives of state variables with their finite difference approximation. The approximation is achieved via the Taylor series expansion, which describes the derivatives of the variables as finite differences between the values of the neighbouring points (Neelz and Pender 2009). The order of accuracy of the approximations is controlled by the order to which the Taylor series is developed and the underlying method, with higher order also requiring a higher number of neighbouring points involved in the calculation (Neelz and Pender 2009). The main advantages of the FDM are its straightforward solution and well defined implementation (Alcrudo 2004). However, because it is limited to structured regular

grids, the FDM lacks flexibility from the geometric point of view and is gradually becoming less popular for hydrodynamic simulations (Alcrudo 2004). Nonetheless, the use of the method is widespread, especially in the 2D hydro-environmental practices, mainly due to the compatibility with high-resolution digital terrain (LiDAR) and bathymetric models (Neelz and Pender 2009) and computational efficiency.

Finite element method

In finite element method, the whole domain is divided into a number of smaller finite elements, where each element is represented by an individual set of simplified equations. After they are divided, all the individual sets are then systematically recombined into a global system of equations, that is solved using known solution techniques and initial conditions (Zienkiewicz and Taylor 2000). A large advantage of the method comes from a very flexible sub-division of the domain that allows for a fully unstructured mesh for more accurate representation of complex geometries (Reddy 1993). Another advantage is a rigorous mathematical foundation of the model that allows a posteriori error estimation and thus better understanding of method's accuracy (Alcrudo 2004). On the other hand, this does make it computationally expensive, with a large amount of computational time consumed at every time-step (Ferziger and Perić 2002). Due to its more convoluted conceptual approach, the method is less commonly used in hydro-environmental engineering practices (Alcrudo 2004; Neelz and Pender 2013).

Finite volume method

The finite volume method is one of the most versatile and most commonly used discretisation techniques for hydrodynamic models (Alcrudo 2004). It is based on the integral form of the conservation laws rather than pure continuum mathematics concepts (Roache 1998). It follows the concept of control volume formulation used in analytical fluid dynamics, where the domain is subdivided into several smaller control volumes, also referred to as cells. The PDEs are then integrated over each cell based on

fluxes through the control volume boundaries (Neelz and Pender 2009). The flux across a given boundary is the same for both cells sharing that boundary, resulting in a theoretically perfect conservation of quantities such as mass, momentum and energy. The method is highly popular in fluid dynamics due to its full conservation of mass and momentum, its applicability to all types of meshes and the simplicity of its formulation (Alcrudo 2004). The FVM offers the same flexibility as FEM, and is at the same time computationally much more efficient. The geometric flexibility, combined with the conceptual simplicity and its conservativeness, has allowed the FVM to become increasingly popular and most widely used for shallow water simulations (Neelz and Pender 2009).

3.3.2 Temporal discretisation

Strategies for time-discretisation of hydrodynamic equations can be divided into three main categories: (i) explicit schemes, (ii) implicit scheme, and (iii) semi-implicit schemes.

Explicit schemes

In explicit or forward-looking schemes, the state of the system at the current time-step is calculated directly from the known values of the state variables from the previous time-step. Because explicit schemes are easy to implement, they are used in the vast majority of the newly developed models and research codes (Hunter et al. 2007). However, they are prone to numerical instability in the shape of unphysical numerical oscillations in the numerical solution (Neelz and Pender 2009). Therefore, they are conditionally stable, which means that a specific condition must be specified to ensure a stable solution to the numerical problem. In order to provide stability, they are subject to a time-step limitation in the form of Courant-Friedrichs-Lewy (CFL) condition (Courant et al. 1967), which can be expressed as:

$$\frac{v\Delta t}{\Delta x} \leq C_{max} \quad (3.7)$$

where C_{max} is the dimensionless Courant number, v is the magnitude of velocity, Δt is the time-step, and Δx is the length interval. The Courant number is typically set to $C_{max} = 1$ for explicit schemes. However, in some cases the CFL condition can result in a time-step that is very small compared to the physics behind the problem under consideration (Hunter et al. 2007). This can lead to an excessive number of time-steps required, rendering the numerical model completely unfeasible (Hunter et al. 2007).

Implicit schemes

In implicit or backward-looking schemes, the calculation of the dependant variables involves both the state of the system at the current time-step and previous time-step. All the computational cells are coupled together to form a single matrix that is solved using an iterative technique. This enables the transmission of the hydraulic effects across the entire computational domain, but also increases the computational cost due to the increased complexity of the model (Hunter et al. 2007). However, implicit schemes ensure unconditional stability of the solution and allow for much larger time-steps, which is generally more desirable in hydraulic modelling, often outweighing the difficult implementation and high computational costs. Despite being unconditionally stable, implicit schemes are often subjected to the CFL condition in order to provide a numerically accurate solution (Neelz and Pender 2009). However, they are still less sensitive to numerical stability than explicit schemes, necessitating a less restrictive CFL condition, generally set to $C_{max} = 8$.

Semi-implicit schemes

Semi-implicit schemes, also used by Delft3D, combine the advantages of both by treating some of the derivatives explicitly and some implicitly. Conceptually, the schemes split up the terms in such a way that the largest stable time-step for the semi-implicit

discretisation is significantly larger than for a corresponding explicit discretisation, significantly reducing the computational time required to solve the equations (Fulton 2004). Therefore, the semi-implicit schemes are computationally efficient, while at the same time producing numerically stable solutions with no loss in accuracy (Rosatti et al. 2011). However, similar to the implicit schemes, their main disadvantage is that they are mathematically complex and complicated to design (Fulton 2004).

3.4 Delft3D-FLOW numerical model

Delft3D is a 3D modelling software suite that integrates flow and transport modelling systems for aquatic environments. It was developed by Deltares in the Netherlands and is available in open source. The software package consists of several integrated modules: Delft3D-FLOW for simulation of hydrodynamic flow; Delft3D-WAVE for short waves generation and propagation; Delft3D-MOR for sediment transport and morphological changes; and D-Water Quality for modelling of ecological processes and water quality parameters (Lesser et al. 2004; Deltares 2014). The FLOW module is software's main engine for the water flow simulations and, at the same time, it is used to provide the hydrodynamic basis for all other modules.

All of the hydraulic simulations presented within this research study were performed with the Delft3D-FLOW numerical model. For brevity we will refer to Delft3D-FLOW as just Delft3D from here on.

3.4.1 Hydrodynamic equations

Delft3D provides a numerical algorithm for the solution of Navier-Stokes equations in shallow-water conditions and for incompressible fluids. It is capable of solving both 2D depth-averaged and 3D unsteady flow problems. The system of PDEs, in combination with an appropriate set of initial and boundary conditions, is solved on a staggered finite difference grid, illustrated in Figure 3.1. This particular arrangement of the variables is

called the Arakawa C-grid in which all scalar variables, for example density and water level, are located at the cell centre, whereas the velocity component in a given direction is stored at the cell side orthogonal to that direction. Using the staggered grid, the number of computational values is decreased by a factor of four, significantly increasing the computational efficiency, while the same level of accuracy is preserved as with a collocated grid (Rijkswaterstaat 2016). One disadvantage of this arrangement is loss of accuracy in simulating the inertia gravity waves because of horizontal averaging of the Coriolis terms, which can be avoided by employing alternative arrangements, such as Arakawa B grid while sacrificing the resolution (Arakwa and Lamb 1977). However, in the case of tidal driven shallow water flow averaging of Coriolis terms does not represent an issue, making the Arakawa C arrangement the most optimal scheme for the semi-implicit finite difference solution algorithm.

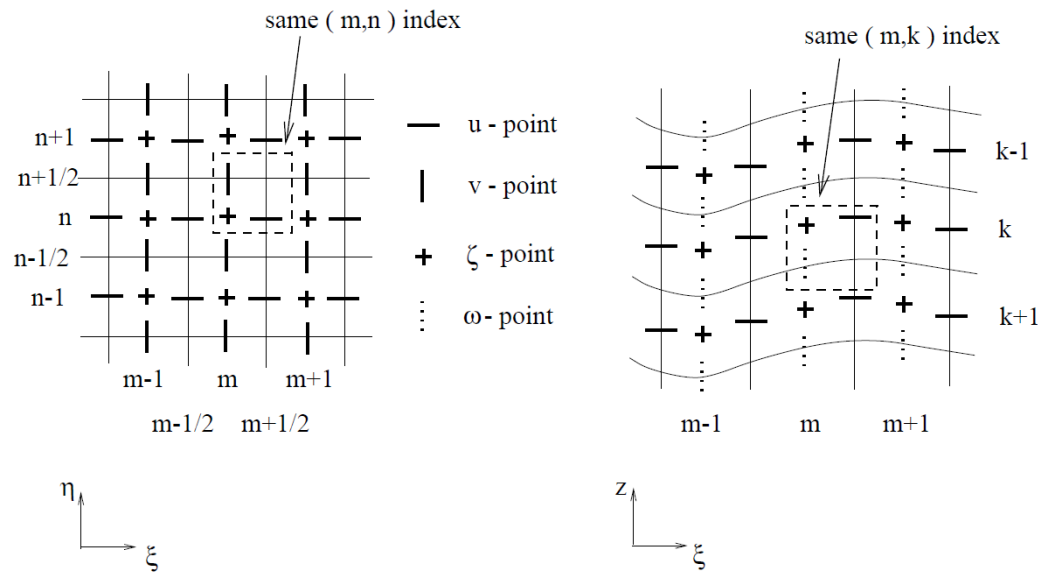


Figure 3.1: Arrangement of the unknowns for staggered grid (Rijkswaterstaat 2016).

Grid and coordinate system

The orthogonal curvilinear grid (Figure 3.2) can be defined in Cartesian or spherical coordinates. The boundary-fitted curvilinear grid can follow the irregular land features, such as rivers, estuaries and coastlines, more smoothly than the rigid rectangular grids. In Cartesian space, the coordinates of the grid nodes are assigned as easting and northing in meters. Alternatively, they can be defined with the spherical coordinates, which are especially useful for large-scale numerical models, where it makes more sense to define the grid in degrees of longitude and latitude (Deltares 2014).

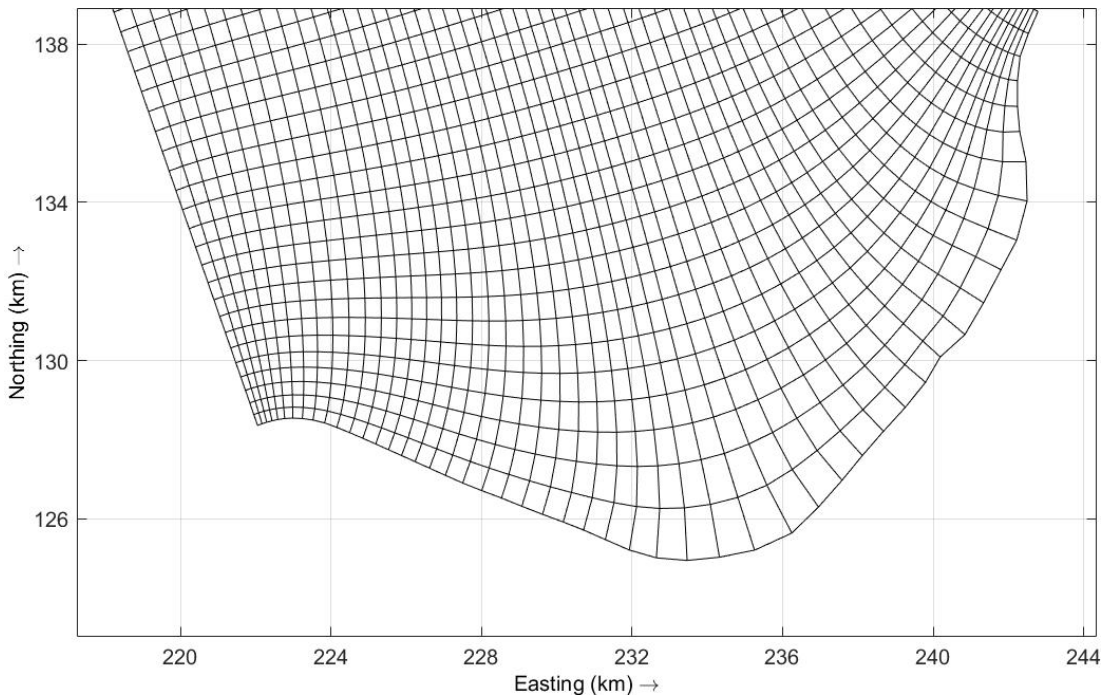


Figure 3.2: Example of a curvilinear grid in Delft3D defined in OSGB 1936 coordinate system.

As demonstrated in Figure 3.3, the curvilinear grid is numerically transformed from the physical space (Ω) to the computational space (G_H), by the way of transformation coefficients $\sqrt{G_{\xi\xi}}$ and $\sqrt{G_{\eta\eta}}$ (Deltares 2014). The coefficients can be computed from the coordinates of the cell vertices, as illustrated in Figure 3.3.

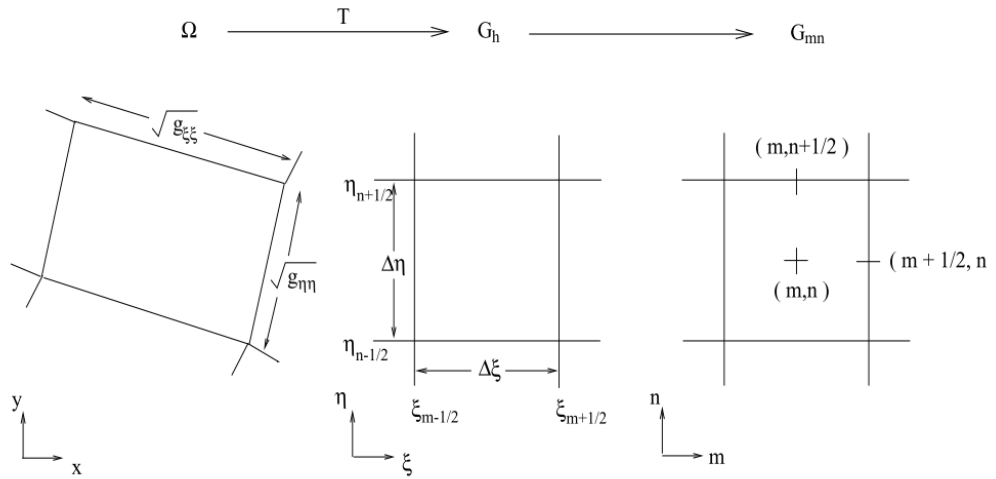


Figure 3.3: Mapping of physical space Ω to computational space G_H . G_{mm} represents the locations of the unknown variables (Rijkswaterstaat 2016).

Vertical grid

Delft3D offers two different grid systems in the vertical direction: i) the σ vertical coordinate system also known as σ -grid for short, and ii) Z vertical coordinate system (also Z-grid). The equations for both systems are similar, as both grids split the model into several layers in the vertical direction (Deltares 2014). The fundamental difference between the two is how these layers are defined (Figure 3.4).

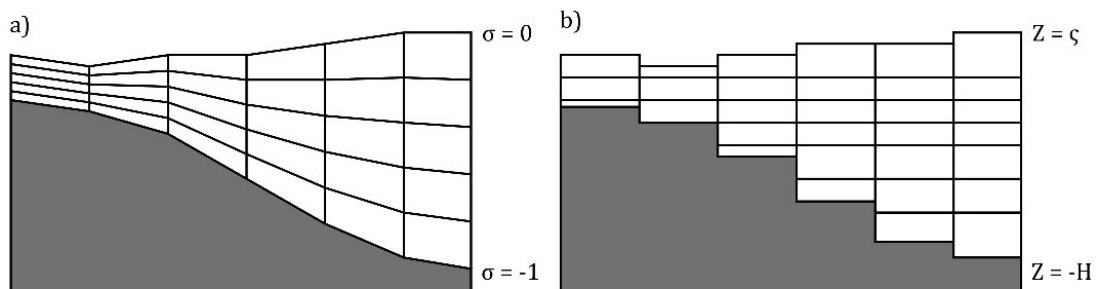


Figure 3.4: Illustration of the fundamental differences between the σ -grid (a) and Z-grid (b) vertical coordinate systems available in Delft3D.

In Z-grid the horizontal boundary of the layer surface is strictly horizontal with the fixed prescribed boundary surface elevation. At the same time, the grid is not boundary fitted in the vertical direction, resulting in a staircase-like bottom and free surface Figure 3.4b. This type of grid is useful for modelling of weakly forced stratified water systems with high-density gradients (Stelling and Van Kester 1994). However, for the more conventional hydraulic problems, like simulations of the free surface flow in rivers, estuaries and seas, the σ -grid has nowadays become the preferred approach in numerical models (Stelling and Van Kester 1994). In σ -grid, the water column is proportionally divided into the same number of layers throughout the domain, independent of the local water depth, smoothly fitting the vertical boundary and allowing for a smooth free surface Figure 3.4a.

The conceptual definition of the physical domain in the vertical direction is summarised in Figure 3.5. The z -coordinate is assumed to be orientated upwards positive. The free surface is described by the function $\zeta = f(x, y, t)$, which is the distance between the time-dependant elevation of the free surface and the plane of reference (at $z = 0$). The bottom topography is described by the time-independent function $d = f(x, y)$, which is defined as the depth below the plane of reference. The function $H(x, y, t) = \zeta(x, y, t) + d(x, y)$ is known as the total water depth, sometimes also called the local temporal depth (Rijkswaterstaat 2016).

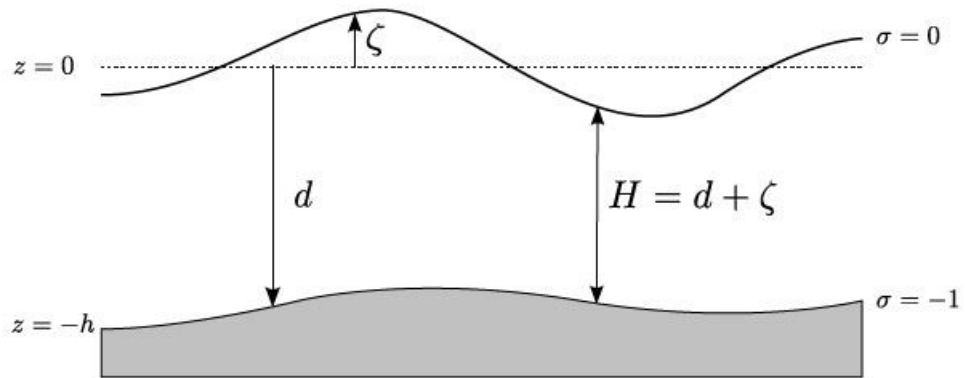


Figure 3.5: Definition of the σ coordinate system and characteristic parameters describing depth (d), water level (ζ) and total depth (H) (Deltares 2014).

Only the σ -grid was used in the simulations performed in this study, therefore a more in-depth description of the system is required. The σ -grid is defined by several layers (Figure 3.6), with the interface between the two layers described by the function $z_k = f(x, y, t)$. Index k denotes the layer interface, with value of zero representing the free surface and value K representing the bottom. At the same time number K is also the total number of layers (Rijkswaterstaat 2016).

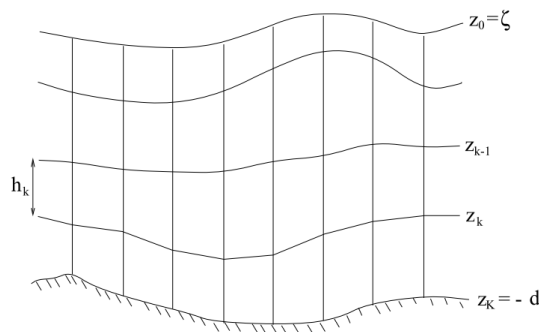


Figure 3.6: Schematic definition of the vertical grid with layer interfaces (Rijkswaterstaat 2016).

The layers of the σ -grid are not strictly horizontal, but instead, follow the shape of the free surface at the top and the shape of the closed boundary at the bottom. The relative thickness of the layers is predetermined at the input by the user and is uniform over the

entire horizontal domain. By definition, the σ -coordinate system always attains the value of $\sigma = 0$ at the free surface and a value of $\sigma = -1$ at the bottom as shown in Figure 3.5. In a 3D shallow-water model each layer is solved with a set of coupled conservation equations, representing the vertical interaction between the layers. The sole exceptions are the topmost and bottommost layers where horizontal boundaries have to be taken into account (Deltares 2014). Based on the definition in Figure 3.5, the σ coordinate can be expressed in the Cartesian form, as described by Equation (3.8):

$$\sigma = \frac{z - \zeta}{d + \zeta} = \frac{z - \zeta}{H} \quad (3.8)$$

where z is the upwards-positive vertical location of each point relative to the reference plane, ζ is the time-dependent free surface elevation above the reference plane, d is the time-independent depth below the reference plane, and H is the total depth, calculated as a sum of the depth and surface elevation.

Continuity equation

The depth-averaged form of the continuity equation (3.9) is derived from the general form for incompressible fluids (Equation (3.2)) by integrating it over the total depth (Deltares 2014):

$$\frac{\partial \zeta}{\partial t} + \frac{1}{\sqrt{G_{\xi\xi}}\sqrt{G_{\eta\eta}}} \frac{\partial HU\sqrt{G_{\eta\eta}}}{\partial \xi} + \frac{1}{\sqrt{G_{\xi\xi}}\sqrt{G_{\eta\eta}}} \frac{\partial HV\sqrt{G_{\xi\xi}}}{\partial \eta} = HQ \quad (3.9)$$

where t is time (s), ξ and η are the horizontal, curvilinear coordinates (m), and $\sqrt{G_{\xi\xi}}$ and $\sqrt{G_{\eta\eta}}$ are the transformation coefficients (m) between the curvilinear grid and rectangular coordinate system, and Q a global source or sink per unit area (ms^{-1}). U and V are the depth averaged velocities (ms^{-1}) in ξ and η directions which can both be, considering Equation (3.8), expressed in the Cartesian and σ -grid forms:

$$U = \frac{1}{H} \int_a^\zeta u \, dz = \int_{-1}^0 u \, d\sigma \quad (3.10)$$

$$V = \frac{1}{H} \int_a^\zeta v \, dz = \int_{-1}^0 v \, d\sigma \quad (3.11)$$

with u and v representing flow velocities (ms^{-1}) in ξ and η directions. Finally, Q represents the contribution of the external water discharge or water withdrawal per unit area, including the precipitation and evaporation:

$$Q = \int_{-1}^0 (q_{in} - q_{out}) \, d\sigma + P - E \quad (3.12)$$

where q_{in} and q_{out} represent the local source and sink terms per unit volume (s^{-1}), while P and E characterise respectively the source term of precipitation and sink term of evaporation (ms^{-1}).

Momentum equations

The momentum equations (3.3) and (3.4) in the horizontal direction are accordingly adapted for the curvilinear grid ξ and η (Deltares 2014). The equations are formulated per layer (layer-averaged), and are given as Equations (3.13) and (3.14):

$$\begin{aligned} \frac{\partial u}{\partial t} + \frac{u}{\sqrt{G_{\xi\xi}}} \frac{\partial u}{\partial \xi} + \frac{v}{\sqrt{G_{\eta\eta}}} \frac{\partial u}{\partial \eta} + \frac{\omega}{d + \zeta} \frac{\partial u}{\partial \sigma} - \frac{v^2}{\sqrt{G_{\xi\xi}} \sqrt{G_{\eta\eta}}} \frac{\partial \sqrt{G_{\eta\eta}}}{\partial \xi} \\ + \frac{uv}{\sqrt{G_{\xi\xi}} \sqrt{G_{\eta\eta}}} \frac{\partial \sqrt{G_{\xi\xi}}}{\partial \eta} - f_v = - \frac{1}{\rho_0 \sqrt{G_{\xi\xi}}} P_\xi + F_\xi + \frac{1}{(d + \zeta)^2} \frac{\partial}{\partial \sigma} \left(\nu_V \frac{\partial u}{\partial \sigma} \right) + M_\xi \end{aligned} \quad (3.13)$$

$$\begin{aligned} \frac{\partial v}{\partial t} + \frac{u}{\sqrt{G_{\xi\xi}}} \frac{\partial v}{\partial \xi} + \frac{v}{\sqrt{G_{\eta\eta}}} \frac{\partial v}{\partial \eta} + \frac{\omega}{d + \zeta} \frac{\partial v}{\partial \sigma} + \frac{uv}{\sqrt{G_{\xi\xi}}\sqrt{G_{\eta\eta}}} \frac{\partial \sqrt{G_{\eta\eta}}}{\partial \xi} \\ - \frac{u^2}{\sqrt{G_{\xi\xi}}\sqrt{G_{\eta\eta}}} \frac{\partial \sqrt{G_{\xi\xi}}}{\partial \eta} + f_u = -\frac{1}{\rho_0 \sqrt{G_{\eta\eta}}} P_\eta + F_\eta + \frac{1}{(d + \zeta)^2} \frac{\partial}{\partial \sigma} \left(\nu_V \frac{\partial v}{\partial \sigma} \right) + M_\eta \end{aligned} \quad (3.14)$$

where u and v are the flow velocities (ms^{-1}) in the ξ and η directions for a horizontal curvilinear coordinate system respectively, ζ is the water level above a reference datum (m), while d is the depth below the reference datum and together they form the total depth H . ω is the vertical velocity related to the moving σ plane (ms^{-1}), f_u and f_v are the Coriolis parameters (s^{-1}), ρ_0 is the density of water (kg/m^3), ν_V is the vertical eddy viscosity (m^2s^{-1}), P_ξ and P_η are the pressure gradients ($\text{kg}/(\text{m}^2\text{s}^2)$), forces F_ξ and F_η represent the imbalance of the horizontal Reynold's stresses (ms^{-2}), M_ξ and M_η represent the contributions due to external body forces (ms^{-2}), such as sources or sinks of momentum resulting from hydraulic structures, and $\sqrt{G_{\xi\xi}}$ and $\sqrt{G_{\eta\eta}}$ are the transformation coefficients between the curvilinear grid and rectangular coordinate system (m).

3D hydrostatic model

Delft3D employs the so-called three-dimensional hydrostatic model. In contrast to fully 3D RANS models, where the system of hydrodynamic equations is solved in all three dimensions, the 3D hydrostatic model instead solves the system under the shallow-water approximation neglecting the variation of velocity across the depth. The vertical momentum equation is thereby reduced to a hydrostatic pressure equation (Casulli and Stelling 1998). To account for the fundamental loss of information in the vertical direction, the model is divided into a fixed number of horizontal layers (Stelling and Van Kester 1994). The loss of information in the vertical direction is reduced by integrating the shallow-water equations over all the layers. The 3D hydrostatic models are therefore not fully 3D, nevertheless, they have proved useful for providing additional information

about the vertical structure of the flow quantities in shallow-water conditions, while not requiring computational resources for solving full 3D RANS models (Lesser et al. 2004).

Vertical velocities are consequently not involved in the process of solving the PDEs. If required, Delft3D calculates the “physical” vertical velocity (w) in the post-processing part of the simulation:

$$w = \omega + \frac{1}{\sqrt{G_{\xi\xi}}\sqrt{G_{\eta\eta}}} \left[u \sqrt{G_{\eta\eta}} \left(\sigma \frac{\partial H}{\partial \xi} + \frac{\partial \zeta}{\partial \xi} \right) + v \sqrt{G_{\xi\xi}} \left(\sigma \frac{\partial H}{\partial \eta} + \frac{\partial \zeta}{\partial \eta} \right) \right] + \left(\sigma \frac{\partial H}{\partial t} + \frac{\partial \zeta}{\partial t} \right) \quad (3.15)$$

where ω is the relative vertical velocity of the moving σ -layer interfaces, which can be calculated from the continuity equation (3.9).

Turbulence

The SWE equations described above do not form a closed system of equations, because the vertical (ν_V) and horizontal eddy (ν_H) viscosities are left undetermined. To determine their values, Delft3D employs turbulence closure modules that are based on the eddy viscosity concept (Deltares 2014). Eddy viscosity is a function of space and time, and its value can vary significantly for 2D and 3D simulations, for different horizontal and vertical turbulence length scales, and for different grid resolutions. For 3D shallow-water models the horizontal eddy viscosity ν_H is significantly larger than the vertical eddy viscosity ν_V due to the an-isotropic nature of stress tensor (Rijkswaterstaat 2016).

In Delft3D, the horizontal eddy viscosity coefficient is defined by the combined contributions of (i) the turbulent motions in the horizontal direction that are not resolved by the grid, namely the Sub-Grid Scale (SGS) turbulence (ν_{SGS}); (ii) the Reynolds-averaged SWE (ν_H^{back}), namely the background viscosity; and (iii) the three-dimensional turbulence (ν_V) in the case of a 3D simulation (Deltares 2014). The coefficient is thereby defined by Equation (3.16):

$$\nu_H = \nu_{SGS} + \nu_H^{back} + \nu_V \quad (3.16)$$

The ν_{SGS} is computed by a dedicated SGS model. The background horizontal viscosity ν_H^{back} is user-defined through input file and is a calibration factor. Finally, the ν_V is only applied for 3D simulations and is defined by Equation (3.17):

$$\nu_V = \nu_{mol} + \max(\nu_{3D}, \nu_V^{back}) \quad (3.17)$$

where ν_{mol} is the kinematic viscosity of water, ν_{3D} the contribution of a selected 3D-turbulence closure model, and ν_V^{back} the user-defined background vertical eddy viscosity that accounts for all other unresolved mixing (Deltares 2014).

For determining the ν_{3D} , Delft3D offers four different 3D-turbulence closure models, listed in ascending order of complexity: (i) constant coefficient; (ii) algebraic eddy viscosity closure model (AEM); (iii) k-L turbulence closure model; and finally (iv) k- ϵ turbulence closure model. The models differ in order of accuracy, based on how the turbulent kinetic energy (k), dissipation rate of turbulent kinetic energy (ϵ), and mixing length (L) are prescribed. The simplest is the model with a constant vertical eddy viscosity, that is specified by the user through the input file. This model is only adequate for simulations of laminar flow (Deltares 2014). Next is the AEM, which is defined as a combination of two zero order closure schemes, where two analytical formulas are used to determine k and L . This model is suitable for the majority of shallow-water applications (Rijkswaterstaat 2016). It is followed by the k-L turbulence closure model, a first order scheme, where L is still prescribed analytically, while determining k requires solving a transport equation that includes energy dissipation, buoyancy and production terms. The most complex is the k- ϵ turbulence closure model, a second order scheme which requires solving transport equations for both k and ϵ , from which the mixing length (L) is determined. It is one of the most common turbulence models used in hydrodynamics and is especially useful for free-shear layer flows with relatively small pressure gradients (Bardina et al. 1997).

The k- ε turbulence closure model was used for 3D simulations performed in this study, therefore, a more in-depth description of the model is required. The transport equations for turbulent kinetic energy (k) and energy dissipation (ε) are given by Equations (3.18) and (3.19):

$$\begin{aligned} \frac{\partial k}{\partial t} + \frac{u}{\sqrt{G_{\xi\xi}}} \frac{\partial k}{\partial \xi} + \frac{v}{\sqrt{G_{\eta\eta}}} \frac{\partial k}{\partial \eta} + \frac{\omega}{(d+\zeta)} \frac{\partial k}{\partial \sigma} \\ = \frac{1}{(d+\zeta)^2} \frac{\partial}{\partial \sigma} \left(D_k \frac{\partial k}{\partial \sigma} \right) + P_k + P_{kw} + B_k - \varepsilon \end{aligned} \quad (3.18)$$

$$\begin{aligned} \frac{\partial \varepsilon}{\partial t} + \frac{u}{\sqrt{G_{\xi\xi}}} \frac{\partial \varepsilon}{\partial \xi} + \frac{v}{\sqrt{G_{\eta\eta}}} \frac{\partial \varepsilon}{\partial \eta} + \frac{\omega}{(d+\zeta)} \frac{\partial \varepsilon}{\partial \sigma} \\ = \frac{1}{(d+\zeta)^2} \frac{\partial}{\partial \sigma} \left(D_\varepsilon \frac{\partial \varepsilon}{\partial \sigma} \right) + P_\varepsilon + P_{\varepsilon w} + B_\varepsilon - c_{2\varepsilon} \frac{\varepsilon^2}{k} \end{aligned} \quad (3.19)$$

where u and v are the flow velocities (ms^{-1}) in the ξ and η directions, ζ is the water level above a reference datum (m), d is the depth below the reference datum, ω is the vertical velocity related to the moving σ plane (ms^{-1}), while σ is the scaled vertical coordinate defined by Equation (3.8). Several empirical constants are also used, where P_k is the production term for turbulent kinetic energy (m^2s^{-3}), P_{kw} is the turbulent energy production due to wave action (m^2s^{-3}), B_k is the buoyancy flux term for turbulent kinetic energy (m^2s^{-3}), P_ε is the production term for the dissipation of turbulent kinetic energy (m^2s^{-4}), $P_{\varepsilon w}$ is the dissipation of turbulent kinetic energy due to wave action (m^2s^{-4}), B_ε is buoyancy flux term for the dissipation of turbulent kinetic energy (m^2s^{-4}), and $c_{2\varepsilon}$ is a calibration constant (-). The transport equations are non-linearly coupled by means of their eddy diffusivity (D_k) and (D_ε), and the dissipation terms. The D_k and D_ε are defined by Equations (3.20) and (3.21):

$$D_k = \frac{\nu_{mol}}{\sigma_{mol}} + \frac{\nu_{3D}}{\sigma_\varepsilon} \quad (3.20)$$

$$D_\varepsilon = \frac{\nu_{3D}}{\sigma_\varepsilon} \quad (3.21)$$

where σ_{mol} is the Prandtl-Schmidt number for molecular mixing (-), and σ_ε is an empirically determined closure constant (-).

The mixing length L is then determined from ε and k according to Equation (3.22):

$$L = c_D \frac{k\sqrt{k}}{\varepsilon} \quad (3.22)$$

Where c_D is an empirically determined constant (-).

Hydraulic structures

Delft3D allows the implementation of hydraulic structures in the numerical model. They are used to model the local effects of sub-grid scale disturbances of the flow, emanating from inclusion of structures such as gates, sluices, porous plates, bridges, weirs, culverts, etc. In the case of culverts, the flow through the object is simulated by a virtual transfer of the flow between the inflow at the intake and the discharge at the outfall. Culverts were used as foundation for the development of the subroutines for TRS operation. This was achieved by modifying the existing culvert subroutine to simulate the turbines and sluice gates of a tidal range power plant. A detailed description of the conceptual approach and implementation of TRS subroutine will be presented in Chapter 4.

3.4.2 Numerical methods

The hydrodynamic equations solver in Delft3D is based on the “WAQUA in SIMONA” system developed by The Dutch National Institute of Coastal and Marine Engineering (Rijkswaterstaat 2016). The “WAQUA in SIMONA” system consists of two hydrodynamic models, solving the shallow-water equations in two- (WAQUA) and three-dimensions

(TRIWAQ). The method is employed on curvilinear orthogonal grids to allow for curved domain boundaries usually associated with irregular boundaries, such as estuaries, rivers and coastal seas. For more efficient modelling capabilities it offers several forms of domain decomposition techniques and guarantees portability of the code between different single processor machines by the use of standard FORTRAN 77/90.

Spatial discretisation

The spatial discretisation of the computational domain is based on the FDM (described in Section 3.3.1). The model employs a staggered curvilinear grid, that is assumed to be orthogonal and well structured. On staggered grids, the state variables are all defined at different locations to optimise the spatial discretisation by using a smaller number of discrete variables while retaining the same level of accuracy (Rijkswaterstaat 2016). Another advantage is to aid the numerical stability, as staggered grids prevent spatial oscillations in the water level (Stelling 1984). The arrangement employed by Delft3D places all the scalar variables (density, water level) at the cell centre (m, n) , which is also called the water level point. The velocity vector components in a given direction are located in the centre of the cell interface $(m+1/2, n)$ and $(m, n+1/2)$ perpendicular to the cell surface, as illustrated in Figure 3.3.

Continuity equation

The spatial derivatives in the depth-averaged continuity equation (3.9) are discretized using the backward difference approximation while temporal derivative is discretized in the time-integration section:

$$\frac{\partial \zeta_{m,n}}{\partial t} + \frac{1}{(\sqrt{G_{\xi\xi}})_{m,n} (\sqrt{G_{\eta\eta}})_{m,n}} \left(HU_{m,n} (\sqrt{G_{\eta\eta}})_{m,n} - HU_{m-1,n} (\sqrt{G_{\eta\eta}})_{m-1,n} \right. \\ \left. + HV_{m,n} (\sqrt{G_{\xi\xi}})_{m,n} - HV_{m-1,n} (\sqrt{G_{\xi\xi}})_{m-1,n} \right) = 0 \quad (3.23)$$

where m, n and k indices denote the position in the curvilinear grid in horizontal ξ, η and vertical ζ directions.

Due to the staggered grid, H is not defined at the velocity point (i.e. the centre of the cell side). Therefore, the discharge through a cell boundary is determined by the sum of the arithmetic average of the depth in the corner points and the average of the water levels on each side of that boundary:

$$H_{m,n}^U = \bar{d}^\eta + \frac{1}{2}(\zeta_{m+1,n} + \zeta_{m,n}) \quad (3.24)$$

where \bar{d}^η is the arithmetic average of the depth in the corner points. The definition of the total depth $H_{m,n}^V$ in η direction is similar.

In the 3D case, the layer-averaged continuity equation is discretized in the same way as equation 3.23 with an addition of the relative vertical velocity $\omega_{m,n,k}$ that couples the adjacent layers:

$$\omega_{m,n,k} = 0, \quad \text{for } k = K$$

$$\begin{aligned} \omega_{m,n,k-1} = \omega_{m,n,k} - \frac{\partial h_{m,n,k}^\zeta}{\partial t} \\ - \frac{1}{(\sqrt{G_{\xi\xi}})_{m,n} (\sqrt{G_{\eta\eta}})_{m,n}} \left(h_{m,n,k}^u u_{m,n,k} (\sqrt{G_{\eta\eta}})_{m,n} \right. \\ - h_{m-1,n,k}^u u_{m-1,n,k} (\sqrt{G_{\eta\eta}})_{m-1,n} + h_{m,n,k}^v v_{m,n,k} (\sqrt{G_{\xi\xi}})_{m,n} \\ \left. - h_{m,n-1,k}^v v_{m,n-1,k} (\sqrt{G_{\xi\xi}})_{m,-1n} \right), \quad \text{for } k = K, K-1, \dots, 1 \end{aligned} \quad (3.25)$$

where h^ζ is the layer thickness at the water level point, while h^u and h^v represent the layer thickness at the respective velocity points.

Momentum equation

Different parts of the momentum equations (3.13 and 3.14) are discretised separately using different methods in order to ensure achieving the second order accuracy in every case. The momentum equation can be split into several distinguishable terms, as illustrated in Figure 3.7. It includes the time-derivative and several spatial-derivatives, including (i) the horizontal advection terms, (ii) the vertical advective term, (iii) the barotropic (water level) and baroclinic pressure gradients, (iv) the horizontal and vertical viscous terms, (v) the Coriolis term and the term for external addition of momentum.

$$\frac{\partial u}{\partial t} + \underbrace{\frac{u}{\sqrt{G_{\xi\xi}}}\frac{\partial u}{\partial \xi} + \frac{v}{\sqrt{G_{\eta\eta}}}\frac{\partial u}{\partial \eta}}_{(i)} + \underbrace{\frac{\omega}{d+\zeta}\frac{\partial u}{\partial \sigma}}_{(ii)} - \underbrace{\frac{v^2}{\sqrt{G_{\xi\xi}}\sqrt{G_{\eta\eta}}}\frac{\partial \sqrt{G_{\eta\eta}}}{\partial \xi}}_{(i)} + \underbrace{\frac{uv}{\sqrt{G_{\xi\xi}}\sqrt{G_{\eta\eta}}}\frac{\partial \sqrt{G_{\xi\xi}}}{\partial \eta}}_{(v)} - \underbrace{f_v}_{(v)} = \underbrace{-\frac{1}{\rho_0\sqrt{G_{\xi\xi}}P_\xi}}_{(iii)} + \underbrace{F_\xi + \frac{1}{(d+\zeta)^2}\frac{\partial}{\partial \sigma}\left(v_v\frac{\partial u}{\partial \sigma}\right)}_{(iv)} + \underbrace{M_\xi}_{(iv)}$$

Labels in the diagram:
 - time derivative: points to $\frac{\partial u}{\partial t}$
 - (i): points to the first two terms of the first row and the third term of the second row.
 - (ii): points to the second term of the first row.
 - (iii): points to the first term of the second row.
 - (iv): points to the second and third terms of the second row.
 - (v): points to the first and second terms of the second row.
 - external addition of momentum: points to the last term of the second row.

Figure 3.7: Distinguishable terms of the momentum equation (3.13).

They are all discretized at the velocity points on the staggered grid, which is in the centre of cell interfaces. For brevity, this section will provide only a brief explanation of the discretisation process. The in-depth description of the discretisation process in Delft3D model can be found in Deltares (2014) and Rijkswaterstaat (2016).

(i) Horizontal advection terms

Delft 3D offers several different advection schemes. All the simulations included in this study employed the so-called Cyclic Method and hence that is the only method described

herein. The Cyclic method is based on the dissipative reduced phase error scheme for both the normal advection term $u \frac{\partial u}{\partial \xi}$ and the cross advection term $v \frac{\partial u}{\partial \eta}$. This scheme splits a third order upwind finite difference scheme into two second order consistent discretized terms, which can be successively used in the two stages of the ADI scheme (which will be described in the next section). The method works well for smooth solutions and is appropriate for tidal simulations (Stelling 1984).

For example, the first horizontal advective term of the u-momentum equation, namely:

$$\frac{u}{\sqrt{g_{\xi\xi}}} \frac{\partial u}{\partial \xi} \quad (3.26)$$

is discretised by central difference following Equation (3.27):

$$S_{0\xi}[u, u] = \frac{1}{2} \frac{u_{m,n,k}}{(\sqrt{g_{\xi\xi}})_{m,n}} (u_{m+1,n,k} - u_{m-1,n,k}) \quad (3.27)$$

where $S_{0\xi}[u, u]$ represents the central difference operator in the ξ -direction.

(ii) Vertical advection term

The vertical advection term $\frac{\omega}{H} \frac{\partial u}{\partial \sigma}$ couples the horizontal velocities of the adjacent layers. A central difference scheme is used for the discretisation, with the second order accuracy approximation of the horizontal velocity u by the means of Taylor series expansion (Rijkswaterstaat 2016).

(iii) The barotropic and atmospheric pressure gradients

The pressure gradient term $\frac{1}{\rho_0 \sqrt{G_{\xi\xi}}} P_\xi$ includes both the barotropic (water level) and the atmospheric pressure gradients:

$$\frac{1}{\rho_0 \sqrt{G_{\xi\xi}}} P_{\xi\xi} = \frac{g}{\sqrt{G_{\xi\xi}}} \frac{\partial \zeta}{\partial \xi} + \frac{1}{\rho_0 \sqrt{G_{\xi\xi}}} \frac{\partial P_{atm}}{\partial \xi} \quad (3.28)$$

Both terms are discretized using the first order upwind difference. The latter is only added in the case of space-varying wind and pressure and is especially important for the simulation of storm surges (Rijkswaterstaat 2016).

(iv) Viscosity terms

The approximations of the vertical viscosity terms $\frac{1}{H^2} \frac{\partial}{\partial \sigma} \left(\nu_V \frac{\partial u}{\partial \sigma} \right)$ are based on the central difference scheme, where the vertical eddy viscosity ν_V is computed at the layer interface. The horizontal viscosity terms, represented by the forces F_ξ and F_η , are discretized using the first order upwind difference (Deltares 2014).

(v) Coriolis term

The Coriolis parameters f_v and f_u are calculated from the geographical latitude. In the staggered grid, they are determined by an arithmetic average of the four surrounding velocity points (Rijkswaterstaat 2016).

Considering all of the above mentioned methods, the ξ -direction momentum equation (3.13) can now be rewritten into its spatially-discretised form as Equation (3.29).

$$\begin{aligned} & \frac{\partial u_{m,n,k}}{\partial t} + S_{0\xi}[u, u] + S_{0\eta}[v, u] \\ & + S_{0\xi}[uv, \sqrt{g_{\xi\xi}}] - S_{0\xi}[v^2, \sqrt{g_{\eta\eta}}] + S_{0z}[h^u, \omega, u] \\ & = -G_{0\xi}[\zeta] - PG_{0\eta}[h^u, h^\zeta, \rho] + S_{0\xi\xi}[u, v] + S_{0\eta\eta}[v, u] \\ & + S_{0zz}[v_v, h^u, u'] - f \bar{v}_{m,n,k}^{\xi\eta} \end{aligned} \quad (3.29)$$

where $S_{0\alpha}[\dots]$ and $G_{0\alpha}[\dots]$ are finite difference operators used for spatial discretisation of the terms. The same is applied to the equation in η -direction. A detailed description of the operators is available in Rijkswaterstaat (2016).

Time discretisation

Delft3D employs the semi-implicit Alternating Direction Implicit (ADI) scheme for marching in time. The ADI method splits one time-step into two half time-steps. Equations are treated implicitly in one horizontal direction at each half time-step leading to a series of 1-dimensional equations and alternating the implicit direction for the next half time-step. The equations are solved in a consistent way across both stages, ensuring at least second order accuracy in space. Advantage of this method is that the implicit coupling of the terms only occurs in one direction at the time, while the terms in the other direction are expressed explicitly. As a consequence, the solutions achieve the second order accuracy after each time-step while maintaining the numerical stability of the simulation. The following notations are employed to present the time integration method. The time-step is denoted as Δt ; the variables without any prime (u, v, ζ) in the superscript are at (previous) time t . The values of the variables with a single prime (u', v', ζ') are taken at the time level $t + \Delta t/2$, and the variables with a double prime (u'', v'', ζ'') are at the new time level $t + \Delta t$.

In the first stage, the time level proceeds from t to the first half of the time-step $t + \Delta t/2$. The water level gradient in the momentum equations and the derivative of the total discharge in the continuity equation are taken implicitly in ξ -direction and explicitly in η -direction. First, the η -direction momentum Equation (3.14) is solved for v' :

$$\begin{aligned}
 \frac{v'_{m,n,k} - v_{m,n,k}}{\Delta t/2} + S_{0\xi}^u[u, v'] + S_{0\eta}^u[v, v'] + S_{0\xi}[uv', \sqrt{g_{\eta\eta}}] - S_{0\eta}[u^2, \sqrt{g_{\xi\xi}}] \\
 + S_{0z}[h^v, \omega, v'] \\
 = -G_{0\eta}[\zeta] - PG_{0\eta}[h^v, h^\zeta, \rho] + S_{0\eta\eta}[u, v] + S_{0\xi\xi}[v, u] \\
 + S_{0zz}[v_v, h^v, v'] - f\bar{u}_{m,n,k}^{\xi\eta}
 \end{aligned} \tag{3.30}$$

followed by the implicitly coupled ξ -direction momentum equation (3.13) and continuity equation (3.9) that provide solutions for u' and ζ' .

$$\begin{aligned}
 \frac{u'_{m,n,k} - u_{m,n,k}}{\Delta t/2} + S_{0\xi}[u', u] + S_{0\eta}[v', u] + S_{0\xi}[u'v', \sqrt{g_{\xi\xi}}] - S_{0\xi}[v'^2, \sqrt{g_{\eta\eta}}] \\
 + S_{0z}[h^u, \omega, u] \\
 = -G_{0\xi}[\zeta'] - PG_{0\eta}[h^u, h^\zeta, \rho] + S_{0\xi\xi}[u, v'] + S_{0\eta\eta}[v', u] \\
 + S_{0zz}[v_v, h^u, u'] - f\bar{v}'_{m,n,k}{}^{\xi\eta}
 \end{aligned} \tag{3.31}$$

$$\begin{aligned}
 \zeta'_{m,n} + \frac{\frac{\Delta t}{2}}{\sqrt{G_{\xi\xi}}\sqrt{G_{\eta\eta}}} \left(U'_{m,n}(\sqrt{g_{\eta\eta}})_{m,n} - U'_{m-1,n}(\sqrt{g_{\eta\eta}})_{m-1,n} \right) \\
 = \zeta_{m,n} + \frac{\frac{\Delta t}{2}}{(\sqrt{g_*})_{m,n}} \left(V_{m,n-1}(\sqrt{g_{\eta\eta}})_{m,n-1} - V_{m,n}(\sqrt{g_{\eta\eta}})_{m,n} \right) \\
 + \frac{\frac{\Delta t}{2}}{(\sqrt{g_*})_{m,n}} \sum_{k=1}^K Q_{m',n',k}
 \end{aligned} \tag{3.32}$$

with

$$U'_{m,n} = \sum_{k=1}^K (h^u)'_{m,n,k} u'_{m,n,k} \tag{3.33}$$

where $Q_{m,n,k}$ represents the local discharge rate due to a discharge source and terms $S_{ii}[u]$, $G_{ii}[u]$ and $PG_{ii}[u]$ that represent various spatially discretized terms of the momentum equation.

In the second stage, the time level proceeds to $t + \Delta t$ and the directions are interchanged. Now, the ξ -direction momentum equation is solved explicitly for u'' :

$$\begin{aligned}
 \frac{u''_{m,n,k} - u'_{m,n,k}}{\Delta t/2} + S_{0\xi}^u[u', u''] + S_{0\eta}^u[v', u''] + S_{0\xi}[u''v'] - S_{0\xi}[v'^2] + S_{0z}[u''] \\
 = -G_{0\xi}[\zeta'] - PG_{0\eta}[\zeta'] + S_{0\xi\xi}[u', v'] + S_{0\eta\eta}[v', u'] + S_{0zz}[u''] \\
 - f\bar{v}'^{\xi\eta}
 \end{aligned} \quad (3.34)$$

and the η -direction momentum equation is coupled with the continuity equation to obtain the v'' and ζ'' :

$$\begin{aligned}
 \frac{v''_{m,n,k} - v'_{m,n,k}}{\Delta t/2} + S_{0\xi}[u'', v'] + S_{0\eta}[v'', v'] + S_{0\xi}[u''v''] - S_{0\eta}[u''^2] + S_{0z}[v''] \\
 = -G_{0\eta}[\zeta''] - PG_{0\eta}[\zeta'] + S_{0\eta\eta}[u'', v'] + S_{0\xi\xi}[v', u''] \\
 + S_{0zz}[v''] - f\bar{u}''^{\xi\eta}
 \end{aligned} \quad (3.35)$$

$$\begin{aligned}
 \zeta'_{m,n} + \frac{\Delta t}{2} \frac{1}{\sqrt{G_{\xi\xi}}\sqrt{G_{\eta\eta}}} \left(V''_{m,n}\sqrt{G_{\eta\eta}} - V''_{m,n-1}\sqrt{G_{\eta\eta}} \right) \\
 = \zeta'_{m,n} + \frac{\Delta t}{2} \frac{1}{\sqrt{G_{\xi\xi}}\sqrt{G_{\eta\eta}}} \left(U'_{m-1,n}\sqrt{G_{\eta\eta}} - U'_{m,n}\sqrt{G_{\eta\eta}} \right) \\
 + \frac{\Delta t}{2} \frac{1}{\sqrt{G_{\xi\xi}}\sqrt{G_{\eta\eta}}} \sum_{k=1}^K Q_{m,n,k}
 \end{aligned} \quad (3.36)$$

Because the two momentum equations are analogous, the same subroutine can be used for solving the equations in both directions (Deltares 2014).

ADI solution algorithm

The time-space discretisation of the hydrodynamic equations yields a set of coupled algebraic equations. A brief description of the solution algorithm for the first time-step is described below, with the second time-step being virtually the same with the interchanged roles of ξ - and η -directions. Consequently, the same subroutine can be used for solving the equations in both directions (Deltares 2014)

At the beginning of each time-step, the solution algorithm starts the iteration process by guessing the unknowns, either initially or from the previous time level. The vertical eddy

viscosity ν_v is computed based on the turbulence characteristics from the previous time-step. Firstly, the discretized equation 3.30 is solved for the v' :

$$\begin{aligned}
 a_{m,n,k} v'_{m,n,k-1} + b_{m,n,k} v'_{m,n,k} + c_{m,n,k} v'_{m,n,k+1} + e_{m,n,k}^{2\xi} v'_{m+2,n,k} + e_{m,n,k}^{1\xi} v'_{m+1,n,k} \\
 + e_{m,n,k}^{-1\xi} v'_{m-1,n,k} + e_{m,n,k}^{-2\xi} v'_{m-2,n,k} + e_{m,n,k}^{2\eta} v'_{m,n+2,k} \\
 + e_{m,n,k}^{1\eta} v'_{m,n+1,k} + e_{m,n,k}^{-1\eta} v'_{m,n-1,k} + e_{m,n,k}^{-2\eta} v'_{m,n-2,k} = d_{m,n,k}
 \end{aligned} \tag{3.37}$$

where a , b , c , d and e are coefficients are constructed from the discretized momentum equation 3.30. A detailed description of each individual coefficient is available in Rijkswaterstaat (2016). The coefficients a , b , c , and e can be arranged into a left-hand side matrix, while the coefficient d forms the right side vector:

$$Av' = d \tag{3.38}$$

Once the solution for v' is obtained, the computation proceeds to the second part of the first half time-step, where u' and ζ' are calculated by solving the implicitly coupled equations 3.31 and 3.32:

$$a_{m,k} \zeta'_m + b_{m,k} \zeta'_{m+1} + c_{m,k} u'_{m,k-1} + e_{m,k} u'_{m,k} + f_{m,k} u'_{m,k+1} = d_{m,k} \tag{3.39}$$

$$U'_m + \zeta'_m \sum p_{m,k} (h^u)'_{m,k} + \zeta'_{m+1} \sum q_{m,k} (h^u)'_{m,k} = \sum r_{m,k} (h^u)'_{m,k} \tag{3.40}$$

This is followed by the evaluation of the vertical velocity using the discretized 3.25 equation. Once all the unknowns are determined, the first half of the ADI time-step is concluded. The algorithm proceeds to the second half time-step (for determining u'' , v'' , and ζ''), which is virtually the same as described above, but with the interchanged role of the ξ - and η -directions (Rijkswaterstaat 2016).

3.5 Summary

Numerical models have become an instrumental tool for hydrodynamic analysis across the water industry. They enable a fast and economical way to study the water flow in contrast to laborious and expensive physical models. The fundamental mathematical equations are flexible and can be successfully applied to a variety of hydro-engineering problems, from simple idealised simulations of the experimental flumes to large ocean models. As it was shown in this chapter, the fundamental equations can be simplified to a certain degree to save computational costs and make the numerical models more attractive for the water industry. Numerical models are developed based on a range of assumptions and simplifications. Therefore, it is essential for users to understand the fundamentals behind the model they are using to assure the appropriateness of the model for the problem they are trying to solve.

This chapter provided a theoretical background for the numerical model used in this study. First, the fundamental hydrodynamic equations were presented in their general form. There are a great number of commercially available and/or academic computer programmes that are based on such equations. While they share the same fundamental equations, the main difference between them is the mathematical approach to solving them. The chapter also provided an overview of the most commonly used numerical approaches. Finally, the software suite used for the simulations performed in this study, namely Delft3D, was presented. The chapter provides a detailed conceptual description, including the 2D depth-averaged and 3D hydrostatic forms of Navier-Stokes equations derived from the general form. In addition, the numerical aspects of the Delft3D model were explained. The modifications applied to the Delft3D model for simulating the TRS are described in the next chapter.

Chapter 4

Modelling tidal range structures

4.1 Introduction

This chapter presents the methodology for hydrodynamic simulations of TRSs, including the theoretical background and implementation of the improved method for modelling the momentum transfer through a TRS, which was one of the key objectives of this study.

The chapter contains conceptual descriptions of the procedures required to represent TRSs in a numerical model, their mathematical formulations, and their implementation into the Delft3D source code. Section 4.2 describes the general concept behind the numerical model and gives an overview of the modifications that were included in the Delft3D source code. It is followed by a description of the three principal modifications that were added to the Delft3D model in order to model the TRSs. Section 4.3 explains the operational sequence of TRSs by describing different power generation schemes. Section 4.4 describes the hydraulic structures that are used for power generation and manipulation of the head difference across the TRS, namely turbines and sluice gates. Section 4.5 presents the method for conservation of momentum transfer through the turbines and sluice gates. Finally, section 4.6 provides a summary of the details presented in this chapter.

4.2 Conceptual approach

TRs are commonly modelled by splitting the domain into two physically separated subdomains by an impermeable structure. One subdomain covers the seaward side, spanning between the open boundary and the impoundment walls, and the other covers the retention basin on the inside of the impoundment walls. The transfer of the water between the two domains is achieved via hydraulic structures that represent the turbines and sluice gates of a TR. There are two conceptually different ways for implementing the hydraulic structures, either as a special type of an internal boundary condition (Falconer et al. 2009), or as an external sink and source terms in the hydrodynamic equations (Brammer et al. 2014). This study employed the latter approach, implementing the hydraulic structures into the Delft3D model through the term Q in the continuity Equation (3.9), and terms M_ξ and M_η in the momentum Equations (3.13-3.14). It is worth emphasising that the flow through a hydraulic structure is not resolved on the grid. It is instead calculated off-grid through a sub-grid scale model of the flow through the hydraulic structure and included in the solutions through sink and source terms in the hydrodynamic equations.

In order to simulate TRs, a new subroutine (Algorithm 4.1) was added to the Delft3D source code. The subroutine is executed at every time step of the simulation, just before the programme proceeds to the routine for solving the system of hydrodynamic equations. Its main task is to determine the instantaneous flow rate and velocity through the implemented hydraulic structures and pass them on to the solution algorithm where they are included in the sink and source terms of the hydrodynamic equations.

Algorithm 4.1: General algorithm for simulation of TRSs added to the Delft3D

GIVEN AT INPUT:
Locations of WL points for head calculation
Locations of turbines and sluices on the grid (intake and outfall)
Turbine Q-H and P-H relationships
Turbine and sluice characteristics
Selected operational sequence

Obtain water levels on either side of the structure
Calculate the head difference
Determine operational stage based on the selected *operational sequence*
For each hydraulic structure:
 Locate the computational cells with intake and outfall
 Calculate head difference between intake and outfall
 Calculate the *discharge* based on the operational stage and head
 Calculate generated *power* (applicable only for active turbines)
 Calculate the *velocity of discharge*
 Determine vertical position (if 3D layers)
End for
Record the discharge and power for output
Pass the *discharge* and *velocity* to the solution algorithm
Prepare variables for next time step

The following modifications that were introduced into the Delft3D source code are described in more detail in the subsequent sections:

- (i) TRS operational sequence algorithm – it determines the operational stage of the power plant based on the head difference across the structure and tide phase.
- (ii) Q-H relationships for determining the flow through the hydraulic structures; hill-chart for turbines and orifice equation for sluice gates.
- (iii) Implementation of the sink and source terms into the momentum equation to guarantee the conservation of momentum.

4.3 Operational sequence

TRSS take advantage of the difference in water level between the high and low tide by impounding the water within a basin (Roberts et al. 2016). When a sufficient hydraulic head difference is created, the water is released through the turbines installed in the impoundment walls to generate the electricity. The potential power of a TRS (P) is fundamentally proportional to the wetted surface area of the impoundment (A) and the square of the head difference (h^2) between the two sides of the structure, as given by the Equation (4.1) (Angeloudis et al. 2016b):

$$P \propto Ah^2 \tag{4.1}$$

Both factors are foremostly determined by the geographical location of the structure, however, the head difference can be artificially altered and hence optimised by adjusting the operational sequence of the scheme.

The operational sequence of a TRS is a pre-programmed list of commands that govern the power generation by manipulating the discharge through the turbines and sluice gates. TRSS can be operated under various operational sequences, such as ebb generation, flood generation (both one-way), and two-way generation (Xia et al. 2010b). The selection of an appropriate scheme is constrained by the location of the impoundment, the design of the installed turbines and sluice gates, the requirements of the National Grid, and other considerations such as environmental constraints or maintaining the required depth for navigation (Angeloudis and Falconer 2017).

4.3.1 One-way operational sequence

In a one-way generation operational sequence, the power can be generated during either ebb or flood tide, but not during both. If, for example, an ebb tide is used for power generation, then the flood tide will be used for filling of the retention basin. This scheme

is commonly known as ebb generation and is illustrated in Figure 4.1. The stage-by-stage description is given from the point of the low tide, just as the water starts rising at the beginning of the flood cycle. At this point, the TRS is at the filling stage, the sluice gates are wide opened and turbines are closed, allowing the water to flow into the impoundment. When the difference in water levels between the two sides falls to zero, the sluice gates are closed and the holding stage is instigated. The role of the holding stage is to achieve a sufficient head difference for power generation between the water levels inside and outside. While the closed sluice gates hold the inside water level at the high point, the water level on the outside is falling due to the ebb tide. The generation stage begins once a sufficient head difference, shown as H_{st} in Figure 4.1, is established. The turbines start operating, allowing the water to flow out of the basin while generating power. The generation stage is terminated as soon as the head difference falls below the minimum required head difference for efficient power generation, denoted by H_{min} . This triggers a second holding stage, preventing the inside water level to fall even further. The sluice gates are reopened when the water surface again starts rising and the whole process is repeated for the next tidal cycle.

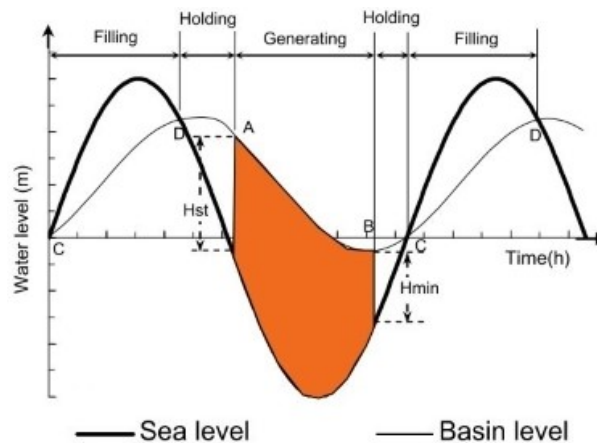


Figure 4.1: Diagram of a one-way operating sequence with generation during ebb tide (i.e. ebb-generation). Adapted from Xia et al. (2010b).

Flood generation operational scheme (Figure 4.2) works in a reverse fashion compared to the ebb generation. Here, power is generated during the flood tide and the releasing stage occurs during the ebb tide instead. The aim of the releasing stage here is to empty the basin as much as possible to maximise the head difference of the next generation stage.

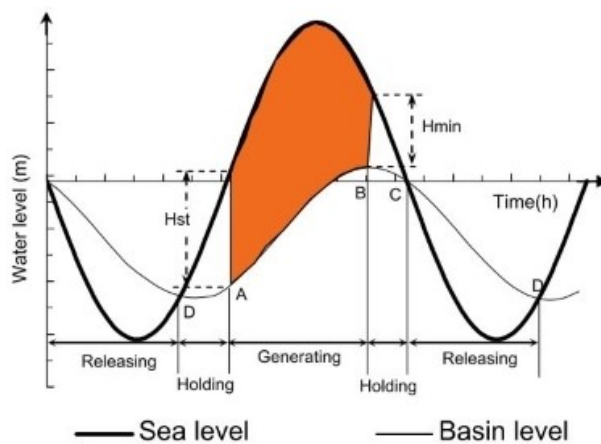


Figure 4.2: Diagram of a one-way operating sequence with generation during flood tide (i.e. flood-generation). Adapted from Xia et al. (2010b).

Flood generation is generally much less efficient as the available head difference reduces more quickly than it would for an ebb generation. This is because the volume in the upper half of the basin, where ebb generation operates, is normally much greater than the volume of the lower half, where flood generation operates (Xia et al. 2010b).

4.3.2 Two-way operational sequence

Two-way generation operational sequence generates power on both ebb and flood tides, as shown in Figure 4.3. The scheme is more complicated and involves more stages compared to the one-way schemes. It also requires a more complex type of turbines that can generate power in both directions (Waters and Aggidis 2016b).

Chapter 4 Modelling tidal range structures

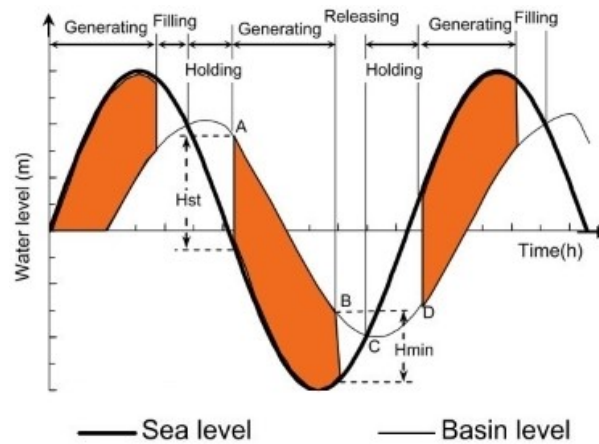


Figure 4.3: Diagram of a two-way operating sequence with generation during both ebb and flood tides. Adapted from Xia et al. (2010b).

Starting at high water, the first generation stage begins during an ebb tide after a sufficient head difference is established, same as in the ebb-only mode. However, when the head difference falls under the minimum value for efficient generation, a releasing (or sluicing) stage is initiated instead of the holding stage. During the releasing stage the turbines are not operating but opened and sluice gates are opened in order to draw down the water level inside the basin as much as possible. Only when the water levels on the inside and outside are equal and no water can flow out of the basin, the holding stage can begin. During the holding stage, the water on the inside is retained at the lowest possible level while the water level outside rises due to the flood tide. The second generation stage (on a flood tide) begins as soon as a sufficient head difference is established. It is followed by a second sluicing stage, with an aim to achieve highest possible water level inside the basin. A second holding stage is then required until a sufficient head difference is reached for the second cycle of operation to begin.

This scheme results in a tidal range inside the basin that is much closer to the natural conditions (Xia et al. 2010b) and is therefore viewed as more acceptable in terms of environmental impacts. Due to four power generation cycles per day instead of just two,

it offers a more evenly distributed power output over time, which makes it easier to be absorbed into the local grid (Baker 1991).

4.3.3 Numerical algorithm

The main function of the operational sequence in a numerical model is to determine the status of the turbines and sluice gates in each time step of the simulation. Once the operational stage is determined, relevant subroutines will be executed to calculate the flow through the turbines and/or sluice gates or just consider them closed and assign zero value to the discharge. In the case of the two-way generation, the operational stage also informs on the direction of the flow (i.e. positive discharge when filling the basin and negative when emptying).

This study employed TRS models based on either the ebb or two-way generation sequence. Both sequences were included in the TRS subroutine (Algorithm 4.1) that was added to the Delft3D source code. A switch for the selection of the required sequence was included in the modifications, giving the user an option to select the appropriate method on a case-by-case basis. Other essential parameters that were required as an input are as follows: (i) required head difference for the start of generation stage (H_{gen}); (ii) minimum required head difference for efficient generation (H_{min}); (iii) maximum holding time (t_{hold}); (iv) locations of the turbines and sluice gates on the numerical grid; as well as (v) the locations of points where water elevations that determine the current head difference (H_{ref}) are taken from. Maximum holding time is used in the rare case when tidal range is too small to establish a sufficient head difference for triggering the generation stage, especially during neap tides of smaller schemes. The routine uses a series of logical expressions that test whether certain conditions that trigger a change of operational stage were met. This information is then passed to the part of the routine that calculates the discharge through the hydraulic structures.

Ebb-only generation

Ebb-only generation consists of four stages as described in Section 4.3.1. In the TRS subroutine, the stages are represented by a numerical value stored in a variable called $(St)^{NEW}$ as summarised in Table 4.1. The routine is given by Algorithm 4.2, with a flow chart of the algorithm included in Appendix A.1.

Table 4.1: Numerical values of operational stages for ebb generation

$(St)^{NEW}$	Operational stage
1	Holding high water
2	Generating (Ebb)
3	Holding low water
4	Filling (Flood)

Algorithm 4.2: Routine for ebb generation operational sequence

GIVEN AT INPUT:
 TRS characteristics: H_{gen} , H_{min} and t_{hold}
 Time step: t_{step}

READ FROM PREVIOUS TIME STEP:
 Stage at previous time step: $(St)^{OLD}$
 Water elevation inside/outside: $(WL)_{IN}$ and $(WL)_{OUT}$
 Time at the previous step: t_{stage}^{OLD}

Calculate current time; $t_{stage}^{NEW} = t_{stage}^{OLD} + t_{step}$
 Calculate the head difference; $H_{ref} = (WL)_{OUT} - (WL)_{IN}$
Select case $((St)^{OLD})$

Case(1) ... previous step was Holding HW
If $H_{ref} \geq H_{gen}$ **then**
 Start Generating; $(St)^{NEW} = 2$
Else if $(H_{min} < H_{ref} < H_{gen})$.and. $(t_{stage}^{NEW} > t_{hold})$ **then**
 Start Generating; $(St)^{NEW} = 2$
Else
 Continue Holding HW; $(St)^{NEW} = 1$
End if

... continues on the next page

Algorithm 4.2 (cont.): Routine for ebb generation operational sequence

```
Case(2) ... previous step was Generating
if  $H_{ref} < H_{min}$  then
    Start Holding LW;  $(St)^{NEW} = 3$ 
Else
    Continue Generating;  $(St)^{NEW} = 2$ 
End if

Case(3) ... previous step was Holding LW
if  $H_{ref} < 0$  then
    Start Filling;  $(St)^{NEW} = 4$ 
Else
    Continue Holding LW;  $(St)^{NEW} = 3$ 
End if

Case(4) ... previous step was Filling
if  $H_{ref} > 0$  then
    Start Holding HW;  $(St)^{NEW} = 1$ 
Else
    Continue Filling;  $(St)^{NEW} = 4$ 
End if
End case select

if  $(St)^{OLD} = (St)^{NEW}$  then
    Reset timer for the new stage to begin;  $t_{stage}^{OLD} = 0$ 
Else if
    Prepare timer for next step;  $t_{stage}^{OLD} = t_{stage}^{NEW}$ 
End if
Prepare stage variable for next step;  $(St)^{OLD} = (St)^{NEW}$ 
Save "old" variables for next time step
```

Two-way generation

The sequence is more complicated compared to the ebb-only generation, as explained in Section 4.3.2. Two additional stages have to be considered – a generation stage during the flood tide and a releasing stage after the ebb generation.

The numerical values $(St)^{NEW}$ of the corresponding stages for the two-way sequence are collected in the expanded table below (Table 4.2). The routine is given by Algorithm 4.3, with a flow chart of the algorithm included in Appendix A.2.

Table 4.2: Numerical values of operational stages for two-way generation

$(St)^{NEW}$	Operational stage
1	Holding high water
2	Generating (Ebb)
3	Releasing
4	Holding low water
5	Generating (Flood)
6	Filling

Algorithm 4.3: Routine for two-way generation operational sequence

GIVEN AT INPUT:
 TRS characteristics: H_{gen} , H_{min} and t_{hold}
 Time step: t_{step}

READ FROM PREVIOUS TIME STEP:
 Stage at previous time step: $(St)^{OLD}$
 Water elevation inside/outside: $(WL)_{IN}$ and $(WL)_{OUT}$
 Time at the previous step: t_{stage}^{OLD}

Calculate current time; $t_{stage}^{NEW} = t_{stage}^{OLD} + t_{step}$
 Calculate the head difference; $H_{ref} = (WL)_{OUT} - (WL)_{IN}$
Select case $((St)^{OLD})$

... continues on the next page

Algorithm 4.3 (cont.): Routine for ebb generation operational sequence

Case(1) ... previous step was Holding HW
If $H_{ref} \geq H_{gen}$ **then**
 Start Generating; $(St)^{NEW} = 2$
Else if $(H_{min} < H_{ref} < H_{gen})$.and. $(t_{stage}^{NEW} > t_{hold})$ **then**
 Start Generating; $(St)^{NEW} = 2$
Else if $(H_{ref} < H_{min})$.and. $(t_{stage}^{NEW} > t_{hold})$ **then**
 Skip to Releasing; $(St)^{NEW} = 3$
Else
 Continue Holding HW; $(St)^{NEW} = 1$
End if

Case(2) ... previous step was Generating Ebb
If $H_{ref} < H_{min}$ **then**
 Start Releasing; $(St)^{NEW} = 3$
Else
 Continue Generating Ebb; $(St)^{NEW} = 2$
End if

Case(3) ... previous step was Releasing
If $H_{ref} = 0$ **then**
 Start Holding LW; $(St)^{NEW} = 4$
Else
 Continue Releasing; $(St)^{NEW} = 3$
End if

Case(4) ... previous step was Holding LW
If $H_{ref} \leq -H_{gen}$ **then**
 Start Generating Flood; $(St)^{NEW} = 5$
Else if $(-H_{min} > H_{ref} > -H_{gen})$.and. $(t_{stage}^{NEW} > t_{hold})$ **then**
 Start Generating Flood; $(St)^{NEW} = 5$
Else if $(H_{ref} > -H_{min})$.and. $(t_{stage}^{NEW} > t_{hold})$ **then**
 Skip to Filling; $(St)^{NEW} = 6$
Else
 Continue Holding LW; $(St)^{NEW} = 4$
End if

... continues on the next page

Algorithm 4.3 (cont.): Routine for ebb generation operational sequence

Case(5) ... previous step was Generating Flood
If $H_{ref} > -H_{min}$ **then**
 Start Filling; $(St)^{NEW} = 6$
Else
 Continue Generating Flood; $(St)^{NEW} = 5$
End if
End case select

Case(6) ... previous step was Filling
If $H_{ref} = 0$ **then**
 Start Holding HW; $(St)^{NEW} = 1$
Else
 Continue Filling; $(St)^{NEW} = 6$
End if
End case select

If $(St)^{OLD} = (St)^{NEW}$ **then**
 Reset timer for the new stage to begin; $t_{stage}^{OLD} = 0$
Else if
 Prepare timer for next step; $t_{stage}^{OLD} = t_{stage}^{NEW}$
End if
Prepare stage variable for next step; $(St)^{OLD} = (St)^{NEW}$
Save "old" variables for next time step

4.4 Turbines and sluice gates

Turbines and sluice gates are the principal components of every TRS. Their main role, from a hydrodynamic point of view, is transferring water between the two subdomains of the TRS. The numerical grids of regional-scale numerical models are typically too coarse to resolve the flow through turbines and sluice gates on the grid. The technique used to reconcile this limitation is to employ a sub-grid scale model of the flow, that calculates it separately from the system of hydrodynamic equations. Once resolved, the flow through the hydraulic structures is included in the solution algorithm through sink and source pairings.

4.4.1 Turbines

A bulb turbine has been the most widely considered and applicable type of a turbine proposed in TRS projects (Atkins 2010). The term “bulb” comes from the shape of the watertight casing that encloses the generator located on the horizontal axis, as can be viewed in the cross-section diagram displayed in Figure 4.4. It is based on the Kaplan-style power unit, redesigned to allow for bi-directional flow and large discharge capacity at low generation heads (Andritz Hydro 2016).

The turbines used in this study are based on the Andritz Hydro model of a bulb turbine, using scaled turbine characteristics that were first presented in a study by Aggidis and Feather (2012). This type of turbine has already been successfully deployed in existing tidal range projects, such as Annapolis and Sihwa tidal range plants in Canada and South Korea respectively, and was also chosen for the on-going design of the units for the Swansea Bay Lagoon tidal plant in the UK (Andritz Hydro 2016).

Chapter 4 Modelling tidal range structures

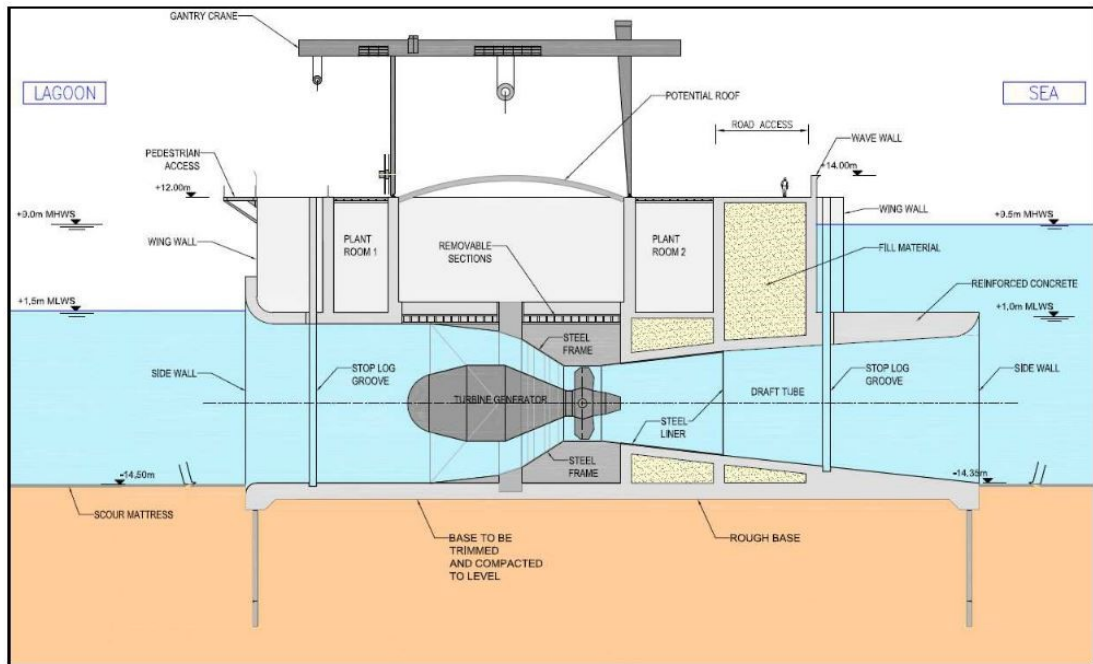


Figure 4.4: Cross-section of a bi-directional bulb turbine proposed for the Swansea Bay tidal lagoon (Tidal Lagoon Plc 2016).

The use of a Q-H relationship (Equation (4.2)), based on the so-called turbine hill chart, has now already been established as the preferred method for determining the flow rate through the turbine (Q_T), in contrast to a more crude orifice equation that was used in the early TRS numerical models (Falconer et al. 2009; Xia et al. 2010b; Angeloudis et al. 2016b; Bray et al. 2016). A hill chart is unique for every type of turbine and is generally obtained experimentally by the manufacturing company.

$$Q_T = f(H) \quad (4.2)$$

Figure 4.5 shows the representative hill chart for the Andritz Hydro double-regulated bulb turbine that was used for the construction of the Q-H relationship used in this study. This hill chart is scalable and can be used for a wide range of turbine sizes. This study included two turbines of 7.2 and 9.0 m diameter size, that were proposed in the design

Chapter 4 Modelling tidal range structures

stages of the Swansea Bay lagoon and Severn barrage projects respectively. The resulting Q-H relationships are shown in Figure 4.6.

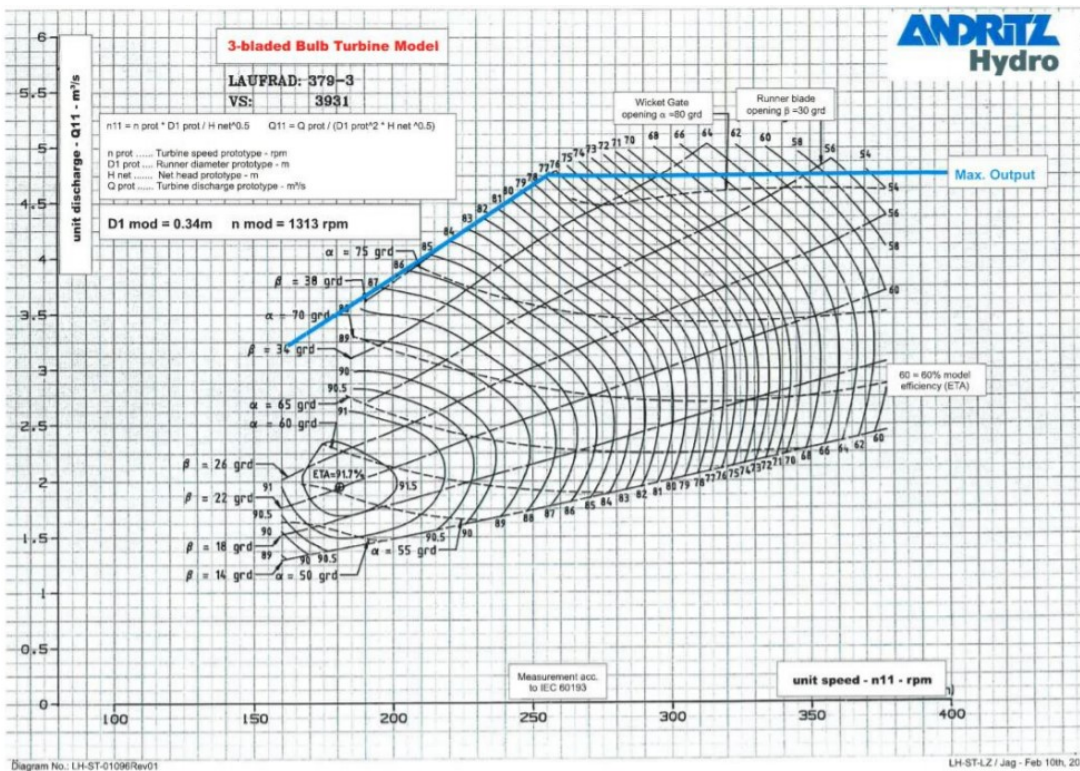


Figure 4.5: A typical Andritz Hydro hill chart for a double-regulated bulb unit on which the Q-H relationships used in this study are based on (Aggidis and Feather 2012).

The values on the hill chart are functions of equations, which enable scaling and from which the head, discharge and efficiency characteristics can be determined. First, the speed of turbine S_p is given by:

$$S_p = \frac{2 \times 60 \times f}{G_p} \quad (4.3)$$

where f is the electricity grid frequency and G_p the number of generator poles, which was 50 Hz and 97 poles in the case of Swansea bay lagoon (Angeloudis and Falconer 2017). The unit speed (n_{11}) of a bulb turbine can be expressed as:

$$n_{11} = \frac{S_p D}{\sqrt{H}} \quad (4.4)$$

where D is the turbine diameter in m. The specific discharge Q_{11} is calculated as:

$$Q_{11} = \frac{Q}{D^2 \sqrt{H}} \quad (4.5)$$

Alternatively, Q_{11} can be represented as a function of n_{11} through the following empirical expression (Aggidis and Feather 2012):

$$Q_{11} = 0.0166n_{11} + 0.4861 \quad \text{if } n_{11} < 255$$
$$Q_{11} = 4.75 \quad \text{if } n_{11} \geq 255 \quad (4.6)$$

As a result, the turbine flow rate Q can now be calculated using the rearranged equation (4.5):

$$Q = Q_{11} D^2 \sqrt{H} \quad (4.7)$$

In addition to a Q-H relationship we can also determine a power-head (P-H) relationship for the turbine by employing the Equation (4.8):

$$P = \eta \rho g H Q_T \quad (4.8)$$

where η is an overall efficiency for the turbine in relation to the available head difference, and ρ is the density of the fluid, g the gravitational acceleration, H the driving head and

Q_T the discharge calculated from the Equation 4.2. The P-H relationships of the selected turbines are plotted next to their respective Q-H relationships in Figure 4.6.

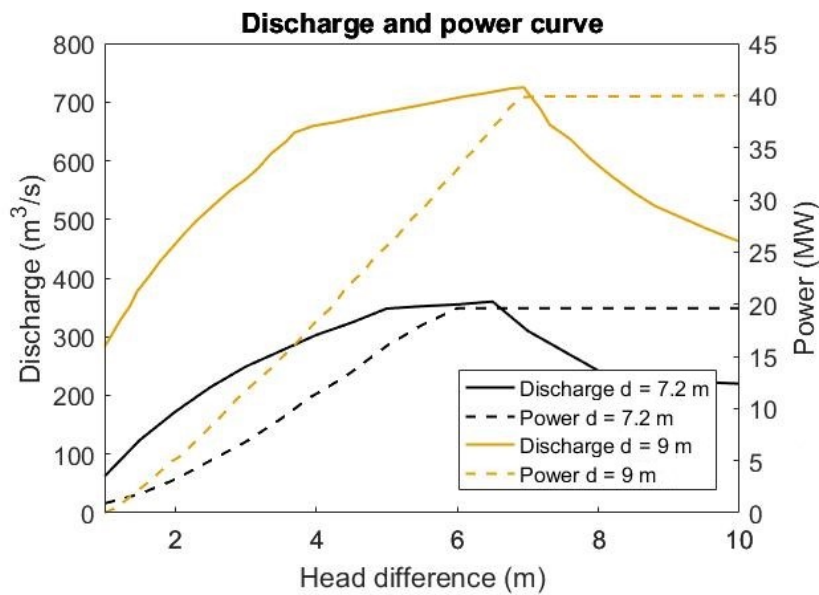


Figure 4.6: Q-H and P-H relationships for bi-directional turbines used in this study.

4.4.2 Sluice gates

Sluice gates are hydraulic structures that can regulate the water flow through an impermeable structure, such as an impoundment wall. In their most simple form, they consist of a channel or a pipe with an installed movable gate that can control the flow rates through the structure. The term sluice gate technically refers to the gate structure only, however, in the context of this study the term is used to describe the entire sluice caisson, including the water passageway (Figure 4.7a) and the mechanical sliding gate (Figure 4.7b).

Chapter 4
Modelling tidal range structures

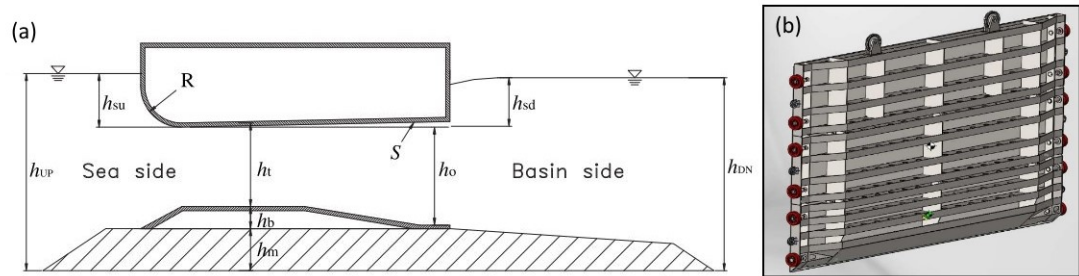


Figure 4.7: An example of (a) a water passageway (Lee et al. 2010) and (b) a sliding gate (Tidal Lagoon Plc 2016) typically used in TRS designs.

The sluice gates in TRSs are designed to maximize the water discharge capability in order to increase the efficiency in tidal power generation (Lee et al. 2010). The gates are lowered (closed) during the generation and holding stages of the operation and raised (opened) during the releasing and filling stages of the operation in order to equalise the water levels on both sides of the structure. A typical design of a sluice gate caisson used in TRS is represented in Figure 4.8.

Chapter 4
Modelling tidal range structures

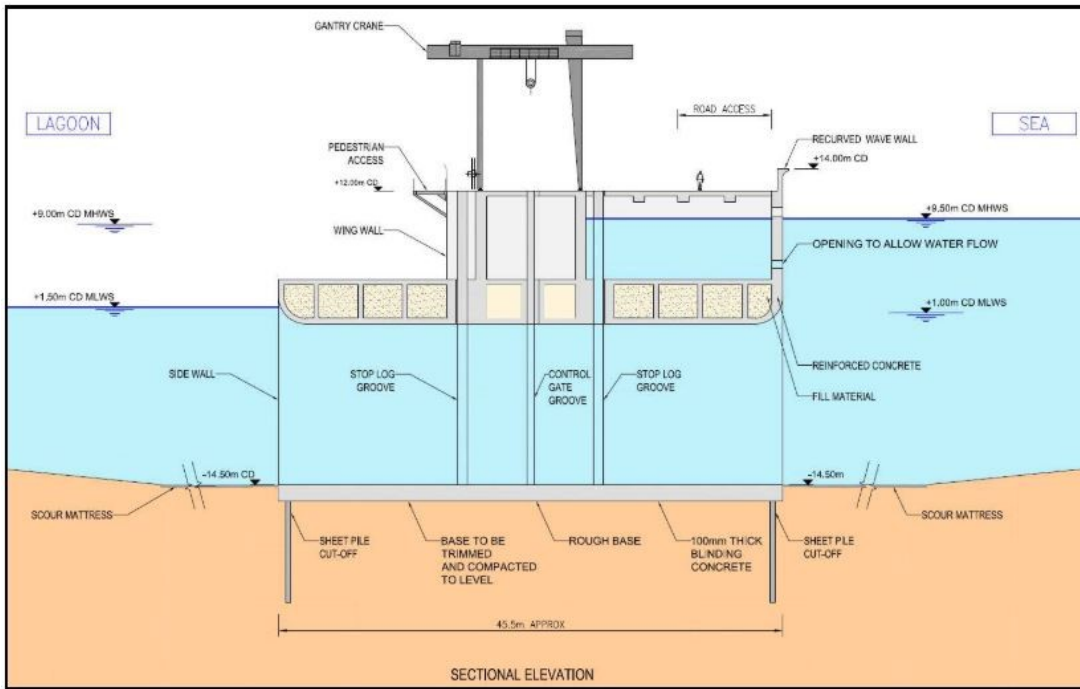


Figure 4.8: Cross-section of a sluice caisson proposed for the Swansea Bay tidal lagoon (Tidal Lagoon Plc 2016).

The instantaneous discharge through sluice gates is described by the orifice equation (4.9), establishing a simple relationship between the flow rate (Q_S) and the corresponding head difference (H) across the structure (Xia et al. 2010b):

$$Q_S = C_d A_S \sqrt{2gH} \quad (4.9)$$

where Q_S is the flow rate through the sluice gate in m^3/s , C_d the discharge coefficient, A_S the flow area through the sluice structure in m^2 , g is gravitational acceleration and H is the driving head.

4.4.3 Implementation into the numerical model

The calculation of the discharge through the hydraulic structures is performed at every time step of the computation, right after the current operational stage is determined, as

described in Algorithm 4.1. The programme proceeds with the calculation of Q_T only when a generation stage is active, during any other stage it assigns a zero value to the variable. Same goes for the calculation of Q_S , however, this time only the sluicing stages (releasing or filling) are considered active. There is an option to include the flow through the turbines in the sluicing stage, to maximize the water transfer. However, in this case the turbines are disconnected from the generator and an orifice equation (4.9) has to be used instead of the hill chart.

Algorithm 4.4: Interpolation of the discharge from the Q-H table.

```

Given:
- Number of points in the Q-H table:  $N_p$ 
- Q and H values in the table:  $Q_T(i)$  and  $H_T(i)$ 
- Water level at intake and outfall:  $z_{W1}$  and  $z_{W2}$ 

Calculate the head difference;  $d_z = |z_{W1} - z_{W2}|$ 
If  $d_z \leq H_T(1)$  then  $disch = 0$ 
If  $d_z > H_T(N_p)$  then  $disch = Q_T(N_p)$ 
For  $i = 2$  to  $N_p$ 
  If  $d_z > H_T(i - 1)$  and  $d_z \leq H_T(i)$  then
    Calculate interpolation factor;  $a = \frac{(d_z - H_T(i - 1))}{(H_T(i) - H_T(i - 1))}$ 
    Interpolate;  $disch = (1 - a) * Q_T(i - 1) + a * Q_T(i)$ 
  End if
End for

```

The Q-H relationship (Figure 4.6) is provided at the input of the model in a form of a two-column table, where each row represents a Q-H pair from the Hill-Chart. The head difference is calculated from the water surface elevation in the two computational cells where the intake and outfall are located. The turbine discharge Q_T is then calculated through interpolation between the two closest points in the table as described in Algorithm 4.4. An equivalent procedure is employed for the calculation of the generated power, this time interpolating a table containing the P-H relationship (Figure 4.6).

The procedure for determining the discharge through the sluice gates Q_s is much simpler. It is calculated directly from the orifice equation (4.9) as described in the Section above.

4.5 Momentum conservation

It has been demonstrated that the discharge velocity exiting the turbines could easily exceed 10 m/s, which is considerably larger than the background velocity of the local flow (Angeloudis et al. 2016b). This high velocity can significantly impact the local water quality, sediment transport, and other morphological and ecological processes, both inside and outside the basin. Therefore, the velocity of jets exiting the turbines must not be neglected, even within larger regional scale hydrodynamic models. The local 3D effects in the vicinity of the turbines also affects the surface elevation profile, as illustrated by Jeffcoate et al. (2013) in their experiments. The depth-averaged model inaccurately predicted the water depth in the region of 20 turbine diameters downstream of the barrage, while the results of the 3D model showed much better agreement with the measured data. Since the operation of the TRS is governed by the difference in water elevation on both sides of the turbine, an inaccuracy in water level predictions may lead to an erroneous turbine flowrate and power output.

There are different conceptual approaches to model the correct transfer of momentum through tidal range turbines. The most accurate method would be a full 3D computational fluid dynamics (CFD) model, where the flow through a turbine itself would be included in the computations (Adcock et al. 2015). However, such simulations are computationally very demanding and too expensive to be used at the regional scale. A more conventional method, also used in the study herein, is to resolve the flow through the hydraulic structures with a sub-grid model. After it is calculated, the information relating to the time varying flow through the structure is added to the appropriate computational cells. This information does not contain only the volume of the water transferred, but more importantly it also includes the velocity of the discharged flow,

which is directly linked to the transfer of momentum. The treatment of momentum is therefore paramount to the accuracy of the flow conditions in the area at the turbine exit.

The momentum flux was treated as an induced external force on the body of water. The momentum was conserved by adding an extra term into the momentum equations. The term represents an external force that is acting on the body of water due to the high-velocity jet entering the domain. An equivalent concept is used in simulations of tidal stream power extraction, where the stream turbine acts as a momentum sink (rather than a source) as it takes the energy out of the passing water flow (Ahmadian et al. 2012). While the approach of momentum sink within the computational domain is already commonly used in tidal stream studies, the momentum source represents a novel method of modelling the TRSs and other hydraulic structures.

In Delft3D, this momentum source term is denoted as M_ξ and M_η in equations (3.13) and (3.14). The force of a jet entering a body of water can be characterised as the rate of change of momentum of the fluid and is commonly defined by Equation (4.10):

$$\vec{F}_T = \rho_0 Q (\vec{v}_1 - \vec{v}_2) \quad (4.10)$$

where ρ is water density, Q is the flow rate entering/leaving the control volume, v_1 and v_2 are velocities of the flow entering and exiting the control volume respectively. For the sake of simplicity, the equation (4.10) can be rewritten into a scalar form for each direction. This is shown for ξ direction through Equation (4.11) below:

$$F_{T\xi} = \rho_0 Q (\hat{u} - u) \quad (4.11)$$

where \hat{u} is the velocity of the incoming jet and u the background velocity in the target cell. From here on, the derivation will be shown only for a component in ξ direction (as in Equation (4.11)), however, the same is applied to the component in η direction.

Assuming the force is acting on the whole volume of the computational cell and taking into account Newton's law of motion, a body force is divided by m_{cell} (the mass of water in the computational cell). The momentum source terms M_ξ and M_η which were introduced in Equations (3.13) and (3.14) can now be rewritten into the following form:

$$M_\xi = \frac{F_{T\xi}}{m_{cell}} = \frac{F_{T\xi}}{\rho_0 V_{cell}} \quad (4.12)$$

where V_{cell} is the volume of the targeted computational cell in m^3 . Substituting the equation (4.11) into the equation (4.12) gives:

$$M_\xi = \frac{\rho_0 Q(\hat{u} - u)}{\rho_0 V_{cell}} = \frac{Q}{V_{cell}}(\hat{u} - u) \quad (4.13)$$

and can be easily simplified to:

$$M_\xi = q_{in}(\hat{u} - u) \quad (4.14)$$

where u is obtained from the existing velocity field, while \hat{u} and q_{in} are calculated from the turbine (Q_T) or sluice gate (Q_S) discharge (Equations (4.2) and (4.9)) during the power generation and sluicing stages of the lagoon's operation:

$$\hat{u} = \begin{cases} \frac{Q_T}{A_T}, & \dots \text{for turbines} \\ \frac{Q_S}{A_S}, & \dots \text{for sluice gates} \end{cases} \quad (4.15)$$

$$q_{in} = \begin{cases} \frac{Q_T}{V_{cell}}, & \dots \text{for turbines} \\ \frac{Q_S}{V_{cell}}, & \dots \text{for sluice gates} \end{cases} \quad (4.16)$$

where A_T and A_S represent the flow-through area of the turbine and sluice gate respectively, and V_{cell} is the volume of the computational cell.

4.5.1 Implementation into the numerical model

The momentum term M_ξ (Equation (4.14)) is added to the momentum equation in a discretized form (Equation (3.37)). The equation (4.14) contains both the velocity of the discharge entering the computational cell, as well as the existing velocity of the water flow in the same computational cell. It can therefore be split into two components:

$$M_\xi = \begin{cases} q_{in}\hat{u} \\ -q_{in}u \end{cases} \quad (4.17)$$

The $(-q_{in}u)$ part of the term, that contains the background velocity, was moved to the left side of the discretized equation (3.37) and was joined with the $(b_{m,n,k}u'_{m,n,k})$ term, while the contribution of the external force $(q_{in}\hat{u})$ was left on the right side of the equation and added to the $d_{m,n,k}$ term:

$$b_{m,n,k}^{MOD}u'_{m,n,k} = (b_{m,n,k} + q_{in})u'_{m,n,k} \quad (4.18)$$

$$d_{m,n,k}^{MOD} = (d_{m,n,k} + q_{in}\hat{u}) \quad (4.19)$$

and the discretized momentum equation (3.37) can be rewritten as:

$$\begin{aligned} a_{m,n,k}u'_{m,n,k-1} + b_{m,n,k}^{MOD}u'_{m,n,k} + c_{m,n,k}u'_{m,n,k+1} + e_{m,n,k}^{2\xi}u'_{m+2,n,k} \\ + e_{m,n,k}^{1\xi}u'_{m+1,n,k} + e_{m,n,k}^{-1\xi}u'_{m-1,n,k} + e_{m,n,k}^{-2\xi}u'_{m-2,n,k} \\ + e_{m,n,k}^{2\eta}u'_{m,n+2,k} + e_{m,n,k}^{1\eta}u'_{m,n+1,k} + e_{m,n,k}^{-1\eta}u'_{m,n-1,k} \\ + e_{m,n,k}^{-2\eta}u'_{m,n-2,k} = d_{m,n,k}^{MOD} \end{aligned} \quad (4.20)$$

The equivalent is true for the momentum equation in the η -direction. The $b_{m,n,k}^{MOD}$ and $d_{m,n,k}^{MOD}$ are updated at the start of every half time-step of the ADI solution algorithm. After that, the algorithm proceeds with solving the hydrodynamic equations as was described in Section 3.4.2.

4.6 Summary

This chapter outlined various elements of a TRS numerical model that were used in this study. First, a conceptual approach to the modelling of the TRS was explained, listing the modifications that were introduced to the Delft3D source code. They include (i) an operational sequence algorithm, (ii) mathematical formulations for the representation of turbines and sluice gates, and (iii) implementation of the source term for conservation of momentum. A background explanation was given for each of them, followed by the algorithms and mathematical formulations, that explained how the modifications were implemented into the Delft3D numerical model.

Chapter 5

Development model: Severn Barrage

5.1 Introduction

This chapter presents the development model for the simulation of TRS in Delft3D. The study has focused on the so-called STPG layout of the Severn Barrage, a scheme that has been the most studied TRS project to date. A rich database of published simulation results was used as a benchmark for assessing the performance of the newly developed model. The model was set up to match the characteristics of the studies from the literature, such as the extents of the numerical domain, turbine parameters, time frame, boundary conditions and operational sequence. The aim of the study was to test the developed methods for TRS simulation, that were described in Sections 4.3 and 4.4. The methodology for this assessment is presented in Section 5.2, providing an explanation of the simulation procedure and model set up, as well as a detailed description of the Severn Barrage characteristics that govern the operation of the barrage. Section 5.3 provides the validation of the hydrodynamic conditions in the domain pre-inclusion of the barrage. The results of the simulations with the barrage in operation are presented in Section 5.4, including the assessment of the far-field and near-field impacts of the scheme. Finally, Section 5.5 provides a summary of the main findings.

5.2 Methodology

This chapter has addressed the first key objective of this thesis, which was to develop and implement a module for simulation of TRS in Delft3D. The module was based on the methodology used in previous TRS simulations found in literature. It was developed to be specifically used for tidal energy analysis in the Severn Estuary and Bristol Channel, however, the flexibility of the Delft3D code means that it can be easily modified and calibrated for assessment of any tidal energy projects worldwide. To date, much of the hydrodynamic analysis of TRSs in the UK has focused on the STPG Severn Barrage proposal, as was systematically portrayed in Section 2.4.2. The same tidal barrage scheme was chosen to be used in this study for comparison and validation of the newly developed routines for TRS simulation in Delft3D. This study acts as a sort of “development model” that will be used for future hydraulic simulations of other tidal power projects proposed in the region.

First, a model without a barrage was used for validation of the hydrodynamics. After the validation was completed, the barrage was introduced into the domain of the Continental Shelf (CS) model. The CS domain is considerably larger than a typical estuary-scale domain and is required when tidal range schemes induce far-field changes to the hydrodynamic conditions. It was used to compare the changes in the hydrodynamic regime, particularly to assess the far-field impacts, pre- and post-construction of the barrage, shown as CS0 and CS1 respectively. The main downside of the CS model is that it is computationally expensive and therefore unpractical for analysis of local hydrodynamic phenomena generated by the barrage operation. The model also employs a coarser computational grid, sacrificing the level of detail for computational efficiency. In practice, the larger scale models are mainly used to obtain boundary conditions for models with smaller domains and high-resolution grids, which are then used for more detailed analysis (Zhou et al. 2014a). Such a model with a smaller and more refined domain was also employed in this study. Its extents were limited to the Severn Estuary and Bristol Channel (for brevity denoted by SE), providing a more detailed

understanding of the local impacts of the barrage on the flow conditions. Boundary conditions for the SE model were exported and converted from the water level results of the CS model. Same as with the CS model, two simulation runs were performed with the SE; first without the barrage (SE0) and second after the inclusion of the barrage (SE1).

5.2.1 Severn Barrage scheme description

The barrage layout used in this study is based on the STPG scheme (Figure 2.13c) as described in Section 2.2.4. This layout has been the most studied of the barrage proposals and is therefore ideal for benchmarking the performance of the developed model. The proposed barrage would be 16 km long, impounding a 573 km² area by spanning the estuary between Barry on the north and Weston-Super-Mare on the south bank. The scheme would incorporate 216 bulb turbines, 166 sluice gates, ship locks and other hydraulic structures such as smaller locks and fish passage (Xia et al. 2010a). Of those, only turbines and sluice gates were included in the numerical model (

Figure 5.1). Other hydraulic structures could be ignored without affecting the results of the simulation. The turbines were located in the central span of the barrage. They were surrounded by two sections of sluice gates on the north part and one section on the south part of the barrage wall. All the turbines were of equal size, measuring 9 m in diameter, with a combined area of the sluice gates amounting to 35 000 m².

The scheme was designed for the ebb-only power generation, as described in Section 4.3. The turbines were designed for a driving head of 4 m with a minimum head of 1.5 m and were represented by a Q-H relationship (Figure 4.6) that was described in Section 4.4. The sluice gates were represented by an orifice equation (Equation (4.9)). A summary of the scheme's specifications is outlined in Table 5.1.

Chapter 5
Development model: Severn Barrage

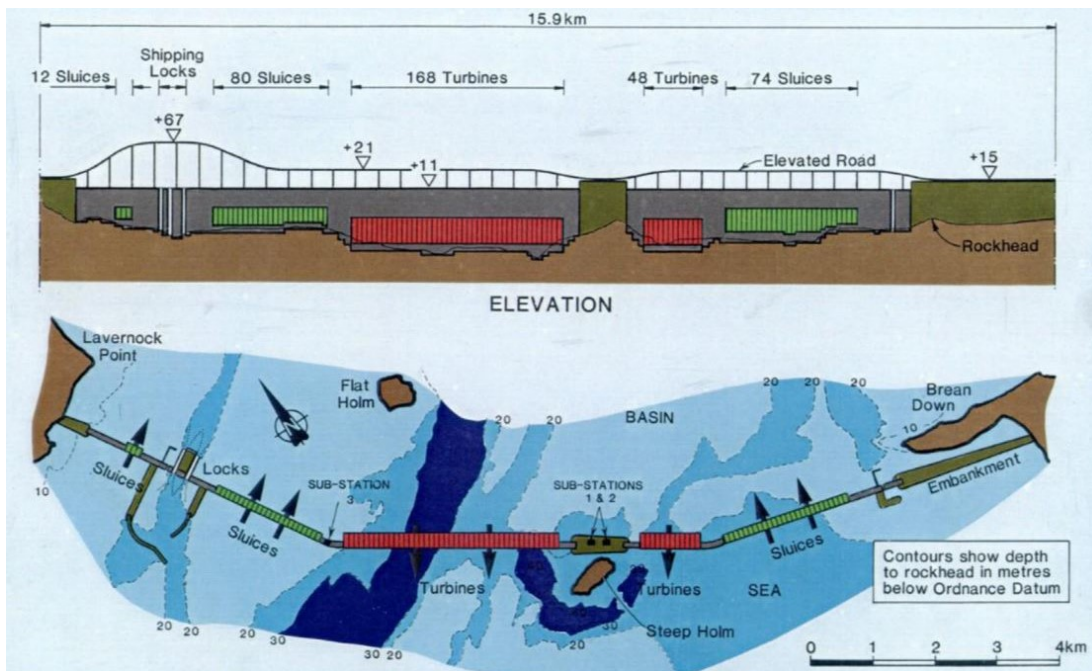


Figure 5.1: Layout of the barrage wall and locations of turbines and sluice gates. Image courtesy of Severn Tidal Power Group (STPG 1989).

Table 5.1: Specifications of the Severn Barrage scheme used in this study.

Severn Barrage specifications	
Starting head (m)	4.0
Minimum head (m)	1.5
Wall length (km)	16
Impounded area (km ²)	573
Turbine number	216
Turbine diameter (m)	9
Turbine capacity (MW)	40
Total capacity (MW)	8 640
Number of sluice gates	166
Combined sluice gate area (m ²)	35 000

5.2.2 Numerical model

Domain extent

The study area (Figure 5.2) was situated off the west coast of the UK, with a particular interest in the Severn Estuary.



Figure 5.2. Study area - showing open boundaries of the Continental Shelf domain (orange) and Severn Estuary model (yellow). Closed boundaries were characterized by the coastline (black).

The Severn Estuary has the second largest tidal range in the world, which can reach more than 14 m during the spring tides. It is around 200 km long and relatively shallow. At its widest point it measures approximately 14 km across, which is between Cardiff and Weston-super-Mare. This is also the presumed location of the Severn Barrage. Continuing westward, the estuary opens up into the Bristol Channel, a major British inlet that separates South Wales from England, extending westward all the way to the Celtic Sea. Its western-most boundary is often denoted by an imaginary line between Hartland Point in England and St. Govan's Head in Wales; the same line was also selected as the

open boundary of the SE domain. The CS domain covered a significantly larger region, encompassing the area between the island of Great Britain and the edge of the continental shelf, including the Irish Sea, entire island of Ireland, and part of the Scotland's west coast in the north, as well as a part of the French Atlantic coast in the south. The extent of the domain and the locations of the SE and CS boundaries are illustrated in Figure 5.2.

The CS domain was represented by a grid with a relatively coarse resolution, covering approximately 850 000 km² surface area at mean tidal level. The grid consisted of nearly 260 000 cells of variable sizes. In the areas of specific interest, i.e. around the barrage, the computational cells measured around 250x250 m², with the cell size gradually increasing towards the open boundary, measuring as much as 5000x5000 m². The area covered a diverse topography (Figure 5.3), with bottom elevations ranging from 5000 m below Ordnance Datum in the deep ocean to 5 m above Ordnance Datum along the narrower reaches of the Severn Estuary.

The SE domain covered a considerably smaller region, with a surface area measuring approximately 5800 km² at the mean tidal level. Its computational grid was obtained by cutting the CS grid at the location of the open boundary (i.e. at the entrance into the Bristol Channel at Heartland Point) and refining it to a higher resolution. For a higher resolution and better accuracy, cells in the area around the barrage were reduced from 250x250 m² to around 100x100 m². The refined mesh introduced additional grid nodes, for which the bottom elevation values were interpolated from the CS grid (Figure 5.4). The water elevation time series for the open boundary condition was extracted from the CS model results, which meant that both CS and SE models used the same time interval for the simulation.

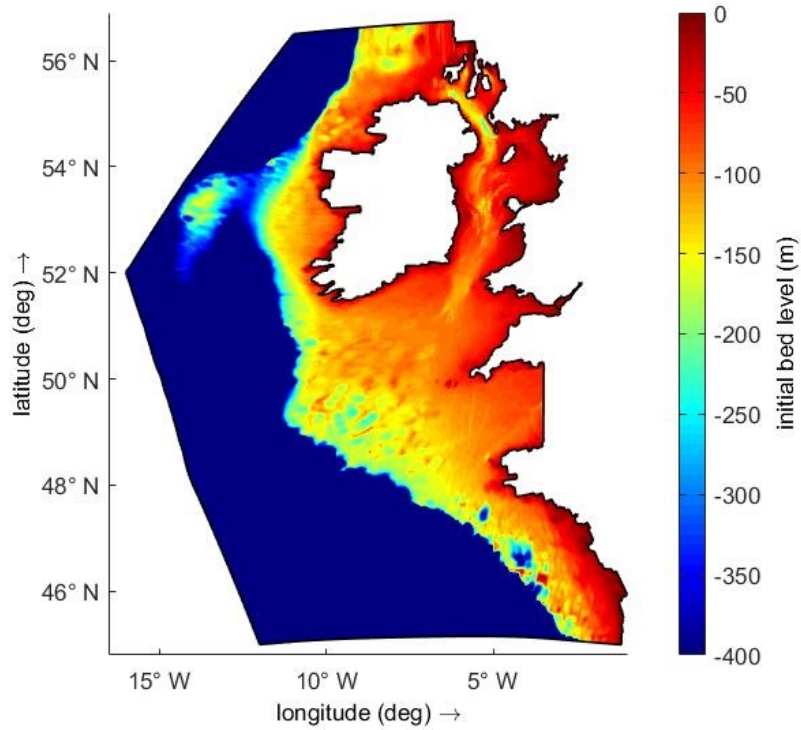


Figure 5.3: Computational domain of the CS model, showing the bathymetry data in Delft3D.

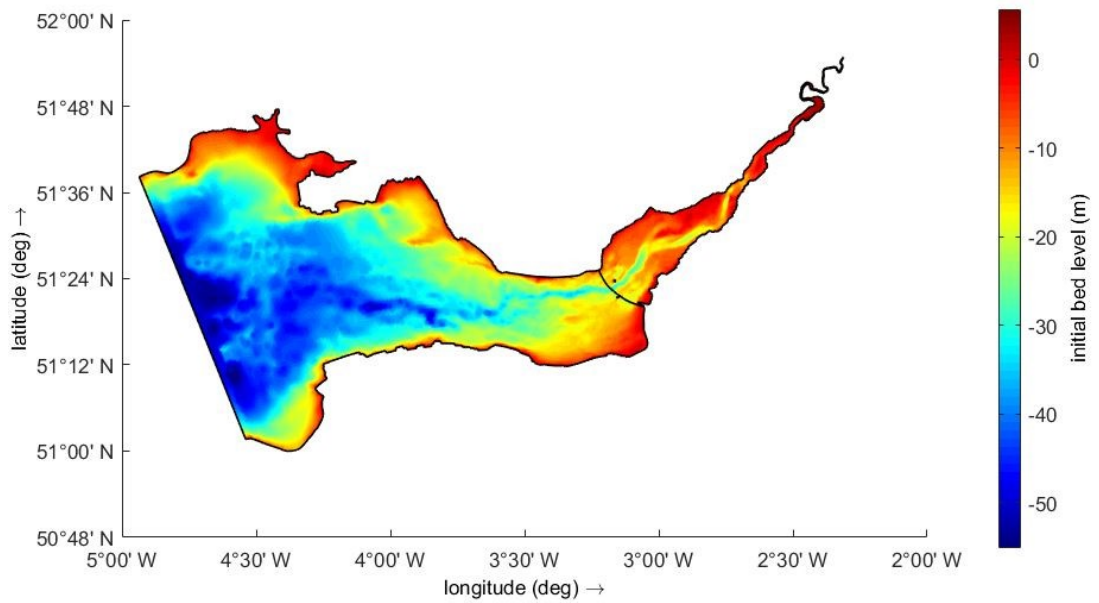


Figure 5.4: Computational domain of the SE model, showing the bathymetry data in Delft3D.

Model set-up

In order to obtain a holistic view of the tidal barrage operation, the simulation time spanned over a 14-day period that covered both neap and spring tidal regimes. Selected was a representative period between 1st and 14th March 2005, that could be used for estimation of the annual power production by extrapolating the results over the entire year. The tidal elevation time series used as the model boundaries were obtained from the MIKE21 global model (Warren and Bach 1992).

All simulations used the same time step of 3 seconds, which was selected to satisfy the CFL condition. On a standard desktop PC, with 3.60 GHz Intel® Core™ i7 series CPU, the total elapsed time for the full simulation of the SE model was 18 hours, while the CS model required almost 90 hours to complete the computation. To increase the efficiency of the CS model, it was subsequently adapted to run on the Cardiff University's High-Performance Computing (HPC) cluster, cutting the computational time to around 36 hours using 6 CPU threads.

5.3 Model validation

Initially, the CS model was run without the barrage. It was validated against observed tidal elevations and velocity data across the whole domain. The domain was split into four regions and a uniform value of the bottom roughness, represented by the Manning's roughness coefficient, was selected for each region. A value of 0.035 was selected for the region of the Severn Estuary, 0.030 and 0.025 in the upper and lower reaches of the Bristol Channel respectively and 0.020 everywhere else. This distribution of roughness coefficient was selected based on an already calibrated model from Bray et al. (2016), which used identical input data as the model presented herein. Figure 5.5 shows the locations of the selected observation points that were representative for the entire domain. Additional observation locations from other parts of the domain were showing similar trends and are included in Appendix A. The data for the direction and magnitude

of the flow velocity was collected from the Admiralty Charts (No. 1123, 1165 and 1826). The velocity was additionally compared to results produced by the EFDC model Bray et al. (2016). The time series for the tidal elevations were obtained from the British Oceanic Data Centre (BODC 2017).

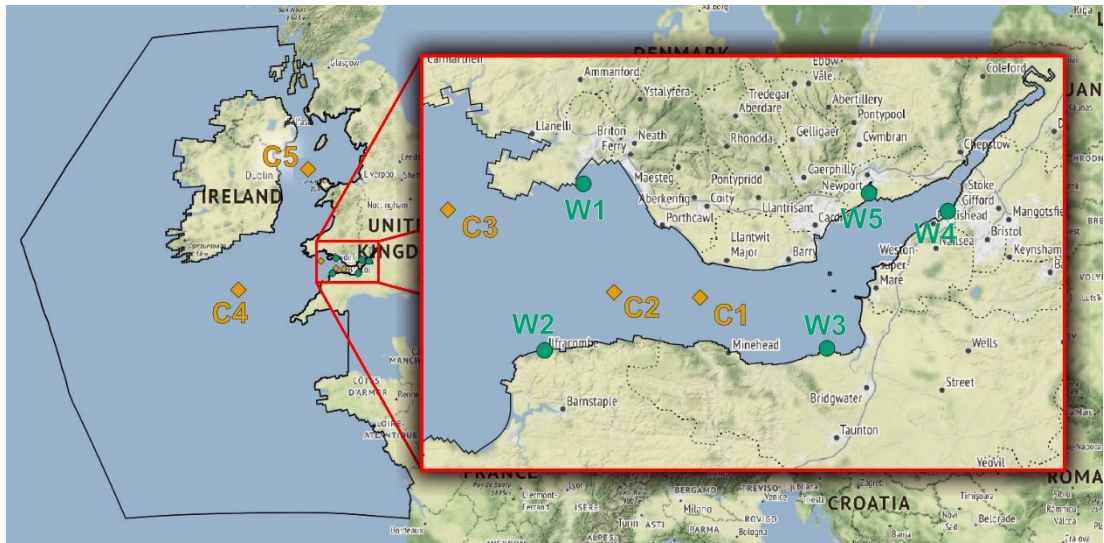


Figure 5.5: Locations of the observation sites used for validation of the tidal flow (yellow) and water levels (green).

Several different performance indicators were used to quantify the performance of the hydrodynamic model. First, the correlation coefficient r was calculated to measure the strength of the linear relationship between predictions and observations, where an r value closer to 1 indicates a strong relationship between the two variables. Correlation was calculated using Equation (5.1):

$$r = \frac{\sum(S_i - \bar{S})(O_i - \bar{O})}{\sqrt{\sum(S_i - \bar{S})^2 \sum(O_i - \bar{O})^2}} \quad (5.1)$$

Where O_i are the observed data points, S_i are the simulation results, and \bar{O} is the mean of the observed data, and \bar{S} mean of the simulation results.

To evaluate the error of the simulation results the Root Mean Squared Error (RMSE) was used, which has the same units as the quantity being estimated. A smaller RMSE value indicates good model performance. RMSE was calculated using Equation (5.2):

$$RMSE = \sqrt{\frac{\sum(O_i - S_i)^2}{n}} \quad (5.2)$$

Where n is the total number of data points in the time series.

The Nash-Sutcliffe model efficiency (NSE) was initially developed to assess the forecasting performance of hydrological models. However, it can be used for evaluation of any predictive model when comparing it to observed data (Nash and Sutcliffe 1970). The NSE is based on the Equation (5.3):

$$NSE = 1 - \frac{\sum_{i=1}^n (O_i - S_i)^2}{\sum_{i=1}^n (O_i - \bar{O})^2} \quad (5.3)$$

An efficiency value of 1 corresponds to an exact match between predictions and observations, while a value of 0 indicates that the model predictions are as accurate as the mean of the observed data and becoming less accurate if the value falls below zero.

In addition to this, scatter index (SI) was also used in the analysis. It is calculated using the Equation (5.4) and presents the proportion of RMSE difference with respect to mean observation:

$$SI = \frac{RMSE}{\bar{O}} \quad (5.4)$$

Figures 5.6 to 5.10 show the validation of the velocity results at three different locations along the centreline of the Bristol Channel (C1–C3) and two additional points further away from the estuary, one in the middle of the Celtic Sea (C4) and the other in the middle

of the Irish Sea (C5). At each site, the predicted tidal currents were compared against the tidal data for a 12-hour interval, showing flow direction of a typical tidal cycle, as well as velocity magnitude of mean spring and neap tides. In addition, four statistical parameters (Equations (5.1) to (5.4)) were calculated for each site to quantify the performance of the hydrodynamic model. The performance indicators for current direction, spring current speed and neap current speed are collected in Tables 5.2, 5.3 and 5.4 respectively.

In general, there was a good agreement between the predicted and observed data at all five locations. Both correlation factor and NSE were very high, above 0.9 for all three variables at all five locations. The only exception was site C5 in the Irish Sea with a slightly worse performance in predicting the current direction (NSE of 0.794). However, because the correlation factor was good (0.933) and since point C5 located far away from the estuary, this result was still considered acceptable. Delft3D has on general produced better predictions than the EFDC model. At the three sites in the Bristol Channel (C1–C3), Delft3D was especially accurate at predicting the incoming tide, showing much closer fit to observations than EFDC (Figures 5.6bc, 5.7bc, 5.8bc). In the Celtic Sea (C4), where larger depths result in a significantly lower velocity, both models predicted the correct amplitude for both spring and neap tides (Figure 5.9bc), however, Delft3D managed to better capture the timing of the slack water, while EFDC was slightly out of phase. The difference between the two models was the least apparent at the location in the Irish Sea (C5), where both models predicted similar velocities, showing a good match with the observed data (Figure 5.10bc). Both models also produced similar predictions for the flow direction at locations C2, C3 and C5, as shown in Figures 5.7a, 5.8a, 5.10a. However, Delft3D again managed to better capture the timing of the slack water at locations C1 and C4, where the EFDC model was approximately 1 hour out of phase (Figures 5.6a, 5.9a).

Table 5.2: Validation results for current speed at five observation locations C1 to C5.

Flow direction				
Location	r (-)	RMSE (deg)	NSE (-)	SI (-)
C1	0.999	8	0.991	0.045
C2	0.959	25	0.902	0.136
C3	0.983	19	0.948	0.099
C4	0.994	10	0.988	0.066
C5	0.933	36	0.794	0.237

Table 5.3: Validation results for spring tide speed at five observation locations C1 to C5.

Spring tide speed				
Location	r (-)	RMSE (m/s)	NSE (-)	SI (-)
C1	0.999	0.334	0.999	0.238
C2	0.999	0.236	0.999	0.226
C3	0.999	0.094	0.999	0.140
C4	0.999	0.048	0.999	0.205
C5	0.999	0.187	0.999	0.173

Table 5.4: Validation results for neap tide speed at five observation locations C1 to C5.

Neap tide speed				
Location	r (-)	RMSE (m/s)	NSE (-)	SI (-)
C1	0.999	0.081	0.999	0.106
C2	0.999	0.098	0.999	0.193
C3	0.999	0.075	0.999	0.210
C4	0.999	0.016	0.999	0.126
C5	0.999	0.194	0.999	0.356

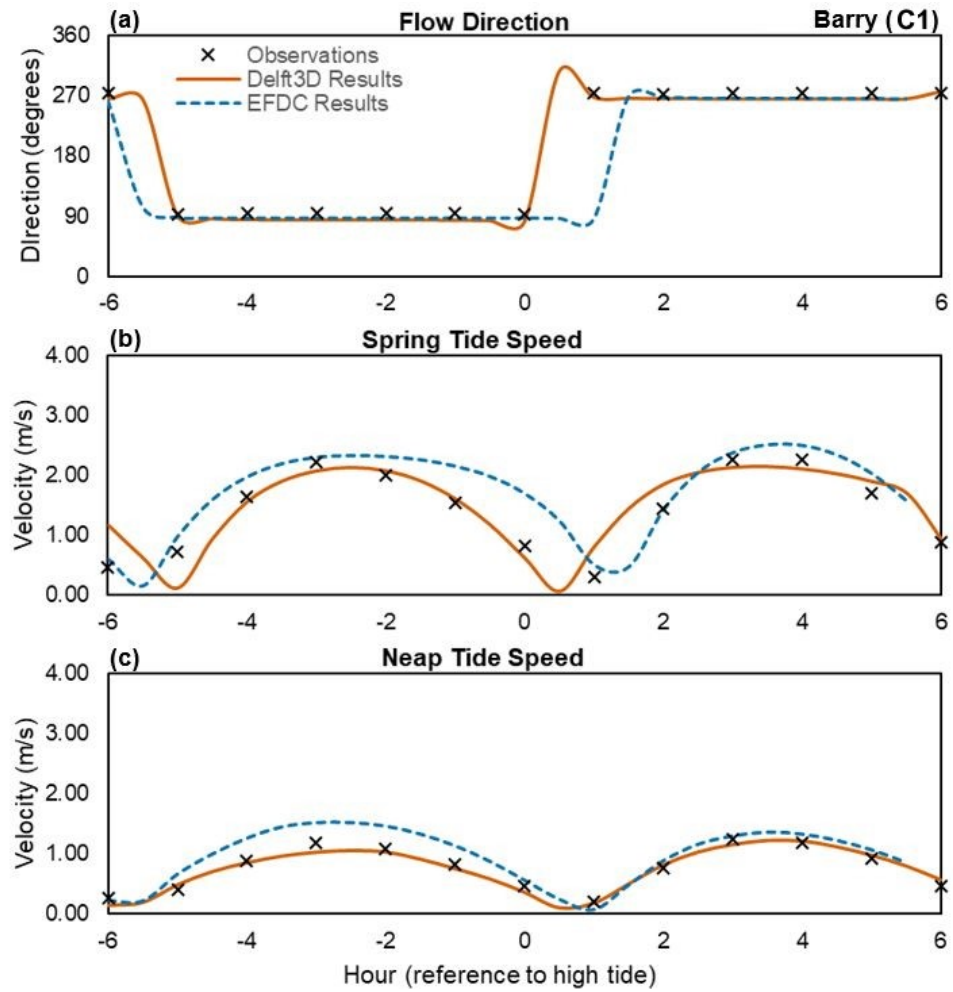


Figure 5.6: Comparisons between Delft3D results, EFDC results and observed data for the validation site C1, located in the upper reaches of the Bristol Channel, near Gower.

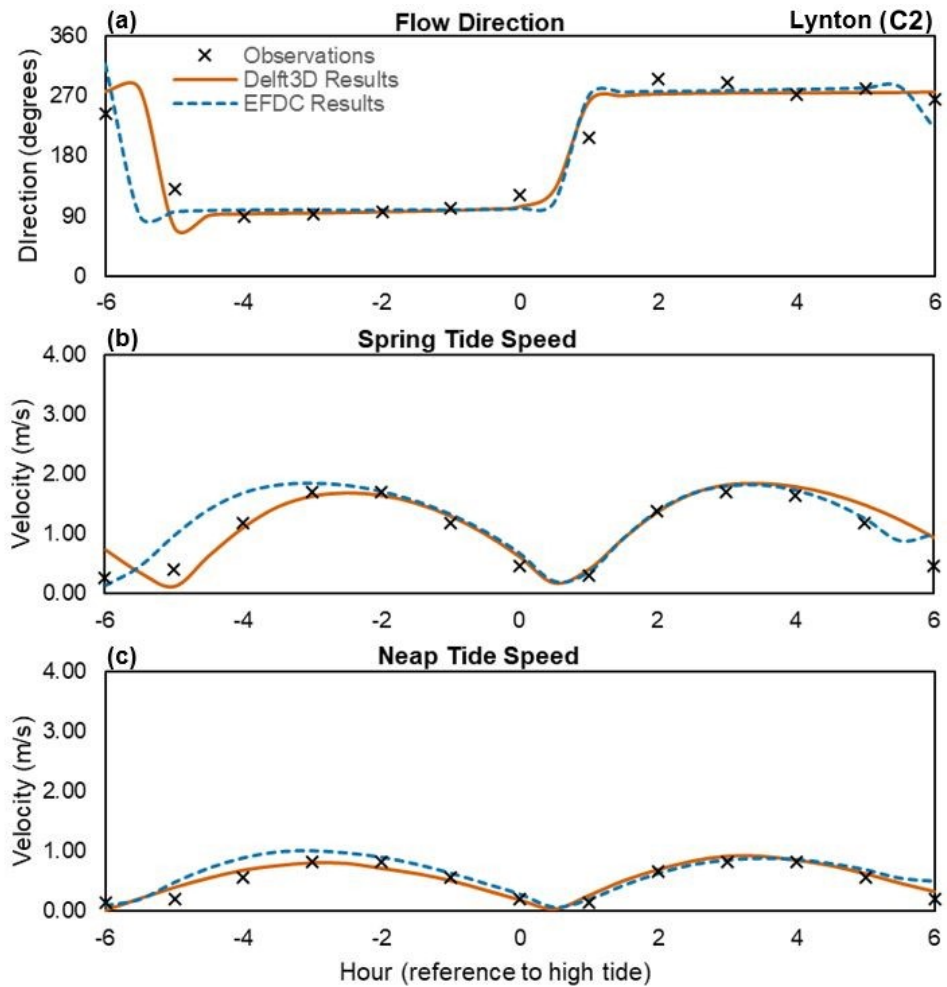


Figure 5.7: Comparisons between Delft3D results, EFDC results and observed data for the validation site C2, located in the middle reaches of the Bristol Channel, near Lynton.

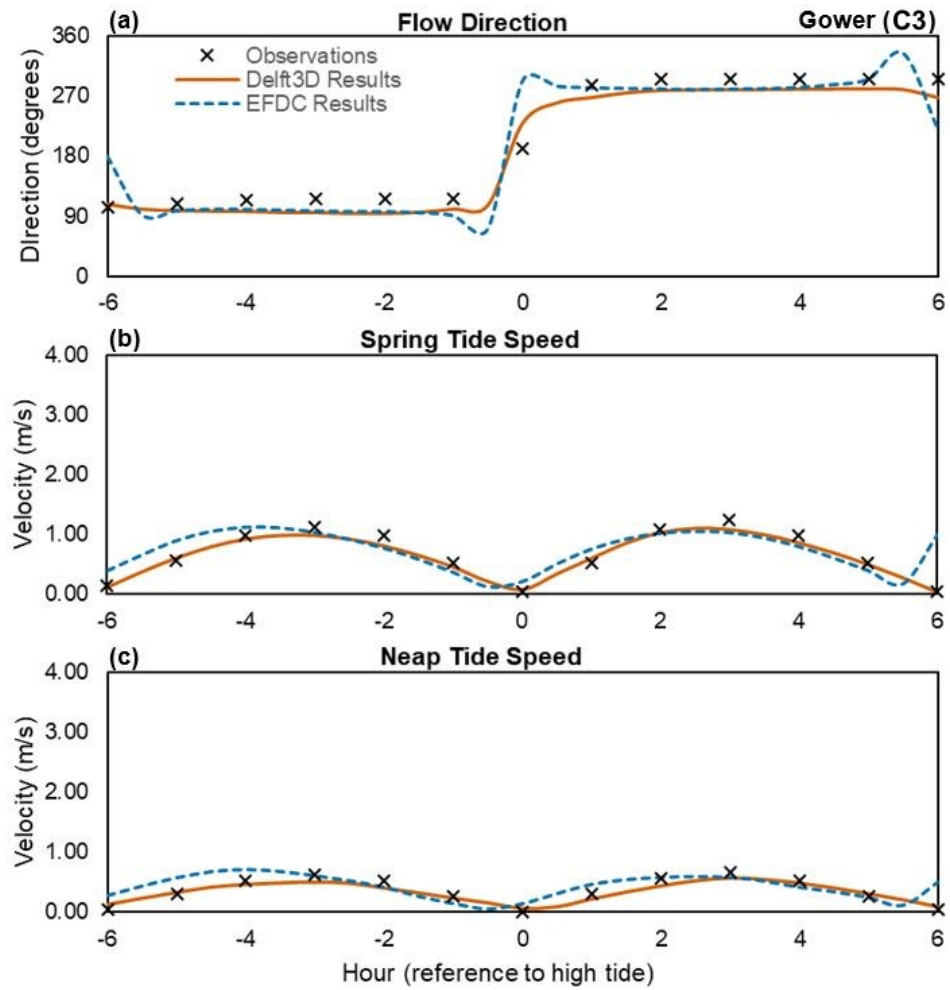


Figure 5.8: Comparisons between Delft3D results, EFDC results and observed data for the validation site C3, located in the middle reaches of the Bristol Channel, near Gower.

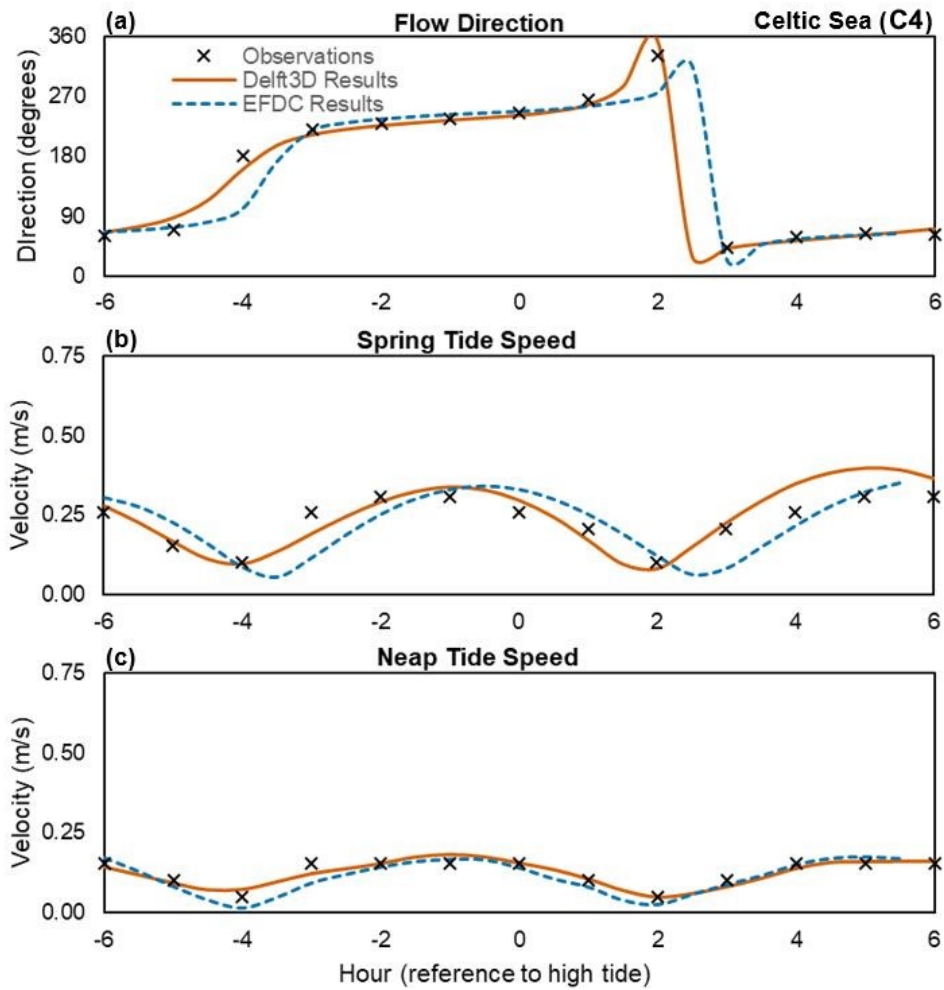


Figure 5.9: Comparisons between Delft3D results, EFDC results and observed data for the validation site C4, located in the Celtic Sea.

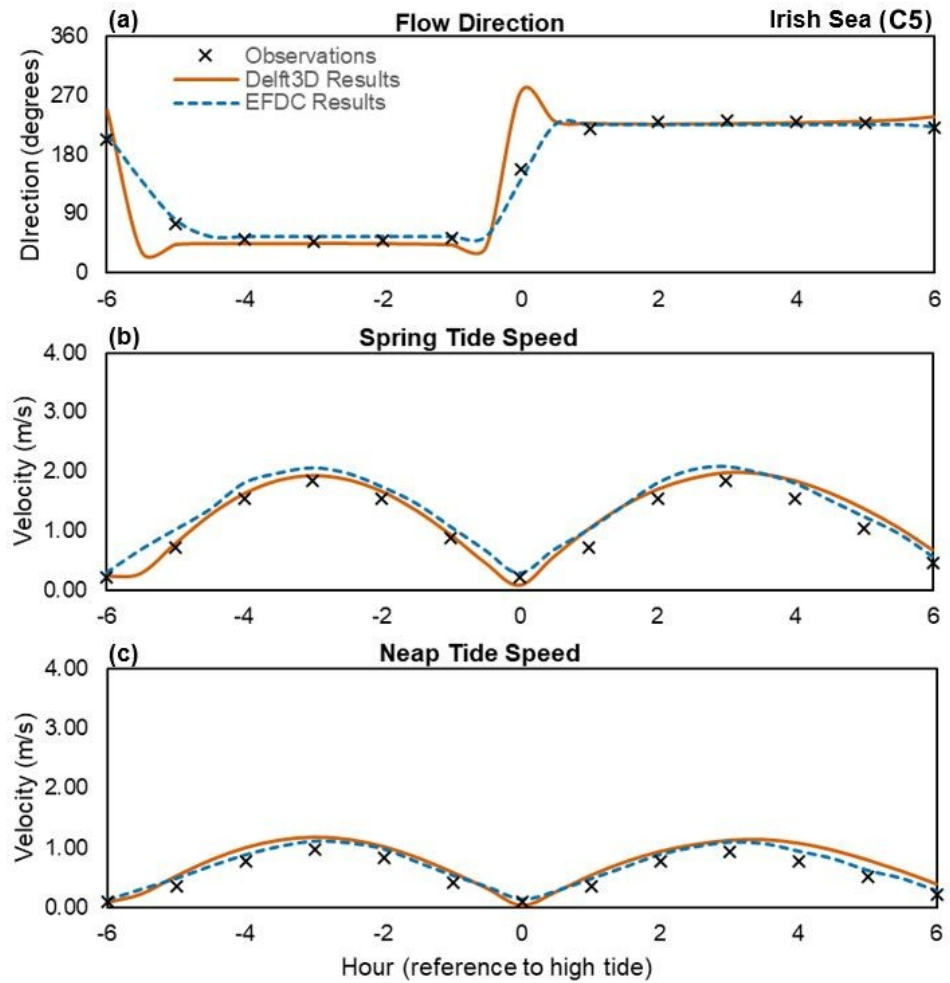


Figure 5.10: Comparisons between Delft3D results, EFDC results and observed data for the validation site C5, located in the Irish Sea.

The predicted water levels were validated against the observed tidal amplitude at five locations across the Severn Estuary and Bristol Channel (Figure 5.5), at Mumbles (W1), Ilfracombe (W2), Hinkley Point (W3), Avonmouth (W4) and Newport (W5). At each site, the comparisons were made over the entire duration of the simulation, including neap and spring tides (Figure 5.11). In addition, four statistical parameters (Equations (5.1) to (5.4)) were calculated at each site to quantify the performance of the hydrodynamic model on water elevations, shown in Table 5.5.

The simulation results showed good agreement with the observation data, especially during the spring tides, matching well in terms of both magnitude and tidal phase. Correlation and NSE were again high at all five locations. Delft3D slightly underpredicted the magnitude of neap tides, which was also reflected in a slightly higher RMSE and SI, however, such discrepancies were consistent with findings from literature (Xia et al. 2010a; Zhou et al. 2014a). In previous studies, this degree of accuracy has been regarded as acceptable, especially when taking into consideration the complexity of the tidal hydrodynamics in such a large domain and for such extreme conditions.

Table 5.5: Validation results for water levels at five observation locations W1 to W5.

Location	Water level			
	r (-)	RMSE (m)	NSE (-)	SI (-)
W1	0.987	0.500	0.963	2.357
W2	0.987	0.497	0.962	1.311
W3	0.992	0.437	0.982	0.416
W4	0.937	0.521	0.877	0.578
W5	0.975	0.570	0.951	0.438

The comparisons between predicted results and field data have shown that Delft3D was able to adequately reproduce the tidal conditions in the studied region, establishing the model as a reliable numerical tool for the assessment of impacts caused by tidal energy projects proposed in the Severn Estuary and Bristol Channel.

Chapter 5
Development model: Severn Barrage

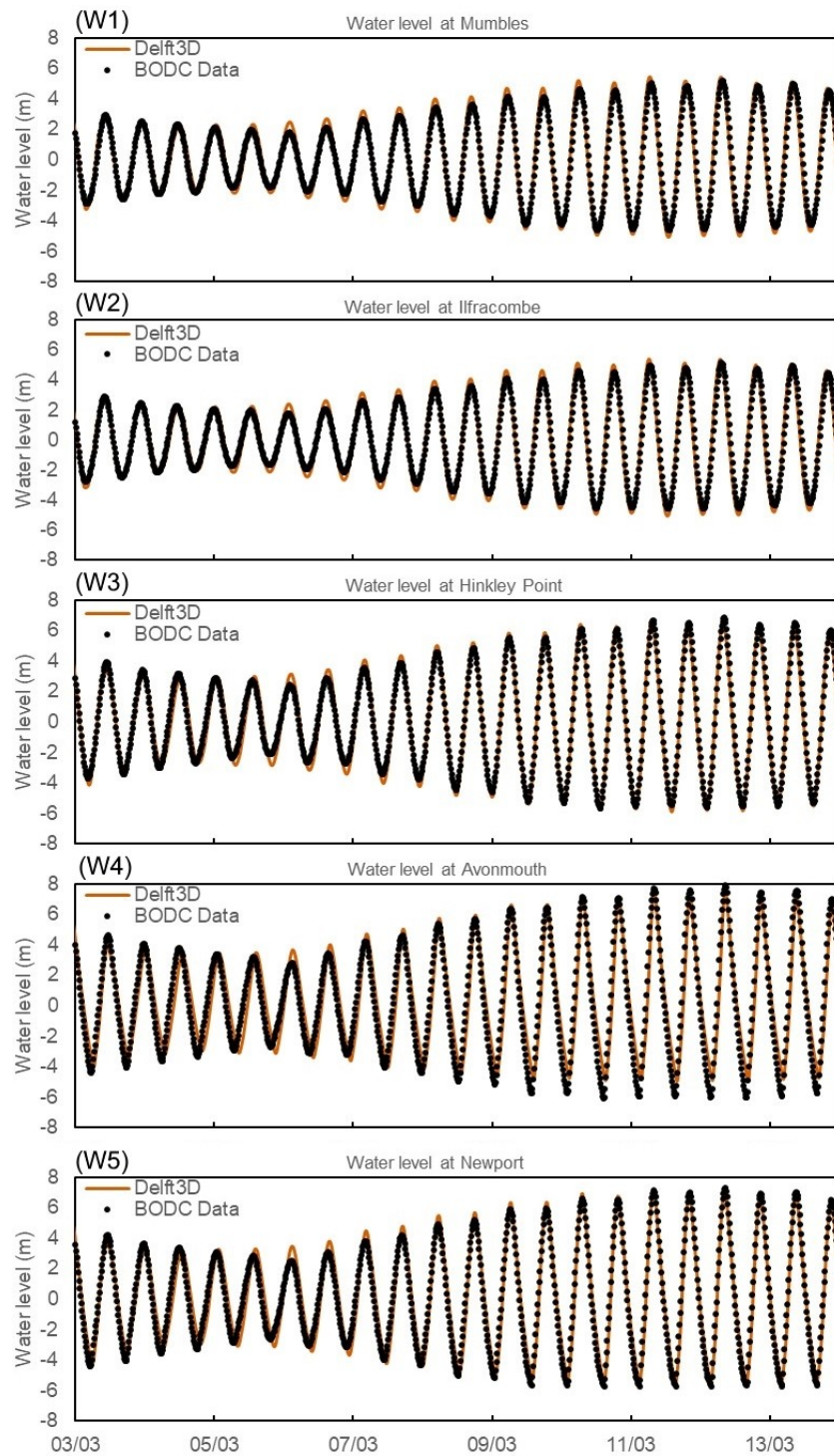


Figure 5.11: Water level results from Delft3D compared with the observed data from BODC in five locations in the Bristol Channel and Severn Estuary.

5.4 Results

5.4.1 Barrage operation

After the validation of the hydrodynamic conditions, the model was modified to include the tidal barrage and was used to simulate the hydrodynamic processes with the barrage in operation. The operation of the barrage is best illustrated by a time series of water levels either side of the barrage. The head difference across the barrage governs the quantity of water passing through the turbines and production of power. To calculate the head difference, the water surface elevations were obtained from 10 evenly distributed points at the distance of approximately 1 km either side of the barrage, as illustrated in Figure 5.12. The final value of the water elevation on each side was calculated as a mean value of the 10 points. This approach guaranteed a more smooth operation of the barrage, avoiding any local disturbances to the water level records that could occur if the measurements were taken from a single point only.

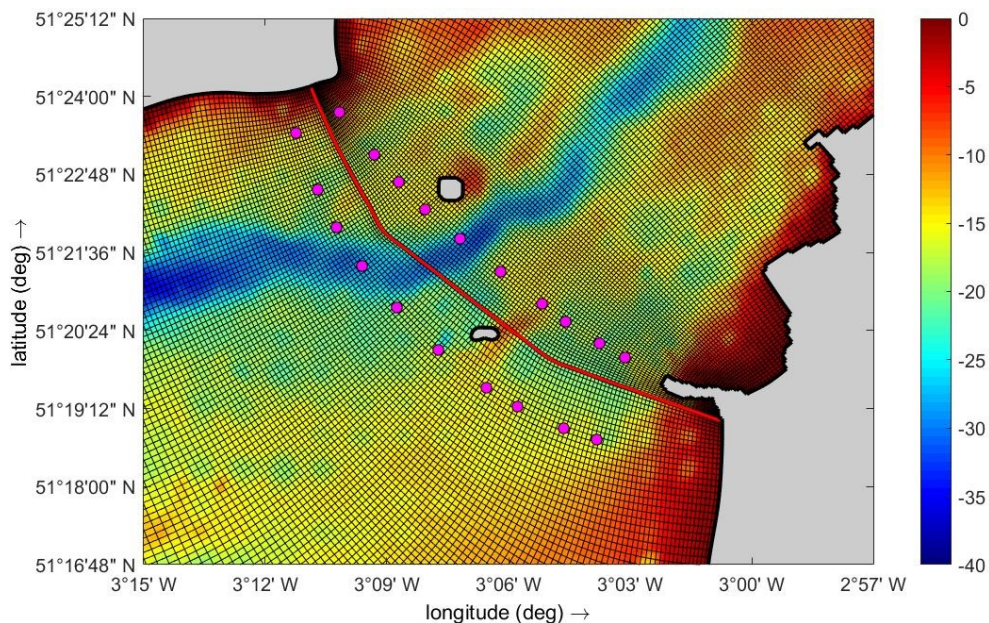


Figure 5.12: Location of the points used to calculate the mean head difference on the SE computational grid, showing the bathymetry and location of the barrage.

During the 14-day period of the simulation the tidal range across the barrage varied significantly from 5 m during neap tides to 11 m during spring tides. This can be observed in Figure 5.13, with blue line representing the tidal amplitude outside the barrage impoundment. A distinct period of smaller tidal amplitudes was observed between 3rd and 7th March, representing the neap tides. During the spring tides, between 9th and 13th March, the tidal amplitudes were noticeably larger and had practically doubled in size. During the spring cycle, the water elevation in the Estuary reached 6 m above Mean Sea Level (MSL) during the high tide and fell to 5 m below MSL at low tides, bringing the tidal range to 11 m. During the neap tides, the tidal range was reduced to only 5 m, with the maximum elevation just short of 3 m above MSL and minimum elevation slightly below 2 m below MSL. Plotted in magenta colour is the tidal amplitude inside the impoundment resulting from the operation of the barrage. The barrage has had a clear impact on the tidal regime, significantly reducing the tidal range inside the impoundment. The change in amplitude was mostly affected by the substantial rise of the minimum water levels. It rose by approximately 2 m during neap and by 4 during spring tides. The maximum water levels have not been affected as much, however, there was a more noticeable reduction of the high water by approximately 1 m during spring tides, while it was almost negligible during neap tides. Such changes to the inside water levels are characteristic of the ebb-only operation sequence. A flood-only generation would result in a reverse situation, where maximum water levels would be reduced and minimum water levels stayed the same, while a two-way generation generally produces a more symmetrical change between the two extremes (Xia et al. 2010b).

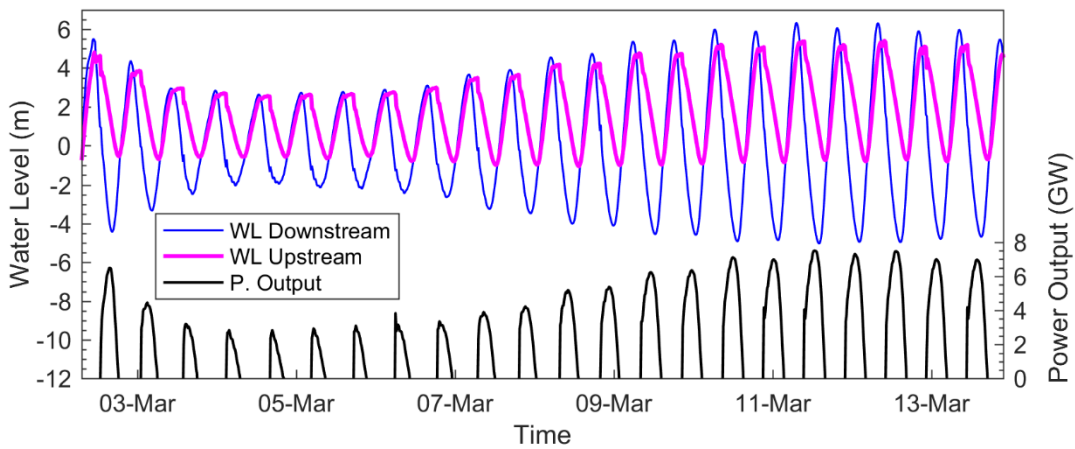


Figure 5.13: Predicted water levels on either side of the Severn Barrage and the corresponding power output over a typical neap-spring tidal cycle.

Figures 5.14 and 5.15 provide a more detailed view of the barrage operation during spring and neap tides respectively, showing a closeup of the predicted water levels either side of the barrage during a 24-hour period. The direct comparison between the two figures illustrates how the operation of the barrage has been affected by the variation of the tidal amplitude. The four distinct operational stages have been marked and numbered on both figures – (1) holding at high water stage, (2) generating stage, (3) holding at low water stage, and (4) filling stage. The duration of both holding stages was evidently longer during the neap tides. It took longer for the Stage (1) to establish the required starting head difference because the water surface was falling at a lower rate compared to spring tides. Similarly, the lower rate of water level change during neap tides also meant that Stage (3) was triggered earlier than during spring tides. This discrepancy between spring and neap tides occur because the operational characteristics (starting and minimum head) are constant throughout the entire cycle. This can be mitigated by the use of variable operational characteristics as was demonstrated in a recent study by Xue et al. (2019). The study used a variable starting head, that was carefully tailored to each individual tidal cycle, thereby maximising the efficiency of power generation even during the neap tides.

Chapter 5 Development model: Severn Barrage

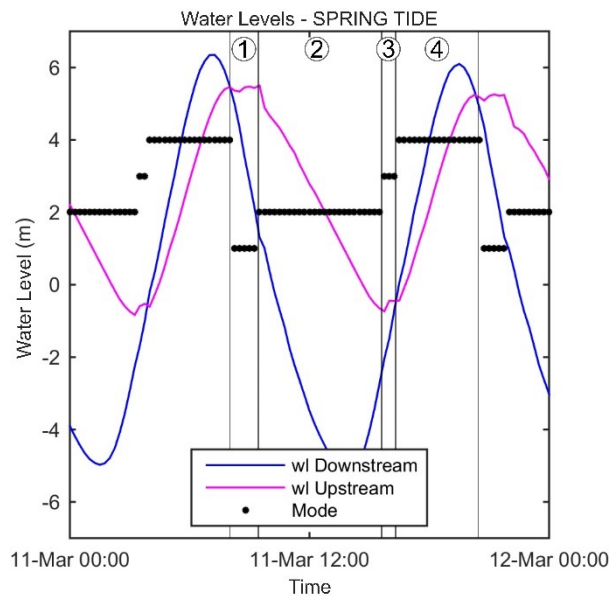


Figure 5.14: Predicted water levels either side of the barrage and operation stages showing the operation of the Severn Barrage during a typical spring tidal cycle. Operational sequences: (1) holding stage - high water, (2) generating stage, (3) holding stage - low water, (4) filling stage.

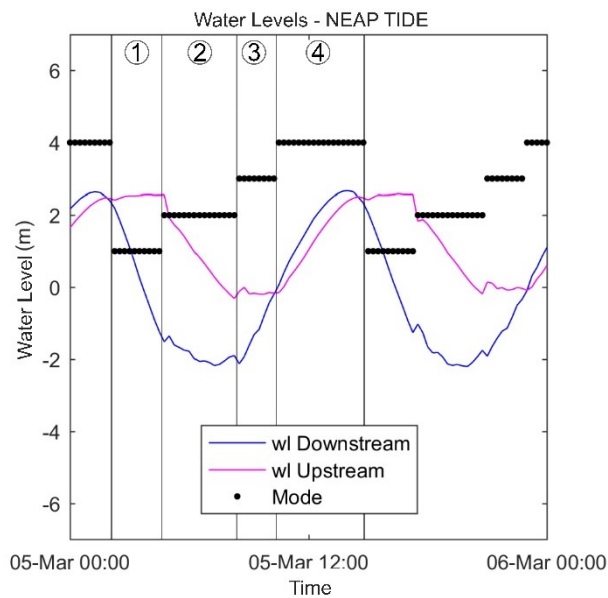


Figure 5.15: Predicted water levels either side of the barrage and operation stages showing the operation of the Severn Barrage during a typical neap tidal cycle. Operational sequences: (1) holding stage - high water, (2) generating stage, (3) holding stage - low water, (4) filling stage.

In both cases, the power could be generated only during the ebb tide, which is twice per day because of the semidiurnal nature of the tides in the Severn Estuary. The longer holding stages during neap tides resulted in a considerably shorter duration of power generation. The generating stage in the case of the neap tide (Figure 5.15, Stage (2)) lasted for only 3.6 hours, significantly shorter compared to 6.3 hours during spring tides (Figure 5.14, Stage (2)). Shorter generating stage, combined with a lower tidal amplitude, meant a significant reduction of the predicted power output during the neap tides. This is also illustrated in Figure 5.13, where power output was plotted in black below the corresponding tidal amplitude. The maximum head difference during neap tides never exceeded 4 m, a value which was also used as the starting head for triggering the generation stage. Integrating power output over the generating period resulted in 7.3 GWh of produced power for a typical neap tidal cycle. The maximum head difference during the spring tides was recorded to be around 6.3 m, corresponding to an instantaneous power output of 7.6 GW. Power production during the maximum spring tidal cycle amounted to 35.3 GWh, almost 5 times more compared to the neap cycle. The total power output over the entire neap-spring tidal cycle was predicted to be 0.63 TWh. Extrapolating this value over the entire year gave a neap-spring-averaged estimation of 15.3 TWh output annually and a capacity factor of 20.2 per cent. These values were consistent with findings from literature (Xia et al. 2012; Bray et al. 2016), confirming the successful development of the modifications for simulating TRSs in Delft3D software.

5.4.2 Continental Shelf model results

To assess the impacts on the extreme water levels, maximum water elevations across the whole CS domain were calculated for cases both with (CS1) and without (CS0) the barrage. Figure 5.16 shows a comparison between the two, obtained by subtracting the maximum water elevations of CS0 from CS1 simulation results. The changes were consistent with the findings of Bray et al. (2016), indicating a correct implementation of the hydraulic structure in the model. The rise of the maximum water levels could be observed throughout the Bristol Channel and beyond. In the Irish Sea and Cardigan Bay

the extent of increased maximum elevation was slightly smaller but of the same order of magnitude (5 cm – 15 cm) as predicted by Bray et al. (2016). Water levels at the entrance into the Bristol Channel have increased for the same order of magnitude, confirming that the open boundary conditions of the SE domain would be affected by the construction of the barrage. The largest increase occurred in the mid-section of the Bristol Channel (between Swansea Bay and Lynton) and was of order magnitude between 15 cm and 25 cm. The maximum water elevations in the estuary have been drastically reduced, decreasing by more than 1 m inside the impoundment and between 5 cm and 25 cm on the seaward side of the barrage.

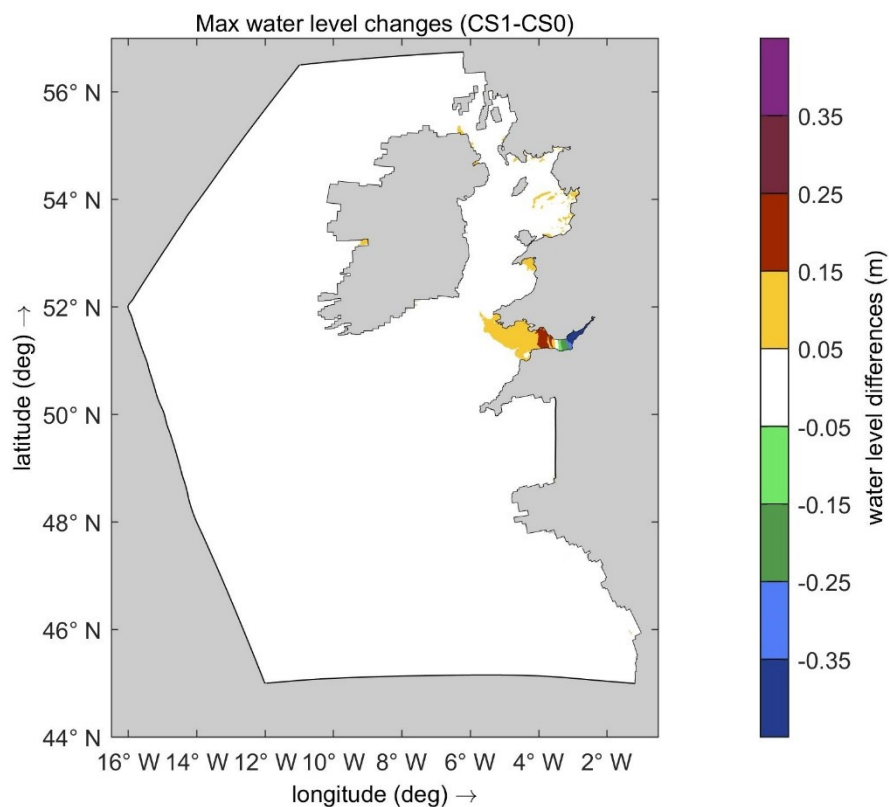


Figure 5.16: Maximum water elevation changes due to the barrage operation. Positive differences denote an increase and negative a decrease in water elevations after including the barrage in the simulation.

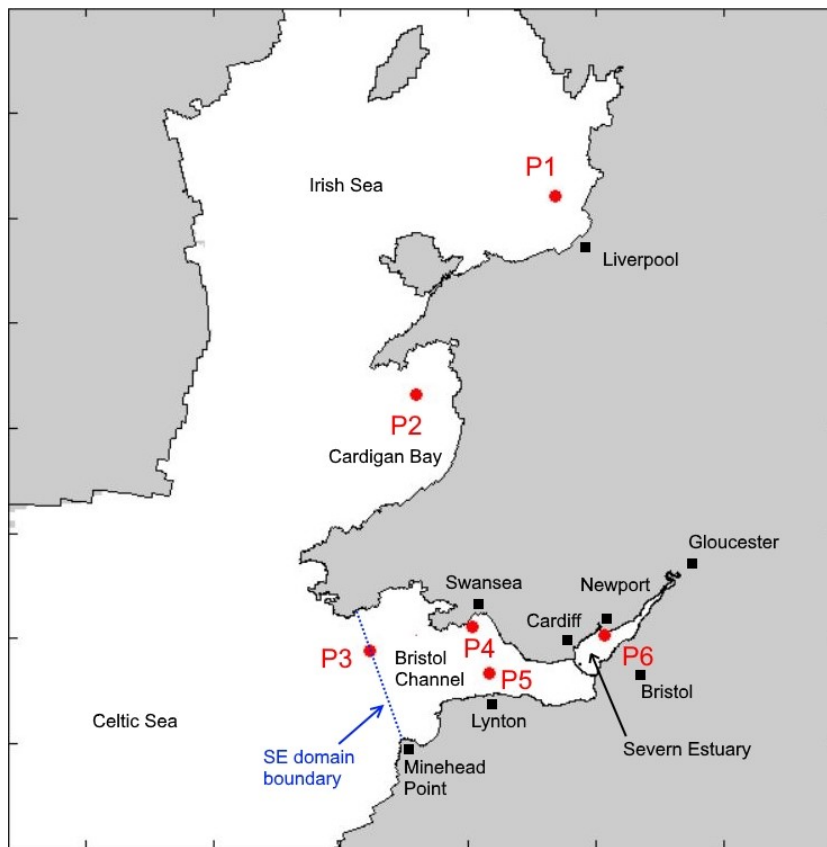


Figure 5.17: Locations of observation points for the analysis of water elevation changes due to the barrage operation.

Six observation sites were selected to provide a more detailed analysis of impacts resulting from the operation of the tidal barrage. The locations of the sites are shown in Figure 5.17. They were selected in the areas where notable changes in the maximum water levels were observed, as can be seen in Figure 5.16. First two sites (P1 and P2) were located beyond the boundary of the SE domain, near Liverpool in the Irish Sea and in Cardigan Bay respectively. To observe the impacts of the barrage on the open boundary the third site (P3) was located directly on the boundary of the SE domain. The rest of the points were located inside the SE domain. Two of them were located in the middle of the Bristol Channel, where the largest increase of maximum water elevations was observed, namely in the Swansea Bay (P4) and just offshore from Lynton (P5). Lastly, a site just offshore from Newport (P6) was selected to illustrate the changes in

water elevation inside the barrage basin. These locations provided good coverage of the entire computational domain, providing a thorough insight into both far-field (P1, P2 and P3) and near-field (P4, P5 and P6) impacts of the barrage on the hydrodynamic processes in the domain.

For each of the observation sites, a water level time series has been extracted from the results to compare the changes in the water elevations due to the operation of the barrage, shown in Figures 5.18 to 5.23. The interval of the time series was taken during the spring tides, during which the largest tidal amplitude and therefore the highest maximum water elevations were to be expected. Because the magnitude of water elevation change was small compared to the tidal amplitude, another time series, representing the difference between the two, was added to the plots (blue line in Figures 5.18 to 5.23). The difference was calculated by subtracting CS0 results from CS1 results, by which positive values denoted a higher water elevation in the post-barrage case compared to pre-barrage construction and vice versa for negative values.

Locations P1, P2 and P3 were specifically chosen to investigate the far-field impacts of the tidal barrage. The tidal range in the Irish Sea (P1) was 9.6 m, while Cardigan Bay (P2) had a much smaller range of 4.8 m. The maximum increase in both locations was around 10 cm which occurred during flood tide. During the ebb tide, the water levels decreased by roughly the same amount. During the high tides the difference still showed an increase, however, it was considerably smaller, contributing only around 5 cm to an overall maximum elevation increase. Tidal amplitude in the Irish Sea (P1) was practically symmetric, unlike in Cardigan Bay where tidal wave formed steep crests but flatter troughs. The same phenomenon was previously observed in a study by Zhou et al. (2014a), where it was attributed to the nonlinearity of the tidal wave, caused by extremely shallow depths of 10-15 m in the bay.

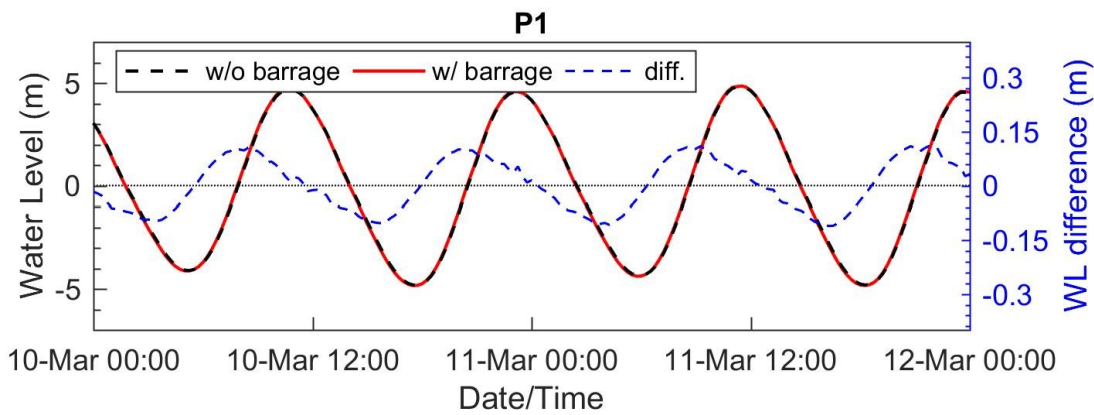


Figure 5.18: Time series of water level change between CS0 (without barrage) and CS1 (with barrage) over two typical neap tidal cycles at the observation site P1 in the Irish Sea.

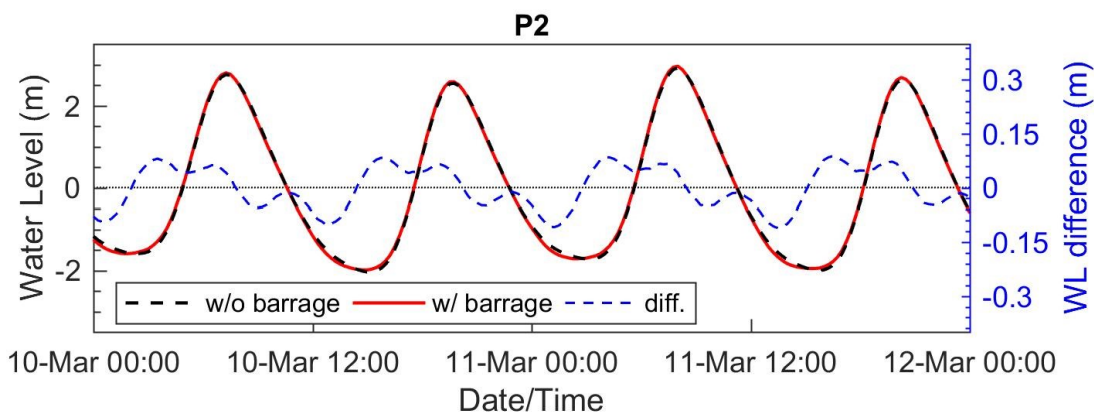


Figure 5.19: Time series of water level change between CS0 (without barrage) and CS1 (with barrage) over two typical neap tidal cycles at the observation site P2 in the Celtic Sea.

Figure 5.20 shows results at site P3, located directly on the open boundary of the SE domain. The tidal range at this location was 8.7 m. The maximum increase of surface elevation was 15 cm, occurring during low tide, flood tide and high tide. Because both high and low tides increased by roughly 7 cm, the tidal range remained the same, only the overall surface elevation was shifted upwards. A decrease occurred only during the ebb tides; it lasted for a much shorter period but by a considerably larger magnitude of 27 cm.

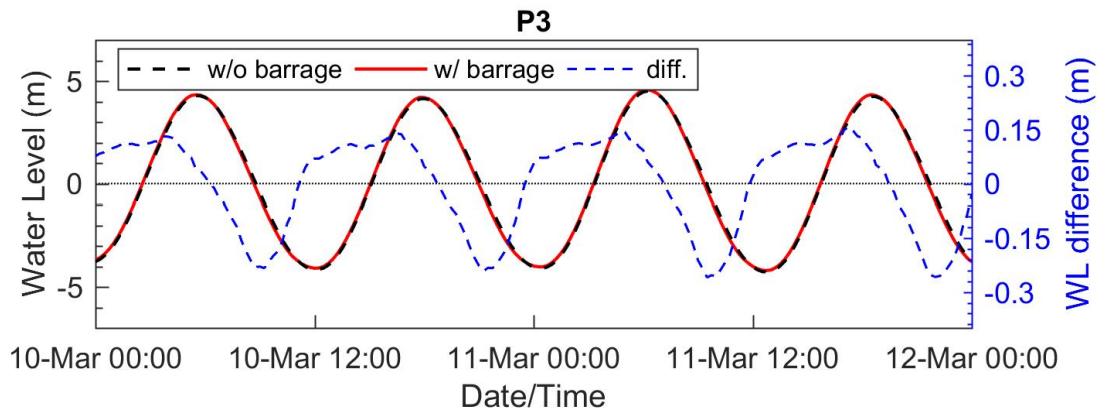


Figure 5.20: Time series of water level change between CS0 (without barrage) and CS1 (with barrage) over two typical neap tidal cycles at the observation site P3 at the location of the SE open boundary.

These results indicate that the impacts from the barrage operation propagate over large distances and can affect areas beyond the entrance to the Bristol Channel. Results at the location of the SE boundary showed a significant change in tidal amplitude. In order to account for these impacts, the SE boundary conditions have to be modified accordingly when barrage is included in the simulations.

Sites laying inside the SE domain were used for assessment of near-field effects caused by the barrage operation. Figures 5.21 and 5.22 show the differences in water elevations for points P4 and P5 respectively. Both sites were located in the part of the Bristol Channel that experienced the largest increase in maximum water elevations (Figure 5.16) after the inclusion of the barrage. The tidal amplitudes at both locations were similar. The value recorded at locations P4 and P5 was 10.4 and 10.8 m respectively. A similar pattern of differences occurred at both locations. Water elevation started increasing right before the slack water of low tide and continued increasing throughout the period of the flood tide when it also reached its maximum increase at approximately 0.4 m at both locations. It stayed above the CS0 elevation during the high tide, before becoming equal at the start of the ebb part of the cycle. During the ebb flow, water elevation experienced a decreased from the CS0 value by as much as 0.75 m at both

locations. Even though the maximum increase was more than 0.4 m, it did not occur during the peak of the high tide. The increase of maximum water elevation during the high peak was instead only around 0.2 m for both locations P4 and P5. A similar increase was also observed during the peak of the low tide, meaning that tidal range remained practically unchanged, only the values of both extremes were shifted upwards.

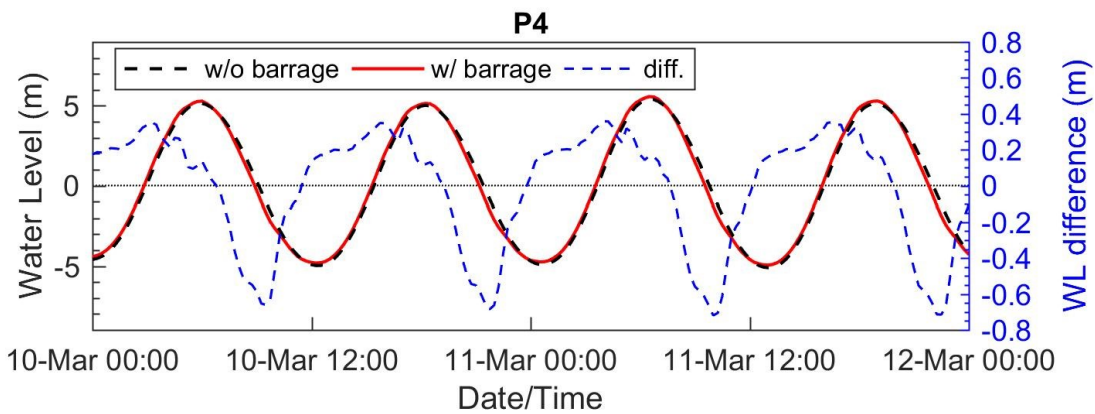


Figure 5.21: Time series of water level change between CS0 (without barrage) and CS1 (with barrage) over two typical neap tidal cycles at the observation site P4 in the Swansea Bay.

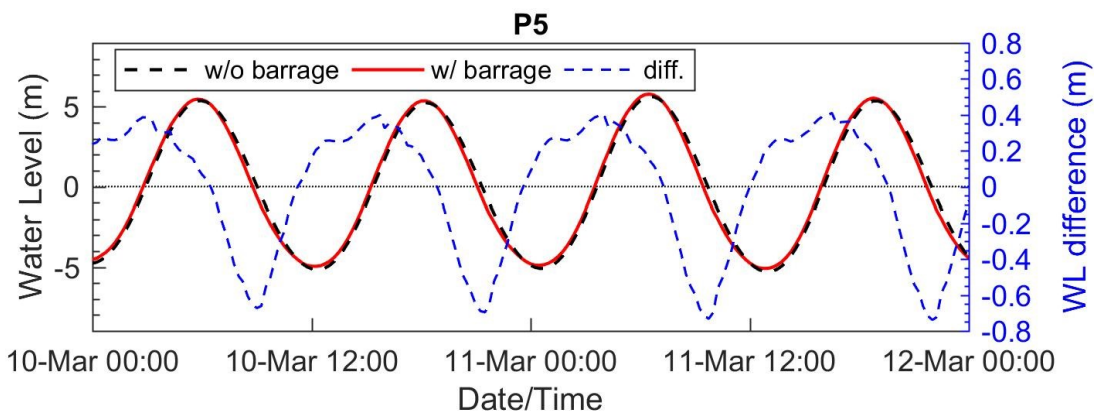


Figure 5.22: Time series of water level change between CS0 (without barrage) and CS1 (with barrage) over two typical neap tidal cycles at the observation site P5 in the middle of Bristol Channel, downstream of the barrage.

Finally, Figure 5.23 shows the time series of water level differences inside the impoundment. The construction of the barrage had radically changed the water level regime on the upstream side of the estuary. The tidal range had decreased from 12.7 m in CS0 to only 6.9 m in CS1. The maximum increase occurred during low tides, with minimum water levels rising by more than 4.5 m. However, the barrage actually helped to lower the maximum water levels during high tides, decreasing by 1.2 m.

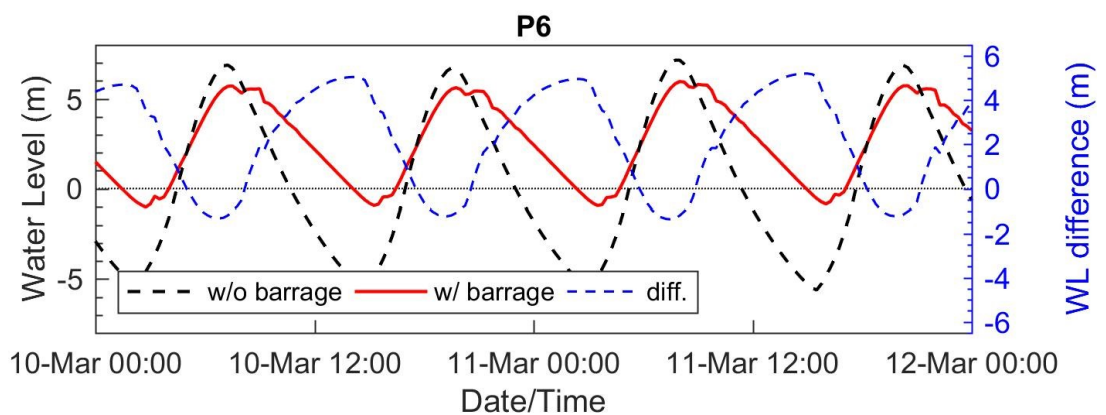


Figure 5.23: Time series of water level change between CS0 (without barrage) and CS1 (with barrage) over two typical neap tidal cycles at the observation site P6 upstream of the barrage, close to Newport.

5.4.3 Severn Estuary model results

The boundary condition for the SE1 model was extracted from the CS1 results. The SE model was used to obtain a high-resolution image of the near-field hydrodynamic impacts due to the barrage operation. To provide a benchmark, the SE model was first run without the barrage and using the initial boundary conditions (SE0). The barrage was included for the second scenario (SE1), using the boundary conditions extracted from CS1 results.

The CS results have already shown that the construction of the barrage caused changes to the maximum water levels throughout the domain. Figure 5.24 focuses on the comparison of the predicted maximum water levels inside the SE domain. The maximum water elevation has occurred during the largest spring tidal cycle when the estuary also experienced the largest tidal range. The barrage has had a lesser influence on the maximum water levels downstream of the barrage, increasing by up to 0.3 m. The increase was more prominent near the barrage and was gradually diminishing towards the open boundary. The change was much more pronounced upstream of the barrage, with maximum water levels decreasing by more than 1 m. Only the uppermost reaches of the Severn Estuary were left unaffected by the inclusion of the barrage.

Figure 5.25 shows the comparison of the minimum depths between the SE0 and SE1 cases. Similar to the changes in maximum elevations, the changes to the minimum depths were much more prominent inside the tidal impoundment. The depths were predicted to increase by more than 5 m, permanently submerging a large portion of intertidal mudflats located upstream of the barrage.

Chapter 5
Development model: Severn Barrage

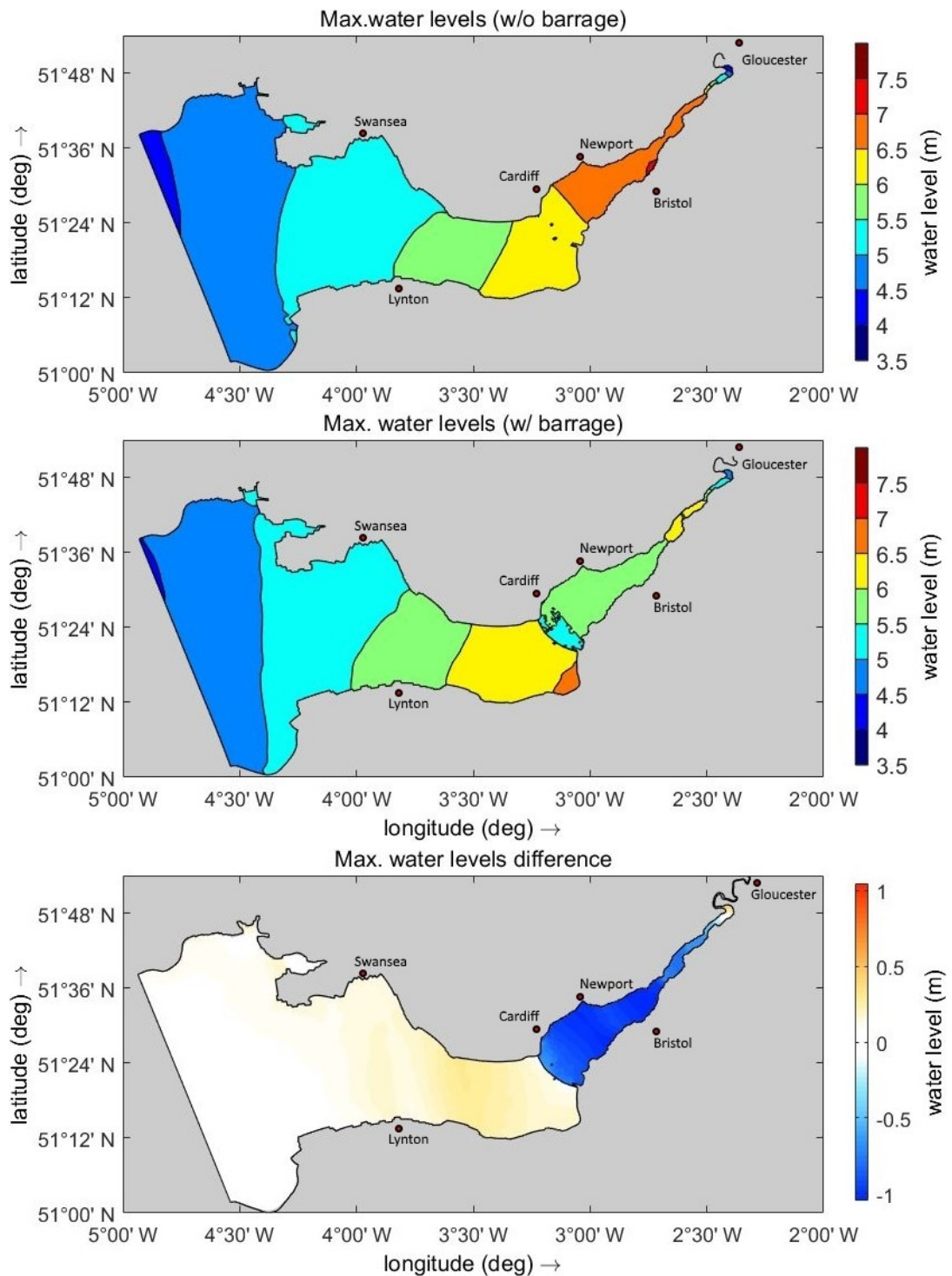


Figure 5.24: Maximum water levels (a) without and (b) with the barrage and (c) the differences between the two.

Chapter 5
Development model: Severn Barrage

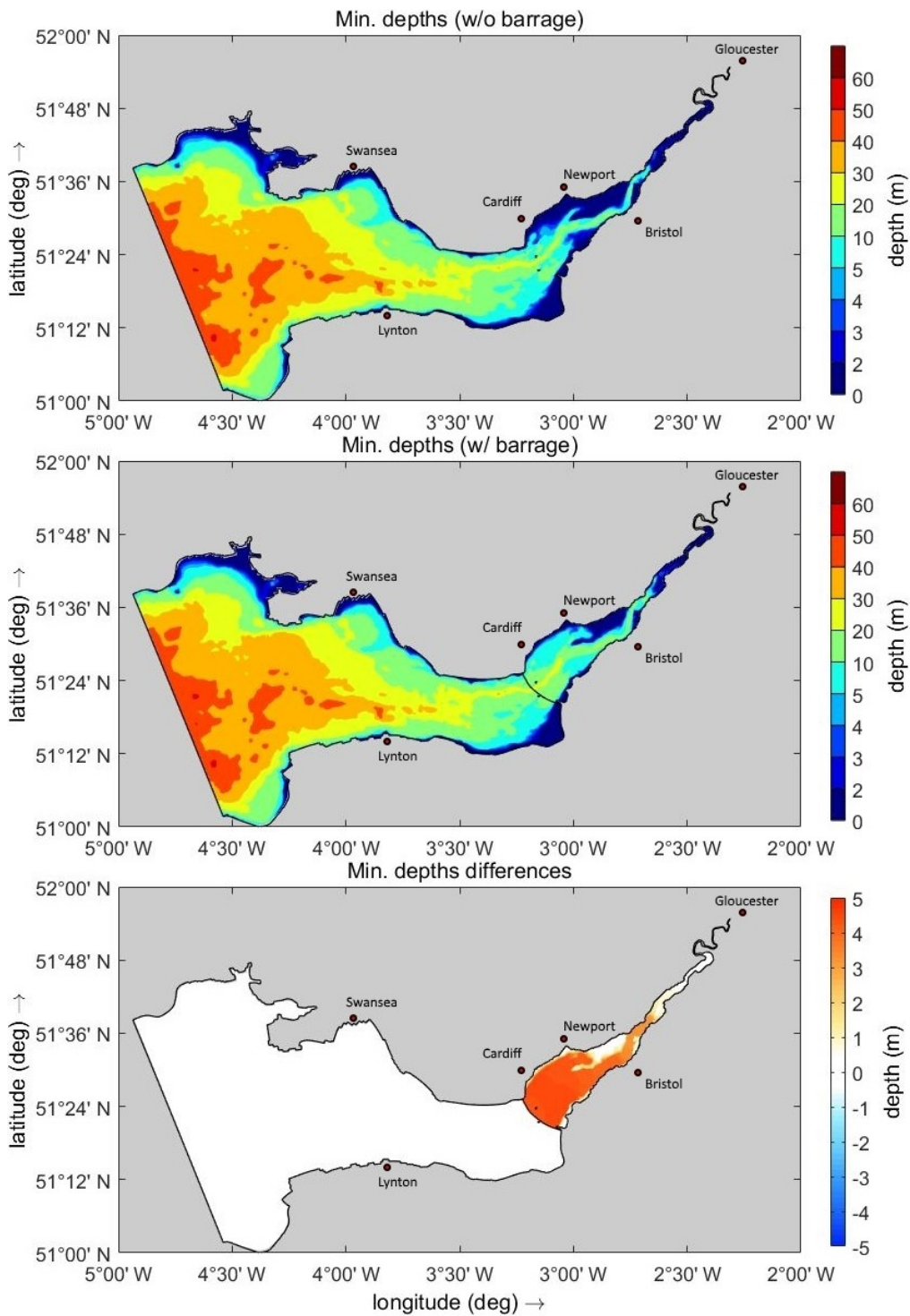


Figure 5.25: Minimum water depths (a) without and (b) with the barrage and (c) the differences between the two.

Figure 5.26 shows the impact of the barrage on tidal currents in the Severn Estuary and Bristol Channel, recorded during a typical spring tidal cycle. The results showed a considerable reduction in maximum tidal currents throughout the SE domain. The decrease in the magnitude of the velocity field came primarily from the decrease in the water volume entering the estuary due to the construction of the barrage. The reduction was therefore especially prominent in the main channel of the Severn Estuary (upstream of the barrage) and in the upper reaches of the Bristol Channel (downstream of the barrage), while the coastal areas remained largely unaffected throughout the domain. Figure 5.26c shows the difference in maximum velocity magnitude in a closeup view around the barrage. The differences illustrate an impact on the near-field velocity profiles due to the barrage operation. Even though the majority of the domain experienced a decrease in velocity magnitude, certain places in the vicinity of the barrage experienced a notable increase. Such was the case just behind the sluice gates, on the upstream side of the barrage, where a large increase in velocity magnitude in a form of jets was recorded. The jets formed during the filling stage of the barrage operation, when the sluice gates were opened and turbines closed, with an aim to fill the impoundment as quick as possible. The velocity of the jets behind sluice gates largely exceeded 2 m/s, while in contrast, the currents behind the turbines fell almost to a standstill. The patterns on the downstream side were just reversed, with a high-velocity jet forming at the exit from the turbines, while the sluice gates remain closed during the generation stage of the barrage operation. This contrast between high and low velocity is not important only from the hydrodynamic point of view, but can also play a significant role in erosion and deposition, as well as on transport processes of suspended sediments and solutes.

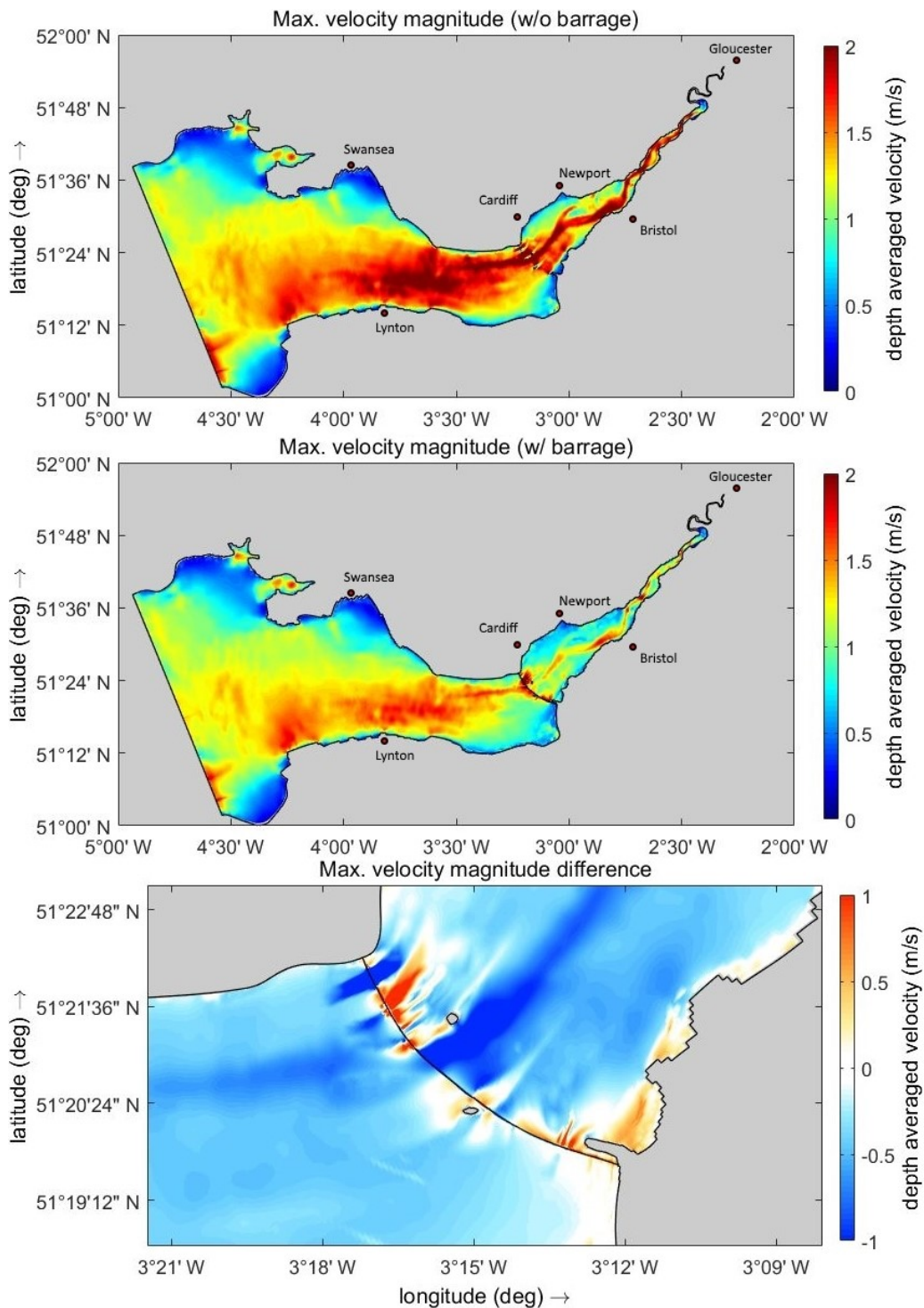


Figure 5.26: Maximum tidal currents (a) without and (b) with the barrage and (c) a close-up of the differences between the two around in the vicinity of the barrage.

5.5 Summary

This chapter addressed the first key objective, which was to develop and test a robust and flexible numerical model for simulation of TRS with Delft3D software. The modified Delft3D model was developed by implementing new subroutines into the source code, that were required to simulate the operation of a tidal power plant. The modifications were based on the existing numerical techniques for TRS simulation, that were judiciously adopted from the literature. The model was tested on the Severn Barrage case study to demonstrate the effectiveness of the developed procedure. Special attention was given to the assessment of the barrage operation regarding the predicted energy output and its impact on local and far-field hydrodynamics. This being the case, the simulations were performed with and without barrage in place. By calculating the difference between the two sets of results, the impacts of the barrage operation could be observed and compared with the results from the literature.

Validation showed that Delft3D was able to adequately reproduce the hydrodynamic conditions of the initial model before the construction of the barrage. Results also showed a good agreement with the results from the literature. A direct comparison between Delft3D and EFDC (Bray et al. 2016) showed that the former actually outperformed the latter in the prediction of flow velocity and direction. Following the successful validation, the results from the simulation with the barrage were analysed. The water levels time series on both sides of the barrage provided an insight into the barrage operation. The ebb-only generation operational sequence showed comparable predictions to similar schemes found in the literature (Xia et al. 2010b; Zhou et al. 2014c; Bray et al. 2016). The estimated annual energy production was predicted to be 15.3 TWh, similar to 14.7 TWh predicted by Angeloudis et al. (2016b), slightly less but still of the same order of magnitude as 17 TWh predicted by Xia et al. (2010c) and 17.1 TWh by Bray et al. (2016). These results were satisfactory within the scope of this study; however, it should be acknowledged that energy output is highly sensitive to the

characteristics of turbines, which are not publicly available, thereby raising the uncertainty of the estimated power production.

The impacts on the far-field water elevations were also consistent with the findings in the literature (Zhou et al. 2014a; Bray et al. 2016), confirming the requirement for extending the domain to the continental shelf to avoid impacts on the boundary conditions. Local impacts were investigated using a smaller domain with a higher resolution for which the boundary conditions were extracted from the continental shelf model. Local impacts were also consistent with findings from the literature, including:

- i) The increase of maximum water surface elevations downstream of the barrage resulting in an increased risk of coastal flooding in the area.
- ii) The decrease of maximum water surface elevations upstream of the barrage resulting in a decreased flood risk of coastal flooding in the area.
- iii) A significant increase of minimum water surface elevations upstream of the barrage, permanently flooding intertidal mudflats, raising concerns from the ecological point of view.
- iv) A significant reduction in maximum current velocities domain-wide and increase in maximum flow velocity at the exit from turbines and sluice gates, substantially altering the sediment transport processes in the estuary.

Overall, the results presented in this chapter indicate that the modifications made to Delft3D are appropriate for modelling the impacts of tidal range energy structures in the Severn Estuary and Bristol Channel. The model includes all the necessary procedures to reliably simulate the operation of any tidal range structure and can be easily modified to include other tidal range projects proposed in the region. The extended domain also allows for the analysis of any large projects that would have the power to disrupt the boundary conditions of the smaller domain.

Chapter 6

Experimental model: barrage in a flume

6.1 Introduction

This chapter presents an experimental study that was undertaken at Tsinghua University, Beijing, China. The experimental study was part of an EPSRC sponsored research visit, hosted by Prof Binliang Lin at the Department of Hydraulics at Tsinghua University.

The experimental study involved a scale model of a simplified barrage that was placed into a large flume to investigate the hydrodynamic properties of jets forming at the exit of a tidal range power plant. The main goal of the physical experimental study was to obtain measured data that could be used for the assessment of the refinements made in Delft3D, to model momentum sources for turbine studies. Since it is difficult to acquire real field data from actual TRSs, a physical experiment offered a practical way of obtaining reliable validation data from controlled laboratory conditions. Excellent laboratory facilities at Tsinghua University allowed the construction of a simplified model of a tidal barrage and the opportunity to record the velocity field of the exiting jet. A series of experiments were performed using different configurations, i.e. varying the number of coaxial jets exiting the barrage as well as the spacing between them. The different experiments were later replicated with a numerical model and the experimental measurements recorded were compared to the numerical model predictions.

Chapter 6

Experimental model: barrage in a flume

Section 6.2 gives an overview of the work process, Section 6.3 and 6.4 describe the experimental and numerical model set-ups respectively, Section 6.5 gives an assessment of the results obtained, and Section 6.6 provides a summary of the main findings.

6.2 Methodology

This study addressed the second and third key objectives, which were to develop and validate the momentum conservation method for modelling complex flow patterns of the jets emanating from TRSs. The experimental studies presented in this chapter were conducted to assess the performance of the Delft3D numerical model, that was modified to include the developed momentum conservation method described in Chapter 4. The study was split into three parts: (i) physical experiments to obtain the validation data; (ii) replicating the experiments with the numerical model; and (iii) analysis and comparison of the experimental and numerical results.

Tsinghua University provided the laboratory facilities to complete the first part of the study. A model tidal barrage had to be constructed and fitted into a large rectangular flume. Recirculation pumps provided a constant flow rate to achieve steady-state conditions, with an ADV velocimeter being used to record the required velocity data. In order to assess the appropriateness of the refined numerical model, three different experiments were undertaken. For the first case five draft tubes were used, with a very dense spacing between them; a case that most closely resembles the compact turbine housing of a typical TRS. In the second and third set of experiments, only two draft tubes were left open, separated further apart, investigating the interaction of only two coaxial submerged jets. It is worth noting that this kind of configuration is not common with TRSs. This would happen if turbines were split further apart, which would mean a construction of multiple turbine housings, raising the construction costs of TRS projects. A dense distribution of turbines in a single housing unit is therefore much more common because it is more favourable from the economical point of view (DECC 2010).

In the second part, the experiments were replicated using the Delft3D numerical model. For each experiment, three different simulations were performed, including: (i) a 2D depth-averaged model with the momentum conservation for the TRS; (ii) a 3D model

with six sigma-layers and momentum conservation for the TRS; and (iii) a 2D depth-averaged model without the momentum conservation for the TRS.

Finally, the simulation results were compared for the different simulations and against the corresponding experimental data. The depth-averaged velocities were compared at five characteristic cross-sections along the flume, with the main objective being to compare the predicted and measured results. Special attention was given to the direct comparison between the 2D and 3D results. Furthermore, the local bed shear stress was compared between the three different simulations, to determine how this parameter was affected by the momentum conservation modelling.

6.3 Physical experiment

6.3.1 Experimental set-up

Laboratory flume

The experiments were conducted in a large rectangular flume, fitted with a model of a tidal barrage, as shown in Appendix C.1. The flume was a planar open channel, 35 m long, 2.1 m wide and allowed for a maximum depth of 0.3 m. The original width of the flume was 3.5 m but was reduced to 2.1 m by retrofitting PVC sidewalls. The reason for a reduction in the flume width was due to a faulty pump, which could only work with a reduced capacity at the time of the experiments. The scale model of the barrage was constructed based upon the Swansea Bay lagoon geometry, given by Tidal Lagoon Plc (2017).

The barrage, pictured in Appendix C.2, was a simple squared-shaped caisson, made from 5 mm thick PVC plates. It was 0.75 m wide and 0.3 m high, spanning 2.1 m across the channel. Five standard PVC pipes of constant diameter, $d = 0.14$ m, were used to represent simplified turbine draft tubes. The technical drawing used for the construction of the barrage is included in Appendix D. The caisson was placed 2.7 m downstream of the beginning of the channel in order to facilitate a uniform lateral distribution of the flow on the upstream side of the impoundment. The tailwater part of the flume extended a further 17.3 m downstream, where a weir was placed to control the downstream water elevation. In addition, the barrage came with plugs that could seal the draft tubes, for running the experiment in different configurations. A diagram of the experimental setup is shown in Figure 6.1 and a to-scale layout of the configuration is included in Appendix E.

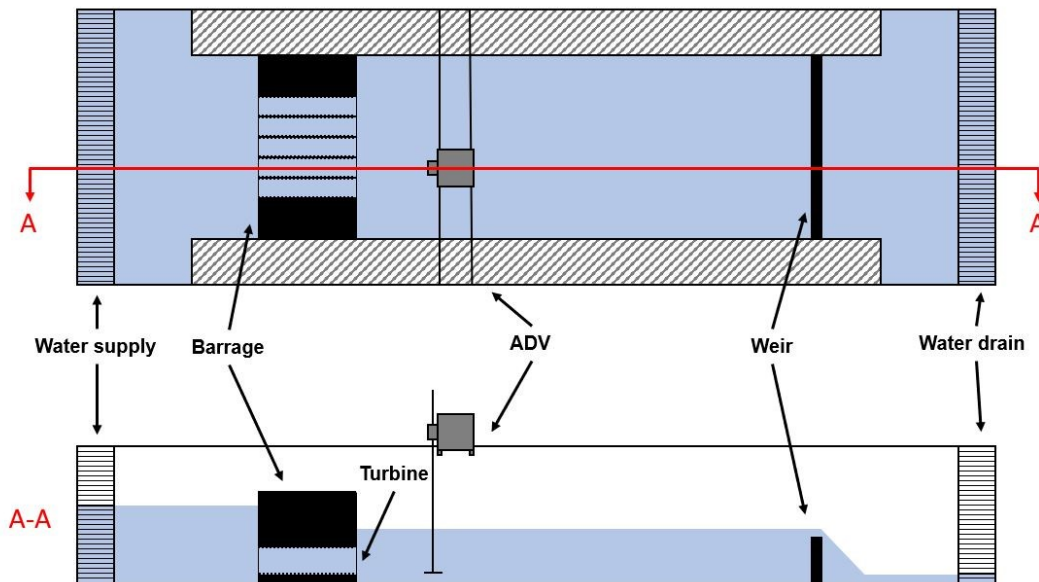


Figure 6.1: A diagram of the experimental setup in the flume (the drawing is not to scale).

Measurement equipment – ADV velocimeter

A three-component Vectrino ADV was used to record the time-varying velocities of the flow. The ADV was suspended from a mobile platform, mounted on a mobile gantry that allowed automated movement in the cross-section plane, as pictured in Appendix C.3. Measurements were taken at five locations (CS1-CS5), at a distance of 0.14 m, 0.28 m, 0.7 m, 1.4 m, and 2.8 m downstream of the barrage. The distances were selected in relation to the draft tube diameter (d_T) and they correspond to values of $1 d_T$, $2 d_T$, $5 d_T$, $10 d_T$, and $20 d_T$, where d_T was 0.14 m. These values were adopted from the study by Jeffcoate et al. (2013) which showed that 3D complexities of a jet become negligible after $20 d_T$. In each cross-section, the velocity was recorded in a 4×35 array of measurement points, as illustrated in Figure 6.2. In the vertical direction, the points were spread 0.04 m apart at elevations of 0.04 m, 0.08 m, 0.12 m, and 0.16 m above the bed. Horizontally, the first measurement was taken 0.2 m away from the right sidewall, with the probe moving in increments of 0.05 m, until it reached the location of the last measurement point at 1.9 m from the right sidewall. At each measurement point, the data were collected for 30

seconds, as pictured in Appendix C.4, at a sampling rate of 200 Hz, to obtain good quality time-averaged velocity data with an error of no more than 0.5% (Nortek 2009).

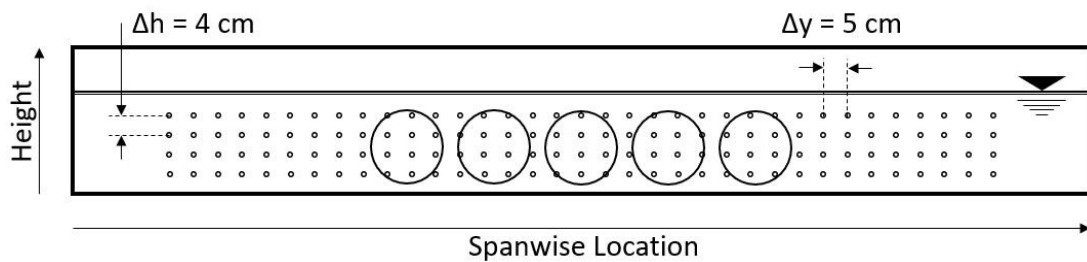


Figure 6.2: Experimental ADV locations on a cross-section with the locations of the ducts visible in the background.

Measurement equipment – Pressure sensors

Water surface elevations were measured using an array of pressure sensors evenly spread throughout the channel bed. Four lines of sensors were located 0.7 m apart in the spanwise direction as illustrated in Figure 6.3. In streamwise direction, sensors were located every 1.8 m along the flume, with the first 6 rows (R01-R06) measuring water surface elevations of the impoundment upstream of the barrage, the middle 10 rows (R07-R15) covering the section between the barrage and the weir, and the last 4 rows (R16-R19) were located downstream of the weir.

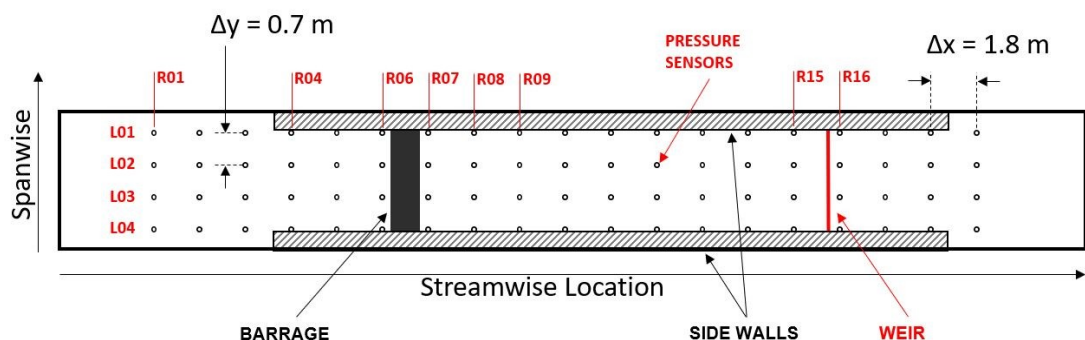


Figure 6.3: Locations of the pressure sensor in the flume (not to scale). Some labels are hidden to prevent overcrowding of the image.

6.3.2 Case studies

Using the described experimental setup three different experimental case studies were performed, using a different number and configuration of the jets (Table 6.1). The experimental runs were named THU 1, THU 2, and THU 3 .

For the first case study (THU 1) all of the draft tubes were left open, resulting in five equidistant coaxial jets entering the downstream domain, pictured in Appendix C.3. This configuration most closely resembled the discharge from a TRS where turbines are constructed close to each other in a powerhouse caisson. A similar configuration was used in the studies by Jeffcoate et al. (2013) where seven coaxial jets were studied. A 0.16 m high weir was placed at the end of the flume, pictured in Appendix C.5, to achieve a tailwater depth of 0.206 m. The flume discharge was set to 41 l/s to achieve an average water level of 0.223 m upstream of the barrage. This facilitated a head difference of 0.018 m and discharge velocity in the range of 0.5 m/s.

In the second part of the experiment three of the five draft tubes were plugged using custom made silicone plugs, pictured in Appendix C.6, to investigate the interaction between only two coaxial jets. For the THU 2 case, the second and fourth draft tubes were left open, pictured in Appendix C.7, separating the centrelines of the two jets by 0.32 m. For the THU 3 case, the distance between the jets was doubled to 0.64 m by opening only the first and fifth draft tubes, as pictured in Appendix C.8. The same flow rate and downstream boundary conditions were used for both cases, however, these conditions differed from THU 1 because of the reduced discharge capacity of the draft tubes. Due to the limitations of the available equipment, it was not possible to match exactly the head difference from THU 1. However, the closest possible conditions were achieved by raising the weir to 0.17 m with a flow rate of 18 l/s. For this case, the average water surface level of the tailwater was recorded at 0.199 m and 0.222 m at the upstream impoundment, which resulted in a slightly higher head difference of 0.023 m.

Table 6.1: Three different barrage configurations for the experimental setup.

Experiment name	THU 1	THU 2	THU 3
Configuration			
Flume discharge	41 l/s	18 l/s	18 l/s
Weir height	16 cm	17 cm	17 cm

6.3.3 Measurements

ADV velocity measurements

Average velocity vectors were obtained by processing the recorded ADV data at each measurement point. The results for all three case studies are shown in Figures 6.4 to 6.6. The flow conditions are presented as three-dimensional velocity vectors, originating from the points where the measurements were taken, with the contours of the axial velocity shown in the background for each cross-section.

For case study THU 1 (Figure 6.4), the five individual jets were distinguishable at the first two cross-sections (CS1 and CS2), with a clearly visible velocity minima separating them. Observing further downstream, the jets gradually merged and by the time they had reached CS4 the velocity magnitude became more uniform across the jet width. A clear asymmetry in the flow was observed as the combined jet attached to the sidewall of the flume. This phenomenon is commonly known as the Coanda effect, where the jet path is deflected towards the nearby horizontal surface (Sobey et al. 1989). The effect occurs when the presence of a solid surface parallel to the flow, such as a flume wall, prevents the jet in entraining the surrounding fluid and attracts it towards the same surface, where it remains attached due to the pressure difference across the flow (Reba 1966). In the experiments outlined herein, the jet was deflected towards the right-hand side of the flume. A low-pressure vortex formed in the right-hand corner of the flume, directly behind the barrage, causing the jet to make a relatively sharp deflection towards the right-hand sidewall. The peak velocity measured at CS1 was just below 0.6 m/s for each

individual jet. With the jets merging into a combined jet the maximum velocity was gradually reduced to 0.43, 0.37 and 0.31 m/s at CS3, CS4 and CS5 respectively.

Similar observations were made for the case studies THU 2 (Figure 6.5) and THU 3 (Figure 6.6). Both experienced the same Coanda effect, with the jet attached to the right-hand sidewall of the flume. Because of the larger separation of the orifices, the two separate jets were even more distinguishable in the first two cross-sections (CS1 and CS2). Because the space between the two draft tubes was blocked by a solid wall, the jets can be classified as unventilated parallel jets. As described by Nasr and Lai (1997), the blockage created by the barrage wall causes the mutual entrainment of the two jets, forming a low-pressure recirculation zone between them, also known as a converging region. This entrainment causes the jet axis to deflect towards the centreline of the flume and eventually the two jets merge into a single jet. The main difference between the flow patterns for cases THU 2 and THU 3 was the length of the converging region. In comparing Figures 6.5 and 6.6, the jets in THU 2 have already merged at the cross-section CS3, whereas the jets in THU 3 were still separated at the same cross-section. The peak velocity at CS1 was approximately 0.65 m/s for both cases. Further downstream, at cross-section CS3, the velocity of the combined jet was reduced to 0.32 m/s for the THU 2 case. For the case THU 3, at the same streamwise distance, the jets were still converging with individual peak velocities of 0.23 m/s each. At CS4 they were already fully merged and attached to the right side of the wall, again due to the Coanda effect.

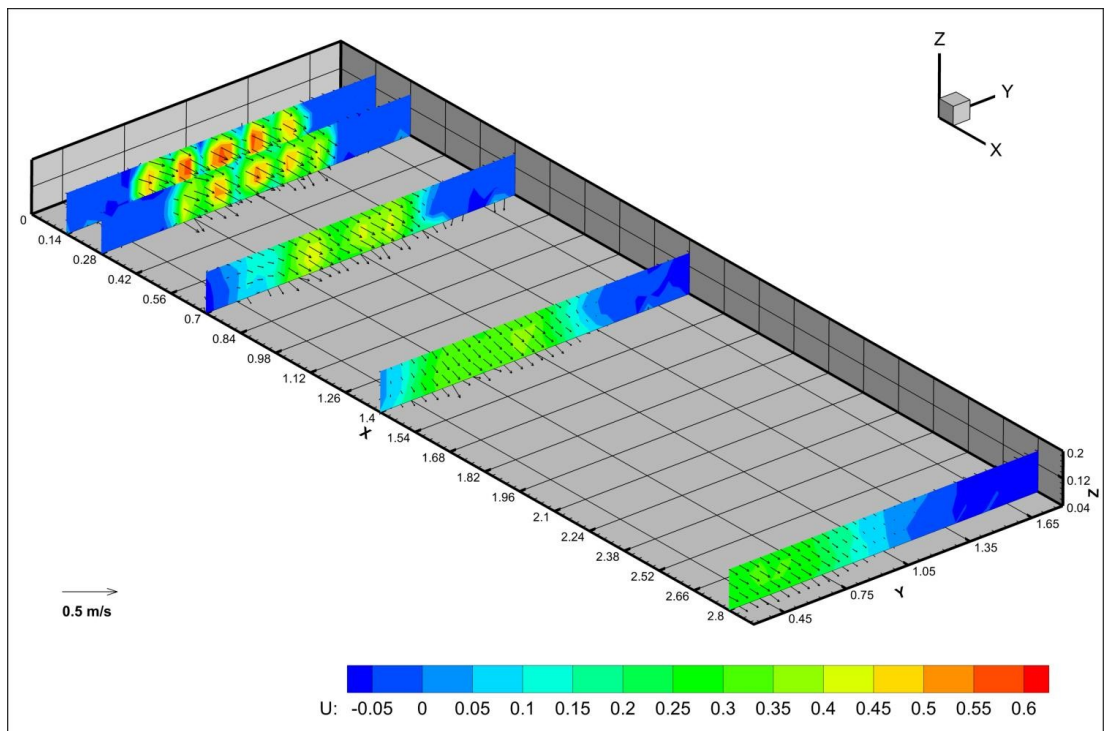


Figure 6.4: ADV measurements for THU 1 presented as 3D velocity vectors and axial velocity contours at 5 locations downstream of the barrage.

Chapter 6
Experimental model: barrage in a flume

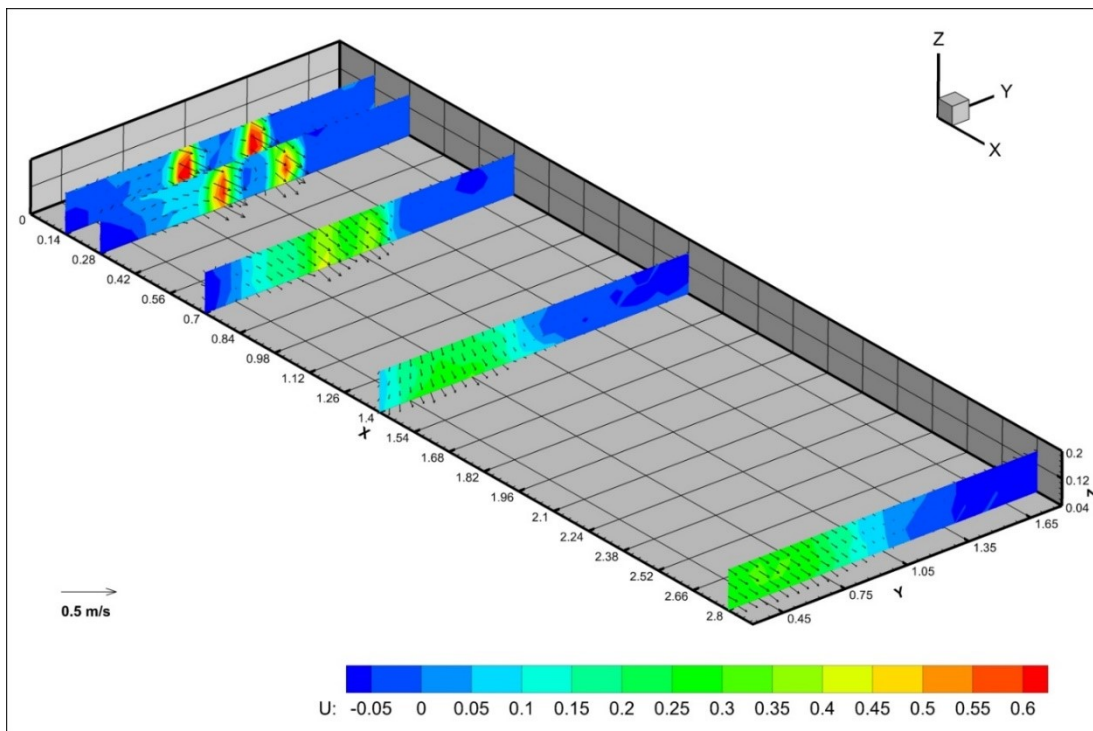


Figure 6.5: ADV measurements for THU 2 presented as 3D velocity vectors and axial velocity contours at 5 locations downstream of the barrage.

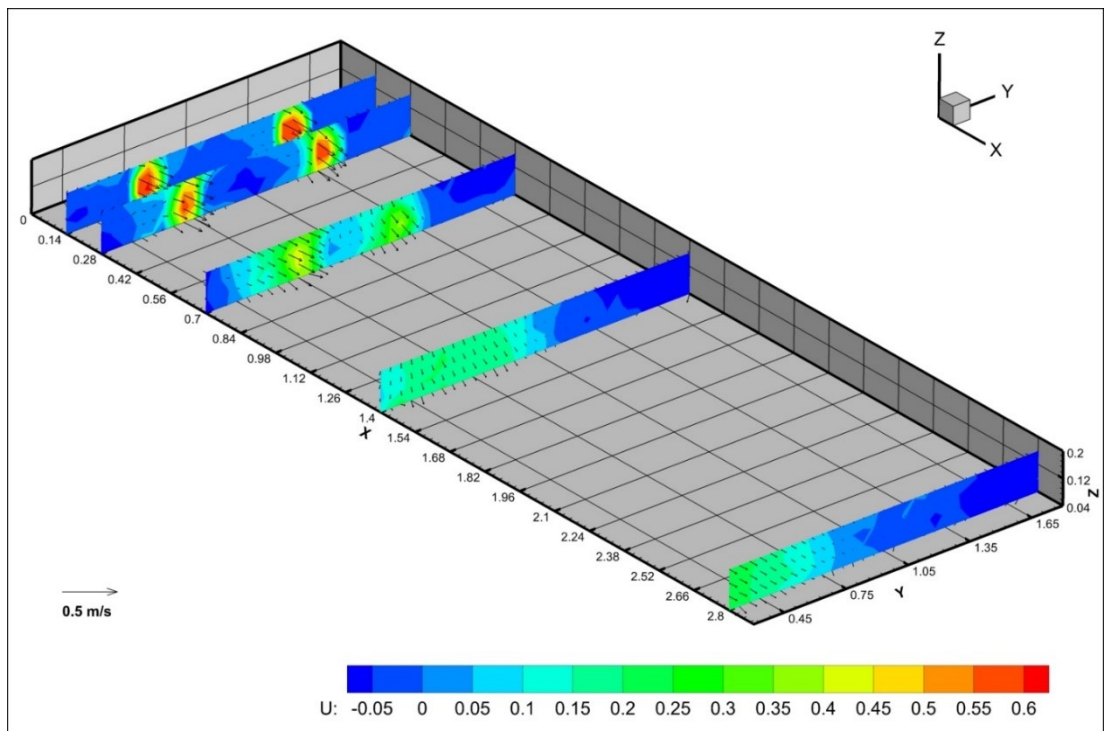


Figure 6.6: ADV measurements for THU 3 presented as 3D velocity vectors and axial velocity contours at 5 locations downstream of the barrage.

Water surface elevation

The observed water levels for both flow rates are shown in Figure 6.7. Some of the pressure sensors at locations R13 to R15 were badly maintained and were showing faulty readings. However, these erroneous measurements were limited to the pressure sensors close to the weir, which were outside of the computational domain used in this study and could, therefore, be disregarded.

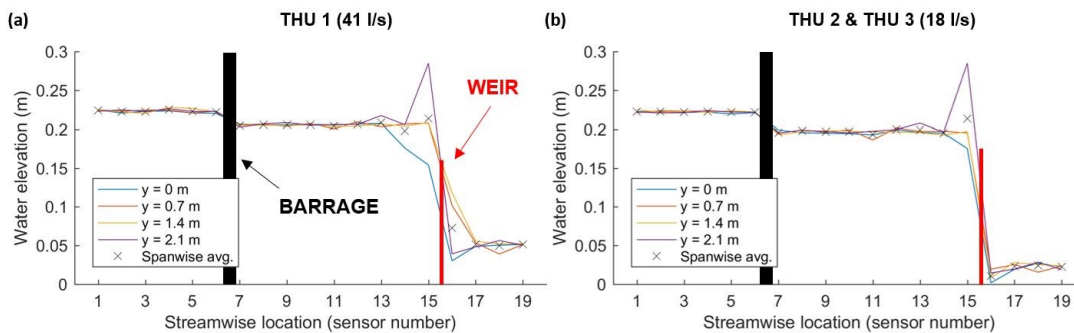


Figure 6.7: Average water elevation in the flume obtained from pressure sensors measurements for (a) THU 1 with 41 l/s and 16 cm weir and (b) THU 2 and THU 3 with 18 l/s and 17 cm.

Different flow rates and different weirs resulted in slightly different water levels between the experiments. Water levels were measured continuously over a longer period and then time-averaged to obtain the average value of the surface elevation. The average recorded elevations for the THU 1 experimental run (Figure 6.7a) were 0.223 m upstream and 0.205 m downstream of the barrage, forming an average head difference of 0.018 m across the barrage. The smaller flow rate and higher weir for experimental runs THU 2 and THU 3 (Figure 6.7b) resulted in elevations of 0.222 m upstream and 0.196 m downstream of the barrage, with an average head difference of 0.026 m. The variation in the streamwise average depth was measured and found to be less than 0.003 m, indicating an almost horizontal water surface.

6.4 Numerical model set-up

The experiments were replicated using the Delft3D modelling suite. The refined methodology for momentum treatment associated with the turbines, as described in section 4.5, was applied to the discharges from the barrage. Each experimental configuration was simulated both in 2D and 3D mode. In addition, a depth-averaged simulation without including the momentum conservation modifications was performed for each experimental case study to act as a benchmark reference.

The numerical model covered only the downstream part of the flume, focusing on the jets emerging from the barrage. The domain spanned across the whole width of the flume and covered a 5.6 m section just downstream of the model barrage, encompassing all five observation cross-sections from the physical model experiments. Due to the simple geometry of the flume, a uniform orthogonal grid was employed. In the streamwise direction there were 112 cells with a cell size of 0.05 m, and 70 cells with a cell size of 0.03 m in the spanwise direction. After a sensitivity analysis of the mesh, the selected resolution was shown to be adequate for this study as further refinements showed no changes to the resulting velocity profile. The flat bottom of the flume meant it had a uniform bathymetry, which was set to 0 m reference elevation. The bottom roughness was specified as a uniform Manning's n roughness coefficient, with the value of 0.009 being selected from the calibration process and a no-slip wall condition was assumed for the side walls. The background horizontal viscosity was another calibration parameter of the model, and a value of 0.0025 m²/s proved to work best with the selected grid resolution.

The 3D model was set-up identically to the 2D model in terms of all of the above parameters etc. In Delft3D a 3D model is created by splitting the vertical dimension of the domain into several vertically linked depth-averaged layers. In 3D the flume was modelled using 6 vertical layers, with a relatively shallow layer at the bottom, followed

by four evenly spaced layers distributed along the height of the draft tubes and a surface layer at the top.

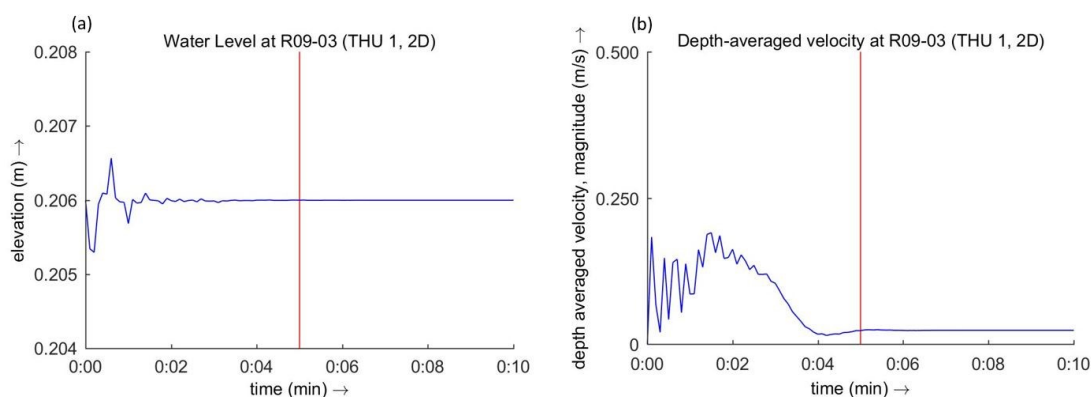


Figure 6.8: Example of (a) Water Levels and (b) Depth-Averaged Velocity time-series for THU 1 case in 2D mode. After 5 minutes the oscillations stop when the steady flow state was reached.

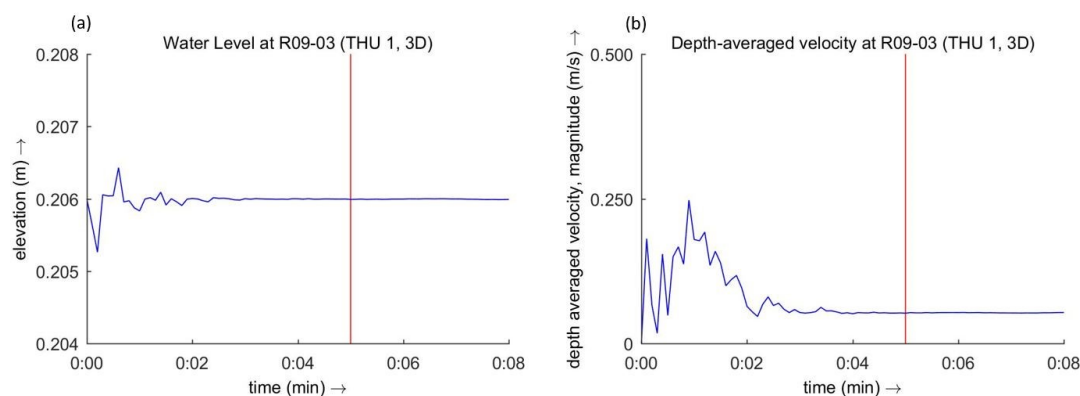


Figure 6.9: Example of: (a) Water Levels and (b) Depth-Averaged Velocities time-series for THU 1 case in 3D mode. After 5 minutes the oscillations stop when the steady flow state was reached.

The downstream depth was set as a water level boundary condition to match the surface elevation measurements from the experiments. The discharge from the draft tubes was the only input at the upstream boundary of the model. It was set-up to match the flow rate of the respective case study runs, as shown in Table 6.1. A depth-averaged width of the draft tube was calculated to provide the equivalent flow-through area of the

discharge and to calculate the corresponding depth-averaged velocity. The discharges were not part of the upstream boundary condition but were instead modelled as a discharge source, by adding an additional term to the momentum equation acting as an external force.

To satisfy the Courant number criteria and assure numerical stability, a 0.06 second time step was used for the 2D simulation, and a 0.006 s for the 3D runs. To guarantee steady-state flow, the model was run over 10 and 8 minutes of simulation time for the 2D and 3D runs respectively and before any results were recorded. Figures 6.8 and 6.9 shows the time-series of water levels and depth-averaged velocities at an arbitrary point in the flume and illustrates how the initial numerical oscillations diminish after 5 minutes, after which time the solution could be assumed to be steady state. With 10,000 time-steps, a 2D run took on average 2 minutes to finish, while a 3D run with 6 layers and 16,000 time-steps required 15 minutes to complete the simulation on a desktop PC utilizing a 3.60 GHz Intel® Core™ i7 series CPU.

6.5 Results

6.5.1 Water levels

The computed water elevations were compared with the experimental measurements at the locations of the first four pressure sensors, downstream of the barrage (R07-R10). Water levels at each downstream location were averaged across the width of the channel. Almost an exact match occurred between the water surface elevations and measured depth from pressure sensors for both the 2D and 3D simulations, for all three case studies.

Case Study THU 1

The recorded water levels for case study THU 1 are given in Table 6.2. The discrepancies between the simulations and observations were, in general, less than 0.1 cm. At the locations R09 and R10 there is practically no difference between the 2D and 3D results. However, this is not the case just downstream of the barrage (R07), where the 2D model slightly overpredicted the water level by 0.5 mm, while in contrast the 3D model underpredicted the level by 0.9 mm.

Table 6.2: Recorded and computed water levels for THU 1 at four locations downstream of the barrage (R07-R10).

THU 1					
Location	Measured [cm]	Delft3D (2D) [cm]	Diff. [cm]	Delft3D (3D) [cm]	Diff. [cm]
R07	20.47	20.52	0.05	20.38	-0.09
R08	20.58	20.58	0.00	20.64	0.06
R09	20.55	20.58	0.03	20.59	0.04
R10	20.58	20.60	0.02	20.60	0.02

Case Studies THU 2 and THU 3

Consistent findings were observed for case studies THU 2 (Table 6.3) and THU 3 (Table 6.4). Similarly, the water levels at locations R09 and R10 were almost identical between the model predictions and the experimental measurements. The differences between the 2D and 3D results at the nearby location (R07) were slightly more pronounced than for case THU 1. The 2D simulation overpredicted the surface level by 1.7 and 1.6 mm for cases THU 2 and THU 3 respectively, while the 3D model again underpredicted the corresponding water elevations by 0.7 and 2.4 mm respectively.

Table 6.3: Recorded and computed water levels for THU 2 at four locations downstream of the barrage (R07-R10).

THU 2					
Location	Measured [cm]	Delft3D (2D) [cm]	Diff. [cm]	Delft3D (3D) [cm]	Diff. [cm]
R07	19.55	19.72	0.17	19.48	-0.07
R08	19.77	19.81	0.04	19.82	0.05
R09	19.66	19.80	0.14	19.80	0.14
R10	19.68	19.80	0.12	19.80	0.12

Table 6.4: Recorded and computed water levels for THU 3 at four locations downstream of the barrage (R07-R10).

THU 3					
Location	Measured [cm]	Delft3D (2D) [cm]	Diff. [cm]	Delft3D (3D) [cm]	Diff. [cm]
R07	19.55	19.71	0.16	19.31	-0.24
R08	19.77	19.81	0.04	19.81	0.04
R09	19.66	19.80	0.14	19.67	0.01
R10	19.68	19.80	0.12	19.78	0.10

6.5.2 Contribution of momentum conservation

Simulations without the addition of the momentum correction term for the operation of TRSs were performed with the aim being to assess the impacts of the momentum conservation method in comparison to the “mass-only transfer” method. In the latter, any acceleration of the flow due to a discharge through the draft tube was ignored and the source was only added to the continuity equation. This method has been commonly used in several TRS studies (Xia et al. 2010c; Zhou et al. 2014a; Bray et al. 2016), and while the simplifications may be acceptable for the assessment of the far-field hydrodynamics, this is not the case for numerical model studies focusing on assessing the near-field flow conditions (Angeloudis et al. 2016b). Figures 6.10 to 6.12 show a comparison of the velocity magnitudes downstream of the barrage for the case studies THU 1, THU 2 and THU 3 respectively.

Case Study THU 1

The most evident difference between the two methods is the maximum velocity of the outflowing jets. The top image in Figure 6.10 shows the results for the THU 1 simulations with the inclusion of the momentum conservation source term. The five jets are clearly distinguishable exiting the barrage, with these results being consistent with the observations from the experimental measurements (Figure 6.4). The individual jets are separated by velocity minima and achieve peak velocities in the range of between 0.4 and 0.5 m/s. In comparison, the velocities of the “mass-only” simulations (bottom in Figure 6.10) were almost 50 % lower, not exceeding 0.25 m/s. The velocity is distributed much more uniformly; the individual jets merged together almost instantly, forming a much more uniform distribution of the velocity across the width of all five duct tubes. The “mass-only” simulations also do not exhibit the Coanda effect, which results in an almost perfectly symmetrical flow. In the momentum conservation model, the effect was triggered by a very small initial declination of the velocity vector, which could not be included in the “mass-only” simulations.

Case Studies THU 2 and THU 3

Results for the case studies THU 2 (Figure 6.11) and THU 3 (Figure 6.12), with only two active jets, were consistent with the THU 1 results. In both cases, the momentum conservation simulations produced velocities higher than 0.5 m/s at the draft tube exit, compared to the “mass-only” simulation where the exit velocity never exceeded 0.3 m/s. In both cases the “mass-only” simulations failed to replicate the Coanda effect, resulting in a perfectly symmetrical velocity distribution. Also, the converging region (i.e. the area between the barrage wall and the point of the two jets merging) was visibly longer in the “mass-only” simulation for both cases.

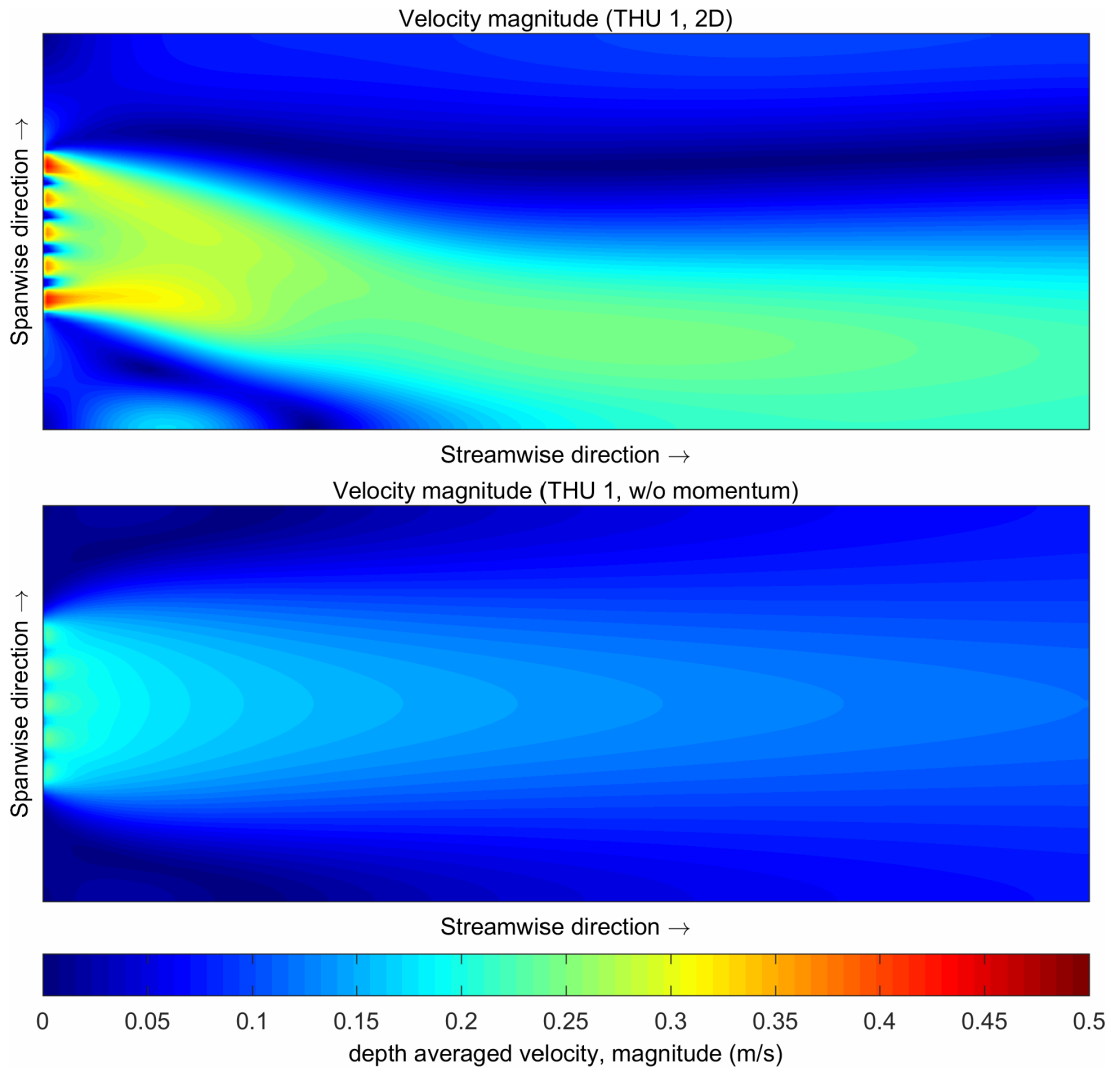


Figure 6.10: Velocity magnitude for THU 1; (top) results of a depth-averaged simulation with the addition of momentum; (bottom) result without the addition of momentum.

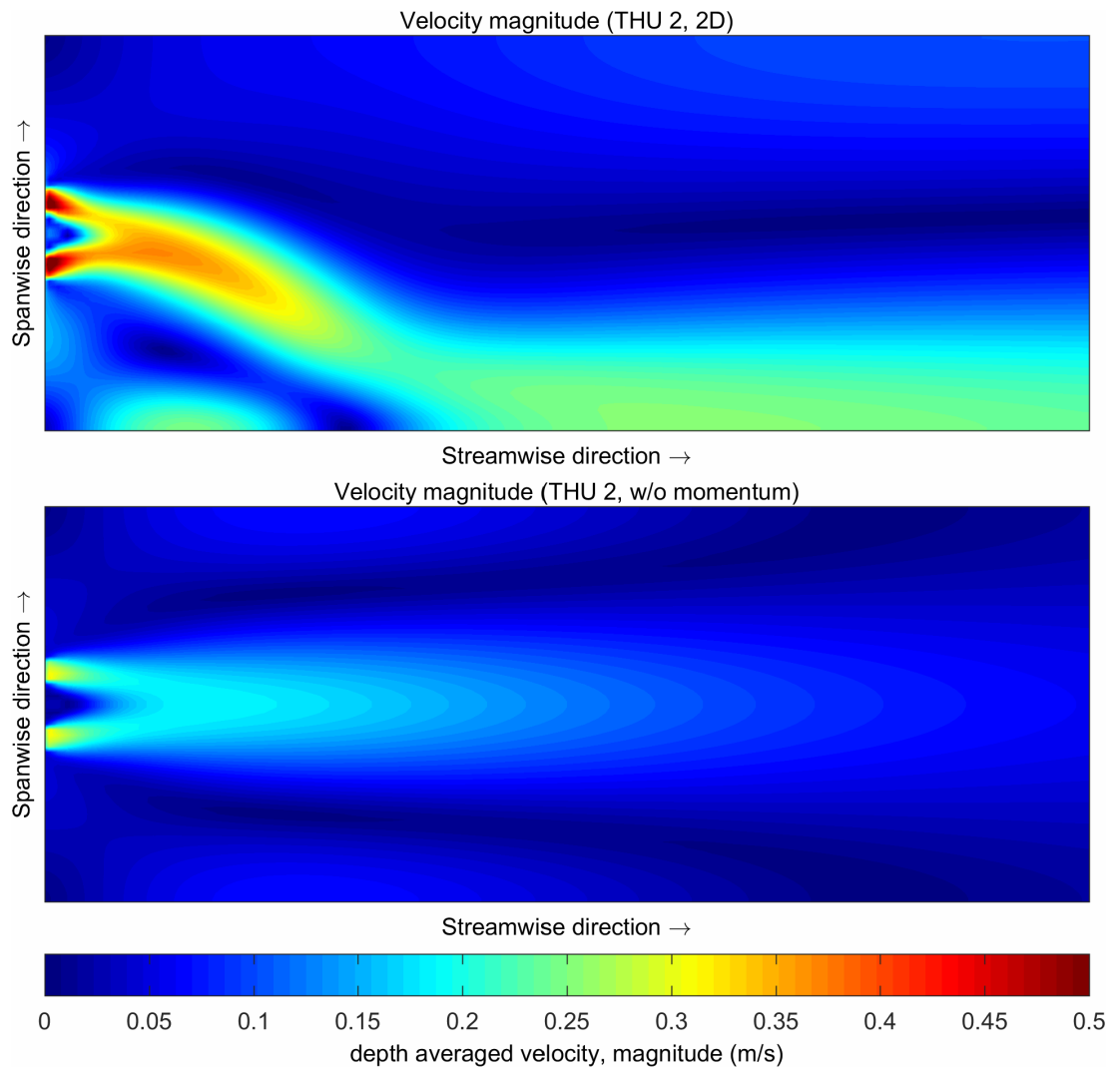


Figure 6.11: Velocity magnitude for THU 2; (top) results of a depth-averaged simulation with the addition of momentum; (bottom) result without the addition of momentum.

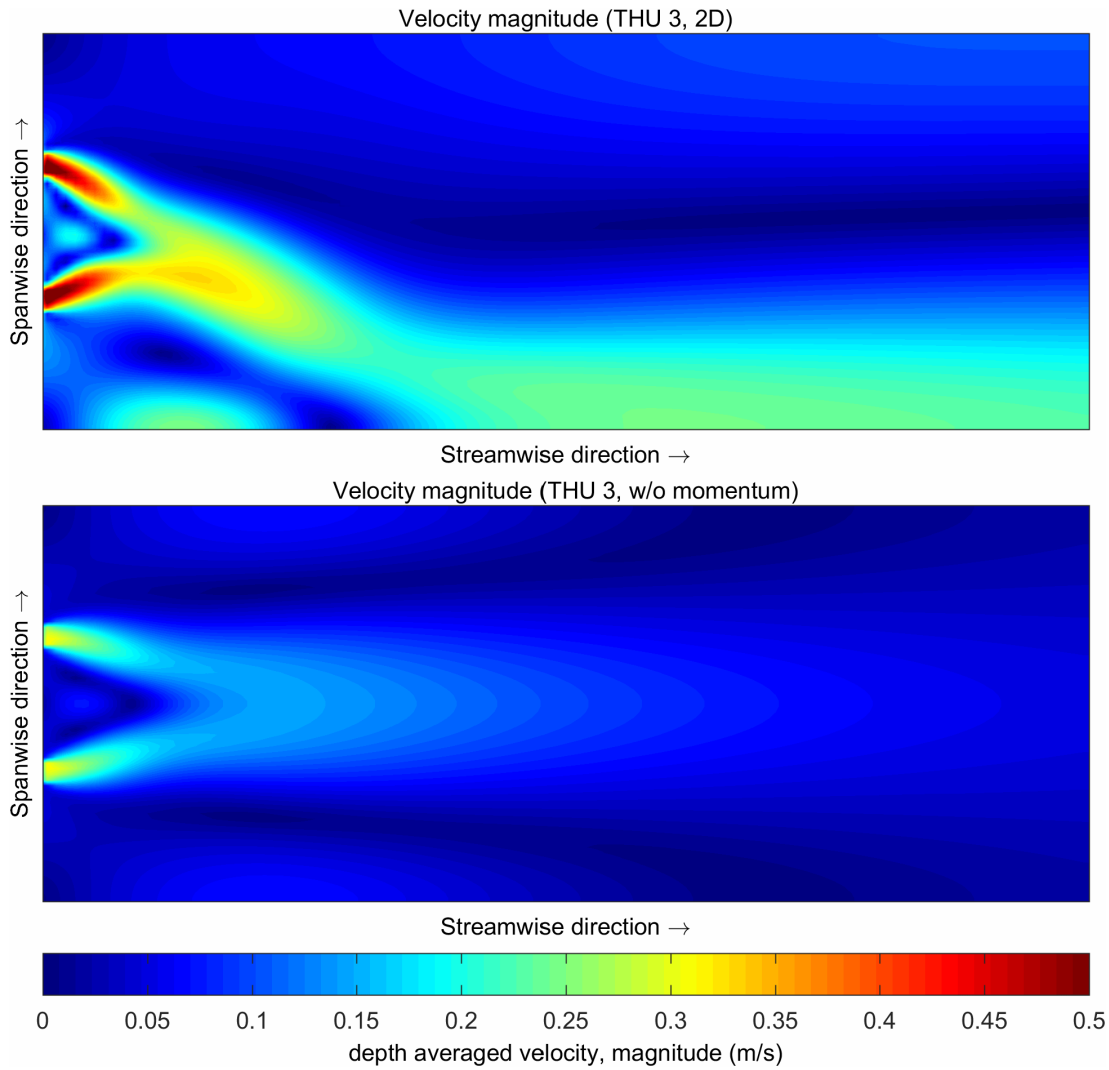


Figure 6.12: Velocity magnitude for THU 3; (top) results of a depth-averaged simulation with the addition of momentum; (bottom) result without the addition of momentum.

6.5.3 Depth-averaged velocity

For a direct comparison with the 2D model results, both the 3D numerical model results and the laboratory measurements were first depth-averaged. Figures 6.13 to 6.15 show the axial and lateral components of the depth-averaged velocity for the case studies THU 1, THU 2 and THU 3 respectively. The velocities are plotted at the 5 selected cross-sections CS1 – CS5 at the locations $1 d_T$, $2 d_T$, $5 d_T$, $10 d_T$, and $20 d_T$.

Some general findings were observed across all three case studies. The simulations were able to recreate the clearly distinguishable jets at the first cross-section (CS1), separated with an evident velocity minimum between them. The negative axial velocity on both sides of the jets indicated the presence of eddies at the side of the flume. With the distance from the barrage increasing, the jets gradually merged into a combined jet, with a more uniform axial velocity distribution at CS5. The distinct Coanda effect was replicated in all three cases, and in both the 2D and 3D simulations. In general, the 3D model simulations managed to capture the jet size and axial velocity at CS1, however, they consistently overpredicted the velocity further downstream at locations CS3-CS5. The 2D simulations, in contrast, managed to better capture the combined jet at the downstream locations (CS4-CS5), but at the same time underpredicted the axial velocity of the jets at the upstream end of the flume (CS1 and CS2).

Case study THU 1

In the case study THU 1 (Figure 6.13) the five jets downstream from the tube exits (at CS1) are evident in both 2D and 3D simulations. Both simulations managed to capture the negative axial flow at the flume sides indicative of the recirculating eddies. A good fit between 3D simulation and experimental data can be observed at CS1, with the predicted axial velocities almost exactly matching the maximum and minimum values of observed peaks and troughs. While the 2D model still managed to capture the individual jets, the axial velocity magnitude was noticeably smaller compared to the experimental and 3D simulation values. Because of the dense distribution of the five draft tubes, the jets

exhibit a very short converging zone and already begin to merge into a combined jet at CS2. Here, the 3D simulation still managed to predict similar axial velocity magnitude to observed data, and the 2D simulation underpredicted them. Both 2D and 3D run failed to capture the complexity of the merging region, with the simulation results already showing a relatively uniform axial velocity profile of the combined jet. Further downstream, at CS4 and CS5, the 3D results have started to overpredict the axial velocity at the centre of the combined jet, however still showed a very good fit at the sides of the jet, including the asymmetry caused by the Coanda effect. The gap between the 2D and 3D predictions has narrowed, however, the 2D results have still slightly underpredicted the velocity magnitude. At CS5 the velocity of the combined jet was much more uniform. At this point, the 2D results were much closer to the observed velocity of the combined jet, while the 3D model continued to slightly overpredict them.

Case study THU 2

For case study THU 2 the two parallel jets were separated by a single closed-off draft tube. At CS1 both the 2D and 3D simulations produced distinct axial velocity peaks and negative velocities at the right-hand side of the flume, indicating a counter-rotating eddy. Interestingly, two jets at CS1 showed asymmetry in the 3D simulations, with the right-hand side jet displaying a much larger axial velocity than its left-hand side neighbour. At CS2, the 2D simulations still produced the individual jets, however, the model failed to predict the correct velocity magnitudes for both the maximum velocity across the jets and the minimum velocity of the convergence region between the jets. The observed results showed that the jets still had not fully merged at CS3, however, both simulations showed an already merged jet, with the 2D model predicting the correct velocity magnitude and the 3D model considerably overpredicting the velocity peak. At CS4 and CS5 the 2D model simulations produced a perfect match with the observational results; the 3D simulations overpredicted the results, even this far downstream. Lateral velocities were another indication of the problems that this 3D model had in dealing with the two converging jets. While the 2D model simulations produced an almost perfect

match with the v_y component of the measured velocity, the 3D model was not accurate with the velocity magnitudes being almost twice the value of the observed data.

Case study THU 3

Similar findings were observed for case study THU 3. The inaccuracies described for case study THU 2 increased as the two jets were separated even further apart. The spacing for THU 3 was equivalent to the width of the three closed-off draft tubes. The 3D model consistently overpredicted both the axial and lateral velocities, while the 2D model again underpredicted the velocities at the first two cross-sections, but provided good agreement with the measured results downstream. Because the jets in THU 3 were further apart than in THU 2, the former case exhibited a much longer converging region compared to the latter. This can be observed for the location CS3 at a distance of $5 d_T$ from the barrage, where the two jets were still distinguishable for case THU 3, but had almost completely merged together for case THU 2. For both cases the jets were already fully merged by cross-section CS4. The THU 3 2D simulations at CS3 showed a relatively accurate magnitude of the axial velocity, but failed to capture the trough between the two jets, similarly as in THU 2 case. However, the 3D results were less accurate when compared to case THU 2, with the already combined jet deflecting closer to the right side-wall than the results from the experiments and the 2D run.

In general, the 2D model captured the complex phenomena of the merging jets considerably better than the 3D model for the case of only two parallel jets (i.e. THU 2 and THU 3). On the other hand, the 3D model performed much better for the situation with five parallel jets (i.e. THU 1). One of the main differences between the two- and five-jet scenarios was the spacing between the draft tubes. The results showed that in the situation with the dense distribution of jets (THU 1), the 3D model produced good results. The jets quickly merged into a combined jet with a more evenly distributed velocity profile in the spanwise direction. In contrast, the cases with a wider separation between the jets (THU 2 and THU 3) formed a much more complex flow pattern at the tube exits and at the merging region. The converging region was much longer, with the

jets not fully combined until CS4, at a distance of $10 d_T$ downstream of the barrage. As the spacing between the two jets increased from case THU 2 to THU 3, so did the inaccuracies in the 3D model predictions.

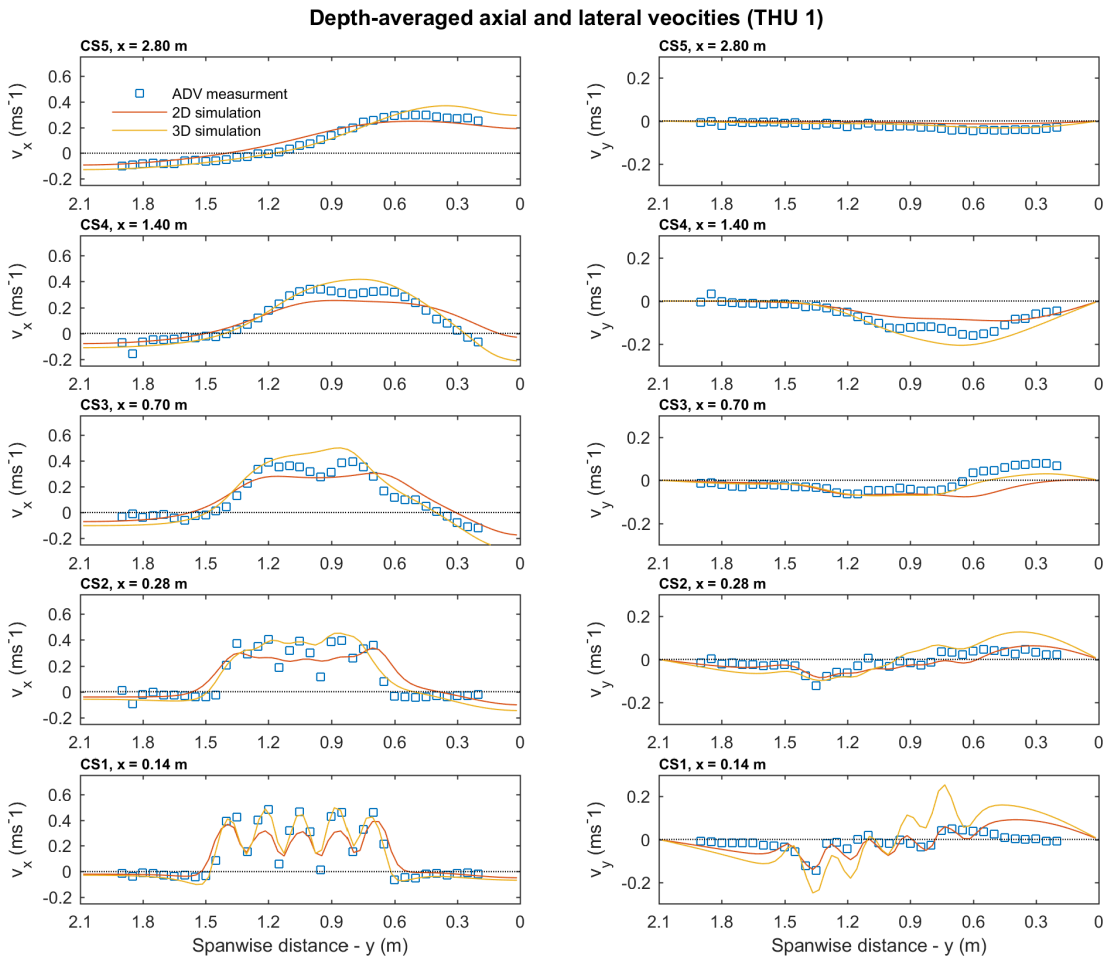


Figure 6.13: Depth-averaged axial (left) and lateral (right) velocities at 5 observational cross-sections downstream of the barrage for the THU 1 case, comparing the experimental measurements with the 2D and 3D model results.

Chapter 6 Experimental model: barrage in a flume

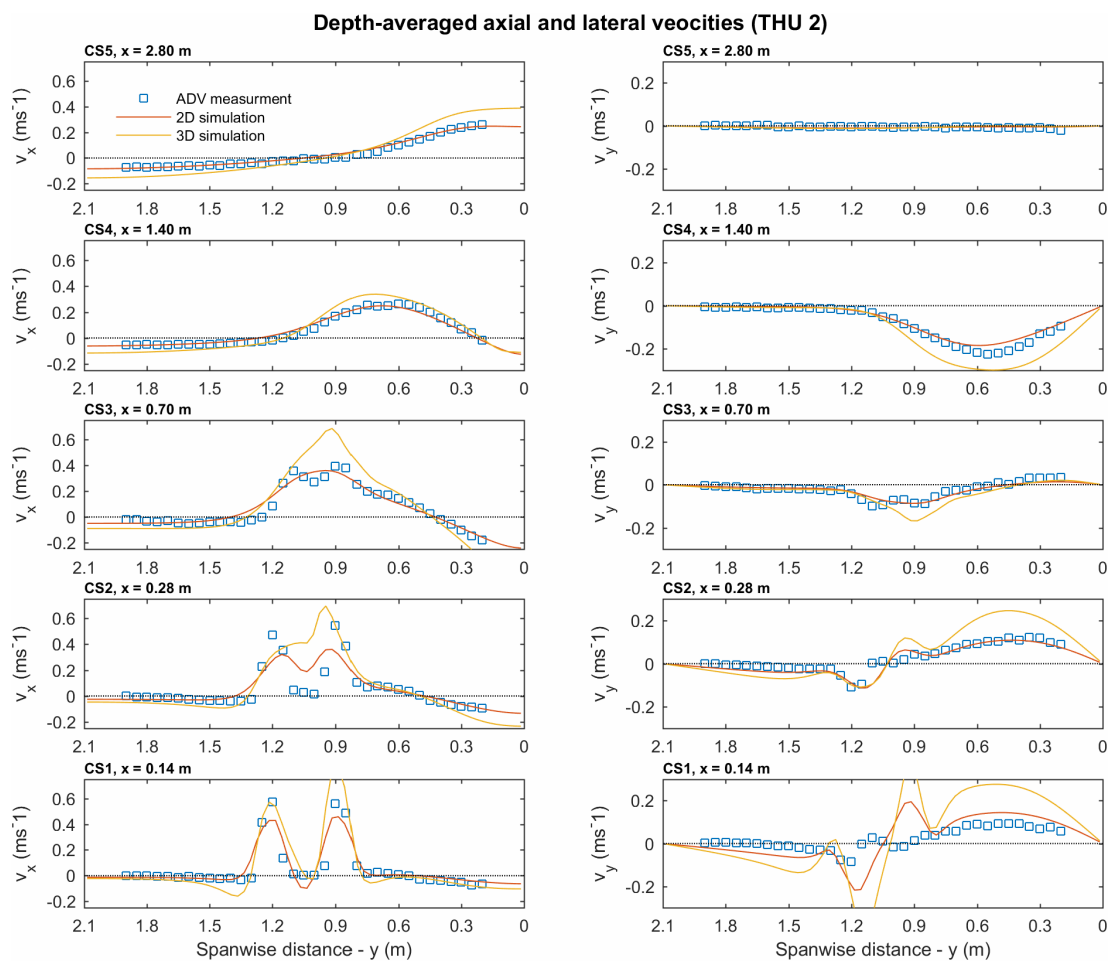


Figure 6.14: Depth-averaged axial (left) and lateral (right) velocities at 5 observational cross-sections downstream of the barrage for the THU 2 case, comparing the experimental measurements with the 2D and 3D model results.

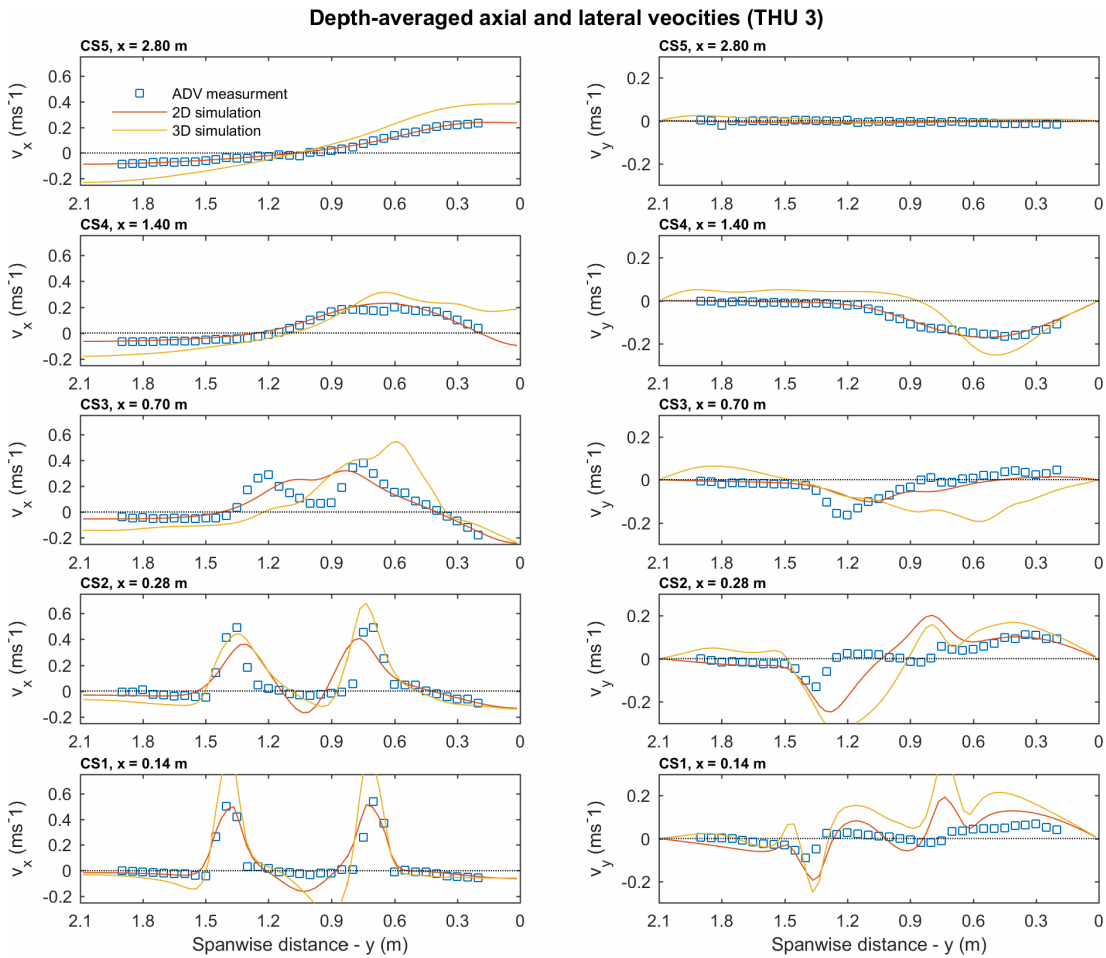


Figure 6.15: Depth-averaged axial (left) and lateral (right) velocities at 5 observational cross-sections downstream of the barrage for the THU 3 case, comparing the experimental measurements with the 2D and 3D model results.

6.5.4 Velocity vectors 2D vs 3D

Figures 6.16 to 6.18 show a comparison of the velocity fields between the 2D and 3D simulations for the case studies THU 1, THU 2 and THU 3 respectively. The velocity of the 3D model was depth-averaged to compare with the results from the 2D model.

Case study THU 1

The five jets forming directly downstream from the tube exits are clearly visible in both the 2D and 3D simulations, as well as the deflected trajectory of the combined jet caused by the Coanda effect Figure 6.16. For both simulations, the jets merge relatively quickly as the distance from the barrage increases. The main difference between the two models was the velocity magnitude. As already observed previously in Figure 6.13, the 3D simulations predicted an accurate velocity magnitude, while the 2D simulations underpredicted the magnitudes considerably. Higher velocities in the 3D run created a larger counter-rotating eddy on the right hand side, narrowing the combined jet in the spanwise direction. This again explains why the 3D model better predicted the shape of the axial velocity distribution at CS2-CS4 in Figure 6.13.

Case study THU 2

The two jets forming directly downstream from the tube exits are again clearly visible for both the 2D and 3D simulations; so too is the deflection due to the Coanda effect. The 3D model simulations produced considerably larger velocities compared to the 2D simulations. The converging region can be seen as a triangular recirculation zone, bounded by the barrage and the two jets, which are clearly visible in both images in Figure 6.17. The recirculation zone between the two jets was almost perfectly symmetrical in the 2D simulation (Figure 6.17 top). However, it was visibly distorted in the 3D simulation (Figure 6.17 bottom), explaining the asymmetry in the axial velocity observed at CS1 in Figure 6.14.

Case study THU 3

The two jets forming directly downstream from the tube exits are again clearly visible for both the 2D and 3D simulations, as well as the deflection due to the Coanda effect. Similarly, as for THU 2, the converging region between the jets was almost perfectly symmetrical in the 2D simulations (Figure 6.18 top), but again visibly distorted in the 3D simulations (Figure 6.18 bottom). For the latter, it can be clearly seen that the jets exhibited considerably larger velocities and were still producing oscillations at the point of merging. This again explains why the axial velocity profile at CS3 in Figure 6.15 had shifted towards the right hand side of the flume.

For THU 2 and THU 3 the results again show that Delft3D's shallow water 3D model was less accurate in terms of dealing with the complex flow patterns that occur between the two merging coaxial jets. In both cases, the predictions of the 2D simulations were much closer to the observed data, even if the model slightly underpredicted the velocity magnitudes. However, the 3D simulations proved to perform better than the 2D for the case THU 1. Here, the five jets were densely spaced, which allowed the jets to entrain each other and avoid the formation of complex recirculation zones between them.

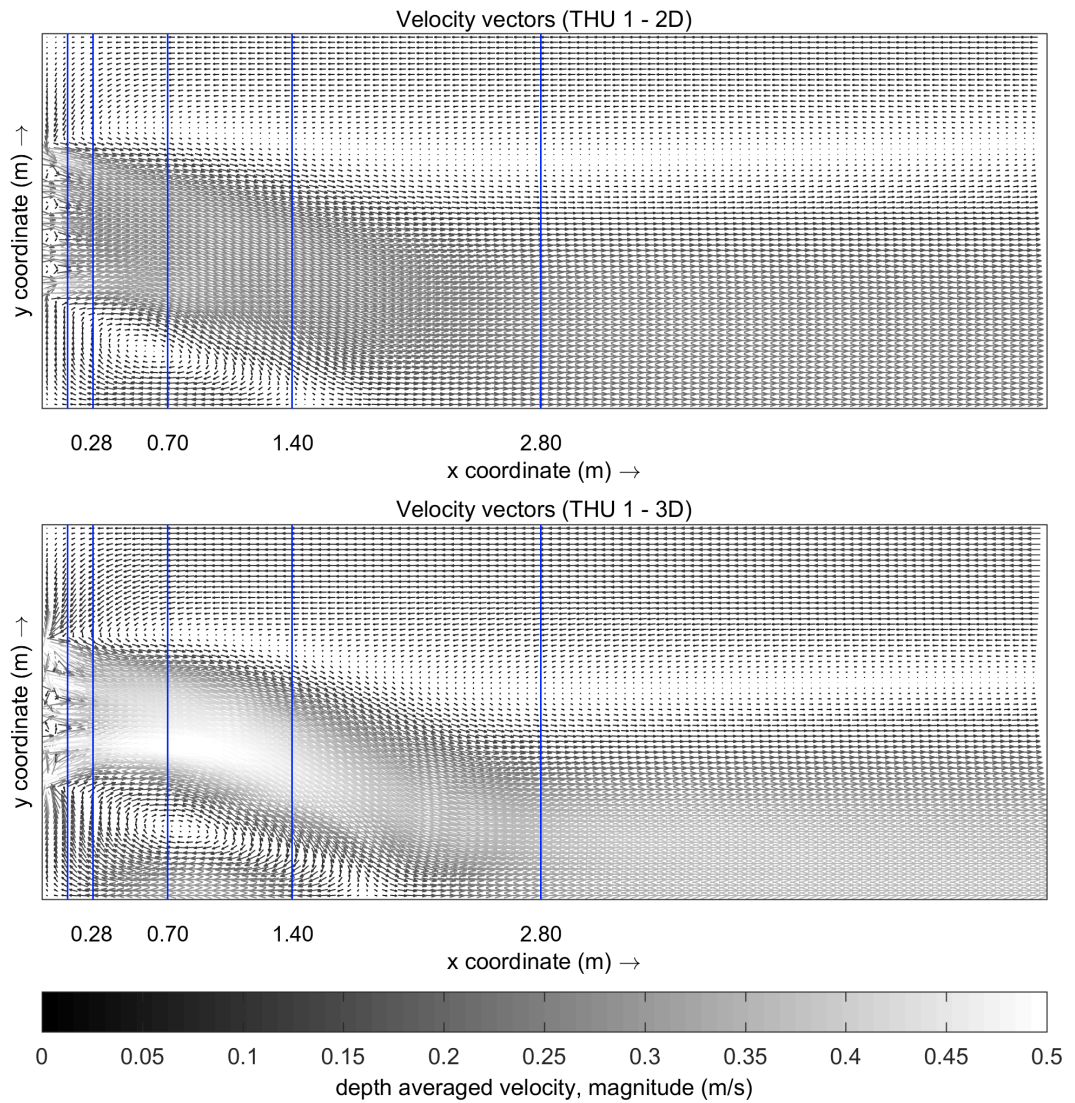


Figure 6.16: Delft3D depth-averaged velocity vectors comparison between 2D (top) and 3D (bottom) simulations for THU 1.

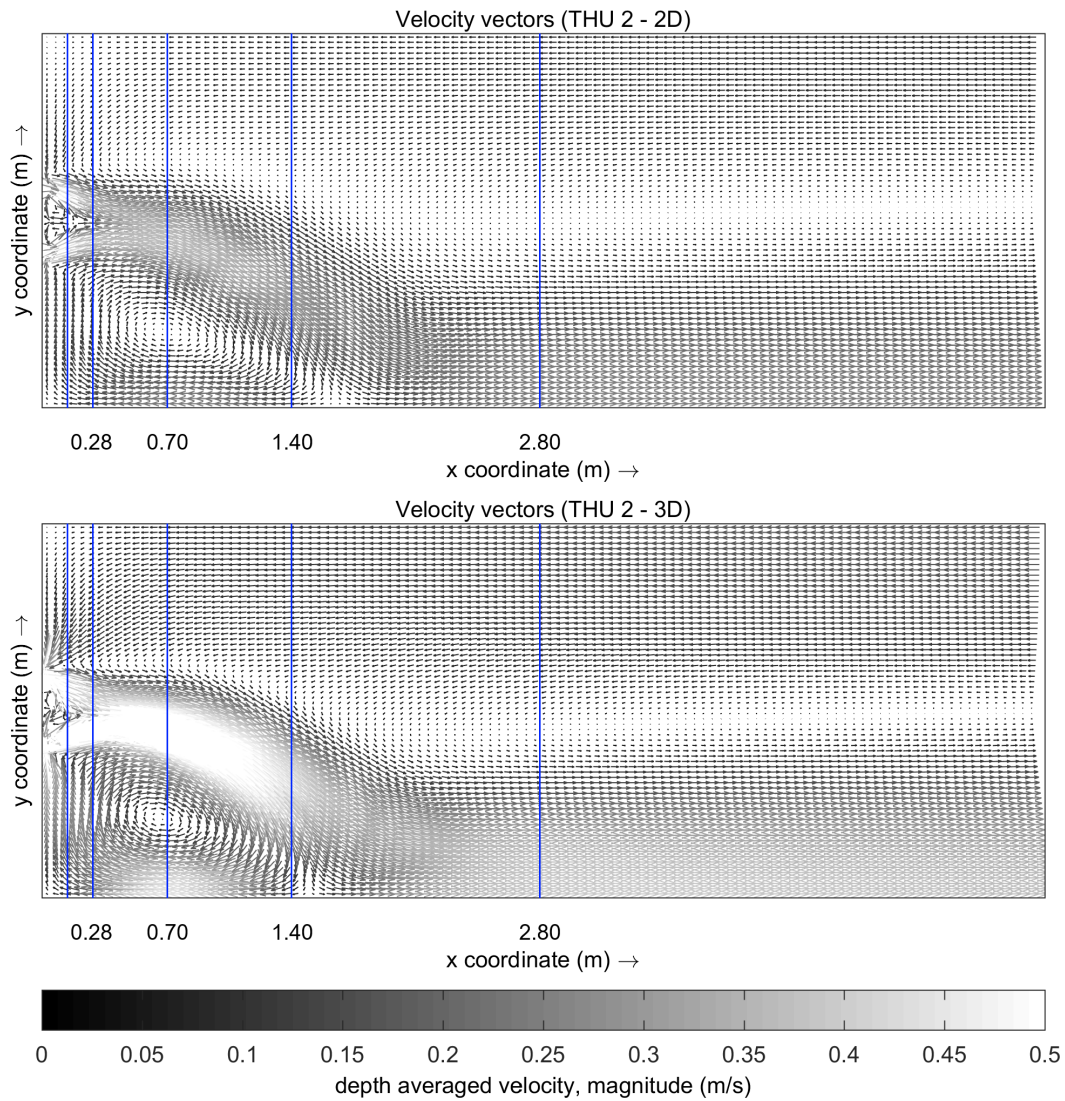


Figure 6.17: Delft3D depth-averaged velocity vectors comparison between 2D (top) and 3D (bottom) simulations for THU 2.

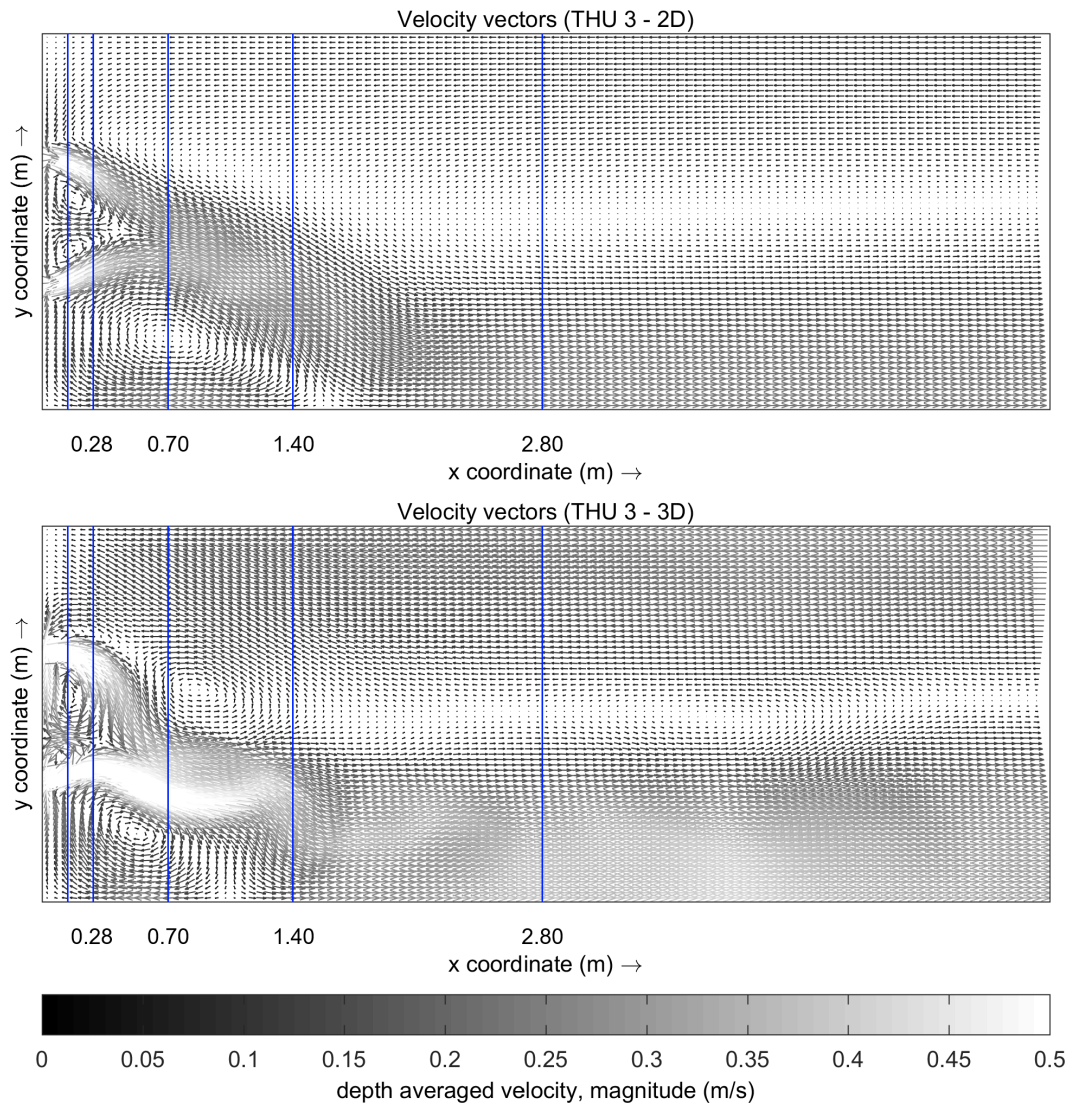


Figure 6.18: Delft3D depth-averaged velocity vectors comparison between 2D (top) and 3D (bottom) simulations for THU 3.

6.5.5 Vertical variation of velocity

To better understand the complexities of the 3D results, described in the sections above, the results were plotted layer by layer and compared with the ADV measurements taken at the respective depths. The 3D model produced results for 6 layers, however, only the layers situated at the same depths as the ADV measurements are shown in the plots. The layers numbered 1, 3, 4, and 5 correspond to the elevations of 0.16, 0.12, 0.08, and 0.04 m respectively above the flume bed.

Case study THU 1

The plots in Figure 6.19 show the THU 1 axial and lateral velocities from the 3D simulations. At CS1 the jets are clearly apparent at all four depths. The simulations predicted similar peak velocities to the experimental results. However, while the measured peak velocity magnitudes were uniform across all five jets, the 3D simulation results produced an asymmetrical distribution. Close to the bed (Figure 6.19a), the peaks occur at the right hand side of the flume. However, the asymmetry was found to be depth-dependant and at 0.08 and 0.12 m from the bed (Figures 6.19b and 6.19c), the peaks moved to the right hand side of the flume. This apparent asymmetry continued into the second cross-section CS2. However, the asymmetry becomes less evident at the later cross-sections. The five jets have still not completely merged together at CS3, with the experimental results showing an almost combined jet with two distinct velocity peaks. While the 3D simulations managed to replicate the two velocity peaks in the lower layer (Figure 6.19a), they failed to do so for further up the water column. At 0.08 m from the bed (Figure 6.19b) the predicted peak velocity magnitude matched the observations, however, the simulations failed to capture an evident trough in the middle of the velocity profile. Similar observations were made at 0.12 and 0.16 m above the bed, with a slightly overpredicted peak axial velocity. Both the 3D simulations and the experimental measurements produced similar results throughout the depth at the cross-sections CS4

and CS5, suggesting that depth-averaging at this distance can produce reasonable results.

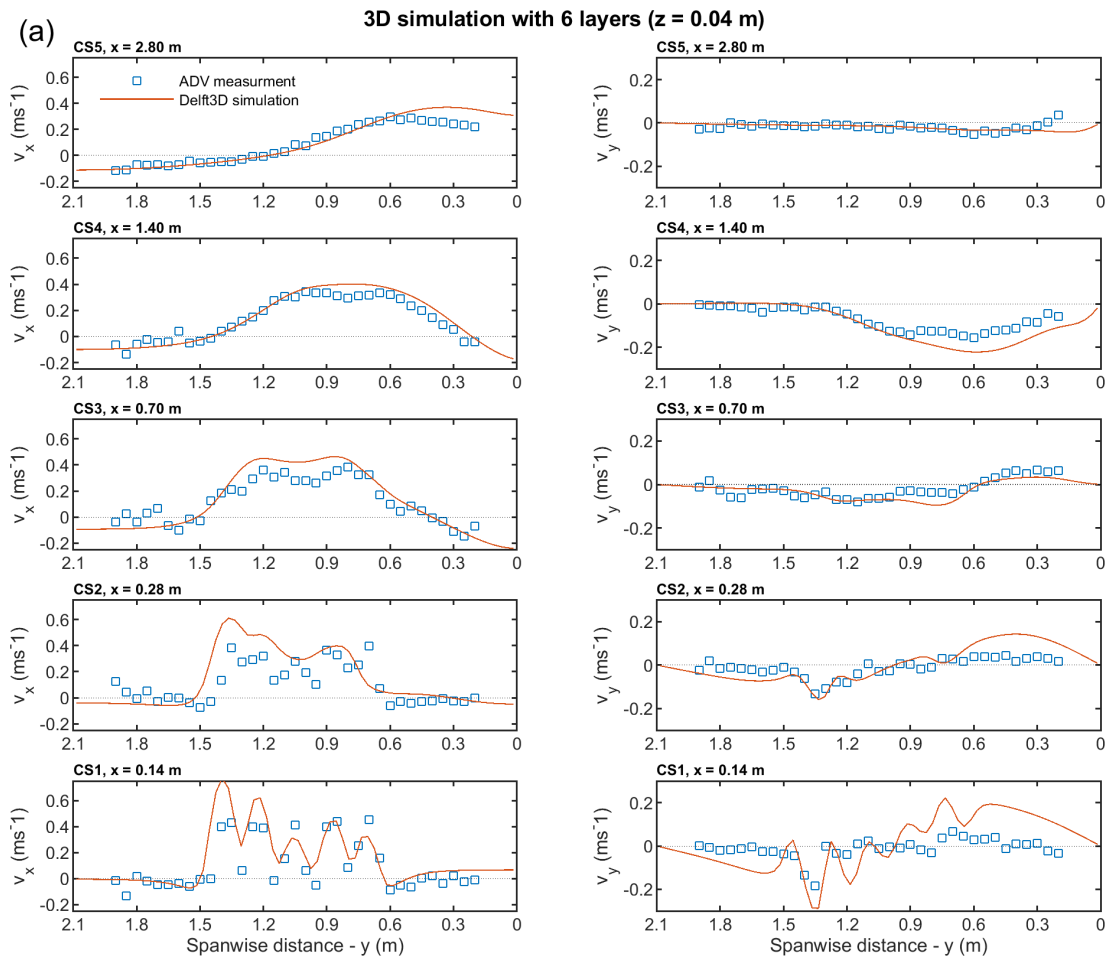


Figure 6.19: Comparison of the velocity profile for THU 1 between laboratory observations and numerical 3D simulation at four depths: (a) 0.04 m, (b) 0.08 m, (c) 0.12 m, and (d) 0.16 m.

Chapter 6
Experimental model: barrage in a flume

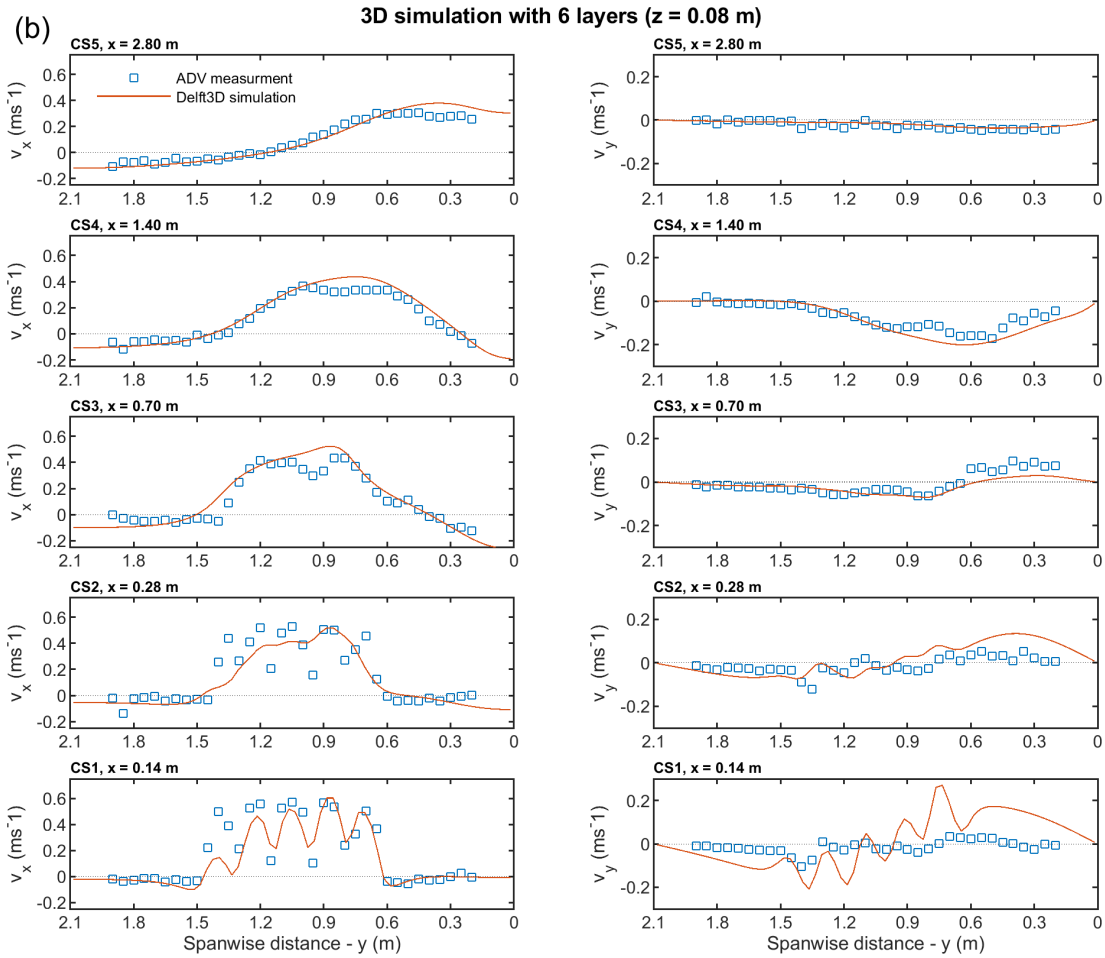


Figure 6.19: Continued from page 13 - Comparison of the velocity profile for THU 1 between laboratory observations and numerical 3D simulation at four depths: (a) 0.04 m, (b) 0.08 m, (c) 0.12 m, and (d) 0.16 m.

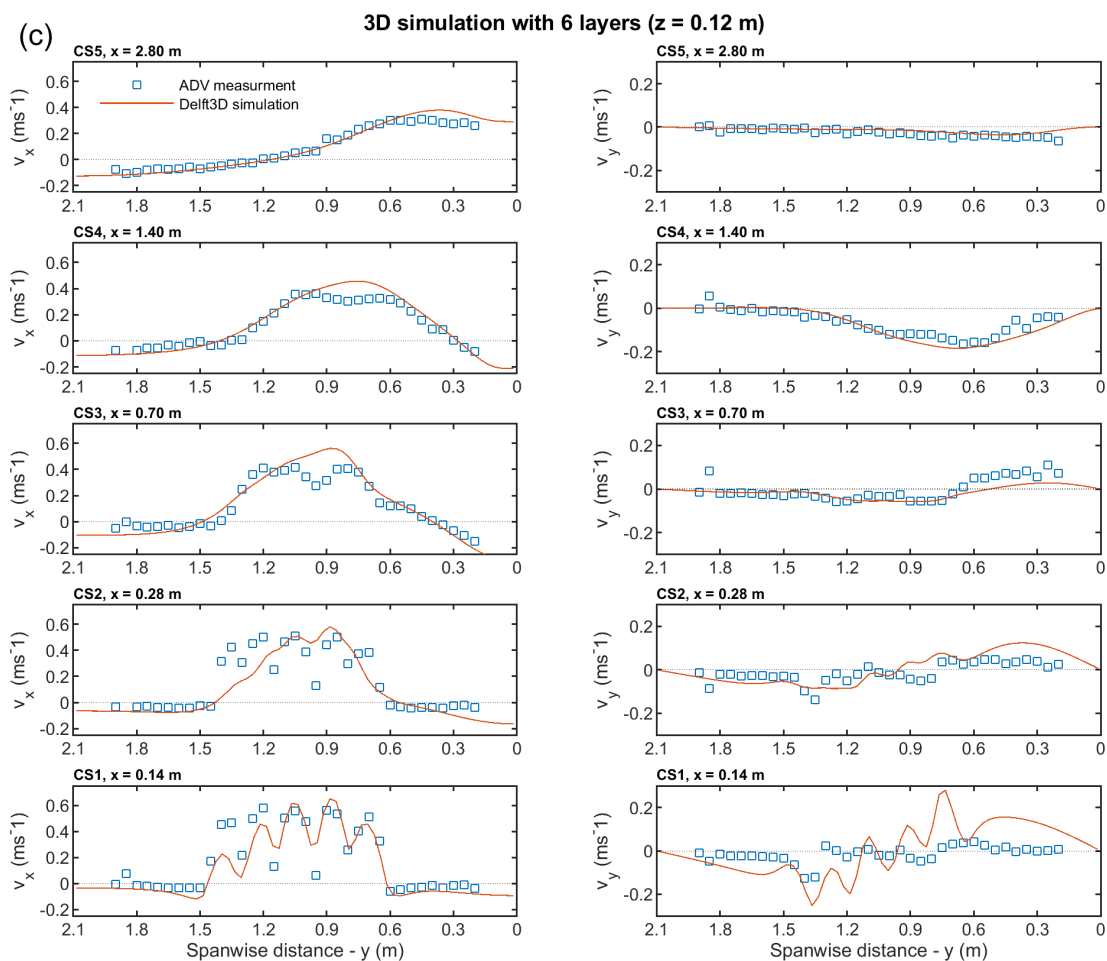


Figure 6.19: Continued from page 13 - Comparison of the velocity profile for THU 1 between laboratory observations and numerical 3D simulation at four depths: (a) 0.04 m, (b) 0.08 m, (c) 0.12 m, and (d) 0.16 m.

Chapter 6
Experimental model: barrage in a flume

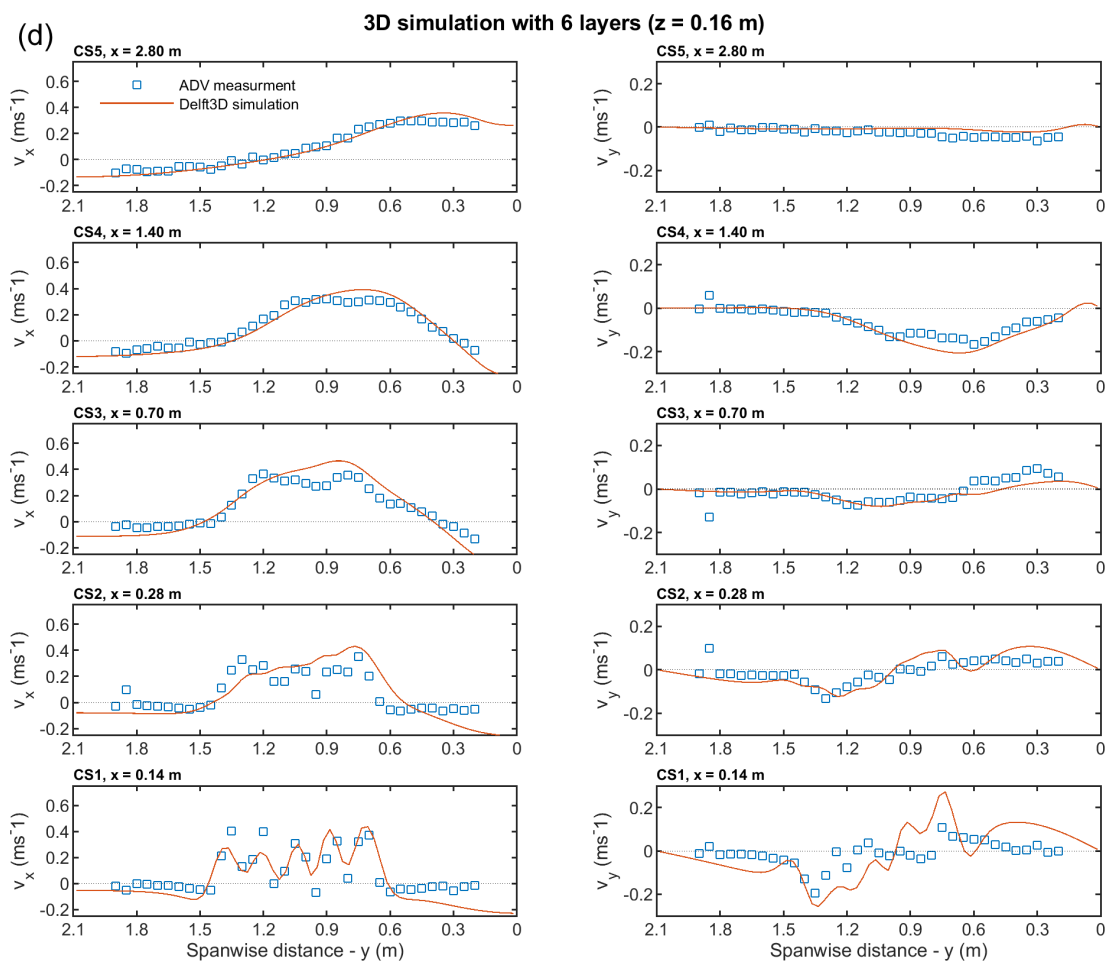


Figure 6.19: Continued from page 13 - Comparison of the velocity profile for THU 1 between laboratory observations and numerical 3D simulation at four depths: (a) 0.04 m, (b) 0.08 m, (c) 0.12 m, and (d) 0.16 m.

Case study THU 2

The plots in Figure 6.20 show the THU 2 axial and lateral velocities from the 3D simulations. At CS1 the 3D model slightly overpredicted the peak velocities of the two jets. Near the bed (Figure 6.20a) and close to the surface (Figure 6.20d), the 3D model slightly overpredicted the axial velocity but predicted a similar magnitude for both jets. At the two levels in between (Figure 6.20b,c) the 3D model overpredicted the right hand jet and underpredicted the left hand jet peak velocity. The lateral velocities of the 3D simulations at CS1 were considerably larger than measured throughout the depth, indicating a formation of stronger eddies in the converging region between the two jets and on the right hand side of the flume. Recirculation on the left hand side of the flume also resulted in larger velocities being predicted, but by a lesser extent than on the opposite side. The stronger eddy on the right hand side was attributed to the Coanda effect, deflecting the jet trajectory towards the right hand side of the flume. The same trend was also observed at CS2 cross-section. At middle locations (Figure 6.20b,c), the 3D results showed an already combined jet deflected slightly towards the right side of the flume, while the jets close to the bed and surface (Figure 6.20a,d) still exhibited two distinct peaks, with an appropriate axial velocity magnitude, but failed to capture the trough between these two jets. After CS3 the 3D complexities of the jet started to diminish gradually and the results showed slightly better predictions, but never reached the same accuracy as for case THU 1 (Figure 6.19).

Chapter 6
Experimental model: barrage in a flume

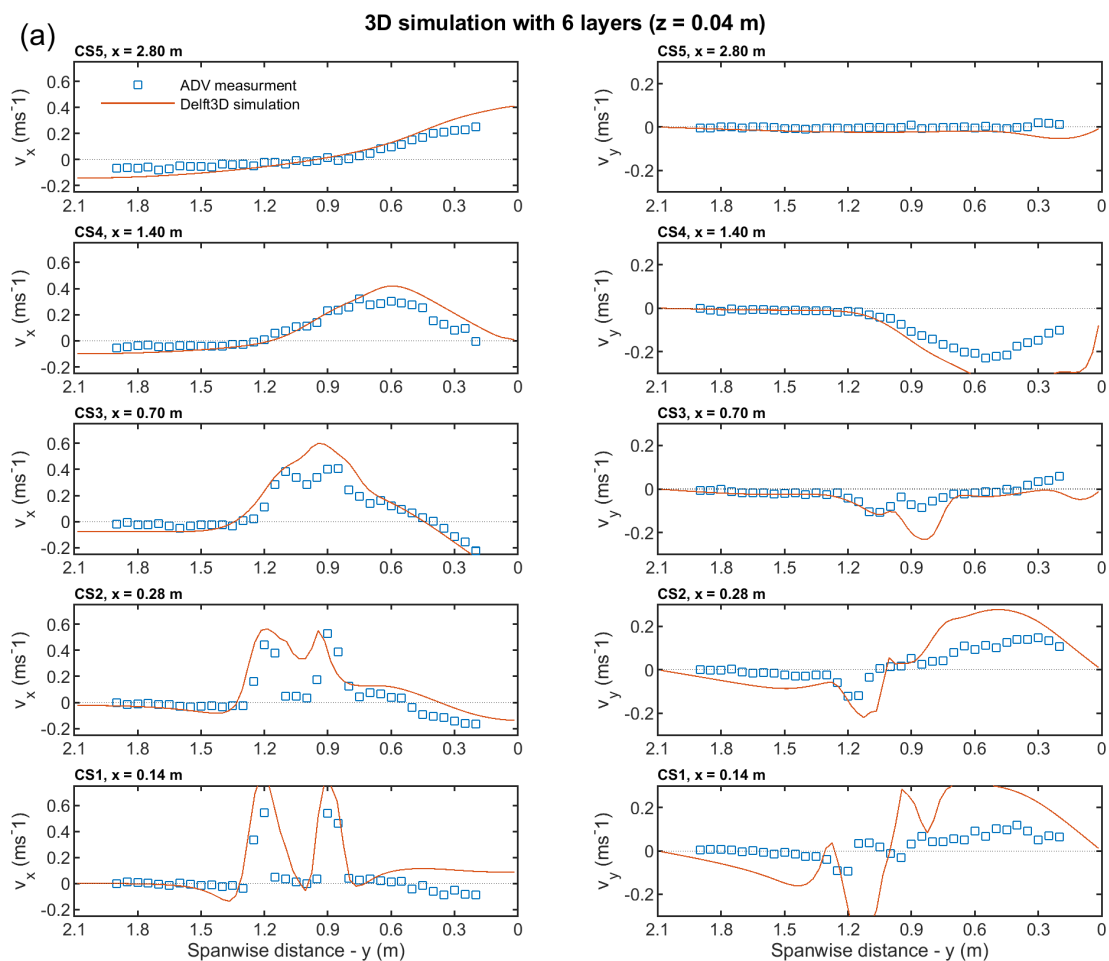


Figure 6.20: Comparison of the velocity profile for THU 2 between laboratory observations and numerical 3D simulation at four depths: (a) 0.04 m, (b) 0.08 m, (c) 0.12 m, and (d) 0.16 m.

Chapter 6
Experimental model: barrage in a flume

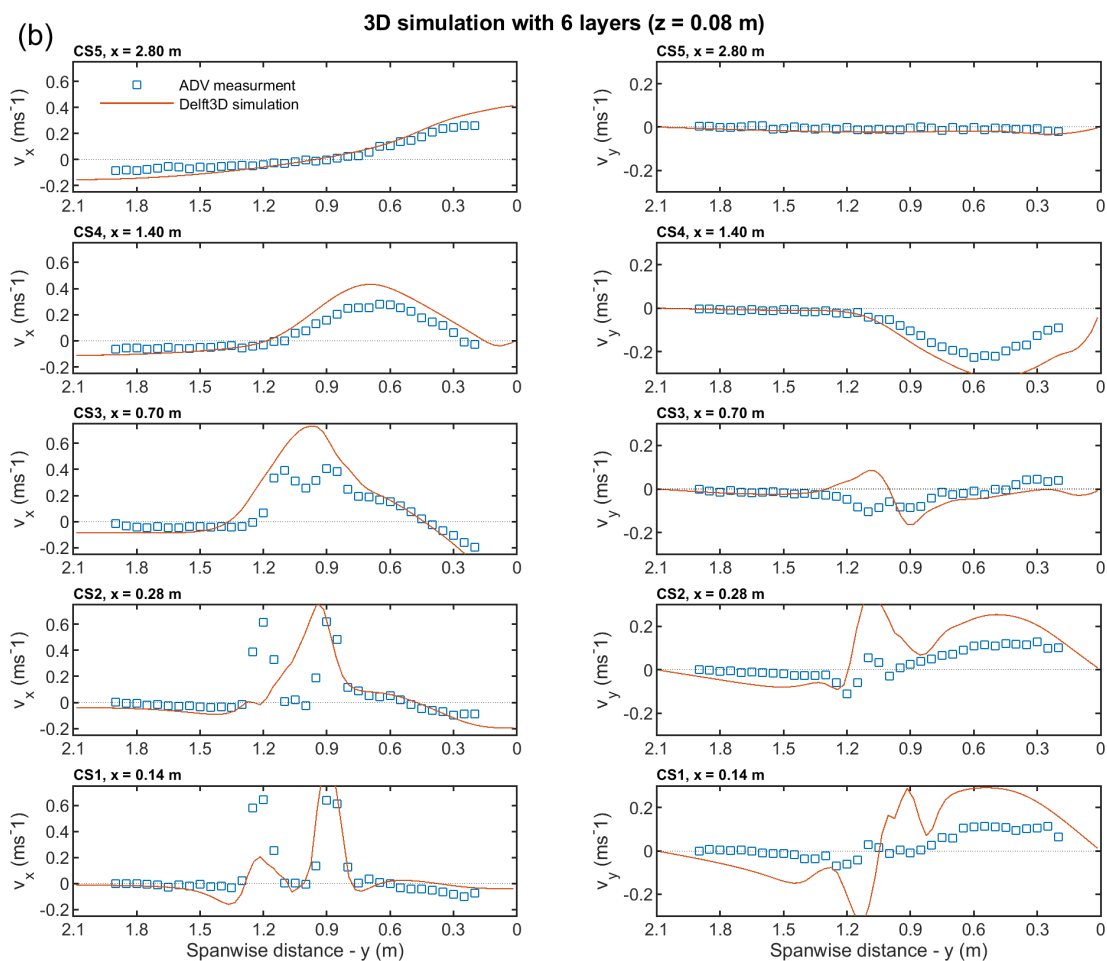


Figure 6.20: Continued from page 190 - Comparison of the velocity profile for THU 2 between laboratory observations and numerical 3D simulation at four depths: (a) 0.04 m, (b) 0.08 m, (c) 0.12 m, and (d) 0.16 m.

Chapter 6
Experimental model: barrage in a flume

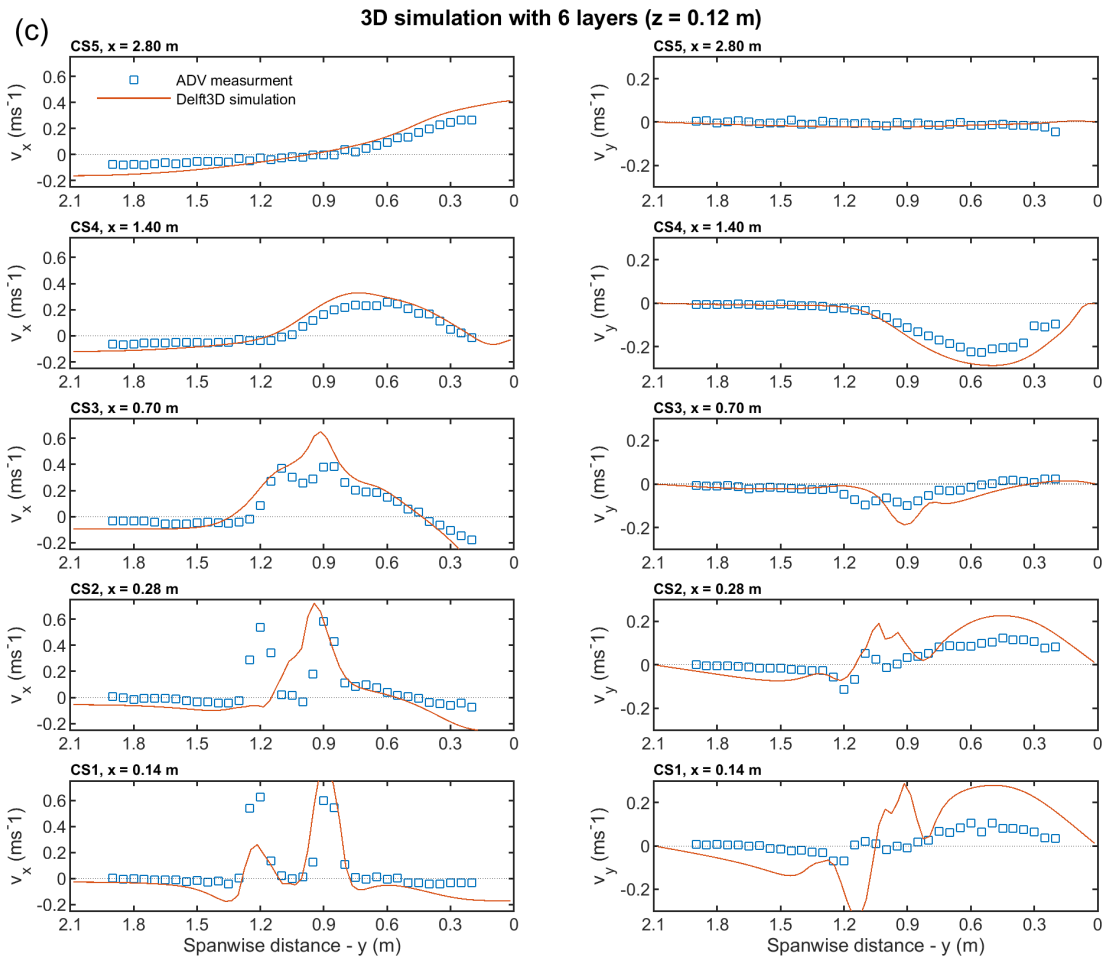


Figure 6.20: Continued from page 190 - Comparison of the velocity profile for THU 2 between laboratory observations and numerical 3D simulation at four depths: (a) 0.04 m, (b) 0.08 m, (c) 0.12 m, and (d) 0.16 m.

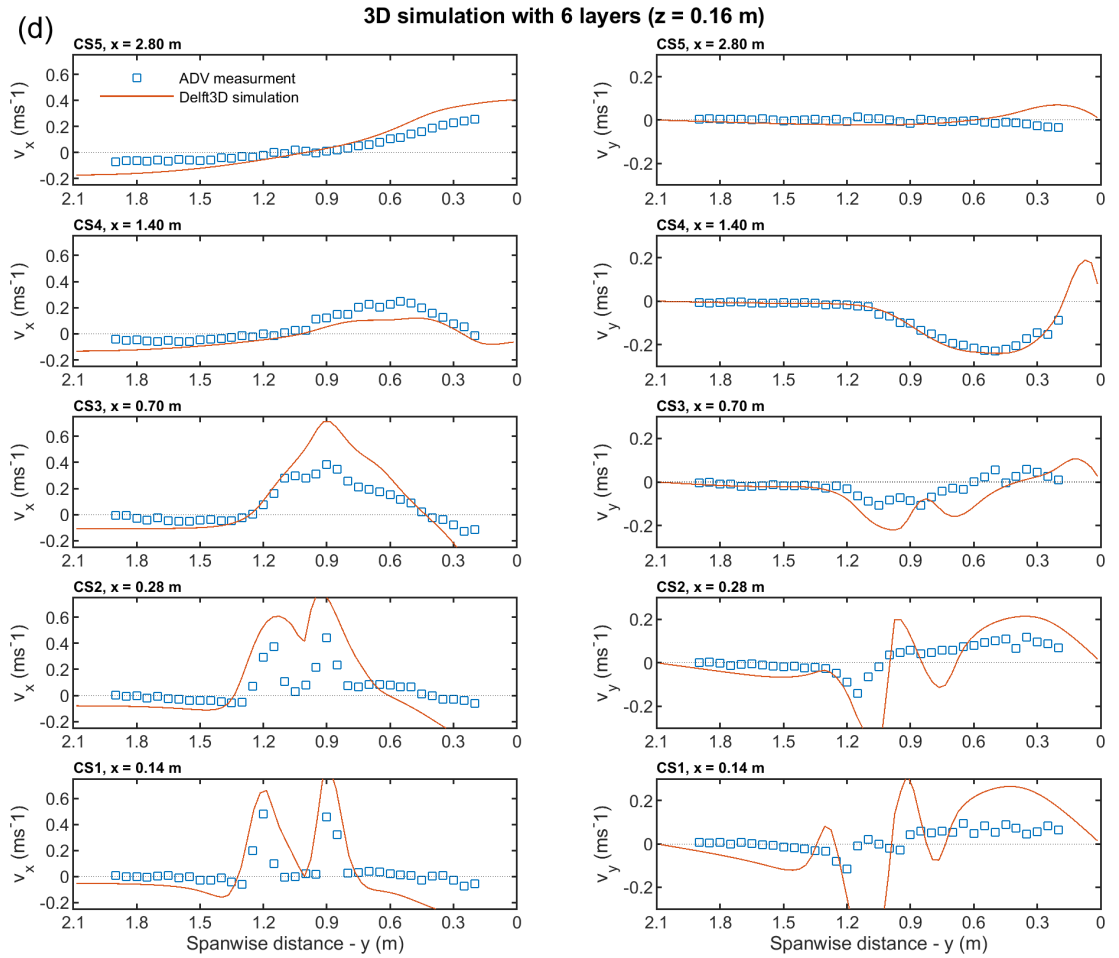


Figure 6.20: Continued from page 190 - Comparison of the velocity profile for THU 2 between laboratory observations and numerical 3D simulation at four depths: (a) 0.04 m, (b) 0.08 m, (c) 0.12 m, and (d) 0.16 m.

Case study THU 3

The plots in Figure 6.21 show the THU 3 axial and lateral velocities for the 3D simulations. Here, similar findings were observed to those reported above for case THU 2. Again, the lateral velocities were larger than measured at all depths, overpredicting the eddies forming between the two jets and on either side of the flume. Due to the Coanda effect, a much stronger eddy was formed on the right hand side of the flume, deflecting the jet trajectory towards the same direction. Because the two jets were spaced further apart than for THU2 a greater distance was required for them to merge. In this case, the 3D model did not accurately replicate the merging of the two jets, showing an even larger discrepancy between the predicted and observed results at locations CS3 and CS4. It was only at CS5 where the results from the 3D simulations replicated the measured values.

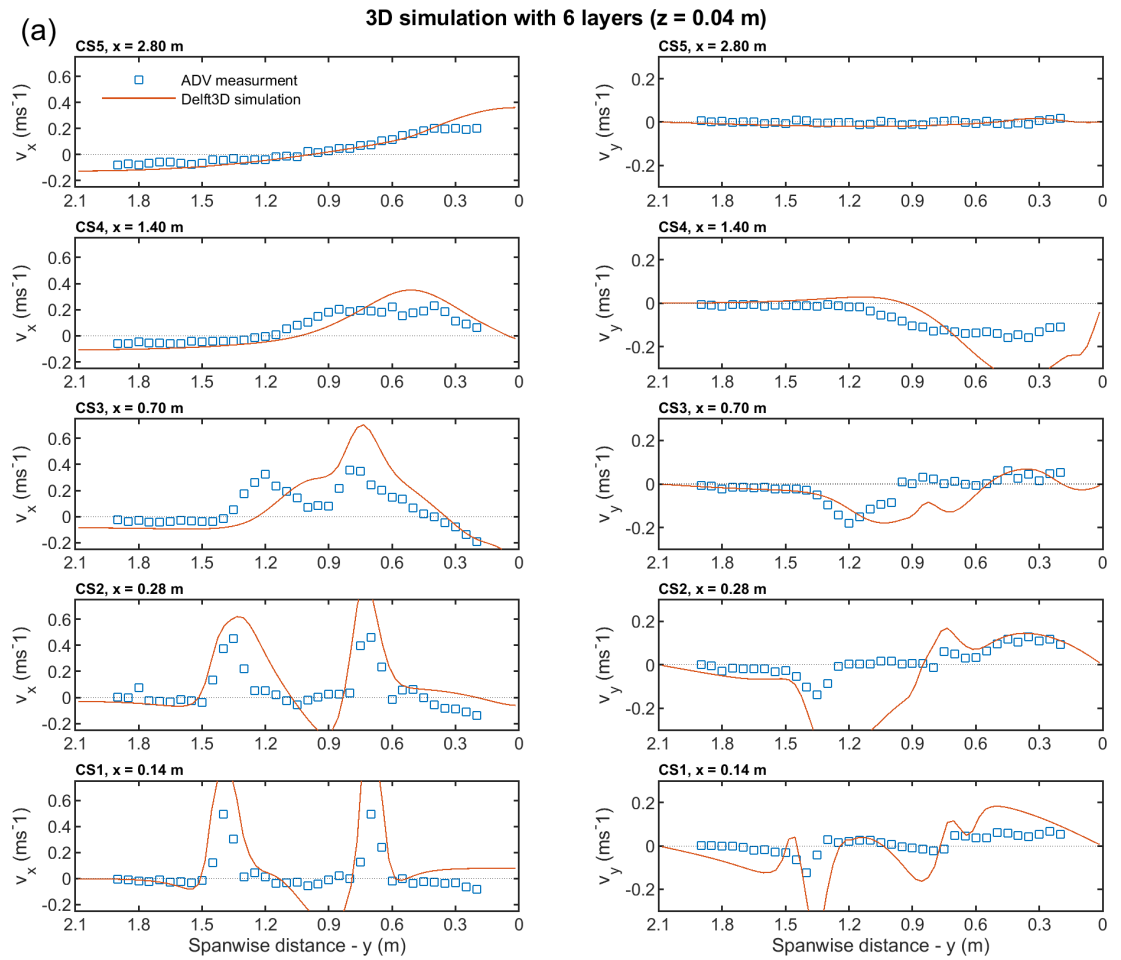


Figure 6.21: Comparison of the velocity profile for THU 3 between laboratory observations and numerical 3D simulation at four depths: (a) 0.04 m, (b) 0.08 m, (c) 0.12 m, and (d) 0.16 m.

Chapter 6
Experimental model: barrage in a flume

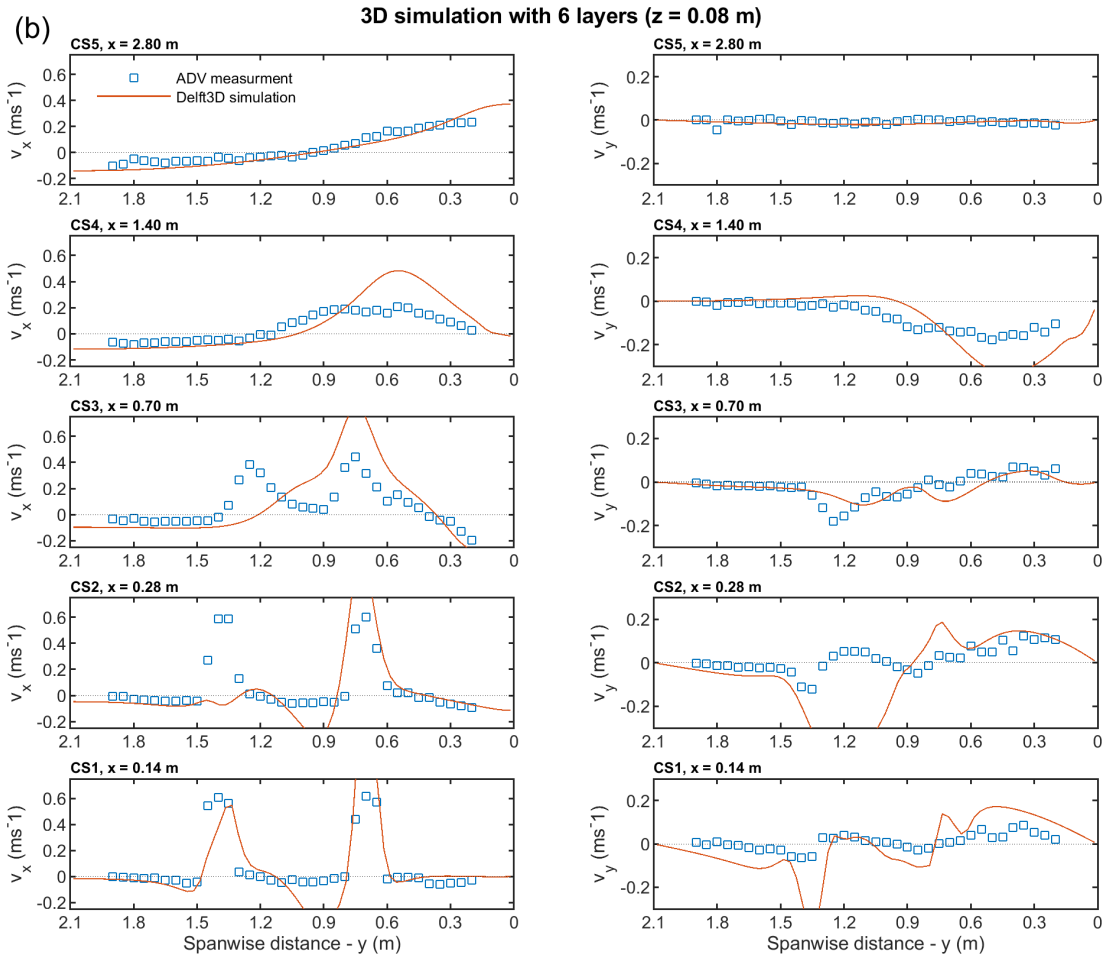


Figure 6.21: Continued from page 195 - Comparison of the velocity profile for THU 3 between laboratory observations and numerical 3D simulation at four depths: (a) 0.04 m, (b) 0.08 m, (c) 0.12 m, and (d) 0.16 m.

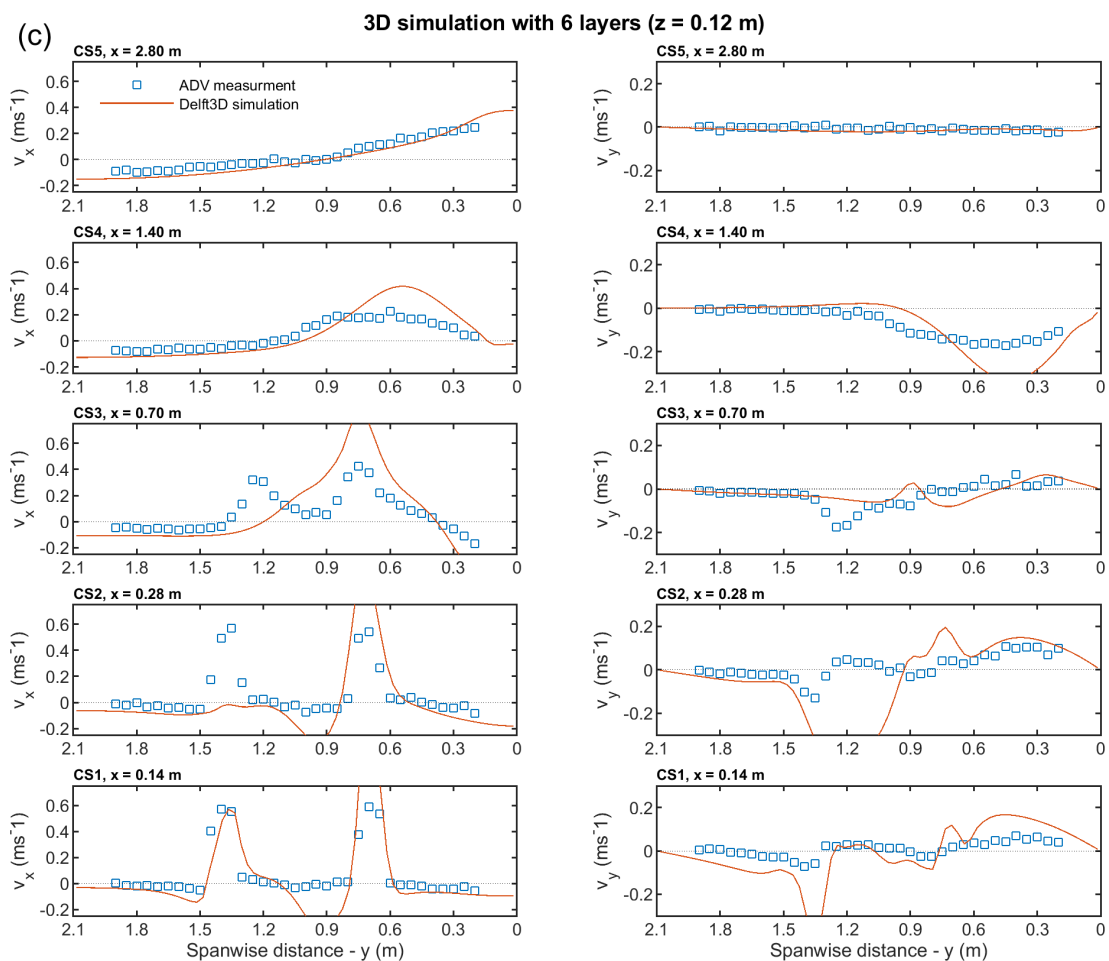


Figure 6.21: Continued from page 195 - Comparison of the velocity profile for THU 3 between laboratory observations and numerical 3D simulation at four depths: (a) 0.04 m, (b) 0.08 m, (c) 0.12 m, and (d) 0.16 m.

Chapter 6
Experimental model: barrage in a flume

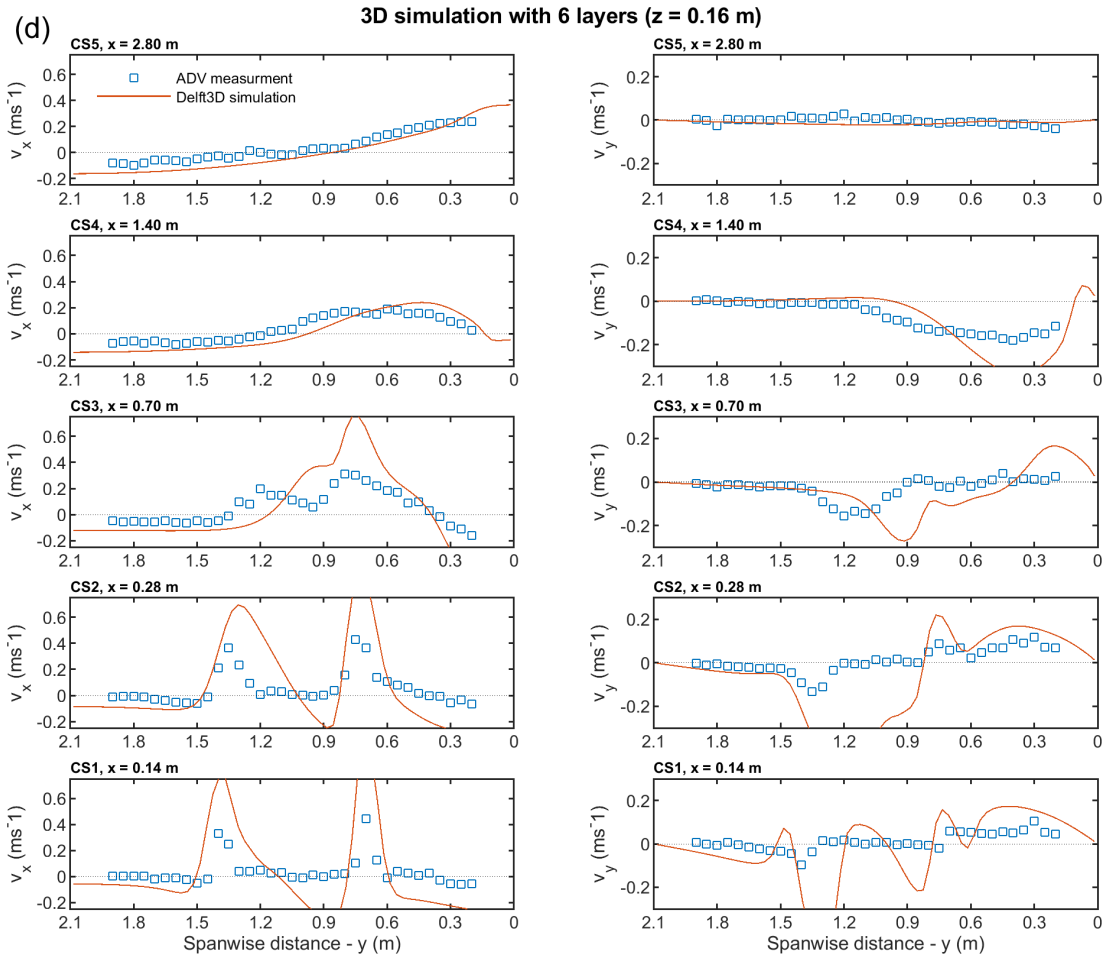


Figure 6.21: Continued from page 195 - Comparison of the velocity profile for THU 3 between laboratory observations and numerical 3D simulation at four depths: (a) 0.04 m, (b) 0.08 m, (c) 0.12 m, and (d) 0.16 m.

6.5.6 Bed shear stress

The magnitude of the bed shear stress is presented as a ratio between the local bed shear stress and a reference stress. The reference stress corresponds to the mean value of the bed shear stress for an empty flume, which was calculated to be 0.0121 N/m² before the barrage was installed. Therefore, a ratio of 1 would mean that the calculated shear stress is of the same magnitude as if there was no barrage in place, with values above one representing the magnification of the reference stress. The local stress was obtained from Delft3D outputs. In the 2D simulations, the local shear stress is assumed to be given by a quadratic friction law including the magnitude of the depth-averaged horizontal velocity, defined by Equation (6.1) (Deltares 2014). For the 3D simulations the same equation is used, but instead of a depth-averaged velocity, the magnitude of the horizontal velocity in the first layer just above the bed is used, defined by Equation (6.2).

$$\bar{\tau}_b = \frac{\rho_0 g \bar{U} |\bar{U}|}{C_{2D}^2} \quad (6.1)$$

$$\bar{\tau}_{b_{3D}} = \frac{\rho_0 g \bar{u}_b |\bar{u}_b|}{C_{3D}^2} \quad (6.2)$$

Where ρ_0 is reference density of water, g is acceleration due to gravity, U is the depth-averaged velocity, u_b is the horizontal velocity in the first layer just above the bed, and C_{2D}^2 and C_{3D}^2 are the 2D- and 3D-Chézy coefficients.

Case study THU 1

Figure 6.22 shows the contours of the bed shear stress ratio for the simulations without the additional momentum conservation term due to the momentum source of the turbines. Just downstream of the barrage, at the five locations where jets enter the domain, the local bed shear stress was 6 times larger than the reference stress. The contours were symmetrical, with a low stress ratio occurring on both sides of the flume. With the addition of the momentum source term in the 2D (Figure 6.23) and 3D (Figure 6.24) simulations, the local stress was visibly increased and the contours followed the right hand deflecting trajectory associated with the Coanda effect. The local shear stress ratio just downstream of the barrage had increased to a factor of 20 in the 2D simulations (Figure 6.23) and a corresponding factor of 35 in the 3D simulations (Figure 6.24). In the merging region of the jets, at CS3, the local stress ratio was increased by up to a factor of 3 for the simulation without the momentum conservation term, a factor 9 for the 2D simulation, and a factor of 22 for the 3D simulation. At CS5 the maximum magnification of the local bed shear stress under the jet was reduced to 2 (w/o momentum), 6 (2D simulations) and remained at 22 (3D simulations). The magnification of the local bed shear stress was a result of the higher velocity of the jets due to the momentum conservation term being included at the discharge locations. The highest ratio followed the centreline of the jets, diminishing across the jets and towards the sides of the flume. In the 3D simulation the jets have attached to the bed of the flume, as was already illustrated in Figure 6.19, which resulted in higher velocities at the layer just above the bed. This meant that the increased ratio appeared over a longer distance compared to the 2D simulation. Consequently, the bed shear stress ratio at CS5 was still above a factor of 20 for the 3D simulation, considerably larger than the factor of 6 predicted from the 2D simulation.

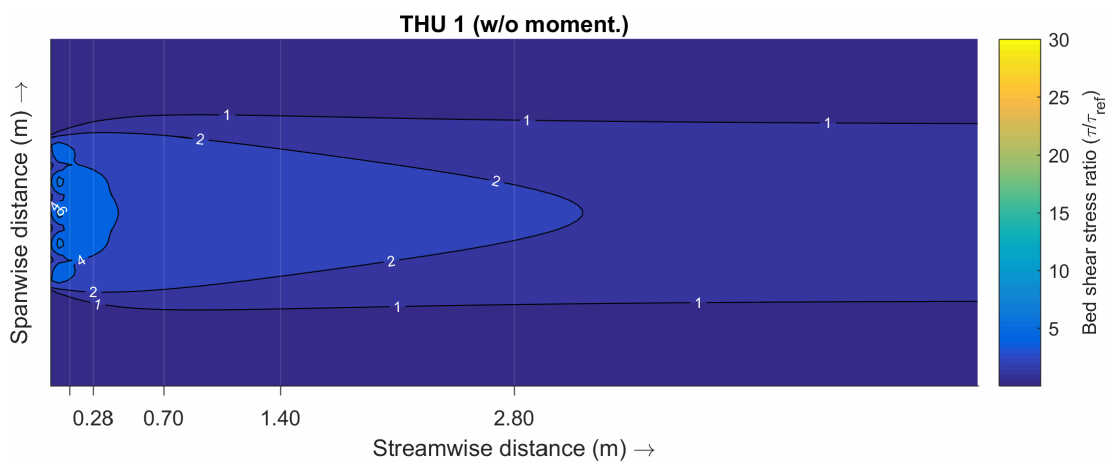


Figure 6.22: Ratio of local bed stress to reference bed stress, “mass-only” simulation, THU 1.

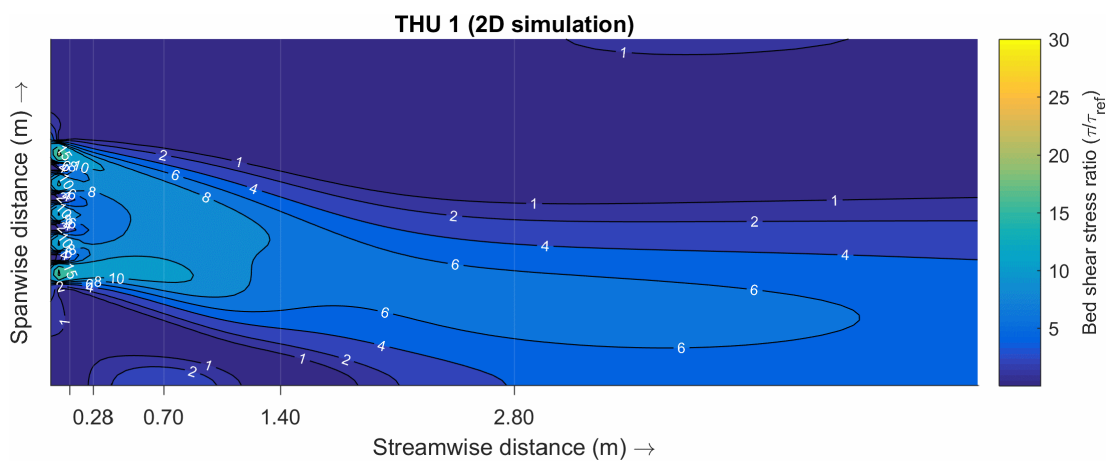


Figure 6.23: Ratio of local bed stress to reference bed stress, 2D with momentum, THU 1.

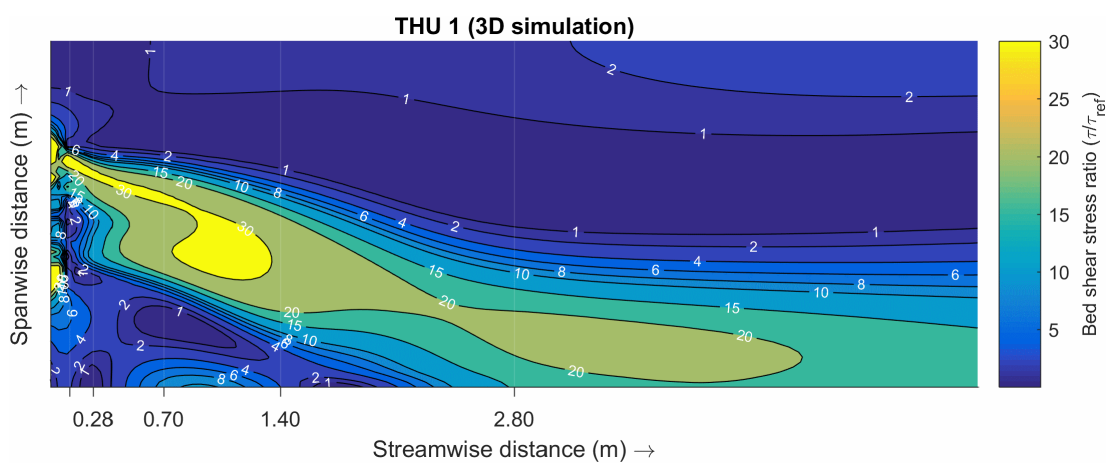


Figure 6.24: Ratio of local bed stress to reference bed stress, 3D with momentum, THU 1.

Case study THU 2

At CS1, i.e. at the location where the two jets enter the domain, the increase in the local shear stress was up to a factor of 12 for the simulations without the momentum conservation term (Figure 6.25) and increased to a factor of 21 in the 2D simulations with the momentum correction term (Figure 6.26) and a factor of 107 in the corresponding 3D simulations (Figure 6.27). In the merging region of the jets, at CS3, the local stress ratio was increased by up to a factor of 5 (w/o momentum), a factor of 12 (2D simulation) and a factor of 75 (3D simulation). At CS5 the maximum increase in the local bed shear stress was reduced to 2 (w/o momentum), 6 (2D simulation) and 23 (3D simulation) respectively.

The main difference from the THU 1 case was that the 3D model (Figure 6.27) showed larger than expected values of the local bed shear stress ratio close to the barrage, especially in the converging and merging regions of the jets. The values were expected to be higher than in 2D simulations, as the horizontal computational layers of the 3D model allowed for a more realistic vertical velocity profile, with higher velocities in the lowest layer due to the attachment of the jets to the bed of the flume. However, as also observed in velocity results (Figure 6.20a), the 3D model was found to be unreliable very close to the barrage for the THU 2 case, in that it overpredicted the axial and lateral velocities and failed to capture correctly the flow complexities of the merging jets. Because bed shear is calculated directly from the velocity, the resulting increase by more than 100 just at the exit from the barrage was thought to be exaggerated. However, this was limited to further away from the barrage, i.e. beyond CS3, the results were not exaggerated and showed a pattern similar to the THU 1 case.

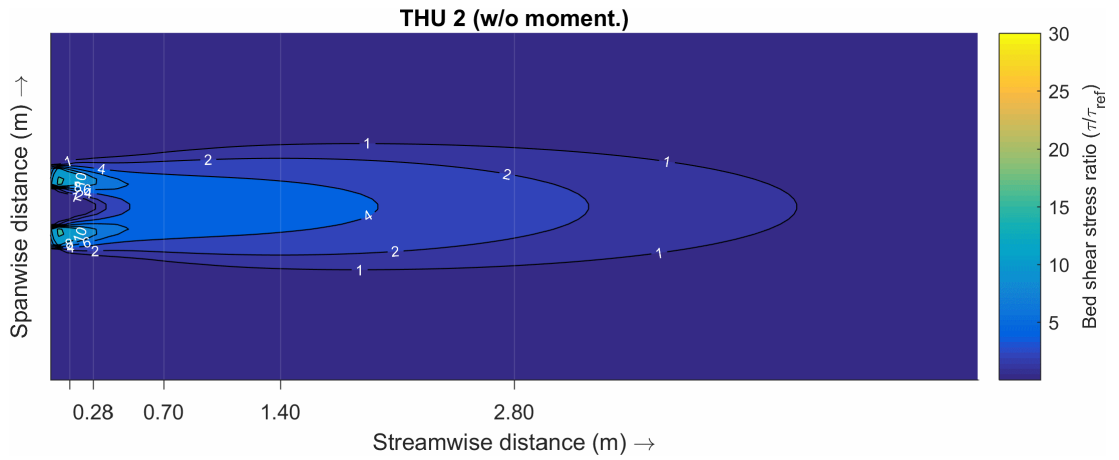


Figure 6.25: Ratio of local bed stress to reference bed stress, “mass-only” simulation, THU 2.

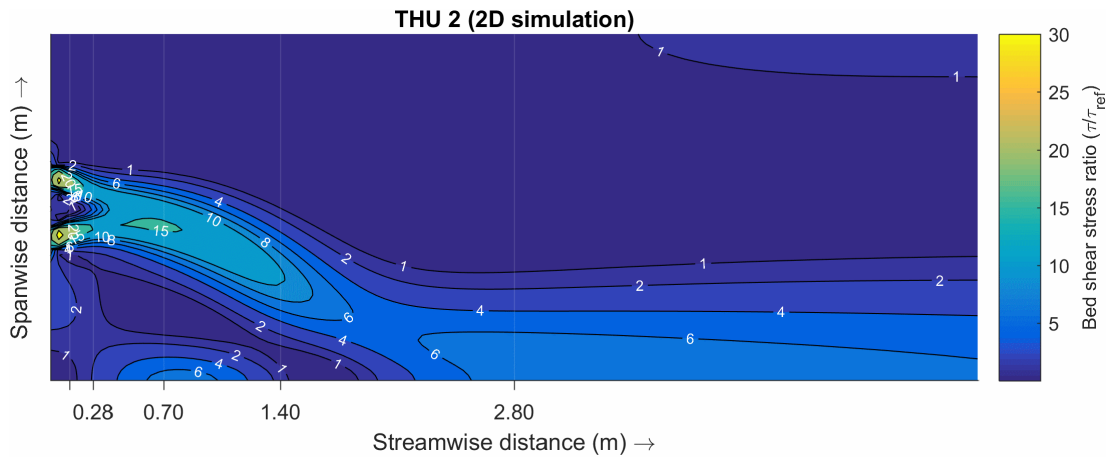


Figure 6.26: Ratio of local bed stress to reference bed stress, 2D with momentum, THU 2.

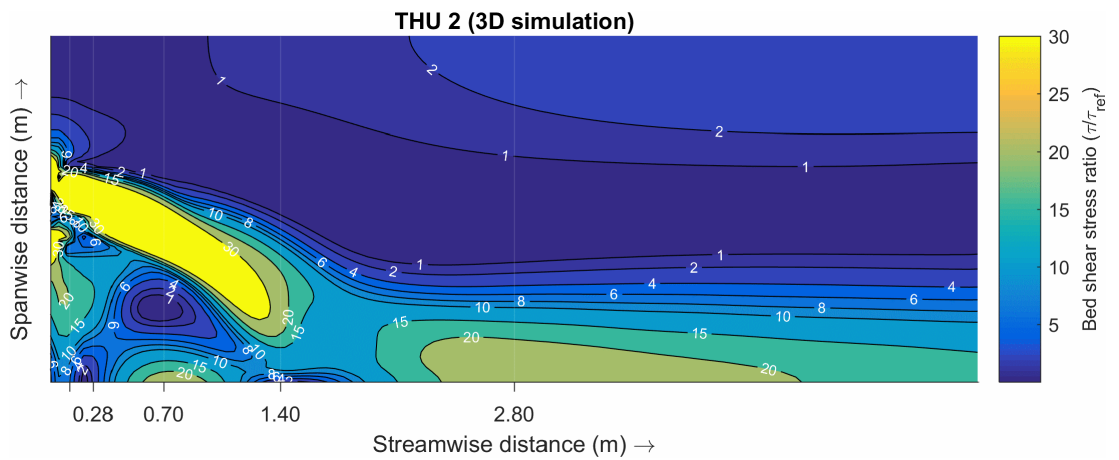


Figure 6.27: Ratio of local bed stress to reference bed stress, 3D with momentum, THU 2.

Case study THU 3

At CS1, i.e. at the location where the two jets enter the domain, the bed stress ratio of the local shear stress was up to a factor 12 in the simulations without the momentum conservation term being included (Figure 6.28) and increased to a factor of 21 in the 2D simulations (Figure 6.29) and a factor of 107 in the 3D simulations (Figure 6.30). In the merging region of the jets, i.e. between CS3 and CS4, the local stress ratio was increased to a factor of 3 (w/o momentum) and a factor of 12 (2D simulations). At CS5 the maximum increase in the local bed shear stress ratio was reduced to 1 (w/o momentum) and 6 (2D simulations) respectively.

The local bed shear stress ratio for the simulation without the momentum conservation (Figure 6.28) and the 2D simulation (Figure 6.29) was very similar to the results observed in the THU 2 case. Because the jets were separated by a longer distance, the converging region was visibly longer and the interaction between the jets did not happen before reaching the cross-section CS3. Consequently, there was little magnification of the bed shear stress in the recirculation zone between the jets. Compared to THU 2, the merging region has moved further upstream, beyond CS3, and that was where the bed shear stress was magnified. Even so, the THU 3 case still exhibited similar values in the 2D simulation as THU 2 case. Similar were also the inaccuracies of the 3D simulation in the vicinity of the barrage. As observed in Figure 6.21a, the inaccuracies in 3D velocity results at CS1 were even worse for THU 3 case when compared to THU 2. Again, the bed shear stress ratio values were larger (Figure 6.30), exceeding a bed stress ratio of 100 at the barrage exit.

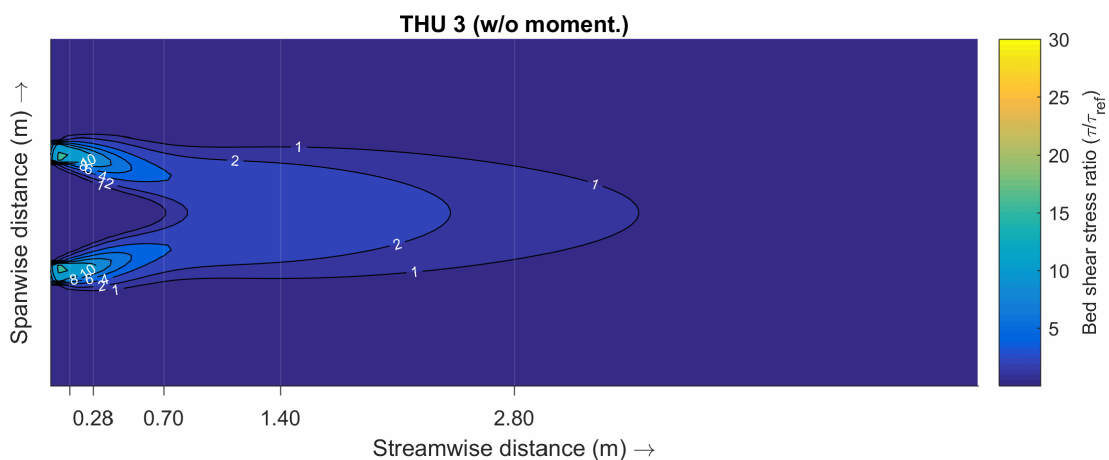


Figure 6.28: Ratio of local bed stress to reference bed stress, “mass-only” simulation, THU 3.

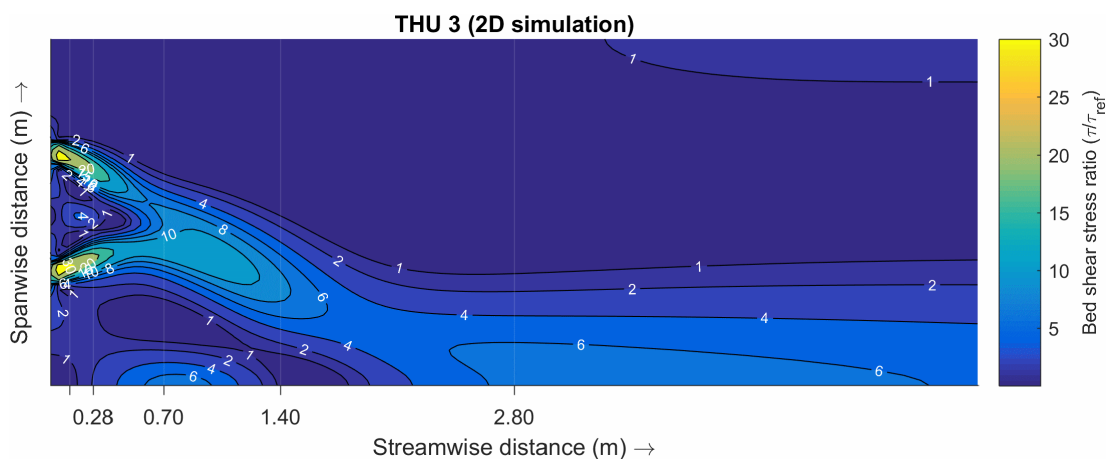


Figure 6.29: Ratio of local bed stress to reference bed stress, 2D with momentum, THU 3.

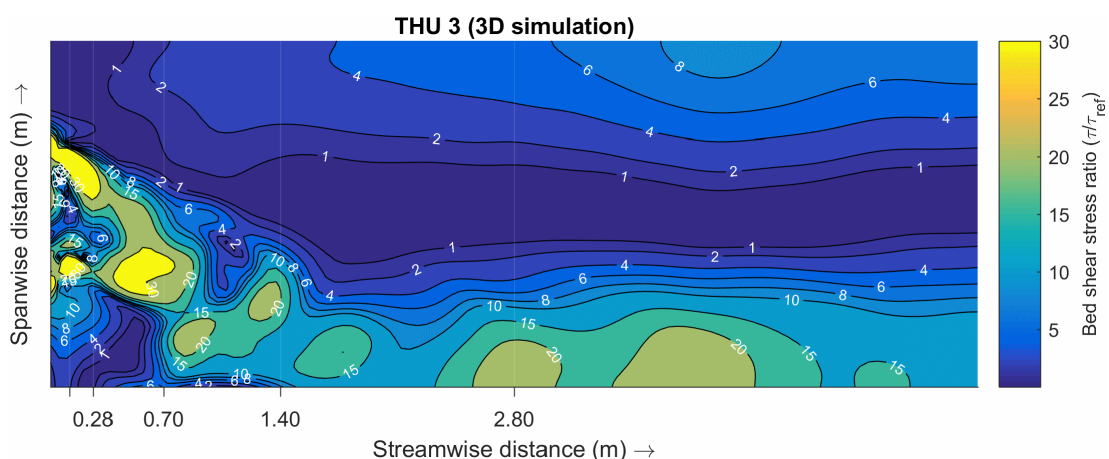


Figure 6.30: Ratio of local bed stress to reference bed stress, 3D with momentum, THU 3.

6.6 Summary

The third key research objective of this study was to investigate the appropriateness of the developed momentum conservation method for modelling complex flow patterns that occur at the discharge from TRSs. In the first instance a series of laboratory experiments were performed to obtain observation data, with which the performance of the developed numerical model could be tested. Three different experimental configurations were conducted, namely: (i) THU 1, where five densely spaced draft tubes were active, to generate a flow pattern most resembling the discharge conditions out of an actual TRS; (ii) THU 2, where only two draft tubes were left open, separated by the width of one tube; and (iii) THU 3, where the two draft tubes were separated even further by the width of three tubes. For each of the experimental case studies, three separate numerical model simulations were performed, comparing: (i) the depth-averaged model without any momentum correction source terms, (ii) the 2D model with momentum correction source terms, and (iii) the 3D model, again with the added momentum conservation source terms.

In comparing the depth-averaged simulations, both with and without the momentum conservation terms, it was confirmed that it is essential to conserve momentum through additional source terms when modelling the discharge through a TRS. The jets in the simulations without the momentum conservation term achieved only about 50 per cent of the measured velocity. At the same time, they were not able to replicate the distinct Coanda effect, where the jets deflect towards the side wall and stay attached throughout the flume length. The simulations with the momentum conservation source terms perfectly replicated the effect, with the combined jets deflecting to the right hand side of the flume for all three experimental case studies. The simulations without the momentum conservation source terms instead consistently predicted a perfectly symmetrical flow structure.

In the second set of simulations was undertaken to compare the predicted velocities for the momentum conservation method included in the 2D depth-averaged model and the 3D model with 6 horizontal layers. It is worth mentioning that Delft3D does not utilise a full RANS 3D model, but instead uses a vertical turbulence closure model to account for vertical momentum transfer between the horizontal layers. The comparisons showed that the 3D results only showed an improvement over the 2D simulation results for the THU 1 case, where the draft tubes were densely spaced and the jets merged very quickly upon exiting the barrage. For cases THU 2 and THU 3 only two jets entered the domain, and a larger spacing between the two resulted in the formation of distinct counter rotating eddies in the converging region between the jets. The 3D model has proved to be unable to replicate this complex flow pattern at selected resolution. In this case, a model with a finer grid resolution needs to be applied to produce more accurate results or if possible, a full 3D RANS model that could better capture the 3D complexities of the converging jets. However, in the case of a TRS, the turbines are normally densely spaced next to each other in the same way as the draft tubes in THU 1, which therefore makes the 3D hydrostatic model used herein more suitable for predicting the jets from a TRS. The 2D models managed to produce better overall predictions across all three experimental case studies. However, in all cases the model underpredicted the velocity magnitude, especially in the first few cross-sections just downstream of the barrage. This makes the 2D model a valuable tool in situations where the local impacts of the TRS are not of so much concern, i.e. where the velocity distribution at a very small distance from the barrage is less important. However, the correct velocity distribution from a 3D model will be vital in near-field studies where scour, deposition, sediment transport, and water quality inputs are important.

Bed shear stress is instrumental in the sediment transfer processes, governing the calculations of scour and deposition. The results of the model without the momentum conservation term have considerably underestimated the magnitude of local bed shear stress in the region of the turbines. For THU 1 case, the local bed shear stress was increased by up to a factor of 20 (2D simulations) and 35 (3D simulations) when the

momentum conservation term was included. The increase in the local bed shear stress as a result of including the momentum conservation term was already substantial in the 2D model. However, it increased even further in the 3D model. The 3D effects were clearly substantial, illustrating the importance of a 3D model for estimation of sediment transport associated with the operation of a TRS.

Chapter 7

Model application: Swansea Bay tidal lagoon

7.1 Introduction

This chapter presents the application of the developed model on the case study of the proposed Swansea Bay tidal lagoon. Previous chapters showed the development stages of the model. The Severn Barrage case study in Chapter 5 was used to validate the methodology for simulating TRS in Delft3D and a laboratory experiment in Chapter 6 was used to validate the method for conservation of momentum in turbine discharge. These modifications were now combined and applied to the regional model of a proposed tidal lagoon in Swansea Bay. The smaller scale of the scheme meant that the boundary conditions were not likely to be affected and the study could avoid employing the extended domain model. This drastically reduced the computational time of the simulations. Because far-field impacts were not prevalent, the study focused more on the hydrodynamics in the locality of the lagoon, with a particular interest to the impact of momentum treatment on the formation of the jet at the turbine exit. The study analysed two different types of the velocity distribution of the discharged water, both in 2D and 3D configuration, and compared them to the conventional (simplified) method where the momentum term is ignored. The methodology for this study is presented in Section 7.2, explaining the different simulation scenarios, providing a detailed description of the Swansea Bay tidal lagoon scheme and describing the model set-up. Section 7.3 provides the validation of the hydrodynamic conditions in the domain pre-inclusion of the

barrage. Section 7.4 presents the comparison and analysis of the results. Finally, Section 7.5 gives a summary of the main findings.

7.2 Methodology

The last key objective of this research study was to assess the impacts of the developed methods on the performance of a hydrodynamic model on a regional scale. Using the proposed Swansea Bay tidal lagoon as a case study, this chapter focuses on the treatment of momentum associated with the jets exiting the lagoon and investigates its impacts on the hydrodynamic predictions. Adding to the developed numerical techniques that were already introduced in Chapter 5, the study also adopted the novel approach to conserving the momentum through hydraulic structures, as described in Section 4.5 and validated through an experimental study in Chapter 6.

A high-resolution 2D modelling approach is commonly considered suitable for a regional scale study of tidal energy projects in estuaries (Angeloudis et al. 2016b). Due to the modifications to the momentum treatment of the turbine discharge, an increase in the flow complexity was expected in the vicinity of the lagoon that would be unlikely to be captured using conventional depth-averaged models. Therefore, an additional 3D model with five horizontal layers was also implemented in this study. The vertical dimension was modelled by splitting the domain proportionally into five layers, where each layer was still considered depth-averaged. The horizontal velocities of adjacent layers were coupled by the vertical advection and the vertical viscosity term (Deltares 2014). For the calculation of the vertical turbulent velocity and eddy diffusivity, a k - ϵ turbulence model was used, which included a second-order turbulence closure model (Launder and Spalding 1974). The new 3D model retained the same resolution of the horizontal grid from the original 2D model as well as all other attributes, such as boundary conditions, bathymetry, bottom roughness etc. Five different model revisions, including different representations of the turbine, were implemented for this study, as explained below and summarised in Table 7.1. Firstly, a 2D model simulation with no modifications to the

momentum treatment (SBL1) was set up to act as a baseline for the subsequent model set-ups. The other four scenarios included the implementation of two different velocity distributions for the exiting jet, for 2D and 3D models. These velocity distribution scenarios are summarised below and are shown in Figure 7.2.

a) Realistic velocity distribution

As illustrated in Figure 7.1, horizontal bulb turbines are designed with a draft tube in the shape of a diffuser behind the turbine runner. The role of the draft tube is to minimise head losses and increase the efficiency of the turbine, by increasing the static pressure while simultaneously decreasing the velocity of the exiting flow (Gubin 1973). The shape of the velocity profile was acquired from the experimental work by Wilhelm et al. (2016b) and was distributed over the square-shaped area of the diffuser. For the case of the 5-layer model, this velocity was equally divided amongst the middle three layers as shown in Figure 7.2. The velocity for momentum conservation in Equation (4.15) was therefore calculated using the square-shaped area at the diffuser exit (A_{T1}) as shown in Figure 7.1. This velocity distribution has been applied to scenarios SBL 2 and SBL 4 (Table 7.1).

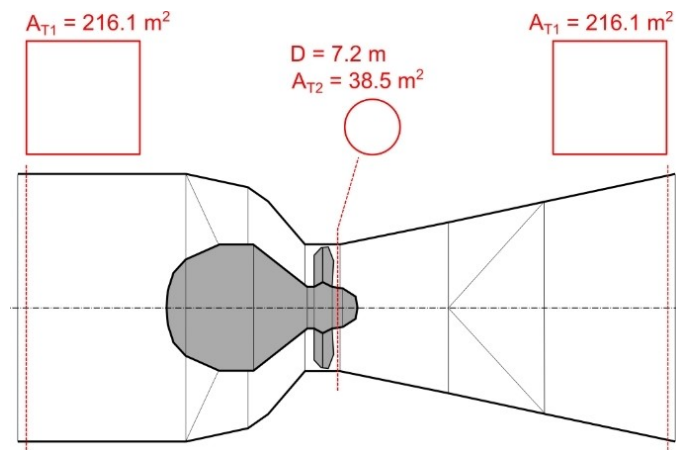


Figure 7.1: Turbine cross-section – the flow-through area at the duct entrance and exit is rectangular and it transitions to a smaller circular shape in the middle at the location of the turbine runner.

b) Simplified velocity distribution

In this case, the velocity stays concentrated in a narrow jet assuming the shape of a bell curve as illustrated in Figure 7.2. The discharge was applied to a single horizontal layer that was located at the same location as the vertical position of the turbine's centreline and the energy loss due to the expansion of the flow through the diffuser was ignored. The velocity for momentum conservation in Equation (4.15) was calculated using the turbine flow-through area at the runner (A_{T2}) as shown in Figure 7.1. This velocity distribution has been applied to scenarios SBL 3 and SBL 5 (Table 7.1).

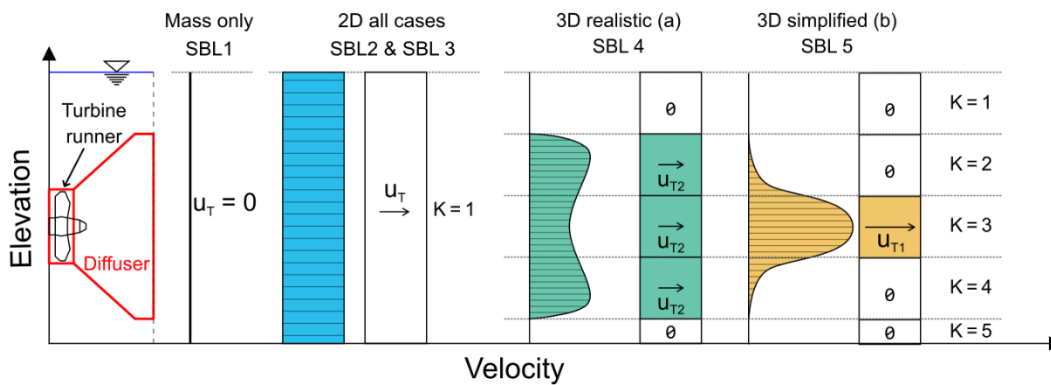


Figure 7.2: Representation of velocity distribution in the numerical model for a 2D and 3D configuration.

Table 7.1: Summary of the five different scenarios investigated in this study.

Dimension	2D			3D	
Simulation Run	SBL1	SBL2	SBL3	SBL4	SBL5
Momentum conservation	No	Yes	Yes	Yes	Yes
Velocity distribution	-	(a) Diffuser	(b) Simplified	(a) Diffuser	(b) Simplified
A_T (m ²)	-	A_{T1} 216.1	A_{T2} 38.5	A_{T1} 216.1	A_{T2} 38.5

7.2.1 Tidal lagoon scheme description

Tidal lagoons are conceptually a novel adaptation of an existing and proven technology of tidal barrages (Waters and Aggidis 2016a). Instead of spanning the entire width of an estuary, the lagoon is created by constructing an embankment in a horseshoe shape attached to the coastline. In the same way as a barrage, the lagoon takes advantage of the large tidal amplitude to create a head difference across the structure that drives flow through the turbines. Swansea Bay is potentially a suitable site for deployment of such a scheme due to its location on the north bank of the Bristol Channel which, together with the Severn Estuary, represents one of the largest tidal range resources in Europe (DECC 2010).

A tidal lagoon in Swansea Bay was first proposed more than a decade ago (Petley and Aggidis 2016). In 2015, the project received a development consent order (DCO) from the UK government (The Planning Inspectorate 2015) and in 2016 a backing from an independent review, namely the Hendry Review of Tidal Lagoons, commissioned by the UK government (Hendry 2016). However, the UK government has recently withdrawn its support for the project and put the project indefinitely on hold, with the main concern being the cost of electricity compared to alternatives, such as wind farms and nuclear power (Guardian Media Group 2018).

Since the initiation of the project, several alternative proposals with different lagoon layouts and turbine capacities were considered. The shape and layout of the structure used in this study were taken from the latest proposal put forward by Tidal Lagoon Plc (Tidal Lagoon Plc 2018) and is shown in Figure 7.3.



Figure 7.3: The distinctive horseshoe shape of the current lagoon proposal and its location in the Swansea Bay (image courtesy of Tidal Lagoon Plc).

If built, Swansea Bay tidal lagoon would become the largest TRS to-date and the first of its kind in the world. The scheme proposes a 9.5 km long embankment that would form an impoundment, with a surface area of 11.5 km² (Tidal Lagoon Plc 2016). The proposed power plant would have an installed capacity of 320 MW, providing power to over 155,000 homes (Hendry 2016). This would be achieved through a set of sixteen bulb turbines, each with a diameter of 7.2 m and an output power of 20 MW, with an additional 800 m² of sluice gates to aid with the maximisation of the head difference. This design allows for a two-way operation, where power is produced during both ebb and flood tides. The starting head for generating was designed to be 2.5 m and a minimum head was designed to be 1.5 m. The same characteristics were also used in other recent studies (Angeloudis et al. 2016b; Petley and Aggidis 2016; Angeloudis and Falconer 2017). A summary of the scheme's specifications is outlined in Table 7.2.

Table 7.2: Specifications of the Swansea Bay lagoon scheme used in this study.

Swansea Bay tidal lagoon specifications	
Starting head (m)	2.5
Minimum head (m)	1.5
Wall length (km)	9.5
Impounded area (km ²)	11.5
Turbine number	16
Turbine diameter (m)	7.2
Turbine capacity (MW)	20
Total capacity (MW)	320
Combined sluice gate area (m ²)	800

7.2.2 Numerical model set-up

The tidal flows in Swansea Bay have been extensively studied (Uncles 1984; Falconer et al. 2009; Ahmadian et al. 2010a; Xia et al. 2010a; Angeloudis et al. 2016b). The hydrodynamics in the region have been shown to be highly complex due to the exceptional tidal range, the complex land boundary and the highly variable gradients of the seabed elevations (Xia et al. 2010a). However, the estuary was found to be well-mixed with no evidence of stratification, suggesting that natural flow conditions are primarily two-dimensional (Uncles 1984). Usually, a high-resolution 2D model would be considered suitable for such a study. A regional scale model covering the Severn Estuary and Bristol Channel was constructed in order to fully model the lagoon. This extent of the model was selected to ensure an appropriate location for the boundaries, enabling the hydrodynamic processes within the area of interest to be captured.

A rectangular, curvilinear grid with a variable mesh resolution was employed to increase the efficiency by reducing the mesh size only in the areas of interest (Figure 7.4). The grid resolution in and around the lagoon was therefore relatively large at 30 m x 30 m while retaining a coarser mesh size of 500 m x 500 m at the edge of the domain. An extended domain model (continental shelf model) was also used during the validation

Chapter 7

Model application: Swansea Bay tidal lagoon

process to determine whether boundary conditions could be affected by the lagoon operation.



Figure 7.4: Domain of the model, overlaid with the computational grid.

The seaward boundary was located at the entrance to the Bristol Channel (Figure 7.4), which stretched from Heartland Point in south-west England, to the south-west tip of Pembrokeshire in Wales. The open boundary condition was set up as a water elevation time series obtained from the National Oceanography Centre (NOC) Continental Shelf Model (CS3) (The National Oceanography Centre 2018). The predictions from the CS3 model are based on up to 50 tidal harmonic constituents (M_2 , S_2 , N_2 , etc.) and the resulting water levels are separated into (i) tidal only results and (ii) residual surge results. Only the tidal component was used for the construction of the boundary condition time series, which covered a full neap-spring tidal cycle between 19 January and 2 February 2012 in 1 hour intervals, as illustrated in Figure 7.5.

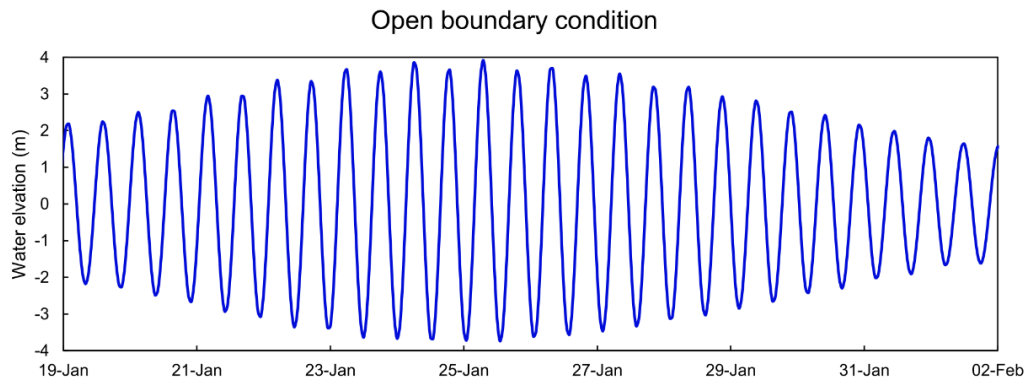


Figure 7.5: Water elevation time-series at the open boundary for a full neap-spring tidal cycle.

The bathymetry for the model was obtained from EDINA Digimap service. The original data was relative to Lowest Astronomic Tide (LAT)/Chart Datum (CD) on a 1 arc-second by 1 arc-second grid (Seazone 2013). The data was converted to the Mean Sea Level (MSL) by subtracting the differences between CD and MSL obtained from the Severn Estuary, Cornwall and Devon coastal charts, which were interpolated to the EDINA grid. Finally, the bathymetry relative to MSL was interpolated onto the Severn Estuary grid used in this model. The bathymetry of the model is shown in Figure 7.6.

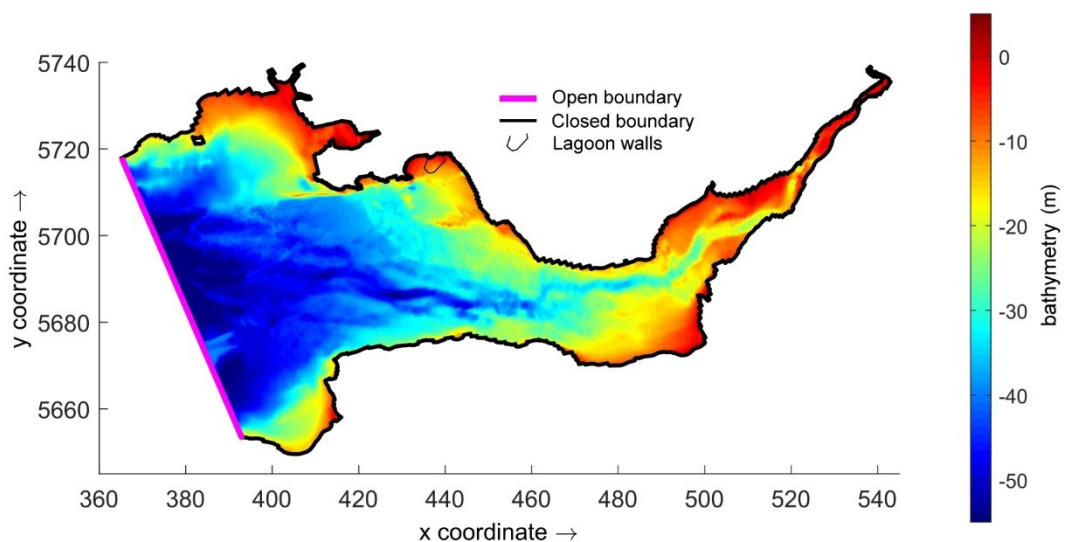


Figure 7.6: Bathymetry of the numerical model, showing the lagoon and domain boundaries.

For simplicity, the Manning's n was set to a constant value across the entire domain. The model could be further improved by using more complex formulations of the roughness coefficient related to the spatial distribution of bed characteristics. However, this was considered beyond the immediate scope of this study given that the focus has been on demonstrating the relative impacts of the momentum conservation method on the jets and wakes exiting the turbines and with the general bed characteristics across the computational domain being fairly uniform and constituting sand and generally smooth bed slope and morphological changes. It was therefore assumed that spatial changes in the Manning's roughness coefficient (without appropriate data) would have little impact on the main thrust of this study, which was to assess the impact of including improved momentum conservation characteristics as potential energy is converted to kinetic energy through the turbines and sluice gates.

All simulations used the same time step of 3 seconds, which was selected to satisfy the CFL condition. The total CPU time for simulating the entire 14-day neap-spring tidal cycle was 7 hrs for the 2D model and 48 hrs for the 3D model, running on a desktop PC with 3.60 GHz Intel® Core™ i7 series CPU.

7.2.3 Far-field impacts

Prior to the validation of the hydrodynamic conditions, the continental shelf (CS) model was used to determine whether the operation of the lagoon would affect the boundary conditions of a smaller model in a similar way as the Severn barrage did in Figure 5.16. The CS model was run for the baseline scenario (SBL1) and compared to the CS run without the lagoon. Figure 7.7 shows a comparison between the maximum water levels predicted by the two models. It can be clearly seen that the impacts of the lagoon alone are negligible comparing to the impacts caused by the barrage. This was to be expected as Swansea Bay lagoon displaces significantly less water with its impoundment surface area of 11.5 km², compared to 573 km² impounded by the Severn Barrage. The only changes to the water level regime were recorded in the Swansea Bay and inside the

lagoon itself, confirming that the CS model is unnecessary for the simulations of this scheme. All the consequent simulation runs were performed only using the Severn Estuary and Bristol Channel model.

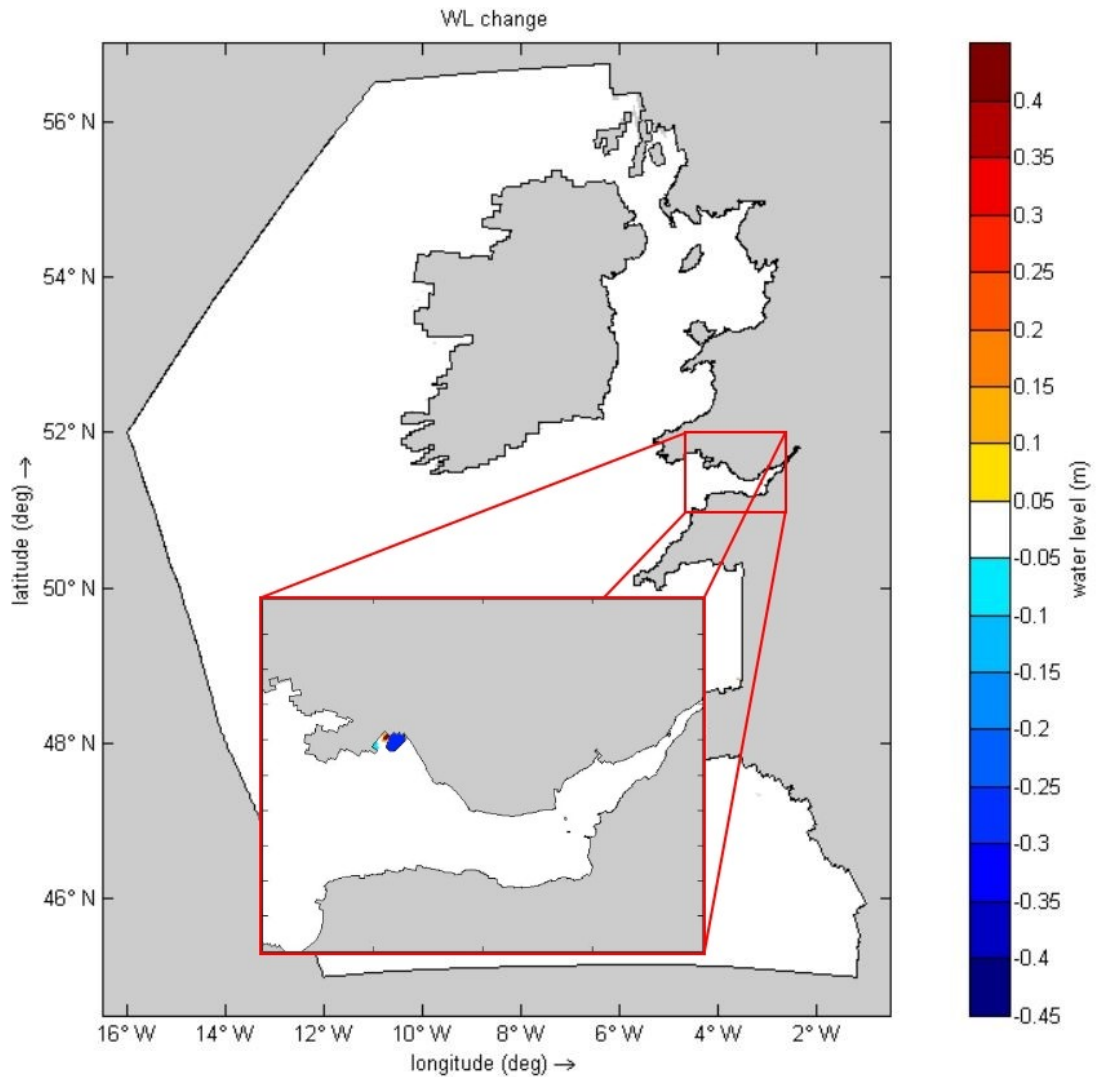


Figure 7.7: Impact of the lagoon on maximum water levels under a two-way operation.

7.3 Calibration and validation

The goal of calibration was to determine what value of Manning's n would provide the best fit between predicted and observed water levels across the estuary. The calibration was carried out by comparing the simulation results with tide gauge records provided by the British Oceanographic Data Centre (BODC), at four sites throughout the Severn Estuary and Bristol Channel, namely Hinkley Point, Ilfracombe, Mumbles and Newport (BODC 2017). Locations of the four sites are presented in Figure 7.8.

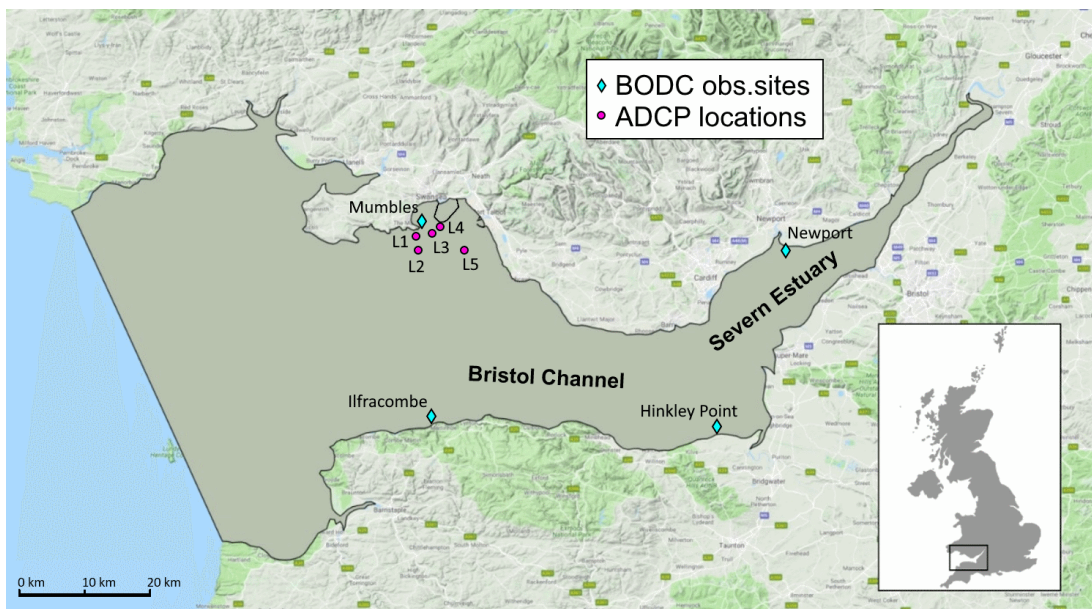


Figure 7.8: Computational domain for the assessment, with the outline of the proposed tidal lagoon in Swansea Bay and with cyan diamonds showing calibration sites and magenta dots showing validation sites (background map from Google Maps service).

Following the calibration at BODC sites, the model was validated against data from a field survey of Swansea Bay. Acoustic Doppler profiler (ADP) measurements were taken at five locations (L1 to L5) throughout the Swansea Bay, where the tidal lagoon is proposed to be built and therefore is expected to have the most impact. The validation was performed over a 14-day period between 25 July and 7 August 2012 to capture the

typical neap-spring tidal variation. The locations of the observation sites are presented in Figure 7.8.

The ADP data was provided through the Smart Coasts project, an EU-funded research study on water quality of bathing waters in Wales (EMU Limited 2012). The deployments consisted of seabed frame mounted ADP located at five different sites in the bay (Figure 7.8). The deployed instruments were Nortek's Aquapro 1 MHz (used on sites L1, L3 and L4) and Aquapro 600 kHz (sites L2 and L5) ADPs, capable of recording current profiles and pressure. They were carried out between July and October 2012 by EMU Limited. All equipment was configured to record in GMT (UT+0000) and all locations were recorded in WGS84. The ADPs were configured to acquire a water level record and current profile every 10 minutes over an averaging period of 60 seconds. To provide data security and quality assurance, each frame was equipped with a lightweight release transponder tilt sensor to make sure that the frame was deployed upright. Raw pressure data were converted to height above the sensor using density values that were pre-set for the conditions in the Swansea Bay. The calculated heights were reduced to the mean of the data set for harmonic analysis, from which the lowest astronomical tide (LAT) and highest astronomical tide (HAT) values extrapolated with reference to the data set mean. The final recordings consisted of (i) a pure tidal height component and (ii) an inconsistent residual height variation. The observed currents were considered to be a combination of (i) a tidal stream component, (ii) a mean drift component, and (iii) an inconsistent residual drift. Because boundary conditions of the model were driven solely by tidal harmonic forcing, only the tidal height and tidal stream components of the ADP measurements were used in the validation of the model.

7.3.1 Calibration

The sensitivity of the Manning's n was tested through a series of hydrodynamic simulations without the lagoon in place, over a complete neap-spring tidal cycle. Previous studies of Severn Estuary have used different values of roughness coefficient in

range between 0.02 and 0.035. Hence, four different roughness coefficients (0.02, 0.025, 0.03 and 0.035) were selected for calibration of the Swansea Bay model.

The results of sensitivity analysis are presented in Tables 7.3 to 7.6, with corresponding scatter plots in Figure 7.9. The model was found to have low sensitivity to bed roughness. Based on the statistical performance indicators, which were calculated using the Equations (5.1) to (5.4), a value of 0.03 was selected as the one producing the best fit.

Table 7.3: Sensitivity analysis of roughness coefficient (Hinkley Point).

Hinkley point				
n	r (-)	RMSE (m)	NSE (-)	SI (-)
0.020	0.986	0.644	0.961	0.560
0.025	0.997	0.297	0.992	0.259
0.030	0.998	0.208	0.996	0.181
0.035	0.991	0.472	0.979	0.410

Table 7.4: Sensitivity analysis of roughness coefficient (Ilfracombe).

Ilfracombe				
n	r (-)	RMSE (m)	NSE (-)	SI (-)
0.020	0.998	0.238	0.991	0.098
0.025	0.999	0.224	0.992	0.093
0.030	0.999	0.229	0.992	0.095
0.035	0.999	0.229	0.992	0.095

Table 7.5: Sensitivity analysis of roughness coefficient (Mumbles).

Mumbles				
n	r (-)	RMSE (m)	NSE (-)	SI (-)
0.020	0.983	0.551	0.954	0.230
0.025	0.988	0.467	0.967	0.254
0.030	0.992	0.390	0.977	0.212
0.035	0.994	0.327	0.984	0.178

Table 7.6: Sensitivity analysis of roughness coefficient (Newport).

Newport				
n	r (-)	RMSE (m)	NSE (-)	SI (-)
0.020	0.971	0.942	0.925	2.170
0.025	0.993	0.499	0.979	1.151
0.030	0.994	0.430	0.984	0.991
0.035	0.979	0.778	0.949	1.794

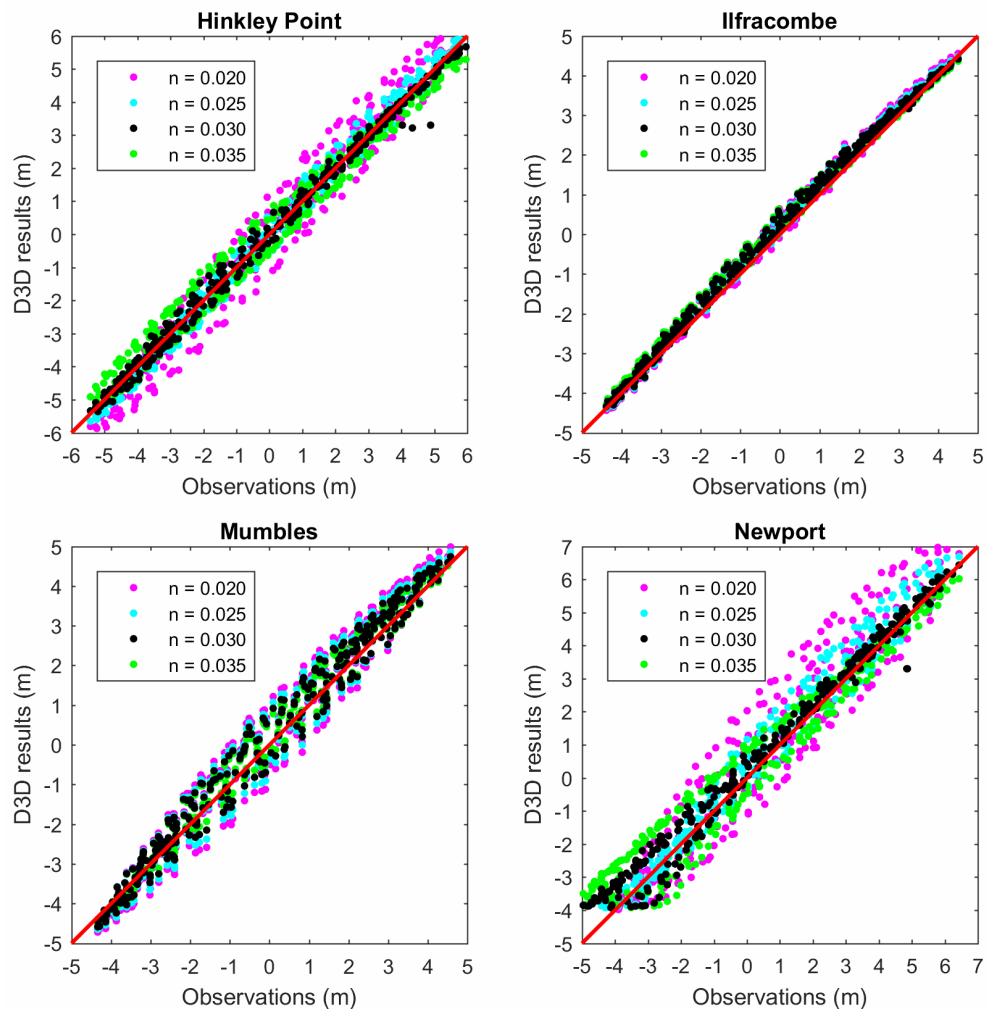


Figure 7.9: Sensitivity analysis of roughness coefficient at locations four observation sites in the Severn Estuary and Bristol Channel

7.3.2 Validation

Figure 7.10 shows the validation results for sites L3 and L5. The validation results of the remainder sites are included in Appendix F. The results showed good agreement with the observed data. They were also consistent with the results reported in the literature,

Chapter 7

Model application: Swansea Bay tidal lagoon

where different numerical models, such as DIVAST and EFDC, have been used in the past to predict the hydrodynamic conditions in the Severn Estuary and Bristol Channel (Ahmadian et al. 2010a; Xia et al. 2010b; Zhou et al. 2014a; Bray et al. 2016).

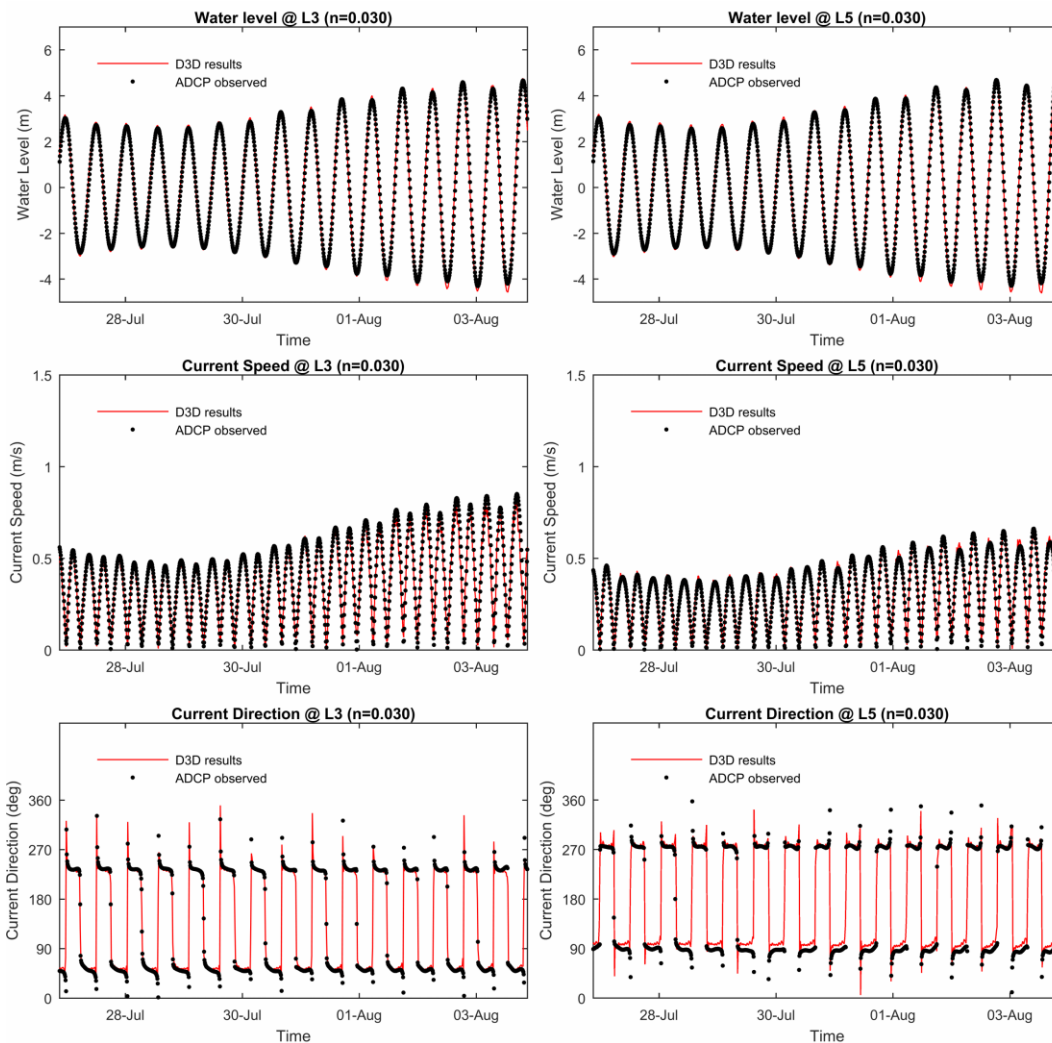


Figure 7.10: Validation results showing water levels and flow velocity at location L3 and L5.

To quantify the performance of the hydrodynamic model, four different performance indicators were used, i.e. correlation coefficient r , RMSE, NSE and SI, which were calculated using the Equations (5.1) to (5.4). The results for all five observation sites are

presented in Tables 7.7 to 7.9, showing performance indicators for water level, current speed and current direction results respectively.

Table 7.7: Validation results for water levels at five observation locations.

Water level				
Location	r (-)	RMSE (m)	NSE (-)	SI (-)
L1	0.992	0.350	0.982	0.189
L2	0.994	0.296	0.987	0.167
L3	0.993	0.324	0.984	0.186
L4	0.993	0.323	0.985	0.185
L5	0.994	0.292	0.988	0.164

Table 7.8: Validation results for current speed at five observation locations.

Current speed				
Location	r (-)	RMSE (m/s)	NSE (-)	SI (-)
L1	0.933	0.118	0.776	0.242
L2	0.976	0.063	0.953	0.112
L3	0.966	0.059	0.928	0.143
L4	0.952	0.056	0.898	0.166
L5	0.984	0.031	0.967	0.093

Table 7.9: Validation results for velocity direction at five observation locations.

Current direction				
Location	r (-)	RMSE (deg)	NSE (-)	SI (-)
L1	0.937	32	0.840	0.198
L2	0.962	26	0.922	0.159
L3	0.936	32	0.874	0.243
L4	0.895	44	0.791	0.332
L5	0.944	33	0.878	0.191

The correlation for water levels was above 0.99 at all five locations and the NSE values ranged from 0.982 to 0.988 suggesting a high level of agreement between the model results and observations. The model consistently underpredicts low tide levels during spring tides, which is reflected through a slightly higher RMSE. This was believed to be due to an error in open boundary condition, however it was regarded as acceptable based on the results from previous studies of the Severn Estuary found in literature (Falconer et al. 2009; Bray et al. 2016). The SI was low in all cases and therefore of no concern.

Analysis of the current speed again showed very high correlation with values well above 0.9 for all five locations. The NSE analysis showed slightly worse performance at site L1 with a value of 0.776, however, still within an acceptable range. This discrepancy can be attributed to the location of the site close to Mumbles headland which can have an impact on velocity predictions in numerical simulations (Stansby et al. 2016). The RMSE and SI were low in all cases and therefore of no concern.

Similarly, NSE values calculated for the current directions were between 0.791 and 0.922, with correlation generally at and above 0.9, again showing strong agreement between the two sets of results. The slightly lower NSE values were due to the sensitivity of the NSE method to data outliers. As observed in Figure 7.10, both the predicted and observed data for flow direction contained “spikes” which occurred during slack water and when the velocity falls close to zero. At the same time, the flow must change the direction between an incoming and outgoing tide, which appeared as outlier points in the flow direction time series. This also explains higher RMSE and SI values for current directions. However, these discrepancies have little impact on the overall performance of the model and are generally considered a good fit.

The direct comparison of the results in Figure 7.10, together with the quantitative statistical analysis Tables 7.7 to 7.9, indicated a robust forecasting ability of the model and justified its use for further hydrodynamic analysis with the lagoon in place.

7.4 Results

7.4.1 Lagoon operation

After the successful validation of hydrodynamics, the scenario SBL 1 was run to provide baseline results and to ensure the correct functioning of the model. The operation of the lagoon can be illustrated by a time series of water levels on both sides of the turbine housing. The water levels on each side were calculated as a mean value of four points

taken at four different observation sites, that were evenly spread about 500 m away from the lagoon (Figure 7.11). This approach was taken to prevent any local disturbances in the water surface, that could potentially affect the head difference across the lagoon. The resulting water levels for the SBL1 case are presented in Figure 7.12, accompanied by the six corresponding stages of the lagoon operation.

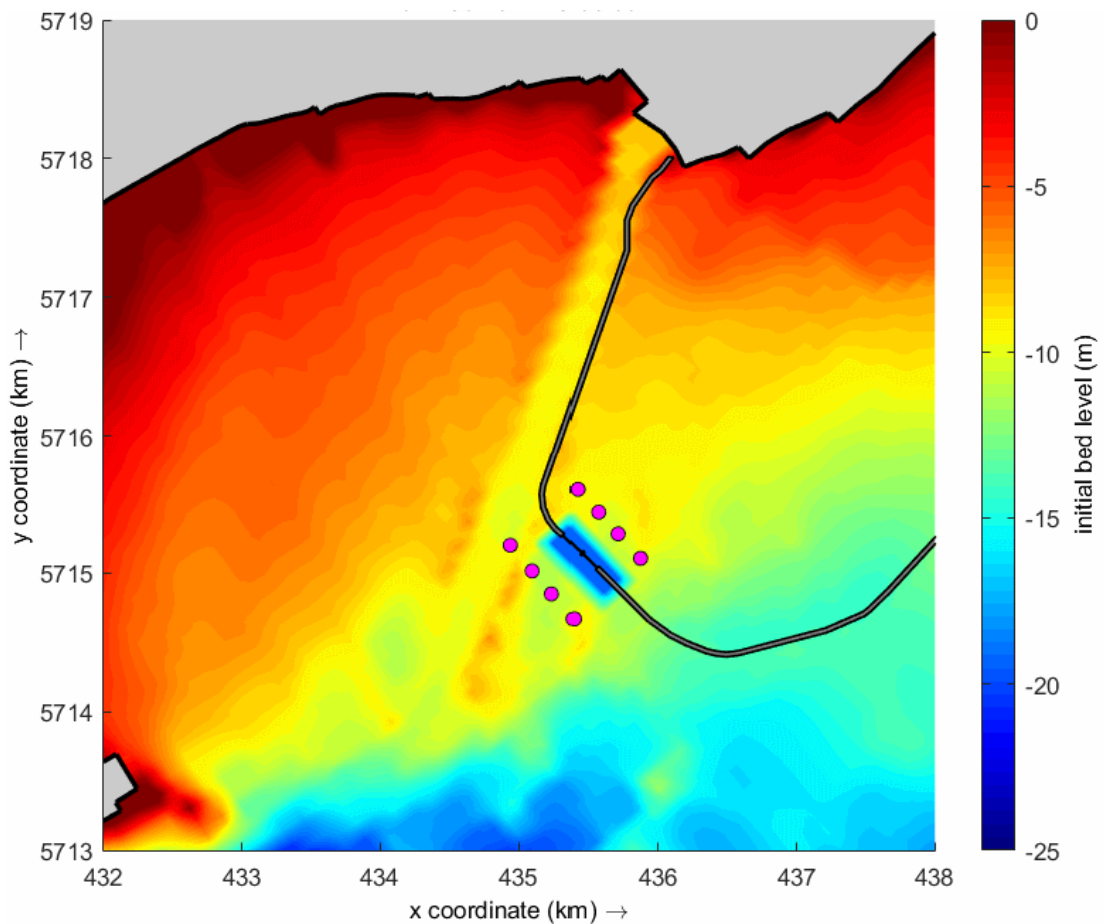


Figure 7.11: Location of points for determining the head difference across the lagoons.

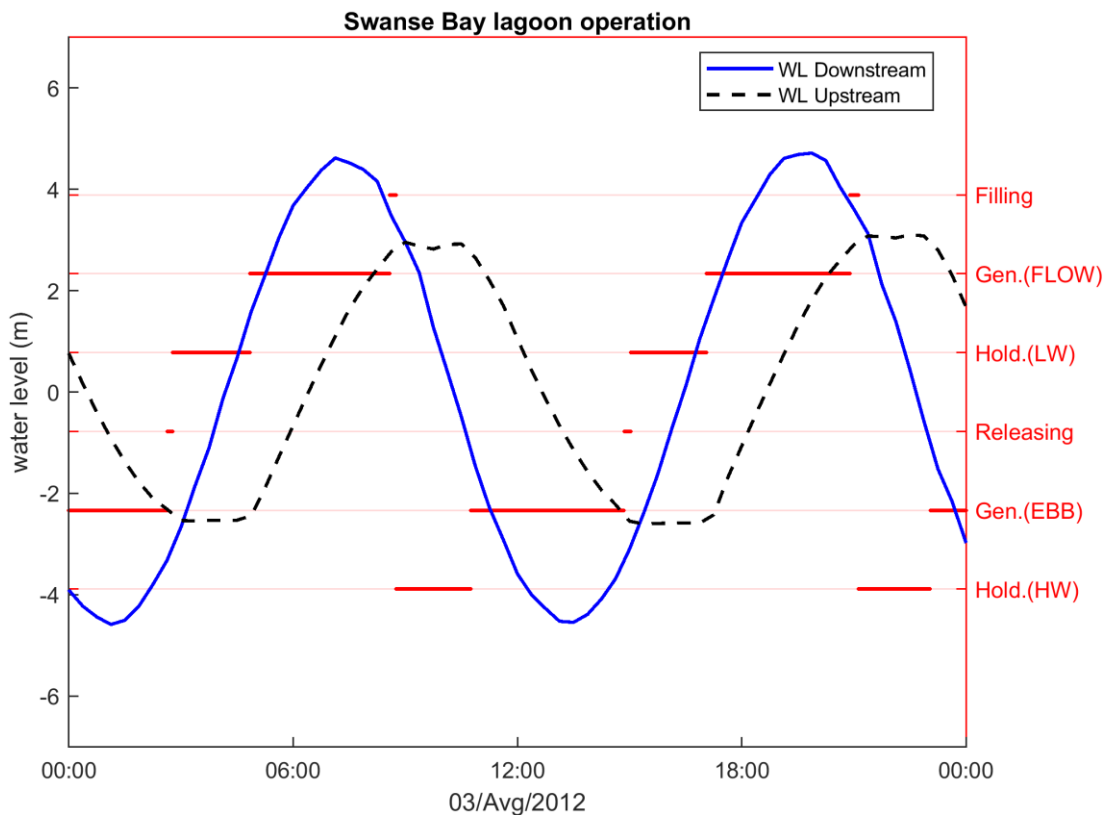


Figure 7.12: Two-way operation of the Swansea Bay lagoon during a typical spring tidal cycle. Showing water levels on both sides of the lagoon and the corresponding operational stages.

The two-way generation sequence has resulted in four cycles of power generation per day. Generating during both flood and ebb tides means that power production is spread more evenly throughout the day compared to the one-way schemes. The water levels in Figure 7.12 were recorded during the maximum spring tidal cycle, during which the largest tidal range of 8.6 m was recorded in Swansea Bay. The tidal range inside the lagoon has been drastically reduced to 6.4 m. The maximum water level inside the lagoon has fallen by 0.76 m, while the minimum water level rose by 1.44 m. Water levels outside the lagoon were left unaffected by the lagoon operation.

7.4.2 Velocity field

Figures 7.13 and 7.14 show the instantaneous velocity fields near the lagoon during the flood and ebb generation stages respectively. Velocities from the 3D models have been depth-averaged to allow for a direct comparison with the 2D model. Changes to the velocity pattern were limited to the vicinity of the lagoon and have never extended further than 2.5 km away. The changes were induced in the form of a high-velocity jet that has alternately formed on the inside and outside of the lagoon. The figures correspond to the peak flow rates during a spring tidal cycle, when the velocity magnitude of the jet was at its extreme. However, the extreme velocities are only an example that represents a general trend which was observed throughout the simulation period, regardless of the size of the tidal range. The peak velocities at the turbine exit for each scenario are collected in Table 7.10 for flood and in Table 7.11 for ebb generation cycle.

The flow patterns in scenarios SBL2 and SBL4, with a realistic velocity distribution (Figures 7.13c,e and 7.14c,e), were very close to the baseline model SBL1 (Figures 7.13b and 7.14b), with a slight increase in the velocity at the turbine exit. For example, during the ebb generation, the velocity increased from 1.37 m/s in SBL1 to 1.48 m/s in SBL2 and 1.47 m/s in SBL4. During flood generation, the velocity increased from 1.32 m/s in SBL1 to 1.41 m/s in SBL2 and 1.40 m/s in SBL4. The average increase in velocity was under 10 per cent for both the SBL2 and SBL4 scenarios. As expected, scenarios SBL3 and SBL5, with a simplified velocity distribution, saw a more significant increase in the velocity coming out of the turbines (Figures 7.13d,f and 7.14d,f). In the 2D model (scenario SBL3), the velocities increased by almost 50 per cent. For example, the peak velocity during ebb tide increased from 1.37 m/s to 2.05 m/s and the peak velocity during flood tide increased from 1.32 m/s to 1.97 m/s. The results from the 3D model (scenario SBL5) predict a slightly lower increase in the range of around 30 per cent, with recorded peak velocities of 1.76 m/s and 1.84 m/s during the ebb and flood tide generation respectively.

Chapter 7
Model application: Swansea Bay tidal lagoon

Table 7.10: Peak flow velocity (u_T) and instantaneous discharge (Q_T) just downstream of the turbine exit for a typical spring tidal cycle during flood power generation and the corresponding head difference (H_T). Velocities for scenarios SBL4 and SBL5 are presented both with a depth-averaged value (u_T) for comparison with 2D models and with separate values for respective computational layers (u_{Tk}).

Flood-generation stage						
	Scenario	Layer	u_T (m/s)	u_{Tk} (m/s)	Q_T (m ³ /s)	H_T (m)
2D, only mass	SBL1	-	1.32	-	4336	3.47
2D, w/ mom.	SBL2	-	1.41	-	4377	3.48
transfer	SBL3	-	1.97	-	5192	4.48
		K=1		0.99		
		K=2		1.20		
	SBL4	K=3	1.40	1.27	4348	3.44
		K=4		1.09		
		K=5		0.62		
3D, w/ mom.		K=1		1.05		
transfer		K=2		1.95		
	SBL5	K=3	1.84	2.77	4954	4.17
		K=4		2.19		
		K=5		1.90		

Table 7.11: Peak flow velocity (u_T) and instantaneous discharge (Q_T) just downstream of the turbine exit for a typical spring tidal cycle during ebb power generation and the corresponding head difference (H_T). Velocities for scenarios SBL4 and SBL5 are presented both with a depth-averaged value (u_T) for comparison with 2D models and with separate values for respective computational layers (u_{Tk}).

Ebb-generation stage						
	Scenario	Layer	u_T (m/s)	u_{Tk} (m/s)	Q_T (m ³ /s)	H_T (m)
2D, only mass	SBL1	-	1.37	-	4408	3.49
2D, w/ mom.	SBL2	-	1.48	-	4411	3.50
transfer	SBL3	-	2.05	-	5364	4.60
		K=1		1.06		
		K=2		1.50		
	SBL4	K=3	1.47	1.40	4381	3.47
		K=4		1.23		
		K=5		0.93		
3D, w/ mom.		K=1		0.88		
transfer		K=2		1.89		
	SBL5	K=3	1.76	2.75	4973	4.13
		K=4		2.18		
		K=5		1.90		

Chapter 7
Model application: Swansea Bay tidal lagoon

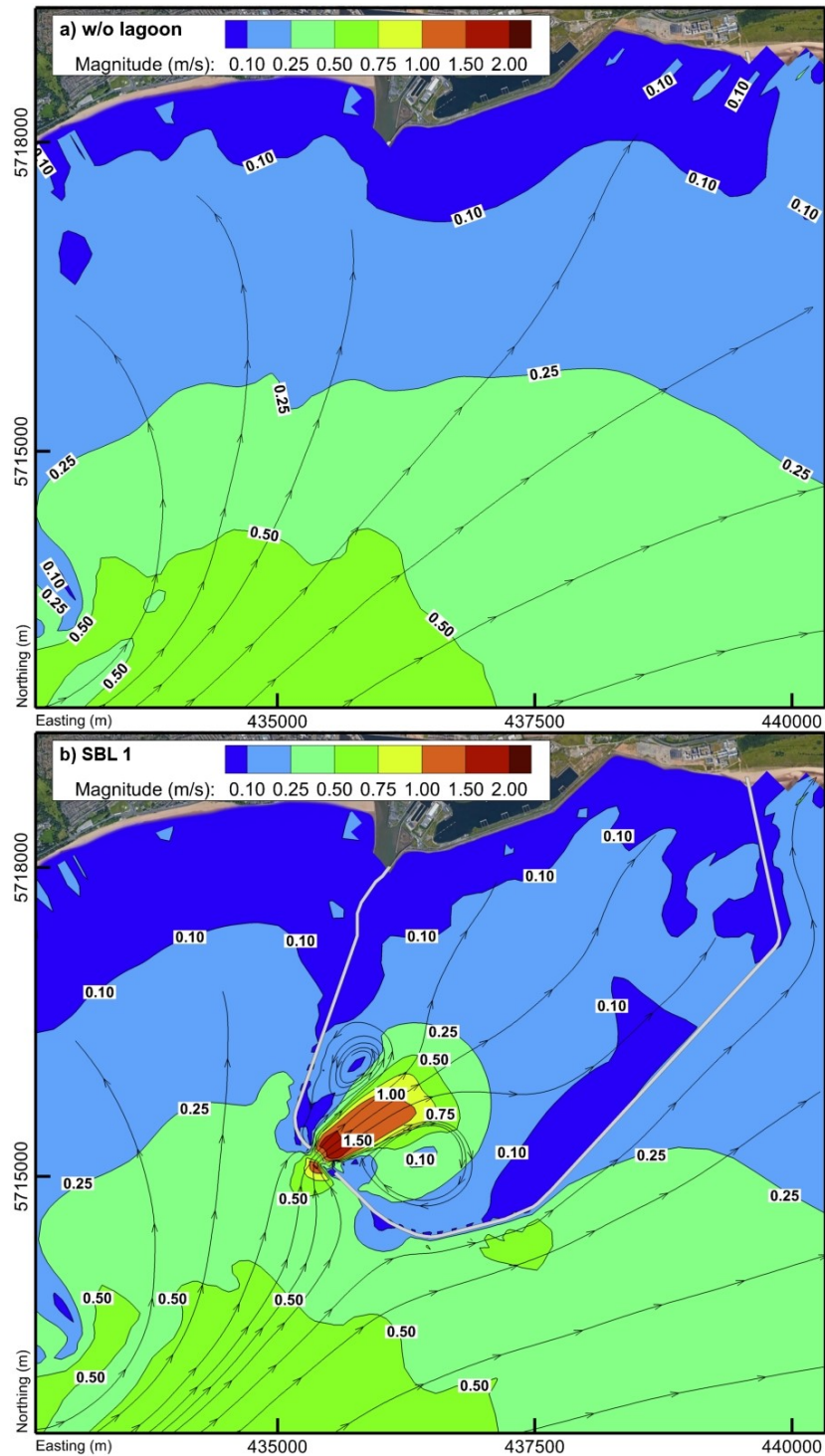


Figure 7.13: A comparison of velocity fields during the flood generation for a typical spring tidal cycle – (a) without lagoon, (b) SBL 1, (c) SBL 2, (d) SBL 3, (e) SBL 4, and (f) SBL 5.

Chapter 7
Model application: Swansea Bay tidal lagoon

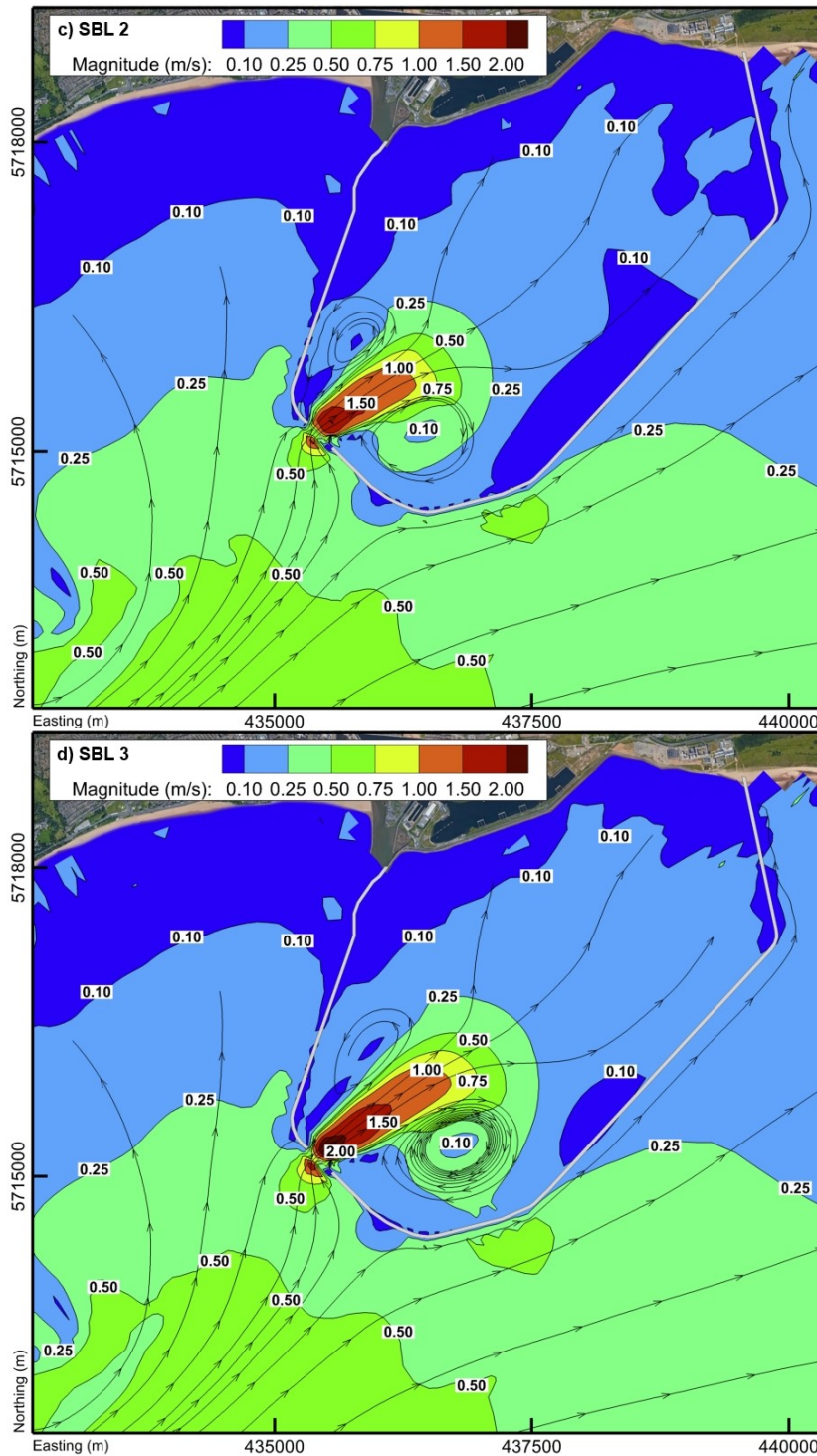


Figure 7.13: Continued – A comparison of velocity fields during the flood generation for a typical spring tidal cycle – (a) without lagoon, (b) SBL 1, (c) SBL 2, (d) SBL 3, (e) SBL 4, and (f) SBL 5.

Chapter 7
Model application: Swansea Bay tidal lagoon

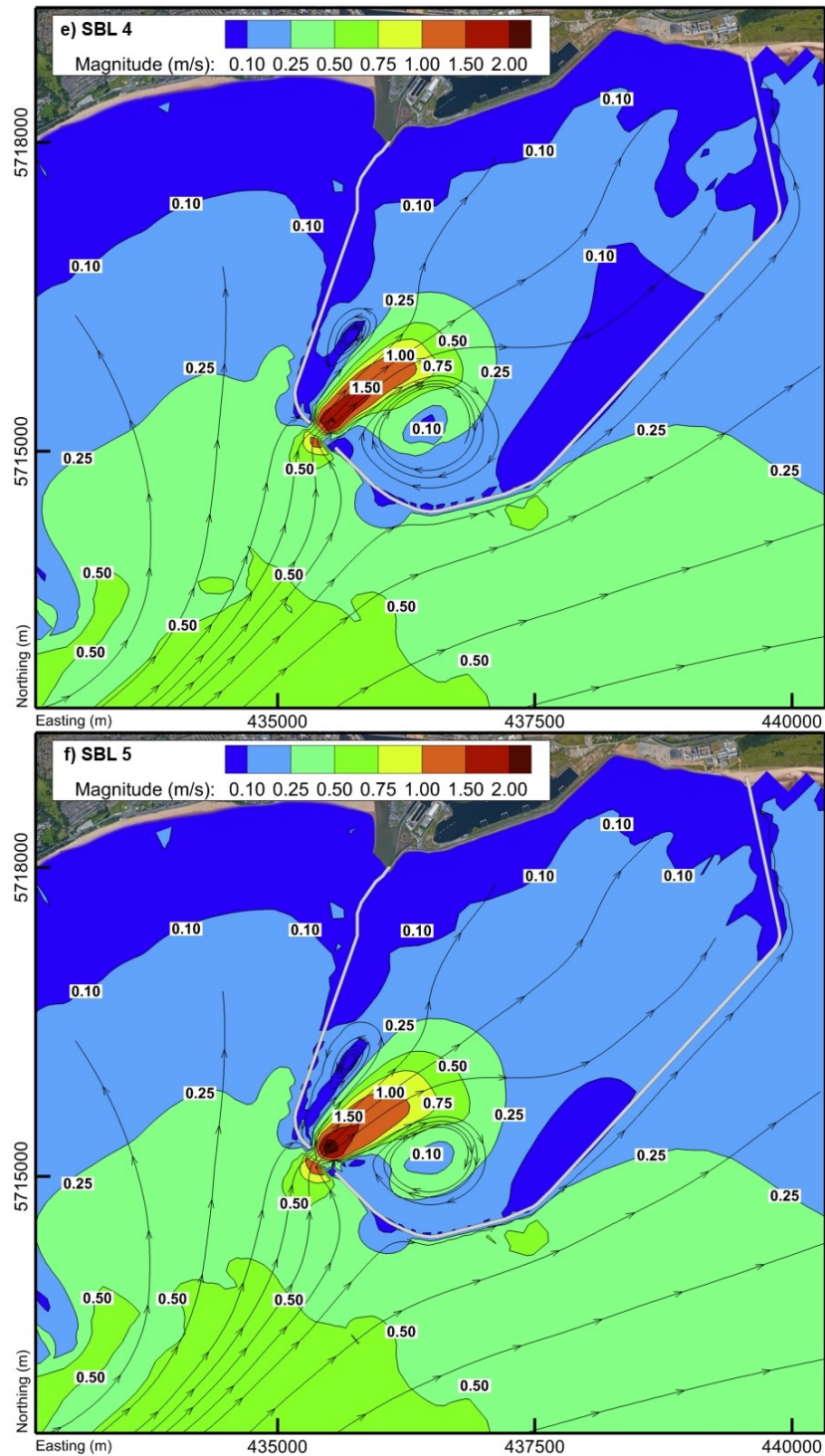


Figure 7.13: Continued – A comparison of velocity fields during the flood generation for a typical spring tidal cycle – (a) without lagoon, (b) SBL 1, (c) SBL 2, (d) SBL 3, (e) SBL 4, and (f) SBL 5.

Chapter 7
Model application: Swansea Bay tidal lagoon

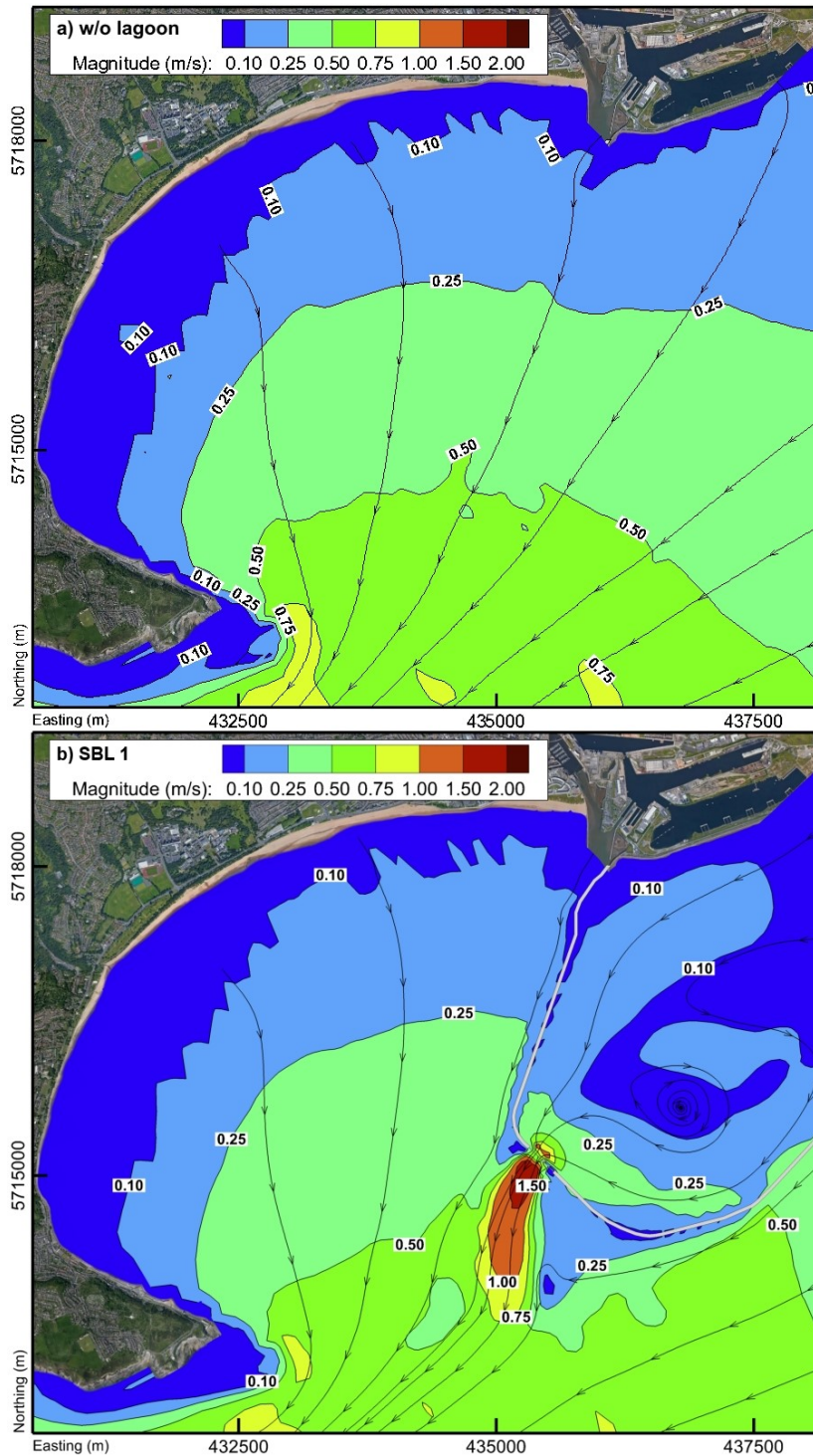


Figure 7.14: A comparison of velocity fields during the ebb generation for a typical spring tidal cycle – (a) without lagoon, (b) SBL 1, (c) SBL 2, (d) SBL 3, (e) SBL 4, and (f) SBL 5.

Chapter 7
Model application: Swansea Bay tidal lagoon

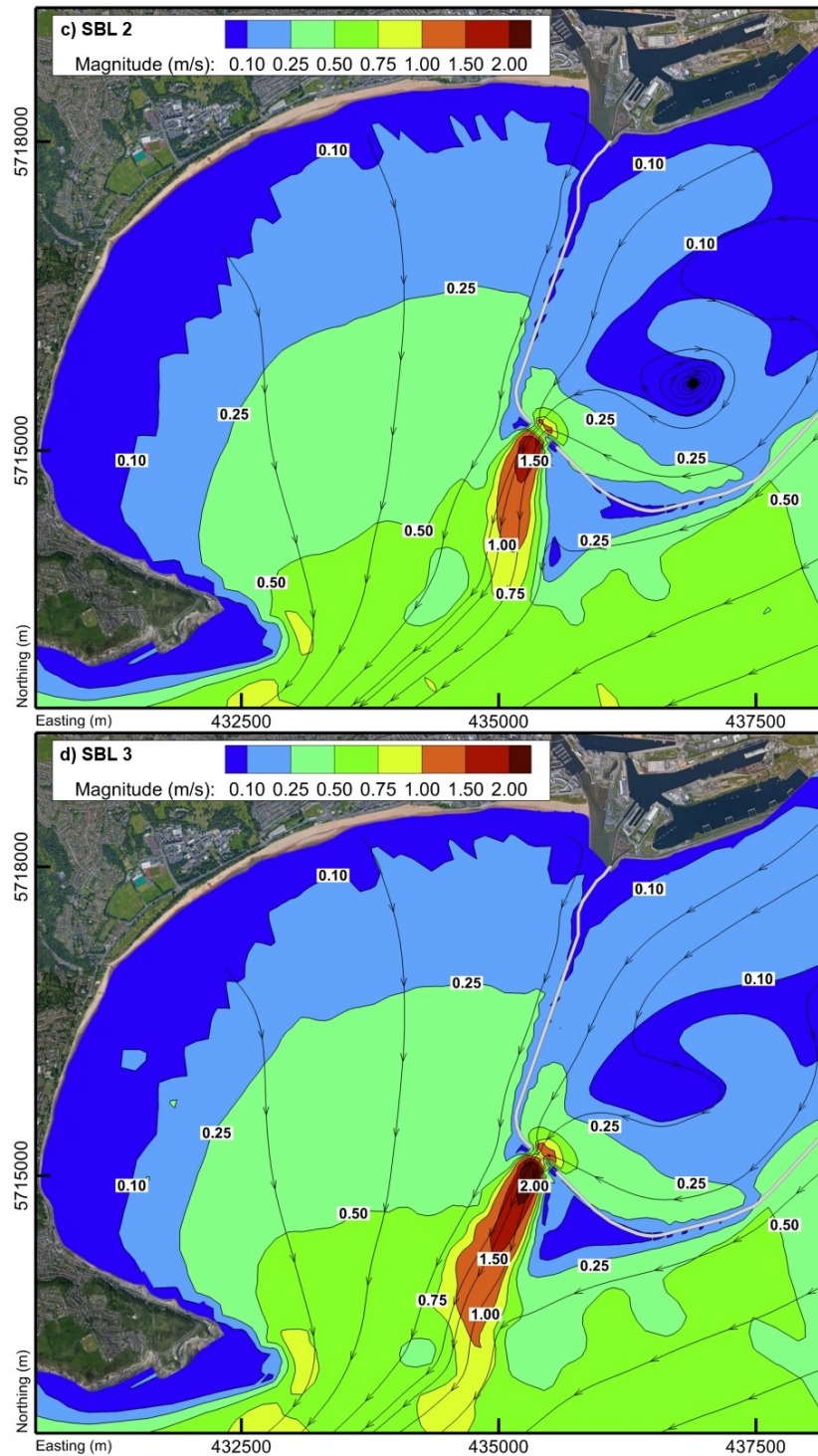


Figure 7.14: Continued – A comparison of velocity fields during the ebb generation for a typical spring tidal cycle – (a) without lagoon, (b) SBL 1, (c) SBL 2, (d) SBL 3, (e) SBL 4, and (f) SBL 5.

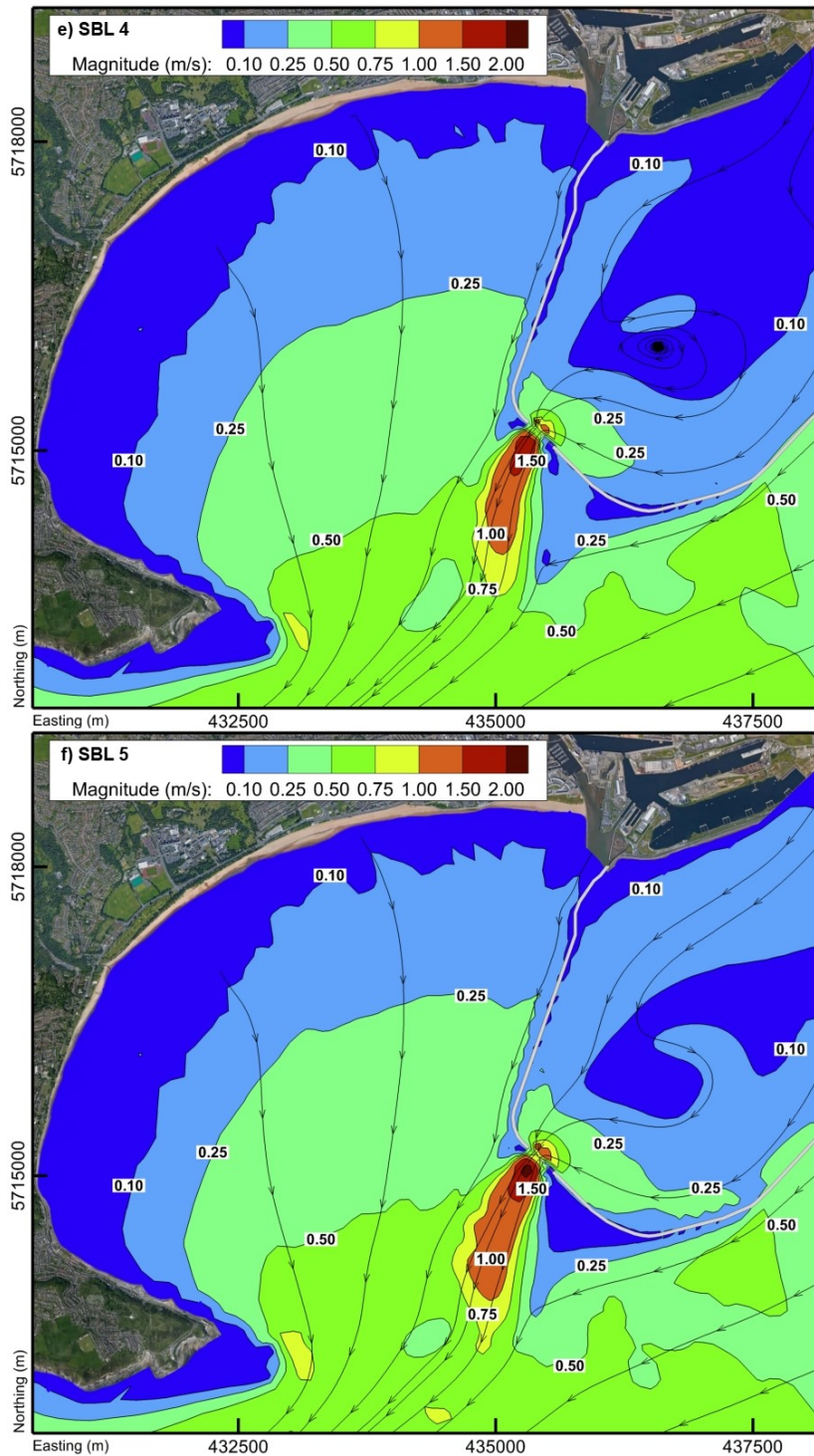


Figure 7.14: Continued – A comparison of velocity fields during the ebb generation for a typical spring tidal cycle – (a) without lagoon, (b) SBL 1, (c) SBL 2, (d) SBL 3, (e) SBL 4, and (f) SBL 5.

The 3D complexity of the velocity profile in scenarios SBL4 and SBL5 is highlighted in Figure 7.15. The predicted velocity profiles have been recorded at 50 m increments from the turbine exit at four locations. At 50 m and 100 m downstream of the turbine, the higher velocity in the middle layers is still clear. However, the jet completely dissipates by the distance of 150 m, where velocity profile transitions to a conventional logarithmic shape of free surface flow. This observation is consistent with the findings of Jeffcoate et al. (Jeffcoate et al. 2013). Even though the effects of the jet were lost after this distance, a direct comparison between the two scenarios indicated a clear difference between simplified and realistic velocity distribution. Scenario SBL5 still retains a higher depth-averaged velocity compared to SBL4. An evident increase in the flow velocity could be observed in all cases with the refined momentum treatment.

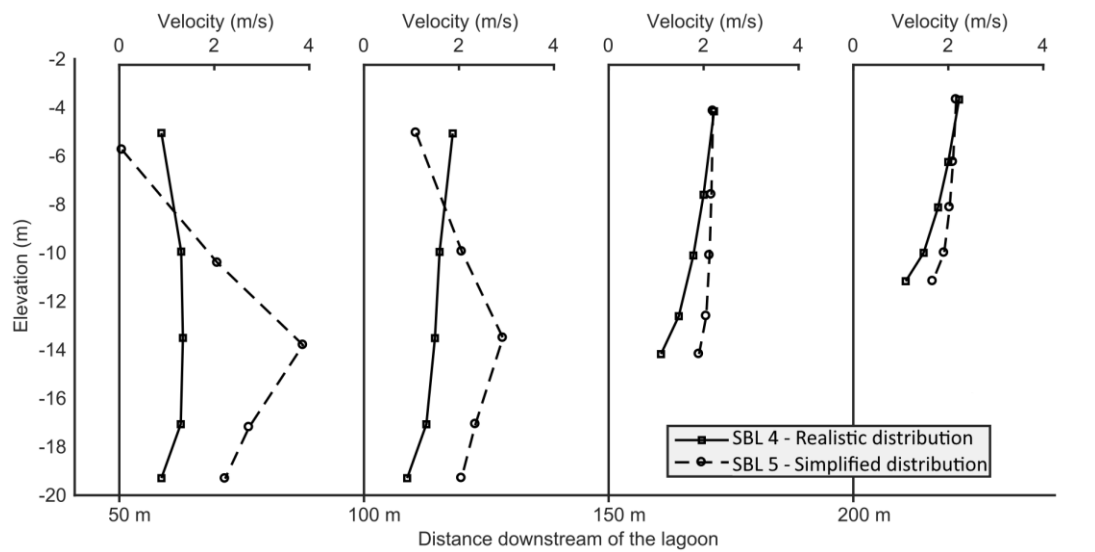


Figure 7.15: Representative 3D velocity profiles for SBL4 and SBL5 during the ebb generation in four locations downstream of the turbine.

7.4.3 Bed shear stress

In general, sediment transport is governed by several factors, including sediment type, salinity, biological interactions and most importantly hydrodynamic conditions in the

region (Wang and Aandutta 2013). Bristol Channel and Severn Estuary are covered by a diverse bed morphology, including bare rock, gravel, sand and mud. Off the Welsh coast, the estuary bed consists predominantly of sand banks with an isolated muddy zone occurring inside the Swansea Bay (Dyer 1984). Previous studies have shown that general distribution of the sediments across the estuary correlates well with the maximum bed shear stress from numerical predictions (Warwick and Uncles 1980). The threshold values for the initiation of erosion and deposition are commonly represented by critical shear stress for erosion (τ_{ce}) and deposition (τ_{cd}) respectively. Shi et al. (2015) investigated the erosion and deposition processes in estuarine environments and proposed threshold values of $\tau_{ce} = 0,14 \text{ N/m}^2$ and $\tau_{cd} = 0,08 \text{ N/m}^2$ for erosion and deposition respectively. The study employed several different empirical equations for calculating the bed shear stress in the Yangtze River estuary in China, including the combined current-wave action based on the models of Soulsby (1995) and van Rijn (1993). The maximum values of the combined current-wave action in the study rose up to 0.446 N/m^2 , from which the currents alone contributed to only 0.224 N/m^2 . Similar values were predicted in the Swansea Bay by the Delft3D simulation prior to the construction of the lagoon, where bed shear never exceeded 0.3 N/m^2 (Figure 7.16).

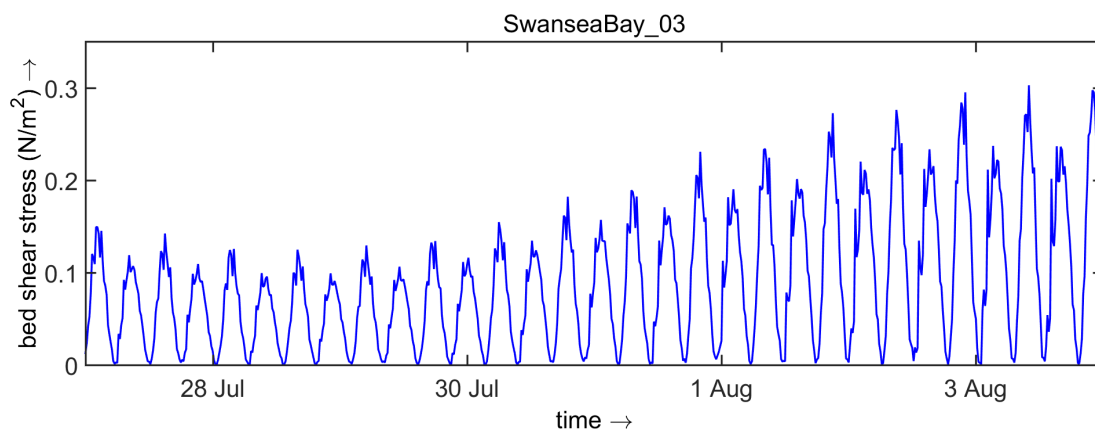


Figure 7.16: Prediction of bed shear stress in Swansea Bay prior to construction of the lagoon.

The construction of the lagoon would mean a significant disruption to the natural sediment transport processes, with maximum bed shear stress multiplied by several

orders of magnitude compared to natural conditions. Even though the affected regions are relatively small, the erosion could lead to disastrous consequences to the environment and structural stability of the lagoon if not addressed before the lagoon is constructed.

Bed shear stress is difficult to measure directly, particularly in turbulent flows, however, there is a way to estimate it from near-bed velocity profiles (Jeffcoate et al. 2017). In the 2D simulations, the local shear stress is assumed to be given by a quadratic friction law including the magnitude of the depth-averaged horizontal velocity (Equation (6.1)). For the 3D simulations, the same equation is used, but instead of a depth-averaged velocity, the magnitude of the horizontal velocity in the first layer just above the bed is used (Equation (6.2)).

Bed shear stress was calculated at the time of maximum flow velocity upstream and downstream of the turbines. Figures 7.17 and 7.18 respectively show the results during the flood and ebb generation stage, corresponding to velocity results in Figures 7.13 and 7.14. Because bed shear stress is directly related to the velocity field, the impact of the tidal lagoon on the results showed similar patterns as the impact of the lagoon on the velocity field. The changes in bed shear stress were the most prominent locally around the lagoon, coinciding with the position of the jets on both sides of the lagoon. The area further away from the site was left largely unaffected by the operation of the lagoon.

Both flood and ebb cycles produced similar results, with the flood cycle affecting the bed shear stress inside the lagoon and ebb cycle affecting it outside, just downstream of the turbine housing block. There was little difference in the bed shear stress between the baseline run (SBL 1) and the 2D run with a realistic velocity distribution (SBL 2). The extent of the area affected was similar, however, SBL 2 case showed a slightly higher value of maximum shear stress with 17.2 N/m^2 , compared to 15.8 N/m^2 in SBL 1. Similarly, the 3D simulation with the same distribution (SBL 4) with 16.9 N/m^2 resulted in only a slight increase from SBL 1. This shows that if the design of the draft tube manages to efficiently dissipate the velocity profile evenly across the diffuser exit, the

shear stress imposed on the bottom surface would not be too dissimilar to the one predicted by the baseline scenario. The results also indicate that under this assumption, where velocity is more evenly distributed across the depth, 2D simulation is sufficient for assessing the bed shear stress, with a 3D model predicting very similar results.

When velocity distribution was simplified the bed shear stress increased dramatically. In the 2D case (SBL 3) the maximum value rose to 29 N/m², while the 3D case produced even higher shear stress, with a maximum value of 50 N/m². The area of impact has noticeably increased in the 2D case (SBL 3), extending further away from the turbines in the shape of the jet. In the 3D case (SBL 5) the affected area stayed roughly the same, but with a much higher concentration of the higher values close to turbines, which then dissipated relatively quickly. This shows that in the case with the simplified velocity distribution, where the jet is assumed to be much more concentrated, a 3D simulation with momentum conservation is essential for providing more accurate results.

The increased bed shear stress caused by the exiting jet indicates extensive erosion on both sides of the lagoon. This is particularly problematic on the inside of the lagoon, where eroded sediment is most likely to be deposited in the lower velocity regions closer to the coast and in the centre of the vortices forming on both sides of the jet (Figure 7.13). In contrast to high-velocity current during the flood generation, velocity magnitude on the inside during the emptying of the lagoon was consistently weaker, resulting in almost insignificant bed shear stress (Figure 7.18). Therefore, it is likely that ebb currents will not be able to flush out sediments accumulated during the filling of the lagoon, inhibiting the long-term performance of the scheme and incurring additional operational costs for dredging. This effect was present even during the baseline scenario (SBL 1) but was further amplified in simulations with conserved momentum. Increased bed shear stress in these cases would result in a higher rate of erosion under the jets and a higher rate of deposition in low velocity regions during the filling stage. The bed shear stress during the emptying stage has remained low even when momentum conservation was considered (Figure 7.18c-f).

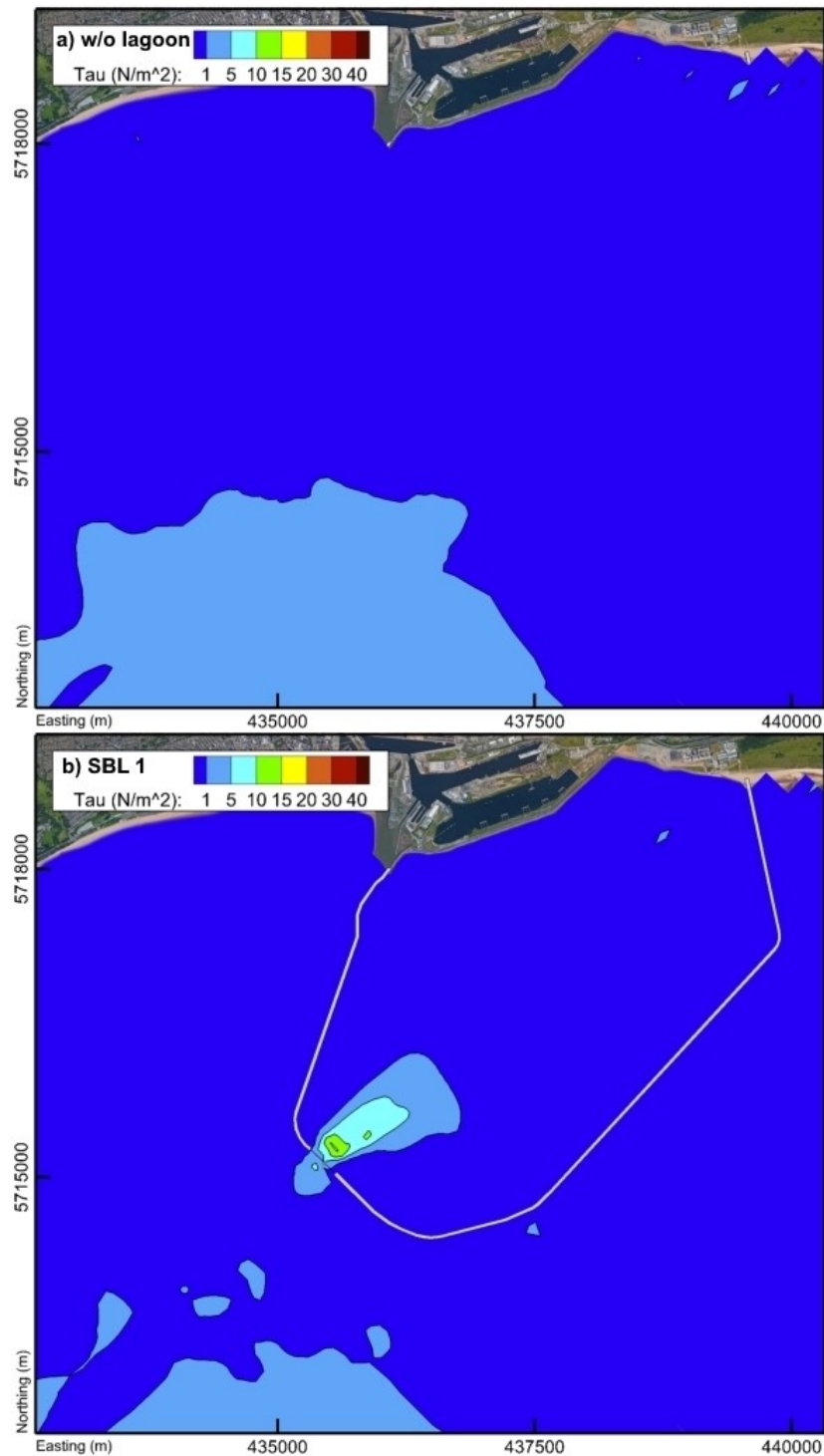


Figure 7.17: Bed shear stress during the flood generation – (a) without lagoon, (b) SBL 1, (c) SBL 2, (d) SBL 3, (e) SBL 4, and (f) SBL 5.

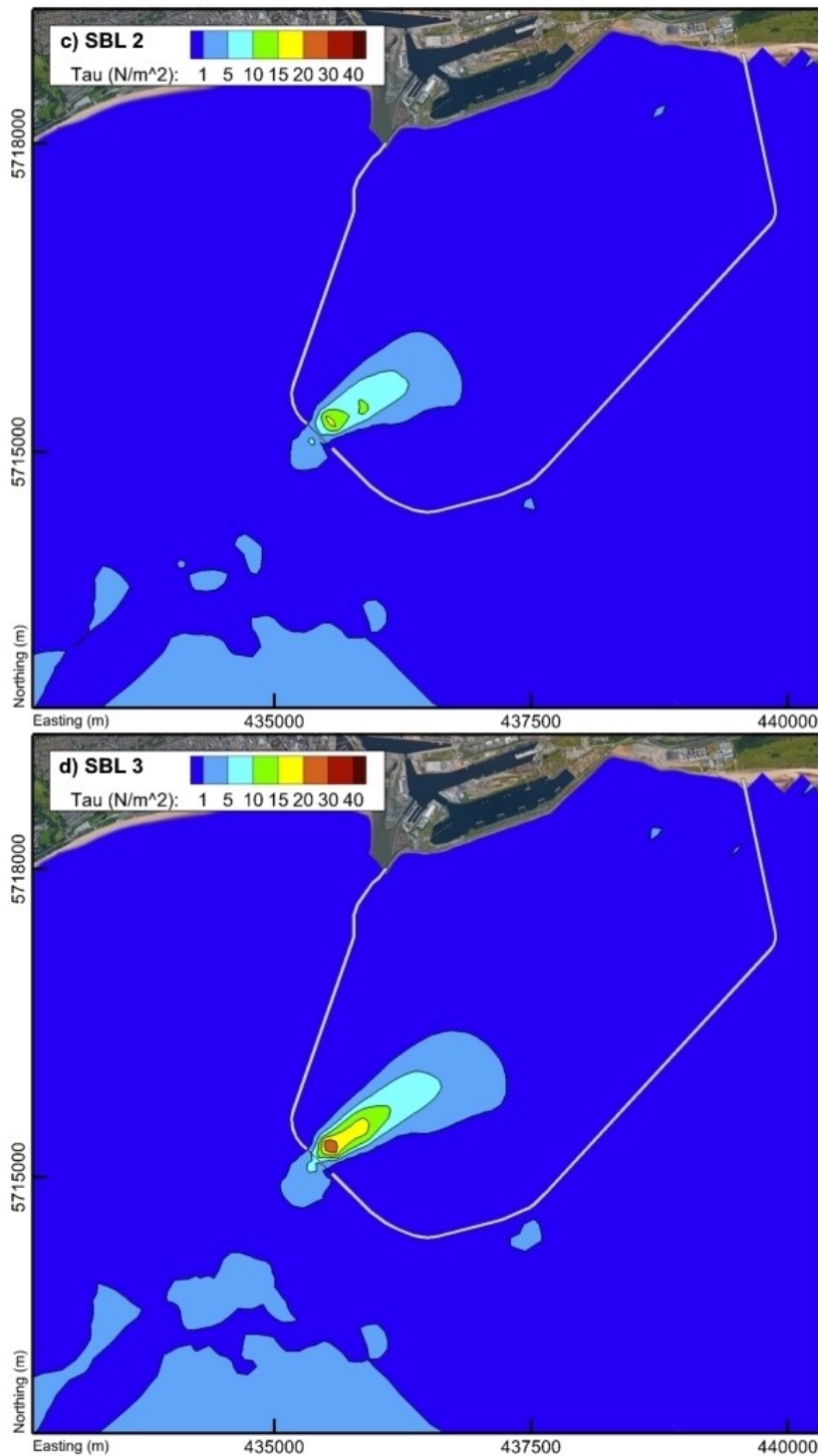


Figure 7.17: Continued – Bed shear stress during the flood generation – (a) without lagoon, (b) SBL 1, (c) SBL 2, (d) SBL 3, (e) SBL 4, and (f) SBL 5.

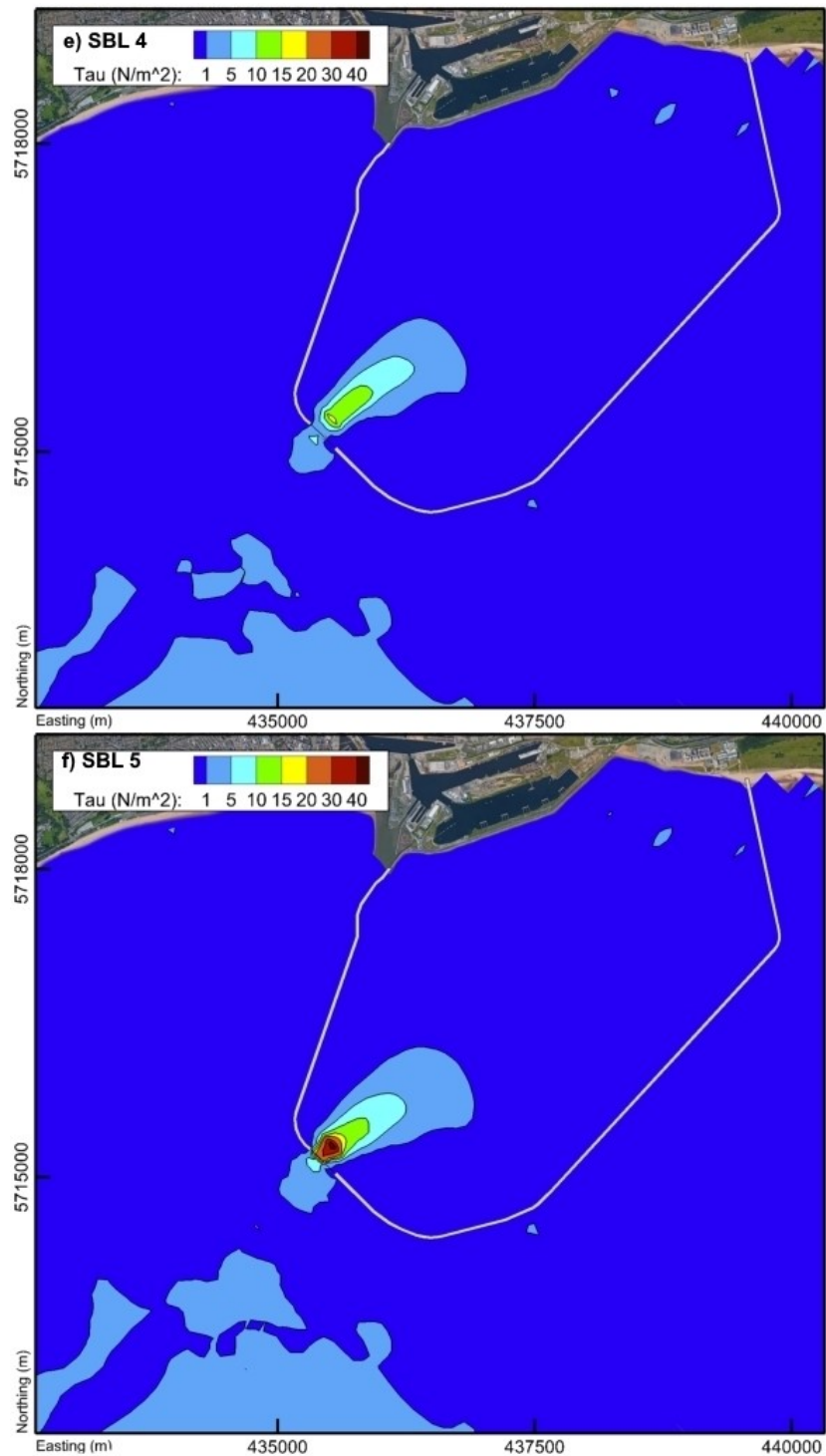


Figure 7.17: Continued – Bed shear stress during the flood generation – (a) without lagoon, (b) SBL 1, (c) SBL 2, (d) SBL 3, (e) SBL 4, and (f) SBL 5.

Chapter 7
Model application: Swansea Bay tidal lagoon

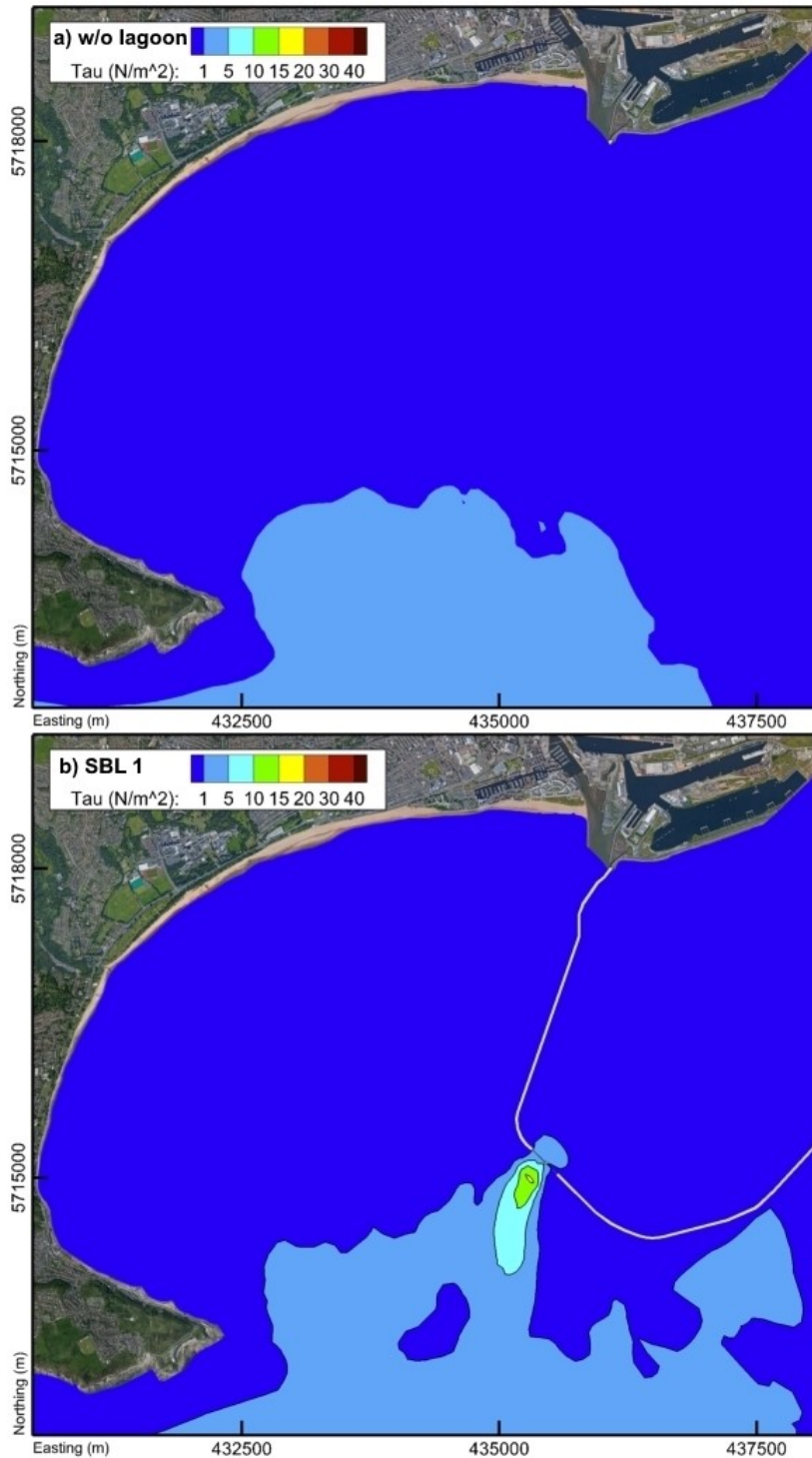


Figure 7.18: Bed shear stress during the ebb generation – (a) without lagoon, (b) SBL 1, (c) SBL 2, (d) SBL 3, (e) SBL 4, and (f) SBL 5.

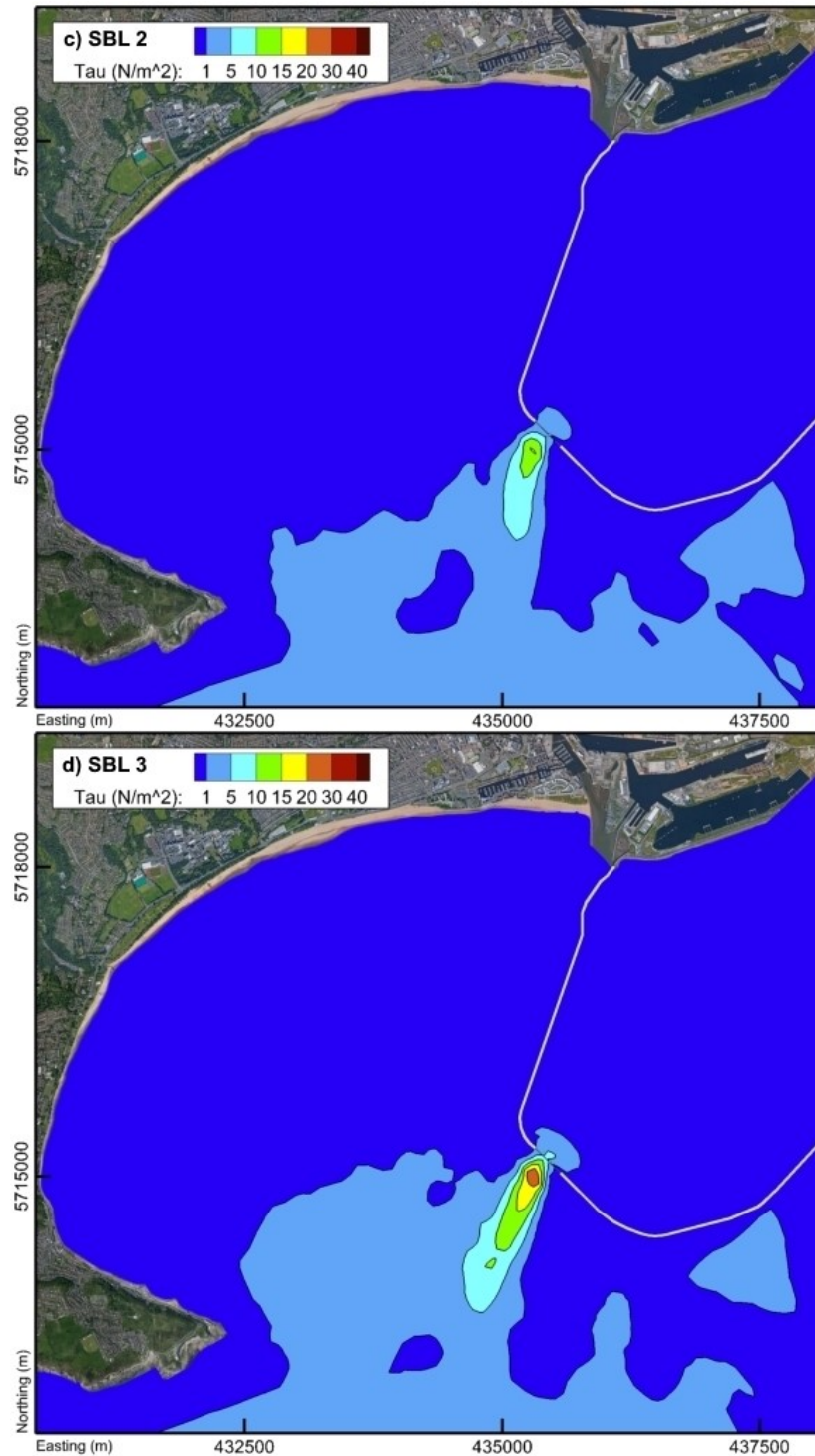


Figure 7.18: Continued – Bed shear stress during the ebb generation – (a) without lagoon, (b) SBL 1, (c) SBL 2, (d) SBL 3, (e) SBL 4, and (f) SBL 5.

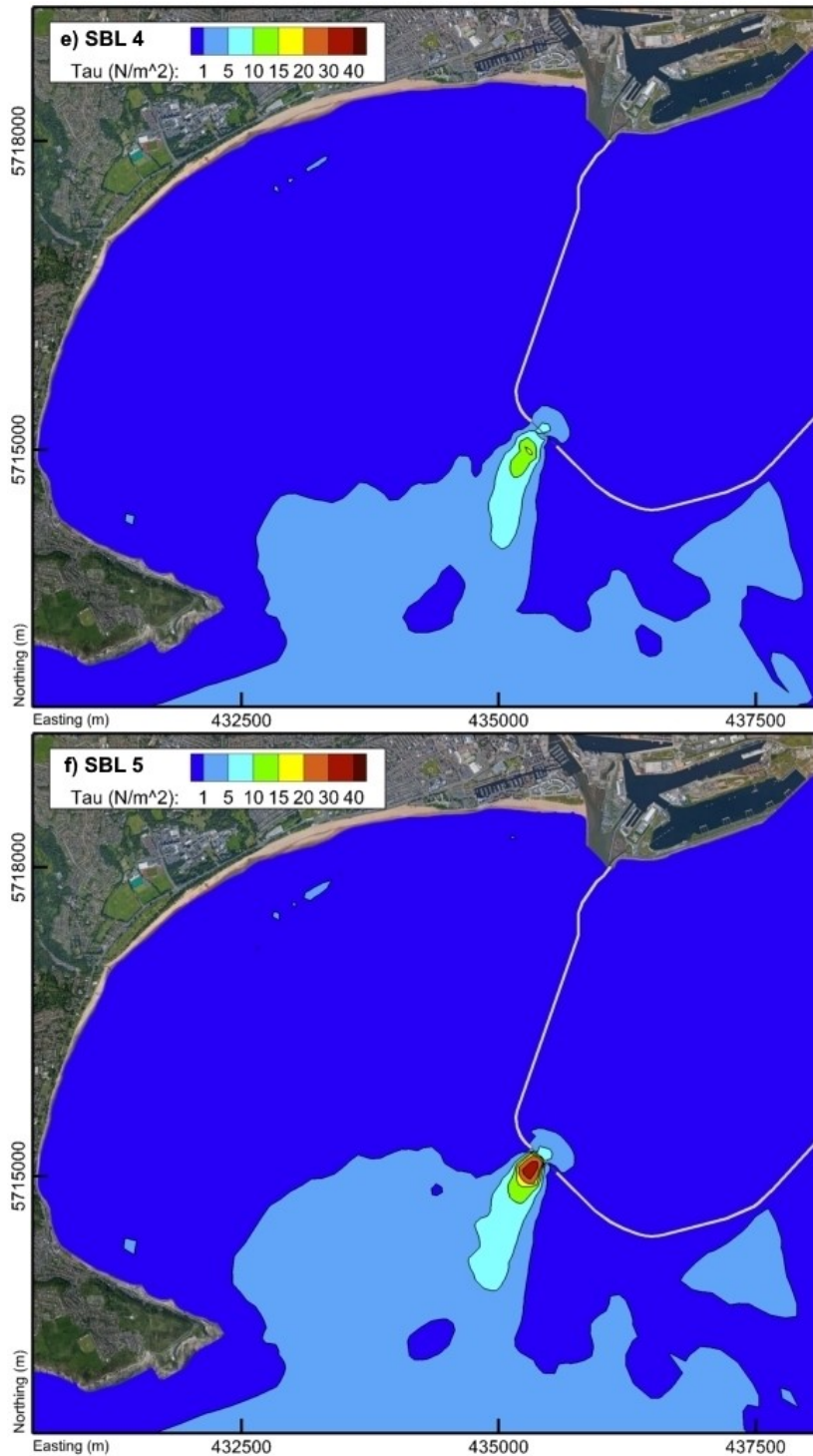


Figure 7.18: Continued – Bed shear stress during the ebb generation – (a) without lagoon, (b) SBL 1, (c) SBL 2, (d) SBL 3, (e) SBL 4, and (f) SBL 5.

7.4.4 Water levels

A comparison between the model predictions for the different scenarios highlighted that the treatment of the momentum had little influence on water surface elevations outside of the lagoon, where both high and low tide water levels were practically unaffected throughout the domain. However, there was a noticeable difference in the water levels inside the lagoon as illustrated in Figure 7.19 and Tables 7.12 and 7.13. The figure shows the water level time series for a typical tidal cycle during a spring tide, with the same trend being observed for the complete 14-day neap-spring tidal cycle.

Table 7.12: Maximum water level values in meters recorded during a typical spring tide, illustrated in Figure 7.19.

	Scenario	Max out (m)	% of SBL1	Max in (m)	% of SBL1
2D, only mass transfer	SBL1	4.24	-	2.80	-
2D, w/ mom. transfer	SBL2	4.24	0.0%	2.83	1.1%
	SBL3	4.25	0.1%	3.24	16.0%
3D, w/ mom. transfer	SBL4	4.22	-0.6%	2.80	0.2%
	SBL5	4.22	-0.5%	3.09	10.6%

Table 7.13: Minimum water level values in meters recorded during a typical spring tide, illustrated in Figure 7.19.

	Scenario	Min out (m)	% of SBL1	Min in (m)	% of SBL1
2D, only mass transfer	SBL1	-4.05	-	-2.72	-
2D, w/ mom. transfer	SBL2	-4.05	0.0%	-2.74	0.8%
	SBL3	-4.05	-0.1%	-3.17	16.8%
3D, w/ mom. transfer	SBL4	-4.04	-0.1%	-2.73	0.4%
	SBL5	-4.05	0.2%	-3.03	11.6%

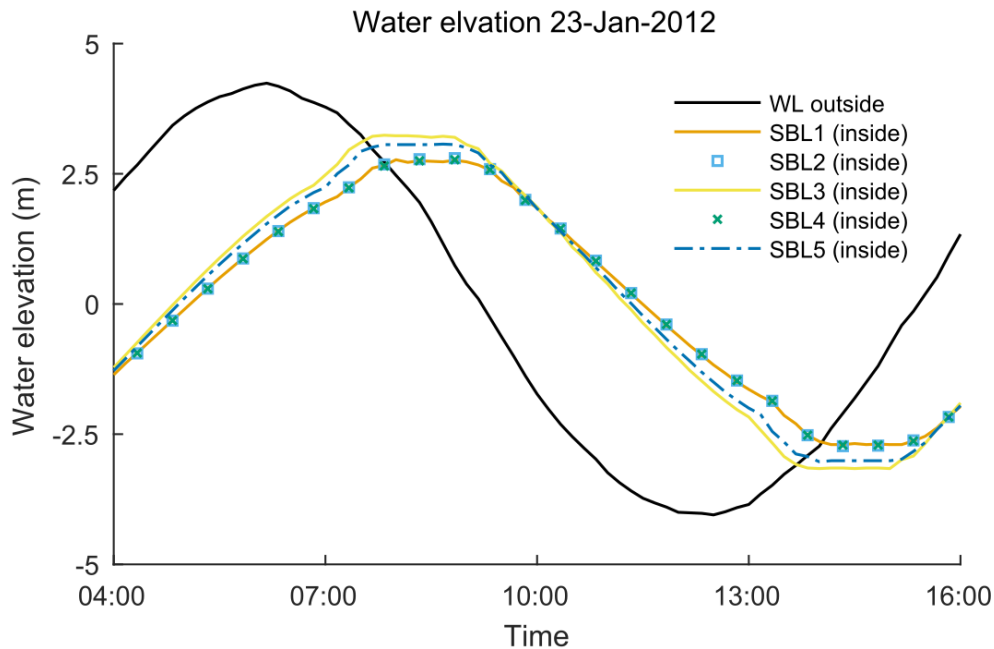


Figure 7.19: Comparison of water elevations inside the lagoon for the five different cases.

The most noticeable difference in the water elevations inside the lagoon occurred for the scenarios with the simplified velocity distribution (SBL3 and SBL5). Compared to SBL1 the maximum expected water level for the two scenarios had increased by 0.44 m and 0.29 m, respectively, and predictions of the lowest water levels had fallen by roughly the same amount. Both runs with the realistic velocity distribution (SBL2 and SBL4) did not result in any significant change of the water levels inside the lagoon. In both cases, the differences were limited to less than 1 per cent compared to the mass conservation only, namely SBL1 scenario.

7.4.5 Power output

Predicted annual energy potential is a critical factor when considering the construction of a tidal power plant. The instantaneous power production was calculated at each timestep using the power-head relationship (Figure 4.6) and then integrated over the time interval of the simulation to obtain total electricity generated in that period. The

simulation time was carefully selected to cover a typical neap-spring tidal cycle spanning over 14 days and taking into account the neap-spring variation in power production. The lagoon operation during this cycle for the baseline scenario (SBL 1) is illustrated in Figure 7.20, where the blue line represents water level outside the lagoon, magenta the water level on the inside and black the instantaneous power output during the generation stages. Neglecting any tidal variations that could develop over the rest of the year, this neap-spring tidal cycle was presumed to be sufficient for this assessment. The estimated annual (neap-spring averaged) energy was then calculated by extrapolating the simulation results over the period of one year (Xue et al. 2019). The total electricity generated for the baseline scenario (SBL1) was estimated to be about 578 GWh/year, which was consistent with predictions from past studies (Angeloudis et al. 2016b; Angeloudis and Falconer 2017; Angeloudis et al. 2018).

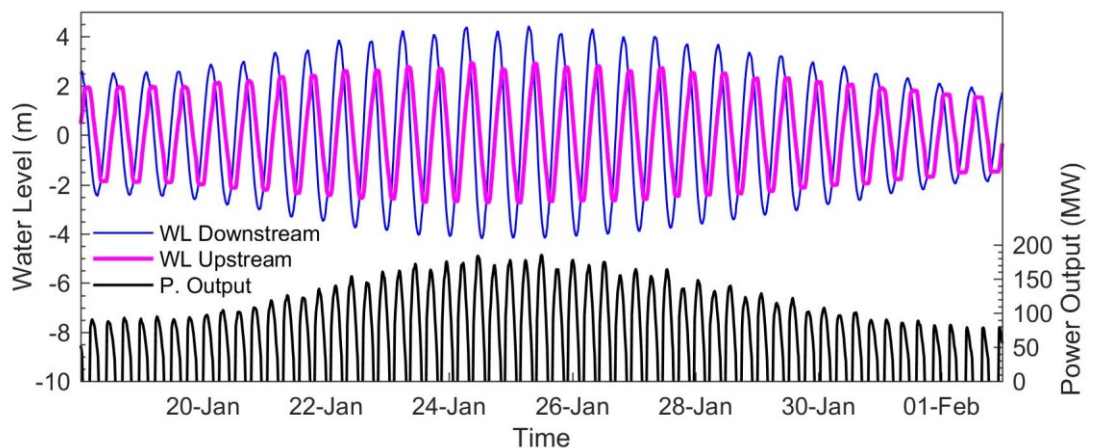


Figure 7.20: Predicted water levels on either side of the Severn Barrage and the corresponding power output over a typical neap-spring tidal cycle for the SBL 1 case.

Table 7.14: Typical annual energy prediction extrapolated from a characteristic neap-spring tidal cycle for the five different cases.

	Scenario	Annual Energy (GWh)	% of SBL1
2D, only mass transfer	SBL1	578.39	-
	SBL2	584.98	1.1 %
2D, w/ mom. transfer	SBL3	515.36	-10.9 %
	SBL4	578.63	0.0 %
3D, w/ mom. transfer	SBL5	532.85	-7.9 %

Unlike the local hydrodynamic conditions, the annual energy potential, which is mainly governed by the water level difference across the lagoon, was less sensitive to including momentum conservation in the numerical model. Predictions from all five simulations are summarised in Table 7.14. The values ranged from 515 GWh/year to 585 GWh/year. In scenarios SBL2 and SBL4, where a more realistic distribution of the velocity was predicted, the impact on the estimated power output was practically negligible with 1.1 per cent and less than 0.05 per cent increase respectively. The predicted power output for scenarios SBL3 and SBL5, with the simplified implementation of the jet, has decreased by 10.9 per cent and 7.9 per cent respectively. This is almost counter-intuitive since we would expect a higher energy output due to the higher water level amplitudes observed inside the lagoon (Figure 7.19). However, this resulted in the lagoon operating at higher heads and generating over shorter time intervals, which considerably decreased its efficiency (Figure 4.6 and Equation 4.8). This re-emphasises the importance of accurate modelling of the discharged jets. By just including the momentum conservation, without careful consideration for the appropriate distribution of the velocity profile, the model may produce inaccurate predictions for power output.

7.5 Summary

This chapter demonstrated how the modified Delft3D model can be used for the assessment of impacts on the hydrodynamic conditions due to the operation of a tidal range energy power plant. A continental shelf model was first used to determine the far-field extent of the impacts. It showed that Swansea Bay lagoon alone does not induce

changes to the tidal regime in the Bristol Channel. Therefore, the focus was shifted to the assessment of more local impacts created by the lagoon operation.

The momentum conservation of the turbine discharge was achieved by adding an extra term to the momentum equations, representing an equivalent external force acting on the volume of the computational cell across the turbine infrastructure. The calculation of the force is highly sensitive to the assumption of the outlet velocity distribution and choosing the most realistic velocity profile is of utmost significance. As was demonstrated for scenarios SBL3 and SBL5, a simplified velocity distribution concentrated over a small flow-through will result in a highly sophisticated 3D velocity field locally. The results showed that it had a noticeable effect on the velocity magnitude of the jet and on the tidal amplitude inside the lagoon, which negatively affected the estimated power output. The realistic distribution, that can be attributed to the flow exiting a diffuser (SBL2 and SBL4), still showed an increase in velocity magnitude, but did not show any drastic changes to the water levels and power estimation.

Regardless of the assumption of the structure of the velocity distribution, it was observed that 2D models generally predict a larger water level amplitude inside the lagoon compared to 3D models. Similar observations were found in literature, where depth-averaging failed to capture the higher complexities of the flow exiting the turbines, thereby affecting water levels in the proximity of the hydraulic structures (Jeffcoate et al. 2013). The differences between the 2D and 3D model in the case of realistic distribution were much closer than those of the simplified velocity distribution. The diffuser-induced flow from the case with the realistic distribution better matched the 2D nature of the tidal hydrodynamics. With larger computational costs of the 3D model, this indicated that depth-average models can be sufficient for performing hydrodynamic simulations, unless the study is concerned specifically about the vertical velocity profile of the jet.

The effects of the correct momentum transfer on the hydrodynamics were constrained to a relatively local area. As observed in Figure 7.15, there was very little change in the

hydrodynamics at a distance of about 20 times the turbine diameter downstream of the turbines. However, this could still have a significant impact on solute transport modelling and sediment fluxes, particularly in the vicinity of the turbines. Unbalanced erosion and deposition inside the lagoon, coupled with low velocities during the emptying stage, suggests that lagoon could be prone to silting. This would lead to a decrease in volume of the impoundment, which could significantly inhibit the performance of the power production, as well as incur additional operational costs for regular dredging of the basin. A downside of such regional-scale models is that they fail to include the rotational velocity of the flow exiting the turbines, which could have a further impact on sediment transport processes. To include such level of detail, it would be necessary to model the hydrodynamics at a much higher grid resolution, which is unnecessary for simulating the hydrodynamics characteristics at the regional scale.

The estimated power production indicated that just including the momentum conservation, without considering the appropriate assumptions, can have a negative effect on the accuracy of the power output predictions. While the momentum treatment is important from the erosion and sediment transport point of view, the results showed that power output was not as affected. Including the momentum, conservation contributed to only about 1 per cent change in the annual energy output for the cases with the realistic velocity distribution (SBL 2 and SBL 4). However, when assuming a simplified velocity distribution at the turbine exit (SBL 3 and SBL 5), the predicted energy output fell by as much as 10 per cent. The higher discharge rates in the case of simplified distribution meant that turbines operated under lower head difference towards the end of the generation cycle, which resulted in a reduced power output. This illustrated the sensitivity of power output to the assumption of the velocity distribution.

This study showed that modifications introduced to the Delft3D software transformed it into a model that is well capable of simulating the operation of any TRS in the estuarine environment. The model was used to assess the changes to the hydrodynamic conditions across the whole domain, including: (i) changes in water levels (ii) impact on the velocity field, (iii) magnification of bed shear stress, and (iv) estimation of power production. This

was achieved through both 2D and 3D simulations. The 3D model showed to be particularly important for the predictions of the maximum water levels inside the lagoon and estimation of bed shear stress, as 2D model failed to capture flow complexities of the discharged jets due to depth-averaging. Conservation of momentum was proved to be very important for correct predictions of hydrodynamics, however, it showed to be very sensitive to assumptions of the velocity distribution.

Future work could consider increasing the number of layers of the 3D model. However, each additional horizontal layer adds to the total computational time and makes the regional model less attractive for practical use and with limitations on the resources available for only a slight increase in the accuracy of the predictions. A multi-scale approach could prove to be more appropriate, where the high-resolution sub-grid scale model can be dynamically linked to a local or regional scale model. This could prove particularly useful for a more detailed investigation of scour and sediment transport associated with the turbine operation.

Chapter 8

Conclusion and future research

8.1 General conclusions

The research presented in this thesis has been directed towards improving hydrodynamic modelling tools for simulation of TRS, and thus improving the reliability of the model for assessing hydrodynamic impacts originating from the operation of TRS.

Climate change is the main driving factor in the accelerated development of renewable energy technologies. Tidal range is one of the most underused sources of renewable energy in the UK and worldwide, mainly due to the risk and uncertainties associated with negative environmental impacts and economic viability. Hydrodynamic simulations of tidal range schemes are one of the main tools that can be used to alleviate such risks and pave the way towards the deployment of the technology. Hydrodynamic simulations can be used to analyse water level change, velocity patterns and sediment transport – results which are fundamental in assessing environmental impacts. They can also be employed to predict power output, which is essential for assessing the efficiency and profitability of a TRS. They can be used before, during and after the TRS design process and can be refined to focus on just specific aspects of TRS operation, making them a versatile tool which can be very useful for informing decision makers. Accurate and efficient hydrodynamic models are therefore paramount for increasing the chance for future deployment of the technology.

The first research objective of this study was to assess the current methodologies for simulation of TRS in hydrodynamic models and implement the numerical techniques into the Delft3D software. The required numerical techniques were identified through

an extensive review of the literature. The study clearly presented their theoretical background and demonstrated their implementation into the source code of Delft3D model. In order to reach this objective, the proposed STPG Severn Barrage scheme was used as a case study throughout the development process. The scheme has already been investigated in many studies in the past, employing several different hydrodynamic models and numerical techniques, thereby making it an ideal case study for validation and benchmarking of the routines developed for the Delft3D model. The TRS module contained four major additions to the source code, including: (i) hydraulic structures modelled as coupled sink and source term in the continuity equation, (ii) an algorithm for determining the operational stages of the TRS operation, (iii) hill chart for modelling discharge through turbines, and (iv) orifice equation governing the discharge through sluices. The impacts of the barrage operation were assessed by analysing the differences between simulation runs with and without the barrage in place.

It was shown that modelling the Severn Barrage requires the extension of the domain to the continental shelf to prevent the scheme to affect open boundary conditions. The estimated annual energy production of an ebb-only generation scheme was predicted to be in the same range as the most recent published predictions (Angeloudis et al. 2016b). There is, however, some measure of uncertainty when it comes to annual power estimations because results are highly sensitive to the turbine manufacturing characteristics. Even though the study herein employed an industry-provided hill chart for the type of turbines intended for deployment in the STPG proposal, it should be acknowledged that actual characteristics are not publicly available and the energy estimation should be considered only as an indicator of the scheme's power generation potential. Also important is the appropriate selection of the representative tidal interval, which should cover the mean neap-spring tidal cycle for the estimation of the annual power production. The near-field impacts were assessed by analysing the changes in hydrodynamics on an estuary-scale. It was shown that ebb-only operation had both positive and negative impacts on the coastal flood risk. The maximum water levels upstream of the barrage (inside the impoundment) fell by more than 1 m, significantly

reducing the risk of flooding due to storm surges for communities in the upper reaches of the estuary. On the other side of the barrage (seaward side) the effect was reversed, with higher maximum water levels which resulted in higher flood risk. With 0.3 m rise just downstream of the barrage and gradually dropping towards the open boundary, the change on the seaward side was not as significant as inside the impoundment, however, it affected a substantially larger region, with impacts observed as far away as Cardigan Bay and the Irish Sea. The operation of the barrage significantly changed the entire tidal amplitude inside the impoundment, also affecting the minimum water elevations, resulting in permanently flooding of intertidal mudflats. Finally, the results showed a significant reduction on maximum current velocities domain-wide and increase in maximum flow velocity at the exit from turbines and sluice gates, substantially altering the sediment transport processes in the estuary. Direct comparisons with the past studies showed that Delft3D performed well in simulating impacts on the tidal regime due to the TRS operation, indicating that the modifications included in the TRS module are appropriate for modelling the hydrodynamics of tidal range projects in the Severn Estuary and Bristol Channel. The results also showed the importance of hydrodynamic modelling when designing TRSs, as they are fundamental for determining the environmental impacts of the scheme and its power production potential.

The second research objective of this study was to develop an improved method for numerical modelling of the momentum transfer through a TRS that can be applied to the finite-difference numerical models, such as Delft3D. The literature review showed the disregard for momentum conservation as one of the more significant shortcomings of existing TRS models. At the time of this writing, the only published example that has addressed the issue was found to be a study by Angeloudis et al. (2016b), where a momentum conservation technique involved artificially changing the water depth of the internal boundary in a finite-volume model. Delft3D is a finite-difference model, where hydraulic structures are instead represented through a coupled sink and source terms in the continuity equation. Thus, to model the momentum conservation, a novel technique was proposed, that parametrised the induced momentum as an external force acting on

the computational cell. This force was included in the computation through a new term added to the momentum equations. The appropriateness of the developed method was first tested on an experimental study involving a tidal barrage, followed by its application to a case study of Swansea Bay lagoon to investigate its impacts on a regional-scale hydrodynamic model.

The third research objective of this study was to validate the developed method for accurate momentum transfer. In order to reach this objective, a physical model of a tidal barrage was set up in a laboratory flume to record the velocity field of discharged jets downstream of the structure. Three different configurations were modelled, one resembling the conditions commonly encountered in TRS where all turbines are densely distributed with almost no gaps between them, and other two with just two active jets separated further apart, representing the situation if a scheme was designed with more than one turbine housing units. For each configuration, three different model structures were considered, including: (i) 2D simulation without the momentum conservation, (ii) 2D simulation with the momentum conservation, and (iii) 3D simulation with the momentum conservation. Simulation results from these three different model structures were compared to the measurements from the experiment.

The direct comparison of the predicted velocity fields with the observed data clearly showed that simulations with momentum conservation were more accurate in terms of velocity magnitude of exiting jets, showing a good match with the measurements. The simulations without momentum conservation were markedly underestimated, achieving only about 50 per cent of the measured velocity. Due to the drastically underpredicted velocity, they also failed to replicate the distinct Coanda effect, which was present in all simulations where momentum conservation was included. In general, the velocity results from the 3D simulation showed slightly better match with the observed data compared to the 2D simulation. The only exceptions were the 3D velocity predictions very close to the barrage in the cases with only two jets (THU 2 and THU 3). The issues were limited to the region of converging jets and were not present beyond the point where the jets merged. The issues were also not present in the THU 1 case where the five

jets have been positioned densely one next to another. However, in THU 2 and THU 3 cases the distance between the jets was increased, which resulted in a longer converging region with increased complexity of the flow. A finer mesh would be required to account for these complexities, thereby increasing the accuracy of the model. However, in practice, the turbines in TRSs are normally densely spaced in the turbine housing section of the structure, akin to the distribution of draft tubes in THU 1, which consequently makes the 3D hydrostatic model used herein suitable for predicting the jets produced during the operation of TRS.

Equivalent conclusions were also made for the bed shear stress results, where simulations without the momentum conservation considerably underestimated the magnitude of local bed shear stress. To illustrate the impact of momentum conservation, a ratio between the local and reference bed shear stress was used, where reference stress represented the mean value of the bed shear stress in an empty flume. Without momentum conservation, the bed shear stress was magnified by factor 6 in the region just downstream of the barrage. With momentum conservation included, the local bed shear was magnified by factors 20 and 35 for 2D and 3D simulations respectively. Extending the 2D model to 3D was found out to be much more important for the estimation of local bed shear, than for predicting the velocity field. While depth-averaged simulation already produced satisfactory velocity predictions, only a slight improvement was achieved through the 3D model. However, the 3D effects were clearly more substantial for bed shear stress results, which increased by 75 per cent from the 2D results. This illustrated the importance of a 3D model for estimation of sediment transport associated with the operation of a TRS. Bed shear stress is governed by the velocity field just above the bottom surface. The 3D model, coupled with momentum conservation, allows for a much more realistic representation of the vertical velocity profile. In the case of TRS, the discharged jets get attached to the bottom, deforming the vertical velocity profile to account for the higher velocities above the bottom surface, distorting the standard logarithmic profile assumed in depth-averaged shallow water flows.

The fourth and final research objective of this study was to assess the impacts of the developed method on the performance of the hydrodynamic model by applying it to a regional-scale tidal range energy project. In order to achieve this research objective, the proposed Swansea Bay lagoon scheme was used as a case study, deployed in an estuary-scale domain. While the model allowed for a full assessment of hydrodynamic impacts due to the TRS operation, the main focus was on the treatment of momentum and its effects on the results. The study combined the TRS module, developed through the first objective, with the momentum conservation technique, developed and validated through the second and third research objectives. To assess the contribution of momentum treatment, five different simulation scenarios were considered, the first one being the baseline scenario – a 2D simulation without momentum conservation. This was followed by two 2D simulation runs with momentum conservation, one assuming a realistic and the other assuming a simplified distribution of vertical velocity profile. Finally, a pair of 3D runs with momentum conservation was performed with both types of vertical distributions.

Simulation results showed that the developed momentum conservation affected only a relatively local area around the lagoon, constrained to the zone dominated by the jets exiting the TRS. In general, including the momentum conservation has visibly enlarged the length and magnitude of the jets. However, no changes to the hydrodynamics were observed beyond the point where the jets have completely dissipated. The results showed to be sensitive to the assumption of vertical velocity distribution. The simplified velocity distribution had a bigger impact on the hydrodynamics and power output estimation than the realistic distribution, emphasising the importance of selecting an appropriate vertical velocity profile for the discharged jet. Comparing the 2D and 3D simulations for the same type of vertical velocity distribution, showed very little change to the hydrodynamic predictions and power output estimations. There was, however, a clear increase in local bed shear stress from 2D to 3D model results. The magnification of bed shear stress was again much more prominent with the simplified vertical velocity distribution and less so with the realistic distribution. In general, these results indicate

that 2D hydraulic models with momentum conservation are sufficient for analysing hydrodynamic impacts of TRS on a regional scale. However, the 3D model has proved to be indispensable for accurate predictions of local-scale impacts, especially in an around the lagoon.

The main finding of this research can be summarised as follows:

- The experimental study in the flume showed that the developed method for momentum conservation significantly improved the accuracy of velocity predictions. Without the momentum conservation, the simulated results underpredicted the velocity magnitude of the jets by more than 50 %. After the momentum conservation was introduced, the simulation results showed a nearly exact fit with the measured velocity data. The results with densely distributed turbines were more reliable than the results with only two turbines that were separated further apart. In the case of the latter, a higher resolution mesh and a more sophisticated model is needed to increase accuracy. However, the case with densely distributed turbines is more common with TRS, making the modified Delft3D model sufficient in most cases.

- It was shown that ignoring momentum conservation leads to significantly underestimated predictions of bed shear stress in the region just downstream of the turbines. This was concluded through a physical experiment and simulations of the Swansea Bay lagoon case study. Results showed that correct momentum treatment is essential for accurate predictions of sediment transport processes in the vicinity of a TRS.

- The effects of the momentum conservation were limited to the area in the vicinity of the Swansea Bay lagoon and had no visible impact on the far-field conditions. While a simplified model might be sufficient for assessment of the regional-scale impacts, the momentum conservation method proved to be essential for accurate

assessment of local conditions, such as the increased velocity of the discharged jet, estimation of power production and magnified bed shear stress, associated with increased erosion and changes to the sediment transport patterns.

- Delft3D showed to be a reliable tool for simulation of the TRSs. Based on the benchmarking results, it performed on par with other established models, such as EFDC and DIVAST. This includes: (i) assessment of water level changes due to the TRS operation, (ii) impact of the TRS operation on the velocity field, (iii) magnification of local bed shear stress, (iv) estimation of instantaneous and annual power output, (v) modelling the impacts on the open boundary by the use of the extended domain (to the continental shelf), and (vi) expanding the depth-averaged model to 3D. The model was further improved with the addition of the technique for momentum conservation of flow through the hydraulic structures. This qualified the model to be used as a multi-scale tool, that can simultaneously produce satisfactory results on the global, regional, and local scales.

8.2 Recommendations for further study

Even though this thesis addressed several topics on tidal range modelling, some areas of interest were left unexplored due to lack of data availability and time constraints. Therefore, a number of considerations are recommended for further research.

To date, most TRS studies have focused on a single tidal range scheme, with some limited studies involving the operation of two or three schemes simultaneously. However, there have been various proposals for a number of different tidal range schemes across the region, including a fleet of 6 tidal lagoons, proposed by Tidal Lagoon Power (2016). To assess such networks of TRS schemes, a multi-scale modelling approach is needed, that includes: (i) assessment of potential far-field impacts due to the cumulative effect, (ii) investigation of potential interactions between the individual schemes and (iii) analysis of impact of those interactions on the combined capacity for power production.

The TRS schemes could be further improved by optimising the operation parameters to maximise the power production and to minimize the environmental impacts. These two factors are usually mutually exclusive, which means that the problem could be further expanded to a multi-objective optimisation study, looking for the best trade-off between the two. In the first instance, the optimisation can be performed in combination with simplified formulations, such as 0D models, and using state of the art techniques, such as genetic algorithms. Once the best trade-off is determined, the resulting parameters could be fed back to the Delft3D model to perform a full analysis of power production and impacts on the environment of the selected parameters.

The results of this study demonstrated the importance of the momentum conservation of the flow through hydraulic structures on predictions of local bed shear stress. The results indicated that the lagoon could be prone to silting due to the large recirculation effects that occur during the filling of the impoundment and low velocities during releasing. Further study on sediment and solutes transport, including the momentum conservation technique, is required to get a better impact of such schemes and importance of the modifications carried out in this study.

This study has shown that momentum treatment is sensitive to the assumption of the vertical velocity distribution in the jets exiting the TRS. Actual velocity profiles are usually hard to obtain because they rely on detail turbine characteristics, which manufacturing companies are often reluctant to share. Obtaining such velocity profiles requires either measuring flow from a laboratory-scale model of a turbine or use of sophisticated CFD models for turbomachinery design. Either way, obtaining such data would considerably reduce the uncertainty associated with the assumption of how the discharge is represented in the simulation.

Vertical velocity profile will also change through the different periods of the operation cycle. The turbines, together with the diffuser, will perform with variable efficiency during different periods of the generation stage. With ever-changing head difference and depth of tailwater, the vertical velocity profile can change significantly over time.

Because of the unavailability of data, the current model assumes a constant velocity distribution throughout the simulation. Acquiring those changes through physical experiments or CFD simulations of the turbines and implementing a routine that could vary the velocity distribution over time could even further increase the accuracy of the model, particularly with the 3D simulations.

Finally, the computational efficiency of the model could be significantly enhanced by high-performance computing (HPC). Even though Delft3D already has capabilities for parallel computations, the technique is not fully operational when TRS module is included in the simulation. Full parallelization of the TRS module would significantly reduce the required computation time, while also enabling the use of more complex model setups, with even larger domains, high-resolution grids and 3D models with a greater number of vertical layers.

References

- Adcock, T.A.A. et al. 2011. The Open Boundary Problem in Tidal Basin Modelling with Energy Extraction. *Proceedings of the 9th European Wave and Tidal Energy Conference. Southampton, UK*, pp. 1–7.
- Adcock, T.A.A. et al. 2015. Tidal power generation – A review of hydrodynamic modelling. *Proceedings of the Institution of Mechanical Engineers, Part A: Journal of Power and Energy* 229(7), pp. 755–771. Available at: <http://journals.sagepub.com/doi/10.1177/0957650915570349>.
- Aggidis, G.A. and Benzon, D.S. 2013. Operational optimisation of a tidal barrage across the Mersey estuary using 0-D modelling. *Ocean Engineering* 66, pp. 69–81. Available at: <http://dx.doi.org/10.1016/j.oceaneng.2013.03.019>.
- Aggidis, G.A. and Feather, O. 2012. Tidal range turbines and generation on the Solway Firth. *Renewable Energy* 43, pp. 9–17. doi: <http://dx.doi.org/10.1016/j.renene.2011.11.045>.
- Ahmadian, R. et al. 2010a. Hydro-environmental modeling of proposed Severn barrage, UK. *Proceedings of the Institution of Civil Engineers - Energy* 163(3), pp. 107–117. Available at: <http://www.icevirtuallibrary.com/doi/10.1680/ener.2010.163.3.107>.
- Ahmadian, R. et al. 2010b. Hydro-environmental modelling of off-shore and coastally attached impoundments of The North Wales coast. In: *Proceedings of the 1st European IAHR Congress*. Edinburgh. Available at: <http://orca.cf.ac.uk/id/eprint/7601>.
- Ahmadian, R. et al. 2012. Far-field modelling of the hydro-environmental impact of tidal stream turbines. *Renewable Energy* 38(1), pp. 107–116. Available at: <http://dx.doi.org/10.1016/j.renene.2011.07.005>.

References

- Ahmadian, R. et al. 2014a. Comparison of hydro-environmental impacts for ebb-only and two-way generation for a Severn Barrage. *Computers & Geosciences* 71, pp. 11–19. Available at: <http://dx.doi.org/10.1016/j.cageo.2014.05.006>.
- Ahmadian, R. et al. 2014b. Sea level rise in the Severn Estuary and Bristol Channel and impacts of a Severn Barrage. *Computers & Geosciences* 66, pp. 94–105. Available at: <http://dx.doi.org/10.1016/j.cageo.2013.12.011>.
- Alcrudo, F. 2004. A state of the art review on mathematical modelling of flood propagation. *IMPACT project*, pp. 1–22.
- Andre, H. 1976. Operating experience with bulb units at the Rance tidal power plant and other French hydro-power sites. *IEEE Transactions on Power Apparatus and Systems* 95(4), pp. 1038–1044.
- Andre, H. 1978. Ten Years of Experience at the ‘La Rance’ Tidal Power Plant. *Ocean Management* 4, pp. 165–178. doi: [http://dx.doi.org/10.1016/0302-184X\(78\)90023-9](http://dx.doi.org/10.1016/0302-184X(78)90023-9).
- Andritz Hydro 2016. Technology Fit for the Future. *Hydro News* (29), pp. 18–21.
- Angeloudis, A. et al. 2016a. Numerical model simulations for optimisation of tidal lagoon schemes. *Applied Energy* 165, pp. 522–536. doi: <http://dx.doi.org/10.1016/j.apenergy.2015.12.079>.
- Angeloudis, A. et al. 2016b. Representation and operation of tidal energy impoundments in a coastal hydrodynamic model. *Renewable Energy* 99, pp. 1103–1115. Available at: <http://www.sciencedirect.com/science/article/pii/S0960148116307042> [Accessed: 19 September 2016].
- Angeloudis, A. et al. 2018. Optimising tidal range power plant operation. *Applied Energy* 212(November 2017), pp. 680–690. Available at: <https://doi.org/10.1016/j.apenergy.2017.12.052>.

References

- Angeloudis, A. and Falconer, R.A. 2017. Sensitivity of tidal lagoon and barrage hydrodynamic impacts and energy outputs to operational characteristics. *Renewable Energy* 114, pp. 337–351. Available at: <http://www.sciencedirect.com/science/article/pii/S0960148116307340> [Accessed: 3 November 2017].
- Arakawa, A. and Lamb, V.R. 1977. Computational Design of the Basic Dynamical Processes of the UCLA General Circulation Model. In: *METHODS IN COMPUTATIONAL PHYSICS: Advances in Research and Applications: Volume 17: General Circulation Models of the Atmosphere*. ACADEMIC PRESS, INC., pp. 173–265. Available at: <http://dx.doi.org/10.1016/B978-0-12-460817-7.50009-4>.
- Atkins 2010. *DECC SETS Bi-Directional Very Low Head Turbine Study*.
- Atkins and Rolls-Royce 2010. *Severn Embryonic Technologies Scheme - Concept design of a very-low head dual generation tidal scheme for the severn estuary*.
- Atlantis Resources Limited 2018. MeyGen, Tidal Projects, Atlantis Resources. Available at: <https://www.atlantisresourcesltd.com/projects/meygen/> [Accessed: 10 May 2018].
- Bae, Y.H. et al. 2010. Lake Sihwa tidal power plant project. *Ocean Engineering* 37(5–6), pp. 454–463. Available at: <http://dx.doi.org/10.1016/j.oceaneng.2010.01.015>.
- Baker, A.C. 1991. *Tidal power*. London: Peter Peregrinus Ltd. on behalf of the Institution of Electrical Engineers.
- Bardina, J.E. et al. 1997. *Turbulence Modeling Validation, Testing, and Development (Report 110446)*. doi: <http://dx.doi.org/10.2514/6.1997-2121>.
- BEIS 2016. Hinkley Point C. Available at: <https://www.gov.uk/government/collections/hinkley-point-c> [Accessed: 7 February 2019].

References

- BEIS 2018a. DUKES 2018 Chapter 5: Electricity. In: *Digest of UK Energy Statistics (DUKES)*. Department for Business, Energy & Industrial Strategy, pp. 111–153. doi: <http://dx.doi.org/10.1016/B978-0-12-374849-2.00005-8>.
- BEIS 2018b. DUKES 2018 Chapter 6: Renewable sources of energy. In: *Digest of UK Energy Statistics (DUKES)*. Department for Business, Energy & Industrial Strategy, pp. 155–187. doi: <http://dx.doi.org/10.1186/gb-2004-5-5-223\rgb-2004-5-5-223> [pii].
- Bernshtein, L.B. 1972. Kislaya Guba Experimental Tidal Power Plant and Problem of the Use of Tidal Energy. In: *Tidal Power*. Boston, MA: Springer US, pp. 215–238. Available at: http://link.springer.com/10.1007/978-1-4613-4592-3_6.
- Boccard, N. 2009. Capacity factor of wind power realized values vs. estimates. *Energy Policy*. doi: <http://dx.doi.org/10.1016/j.enpol.2009.02.046>.
- BODC 2017. Download UK Tide Gauge Network data from BODC. Available at: https://www.bodc.ac.uk/data/hosted_data_systems/sea_level/uk_tide_gauge_network/ [Accessed: 30 January 2017].
- Bourban, S.E. et al. 2014. Coastal shelf model of northern European waters to inform tidal power industry decisions: SMARTtide. *Underwater Technology* 32(1), pp. 15–26. doi: <http://dx.doi.org/10.3723/ut.32.015>.
- Brammer, J. et al. 2014. Physical and numerical modelling of the Severn Barrage. *Science China Technological Sciences* 57(8), pp. 1471–1481. doi: <http://dx.doi.org/10.1007/s11431-014-5602-5>.
- Bray, S. et al. 2016. Impact of representation of hydraulic structures in modelling a Severn barrage. *Computers & Geosciences* 89, pp. 96–106. Available at: <http://linkinghub.elsevier.com/retrieve/pii/S0098300416300206> [Accessed: 19 September 2016].
- Burrows, R. et al. 2009. The tidal range energy potential of the West Coast of the United Kingdom. *Applied Ocean Research* 31(4), pp. 229–238. doi: <http://dx.doi.org/10.1016/j.apor.2009.10.002>.

References

- Carne, B.G. 1995. Thomas Fulljames, 1808-74: Surveyor, Architect, and Civil Engineer. *Transactions of the Bristol and Gloucestershire Archaeological Society* 113, pp. 7–20.
- Casulli, V. and Stelling, G.S. 1998. Numerical Simulation of 3D Quasi-Hydrostatic, Free-Surface Flows. *Journal of Hydraulic Engineering* 124(7), pp. 678–686. Available at: <https://ascelibrary.org/doi/abs/10.1061/%28ASCE%290733-9429%281998%29124%3A7%28678%29>.
- Cebr 2014. *The Economic Case for a Tidal Lagoon Industry in the UK*. London.
- Chaineux, M.C. and Charlier, R.H. 2008. Women's tidal power plant Forty candles for Kislaya Guba TPP. *Renewable and Sustainable Energy Reviews* 12(9), pp. 2508–2517. doi: <http://dx.doi.org/10.1016/j.rser.2007.03.013>.
- Charlier, R.H. 2007. Forty candles for the Rance River TPP tides provide renewable and sustainable power generation. *Renewable and Sustainable Energy Reviews* 11(9), pp. 2032–2057. doi: 10.1016/j.rser.2006.03.015.
- Charlier, R.H. and Menanteau, L. 1997. The saga of tide mills. *Renewable and Sustainable Energy Reviews* 1(3), pp. 171–207. doi: [http://dx.doi.org/10.1016/S1364-0321\(97\)00005-1](http://dx.doi.org/10.1016/S1364-0321(97)00005-1).
- Cho, Y.S. et al. 2012. The construction of a tidal power plant at Sihwa Lake, Korea. *Energy Sources, Part A: Recovery, Utilization and Environmental Effects* 34(14), pp. 1280–1287. doi: <http://dx.doi.org/10.1080/15567030903586055>.
- Clarke, J.A. et al. 2006. Regulating the output characteristics of tidal current power stations to facilitate better base load matching over the lunar cycle. *Renewable Energy* 31(2), pp. 173–180. Available at: <https://linkinghub.elsevier.com/retrieve/pii/S0960148105002247>.
- Cornett, A. et al. 2013. Assessment of hydrodynamic impacts from tidal power lagoons in the Bay of Fundy. *International Journal of Marine Energy* 1, pp. 33–54. Available at: <http://dx.doi.org/10.1016/j.ijome.2013.05.006>.

References

- Courant, R. et al. 1967. On the Partial Difference Equations. *IBM Journal of Research and Development* 11(March), pp. 215–234. doi: <http://dx.doi.org/10.1147/rd.112.0215>.
- Crown Estates 2016. *Severn Estuary Long Term Morphology*. The Crown Estate.
- Dadswell, M.J. and Rulifson, R.A. 1994. Macrotidal estuaries: a region of collision between migratory marine animals and tidal power development. *Biological Journal of the Linnean Society* 51(1–2), pp. 93–113. Available at: <https://academic.oup.com/biolinnean/article-lookup/doi/10.1111/j.1095-8312.1994.tb00947.x>.
- DECC 2008. *Analysis of Options for Tidal Power Development in the Severn Estuary*.
- DECC 2010. Severn Tidal Power - Feasibility Study: Conclusions and Summary Report. Available at: <https://www.gov.uk/government/publications/1-severn-tidal-power-feasibility-study-conclusions-and-summary-report> [Accessed: 10 November 2016].
- Deltares 2014. Delft3D-FLOW User Manual Hydro-Morphodynamics, Version 3.15. Available at: [https://oss.deltares.nl/documents/183920/185723/Delft3D-FLOW User Manual.pdf](https://oss.deltares.nl/documents/183920/185723/Delft3D-FLOW%20User%20Manual.pdf) [Accessed: 25 October 2015].
- Dincer, I. 2000. Renewable energy and sustainable development: a crucial review. *Renewable and Sustainable Energy Reviews* 4(2), pp. 157–175. Available at: <http://linkinghub.elsevier.com/retrieve/pii/S1364032199000118>.
- DTI 2003. *Our energy future - creating a low carbon economy*.
- Du, M. et al. 2017. Assessment of tidal range energy resources based on flux conservation in Jiantiao Bay, China. *Journal of Ocean University of China* 16(6), pp. 1090–1096. Available at: <http://link.springer.com/10.1007/s11802-017-3247-2>.
- Dyer, K.R. 1984. Sedimentation processes in the Bristol Channel/Severn Estuary. *Marine Pollution Bulletin* 15(2), pp. 53–57. Available at: <https://linkinghub.elsevier.com/retrieve/pii/0025326X84904624>.

References

- Ellabban, O. et al. 2014. Renewable energy resources: Current status, future prospects and their enabling technology. *Renewable and Sustainable Energy Reviews* 39, pp. 748–764. Available at: <http://dx.doi.org/10.1016/j.rser.2014.07.113>.
- EMU Limited 2012. *Report for Centre for Research into Environment and Health (CREH) – Aberystwyth University, Swansea Bay Current Monitoring – Operational Report*. Southampton.
- Evans, S.E. et al. 2004. The North Wales offshore tidal impoundment scheme: a preliminary study of requirements, constraints and opportunities. In: *Proceedings of MAREC 2004 3rd International Conference on Marine Renewable Energy*. Bristol, pp. 97–107. Available at: <http://orca.cf.ac.uk/id/eprint/16531>.
- Falconer, R.A. et al. 2009. The Severn Barrage and other tidal energy options: Hydrodynamic and power output modeling. *Science in China, Series E: Technological Sciences* 52(11), pp. 3413–3424. doi: <http://dx.doi.org/10.1007/s11431-009-0366-z>.
- Ferziger, J.H. and Perić, M. 2002. *Computational Methods for Fluid Dynamics*. Berlin, Heidelberg: Springer Berlin Heidelberg. Available at: <http://link.springer.com/10.1007/978-3-642-56026-2>.
- Fulton, S.R. 2004. *Semi-Implicit Time Differencing*. Potsdam, New York, USA.
- Gao, C. and Adcock, T.A.A. 2015. Numerical Investigation of Resonance in the Bristol Channel.
- Guardian Media Group 2018. Government rejects plan for £1.3bn tidal lagoon in Swansea. Available at: <https://www.theguardian.com/business/2018/jun/25/government-rejects-plan-for-tidal-lagoon-in-swansea> [Accessed: 18 September 2018].
- Gubin, M.F. 1973. *Draft tubes of hydro-electric stations*. Published for the Bureau of Reclamation, U.S. Dept. of the Interior and National Science Foundation, Washington, D.C. by Amerind Pub. Co. Available at: <https://books.google.co.uk/books?id=ex3dAAAAIAAJ>.

References

- Hammons, T.J. 1993. Tidal power. *Proceedings of the IEEE* 81(3), pp. 419–433. Available at: <http://ieeexplore.ieee.org/document/241486/>.
- Hamrick, J.M. 1992. A Three-Dimensional Environmental Fluid Dynamics Computer Code: Theoretical and Computational Aspects. *The College of William and Mary, Virginia Institute of Marine Science. Special Report 317*, 63 pp. (317). doi: <http://dx.doi.org/10.21220/V5TT6C>.
- Hendry, C. 2016. The role of tidal lagoons. Available at: <https://hendryreview.files.wordpress.com/2016/08/hendry-review-final-report-english-version.pdf> [Accessed: 6 January 2017].
- Hinson, S. 2018. Tidal lagoons. *BRIEFING PAPER* (7940), p. 25. Available at: <researchbriefings.files.parliament.uk/documents/CBP-7940/CBP-7940.pdf>.
- Hooper, T. and Austen, M. 2013. Tidal barrages in the UK: Ecological and social impacts, potential mitigation, and tools to support barrage planning. *Renewable and Sustainable Energy Reviews* 23, pp. 289–298. Available at: <http://dx.doi.org/10.1016/j.rser.2013.03.001>.
- Hulsbergen, K. et al. 2008. Dynamic Tidal Power (DTP) – A new approach to exploit tides. *Proceedings of the 2nd International Conference on Ocean Energy* (October), pp. 1–10.
- Hunter, N.M. et al. 2007. Simple spatially-distributed models for predicting flood inundation : A review. *Geomorphology* 90, pp. 208–225. doi: <http://dx.doi.org/10.1016/j.geomorph.2006.10.021>.
- IRENA 2018a. Hydropower. Available at: <https://www.irena.org/hydropower> [Accessed: 6 November 2018].
- IRENA 2018b. Ocean energy. Available at: <https://www.irena.org/ocean> [Accessed: 6 November 2018].

References

- Jeffcoate, P. et al. 2013. Flow Due to Multiple Jets Downstream of a Barrage: Experiments, 3D Computational Fluid Dynamics, and Depth-Averaged Modeling. *Journal of Hydraulic Engineering* 139(7), pp. 754–762. Available at: <http://ascelibrary.org/doi/10.1061/%28ASCE%29HY.1943-7900.0000729>.
- Jeffcoate, P. et al. 2017. Flow and bed-shear magnification downstream of a barrage with swirl generated in ducts by stators and rotors. *Journal of Hydraulic Engineering* 143(2), pp. 1–8. doi: [http://dx.doi.org/10.1061/\(ASCE\)HY.1943-7900.0001228](http://dx.doi.org/10.1061/(ASCE)HY.1943-7900.0001228).
- Kadiri, M. et al. 2012. A review of the potential water quality impacts of tidal renewable energy systems. *Renewable and Sustainable Energy Reviews* 16(1), pp. 329–341. Available at: <http://dx.doi.org/10.1016/j.rser.2011.07.160>.
- Kelly, K.A. et al. 2012. An energy and carbon life cycle assessment of tidal power case study: The proposed Cardiff-Weston severn barrage scheme. *Energy* 44(1), pp. 692–701. Available at: <http://dx.doi.org/10.1016/j.energy.2012.05.023>.
- Kirby, R. and Retière, C. 2009. Comparing environmental effects of Rance and Severn barrages. *Proceedings of the Institution of Civil Engineers - Maritime Engineering* 162(MA1), pp. 11–26. Available at: <http://www.icevirtuallibrary.com/doi/10.1680/maen.2009.162.4.155>.
- Lauder, B.E. and Spalding, D.B. 1974. The numerical computation of turbulent flows. *Computer Methods in Applied Mechanics and Engineering* 3(2), pp. 269–289. doi: [http://dx.doi.org/10.1016/0045-7825\(74\)90029-2](http://dx.doi.org/10.1016/0045-7825(74)90029-2).
- Lee, D.S. et al. 2010. Experimental investigation on the relationship between sluice caisson shape of tidal power plant and the water discharge capability. *Renewable Energy* 35(10), pp. 2243–2256. Available at: <http://dx.doi.org/10.1016/j.renene.2010.02.018>.
- Lee, H.S. 2011. Ocean renewable energy: Tidal power in the Yellow Sea. *Journal of International Development and Cooperation* 17(3), pp. 29–44.

References

- Lesser, G.R. et al. 2004. Development and validation of a three-dimensional morphological model. *Coastal Engineering* 51(8–9), pp. 883–915. doi: <http://dx.doi.org/10.1016/j.coastaleng.2004.07.014>.
- Li, Y. and Pan, D.-Z. 2017. The ebb and flow of tidal barrage development in Zhejiang Province, China. *Renewable and Sustainable Energy Reviews* 80, pp. 380–389. Available at: <http://www.sciencedirect.com/science/article/pii/S1364032117307578> [Accessed: 5 July 2017].
- Liang, D. et al. 2014. Study on Tidal Resonance in Severn Estuary and Bristol Channel. *Coastal Engineering Journal* 56(1), pp. 1450002-1-1450002–18. Available at: <http://www.worldscientific.com/doi/abs/10.1142/S0578563414500028>.
- Lin, J. et al. 2015. Refined representation of turbines using a 3D SWE model for predicting distributions of velocity deficit and tidal energy density. *International journal of energy research* 39(13), pp. 1828–1842.
- Marshall, J. et al. 1997. Hydrostatic, quasi-hydrostatic, and nonhydrostatic ocean modeling. *Journal of Geophysical Research: Oceans* 102(C3), pp. 5733–5752. Available at: <https://agupubs.onlinelibrary.wiley.com/doi/abs/10.1029/96JC02776>.
- Nash, J.E. and Sutcliffe, J. V. 1970. River Flow Forecasting Through Conceptual Models Part I-a Discussion of Principles. *Journal of Hydrology* 10, pp. 282–290. doi: [http://dx.doi.org/10.1016/0022-1694\(70\)90255-6](http://dx.doi.org/10.1016/0022-1694(70)90255-6).
- Nasr, A. and Lai, J.C.S. 1997. Two parallel plane jets: Mean flow and effects of acoustic excitation. *Experiments in Fluids* 22(3), pp. 251–260. doi: <http://dx.doi.org/10.1007/s003480050044>.
- Neelz, S. and Pender, G. 2009. *Desktop review of 2D hydraulic modelling packages*. Bristol.
- Neelz, S. and Pender, G. 2013. *Benchmarking the latest generation of 2D hydraulic modelling packages*. Bristol.

References

- Neill, S.P. et al. 2017. The Impact of Marine Renewable Energy Extraction on Sediment Dynamics. In: Yang, Z. and Copping, A. eds. *Marine Renewable Energy*. Springer International Publishing, pp. 279–304. Available at: https://doi.org/10.1007/978-3-319-53536-4_12.
- Neill, S.P. et al. 2018. Tidal range energy resource and optimization – Past perspectives and future challenges. *Renewable Energy* 127, pp. 763–778. Available at: <https://doi.org/10.1016/j.renene.2018.05.007>.
- Neill, S.P. and Hashemi, M.R. 2018. Tidal Energy. In: *Fundamentals of Ocean Renewable Energy*. Elsevier, pp. 47–81. Available at: <https://linkinghub.elsevier.com/retrieve/pii/B9780128104484000033>.
- Nortek 2009. VECTRINO User Guide 2009., p. 42.
- Nova Innovation 2019. Bluemull Sound, Shetland. Available at: <https://www.novainnovation.com/bluemull-sound> [Accessed: 1 September 2019].
- Oh, S.H. et al. 2016. Three-dimensional experiment and numerical simulation of the discharge performance of sluice passageway for tidal power plant. *Renewable Energy* 92, pp. 462–473. Available at: <http://dx.doi.org/10.1016/j.renene.2016.02.023>.
- Parker, B.B. 2007. *Tidal analysis and prediction*. Silver Spring, Maryland: NOAA, NOS Center for Operational Oceanographic Products and Services. Available at: https://tidesandcurrents.noaa.gov/publications/Tidal_Analysis_and_Predictions.pdf.
- Petley, S. and Aggidis, G.A. 2016. Swansea Bay tidal lagoon annual energy estimation. *Ocean Engineering* 111, pp. 348–357. Available at: <http://dx.doi.org/10.1016/j.oceaneng.2015.11.022>.
- Prandle, D. 1984. Simple theory for designing tidal power schemes. *Advances in Water Resources* 7(1), pp. 21–27. doi: [http://dx.doi.org/10.1016/0309-1708\(84\)90026-5](http://dx.doi.org/10.1016/0309-1708(84)90026-5).

References

- Rahman, A. and Venugopal, V. 2015. Inter-Comparison of 3D Tidal Flow Models Applied To Orkney Islands and Pentland Firth. *11th European Wave and Tidal Energy Conference (EWTEC 2015)* (September), pp. 1–10.
- Rajar, R. 1997. *Hidromehanika*. Hydromecha. Ljubljana: University of Ljubljana, Faculty of Civil and Geodetic Engineering.
- Reba, I. 1966. APPLICATIONS OF THE COANDA EFFECT. *Scientific American* 214(6), pp. 84–93. Available at: <http://www.jstor.org/stable/24930967>.
- Reddy, J.N. 1993. *An introduction to the finite element method*. McGraw-Hill New York.
- REN21 2018. *Renewables 2018 Global Status Report*. Paris.
- Retiere, C. 1994. Tidal power and the aquatic environment of La Rance. *Biological Journal of the Linnean Society* 51(1–2), pp. 25–36. Available at: <http://linkinghub.elsevier.com/retrieve/doi/10.1006/bijl.1994.1004>.
- Rijkswaterstaat 2016. *WAQUA/TRIWAQ - two- and three-dimensional shallow water flow model. Technical documentation*. Available at: <http://simona.deltares.nl/release/doc/techdoc/waquapublic/sim1999-01.pdf> [Accessed: 12 April 2017].
- van Rijn, L.C. 1993. *Principles of sediment transport in rivers, estuaries and coastal seas*. Aqua Publications: Amsterdam.
- Roache, P.J. 1998. *Fundamentals of computational fluid dynamics*. NM: Hermosa Publishers, Albuquerque.
- Roberts, A. et al. 2016. Current tidal power technologies and their suitability for applications in coastal and marine areas. *Journal of Ocean Engineering and Marine Energy* 2(2), pp. 227–245. doi: <http://dx.doi.org/10.1007/s40722-016-0044-8>.
- Roberts, F. 1982. Energy accounting of river severn tidal power schemes. *Applied Energy* 11(3), pp. 197–213. Available at: <http://linkinghub.elsevier.com/retrieve/pii/0306261982900022>.

References

- Rosatti, G. et al. 2011. An accurate and efficient semi-implicit method for section-averaged free-surface flow modelling. *International Journal for Numerical Methods in Fluids* 65(4), pp. 448–473. Available at: <http://doi.wiley.com/10.1002/flid.2191>.
- Rourke, F.O. et al. 2010. Tidal energy update 2009. *Applied Energy* 87(2), pp. 398–409. Available at: <http://dx.doi.org/10.1016/j.apenergy.2009.08.014>.
- Seazone 2013. 1 Arcsecond Gridded Bathymetry [ASC geospatial data]. Available at: <http://digimap.edina.ac.uk> [Accessed: 1 September 2016].
- Shi, B. et al. 2015. Determination of Critical Shear Stresses for Erosion and Deposition Based on In Situ Measurements of Currents and Waves over an Intertidal Mudflat. *Journal of Coastal Research* 316(November), pp. 1344–1356. Available at: <http://www.bioone.org/doi/10.2112/JCOASTRES-D-14-00239.1>.
- Sobey, B.R.J. et al. 1989. Horizontal round buoyant jet in shallow water. *Journal of Hydraulic Engineering* 114(8), pp. 910–929. doi: [http://dx.doi.org/10.1061/\(ASCE\)0733-9429\(1988\)114:8\(910\)](http://dx.doi.org/10.1061/(ASCE)0733-9429(1988)114:8(910)).
- Soulsby, R.L. 1995. Bed shear-stresses due to combined waves and currents. In: M.J.F. Stive, H.J. de Vriend, J. Fredsøe, L. Hamm, R.L. Soulsby, C. T. and Winterwerp, J. C. eds. *Advances in Coastal Morphodynamics*. Delft Hydraulics, The Netherlands, pp. 4–20 to 4–23.
- Stansby, P.K. et al. 2016. Oscillatory flows around a headland by 3D modelling with hydrostatic pressure and implicit bed shear stress comparing with experiment and depth-averaged modelling. *Coastal Engineering* 116, pp. 1–14. Available at: <http://dx.doi.org/10.1016/j.coastaleng.2016.05.008>.
- Stelling, G.S. 1984. *On the construction of computational methods for shallow water flow problems*. Delft University of Technology. Available at: <http://resolver.tudelft.nl/uuid:d3b818cb-9f91-4369-a03e-d90c8c175a96>.

References

- Stelling, G.S. and Van Kester, J.A.T.M. 1994. On the approximation of horizontal gradients in sigma co-ordinates for bathymetry with steep bottom slopes. *International Journal for Numerical Methods in Fluids* 18(10), pp. 915–935. Available at: <https://onlinelibrary.wiley.com/doi/abs/10.1002/flid.1650181003>.
- STPG 1989. *The Severn Barrage Project : general report*.
- The National Oceanography Centre 2018. Continental Shelf Model (CS3 and CS3-3D). Available at: <https://www.noc.ac.uk/> [Accessed: 18 August 2018].
- The Planning Inspectorate 2015. Tidal Lagoon Swansea Bay. Available at: <https://infrastructure.planninginspectorate.gov.uk/projects/wales/tidal-lagoon-swansea-bay/> [Accessed: 18 September 2018].
- Tidal Lagoon Plc 2016. Key Statistics - Tidal Lagoon. Available at: <http://www.tidallagoonpower.com/projects/swansea-bay/key-statistics/> [Accessed: 19 April 2017].
- Tidal Lagoon Plc 2017. Environmental Statement Chapter 4. Project Description. Available at: <http://www.tidallagoonpower.com/wp-content/uploads/2017/05/DCO-Application-ES-4.0-project-description.pdf> [Accessed: 6 July 2017].
- Tidal Lagoon Plc 2018. Swansea Bay - Tidal Lagoon. Available at: <http://www.tidallagoonpower.com/projects/swansea-bay/> [Accessed: 18 September 2018].
- Tidal Lagoon Power 2016. Ours to Own - Building a new British industry from our natural advantage. *TLP Publication* (October). Available at: <http://www.calvertfoundation.org/initiatives/oto>.
- Uncles, R.J. 1984. Hydrodynamics of the Bristol Channel. *Marine Pollution Bulletin* 15(2), pp. 47–53. doi: [http://dx.doi.org/10.1016/0025-326X\(84\)90461-2](http://dx.doi.org/10.1016/0025-326X(84)90461-2).

References

- Uncles, R.J. 2010. Physical properties and processes in the Bristol Channel and Severn Estuary. *Marine Pollution Bulletin* 61(1–3), pp. 5–20. Available at: <http://dx.doi.org/10.1016/j.marpolbul.2009.12.010>.
- United Nations 2016a. Paris Agreement - Status of Treaties XXVII.7.d. *United Nations Treaty Collection* 21(December 2015), pp. 1–7. Available at: https://treaties.un.org/pages/ViewDetails.aspx?src=TREATY&mtdsg_no=XXVII-7-d&chapter=27&clang=en.
- United Nations 2016b. Paris Agreement Signature Ceremony. *UNFCCC* (April), pp. 1–6. Available at: <http://newsroom.unfccc.int/media/632121/list-of-representatives-to-high-level-signature-ceremony.pdf>.
- Uqaili, M.A. and Harijan, K. 2012. Energy, environment and sustainable development. *Energy, Environment and Sustainable Development* 12, pp. 1–349. doi: <http://dx.doi.org/10.1007/978-3-7091-0109-4>.
- Wang, S. et al. 2011. An overview of ocean renewable energy in China. *Renewable and Sustainable Energy Reviews* 15(1), pp. 91–111. Available at: <http://dx.doi.org/10.1016/j.rser.2010.09.040>.
- Wang, X.H. and Aandutta, F.P. 2013. Sediment Transport Dynamics in Ports, Estuaries and Other Coastal Environments. In: *Sediment Transport Processes and Their Modelling Applications*. InTech, p. 13. Available at: <https://www.intechopen.com/books/advanced-biometric-technologies/liveness-detection-in-biometrics>.
- Warren, I.R. and Bach, H.K. 1992. MIKE 21: a modelling system for estuaries, coastal waters and seas. *Environmental Software* 7(4), pp. 229–240. Available at: <https://linkinghub.elsevier.com/retrieve/pii/026698389290006P>.
- Warwick, R. and Uncles, R. 1980. Distribution of Benthic Macrofauna Associations in the Bristol Channel in Relation to Tidal Stress. *Marine Ecology Progress Series* 3, pp. 97–103. doi: <http://dx.doi.org/10.3354/meps003097>.

References

- Waters, S. and Aggidis, G.A. 2016a. A world first: Swansea Bay tidal lagoon in review. *Renewable and Sustainable Energy Reviews* 56, pp. 916–921. Available at: <http://www.sciencedirect.com/science/article/pii/S1364032115013945> [Accessed: 20 April 2017].
- Waters, S. and Aggidis, G.A. 2016b. Tidal range technologies and state of the art in review. *Renewable and Sustainable Energy Reviews* 59, pp. 514–529. Available at: <http://dx.doi.org/10.1016/j.rser.2015.12.347>.
- Wilhelm, S. et al. 2016a. Analysis of Head Losses in a Turbine Draft Tube by Means of 3D Unsteady Simulations. *Flow, Turbulence and Combustion* 97(4), pp. 1255–1280. doi: <http://dx.doi.org/10.1007/s10494-016-9767-9>.
- Wilhelm, S. et al. 2016b. Head losses prediction and analysis in a bulb turbine draft tube under different operating conditions using unsteady simulations. *28th AHR Symposium on Hydraulic Machinery and Systems, Grenoble, July 4-8*, pp. 839–848. doi: <http://dx.doi.org/10.1088/1755-1315/49/2/022010>.
- Wolanski, E. and Elliott, M. 2016. Estuarine water circulation. In: *Estuarine Ecohydrology*. doi: <http://dx.doi.org/10.1016/b978-0-444-63398-9.00002-7>.
- Wolf, J. et al. 2009. Environmental impacts of tidal power schemes. *Proceedings of the Institution of Civil Engineers - Maritime Engineering* 162(4), pp. 165–177. Available at: <http://www.icevirtuallibrary.com/doi/10.1680/maen.2009.162.4.165>.
- Xia, J. et al. 2008. Impact of the barrage construction on the hydrodynamic process in the Severn Estuary using a 2D finite volume model. *Flood Risk Management: Research and Practice* Extended A, p. 8.
- Xia, J. et al. 2010a. Hydrodynamic impact of a tidal barrage in the Severn Estuary, UK. *Renewable Energy* 35(7), pp. 1455–1468. Available at: <http://dx.doi.org/10.1016/j.renene.2009.12.009>.
- Xia, J. et al. 2010b. Impact of different operating modes for a Severn Barrage on the tidal power and flood inundation in the Severn Estuary, UK. *Applied Energy* 87(7), pp. 2374–2391. Available at: <http://dx.doi.org/10.1016/j.apenergy.2009.11.024>.

References

- Xia, J. et al. 2010c. Impact of different tidal renewable energy projects on the hydrodynamic processes in the Severn Estuary, UK. *Ocean Modelling* 32(1–2), pp. 86–104. Available at: <http://dx.doi.org/10.1016/j.ocemod.2009.11.002>.
- Xia, J. et al. 2011. Estimation of future coastal flood risk in the Severn Estuary due to a barrage. *Journal of Flood Risk Management* 4(3), pp. 247–259. Available at: <http://doi.wiley.com/10.1111/j.1753-318X.2011.01106.x> [Accessed: 6 November 2014].
- Xia, J. et al. 2012. Estimation of annual energy output from a tidal barrage using two different methods. *Applied Energy* 93, pp. 327–336. Available at: <http://dx.doi.org/10.1016/j.apenergy.2011.12.049>.
- Xue, J. et al. 2019. Optimising the Operation of Tidal Range Schemes. *Energies* 12(15), p. 2870. Available at: <https://www.mdpi.com/1996-1073/12/15/2870>.
- Zhou, J. et al. 2014a. Effects of open boundary location on the far-field hydrodynamics of a Severn Barrage. *Ocean Modelling* 73, pp. 19–29. Available at: <http://www.sciencedirect.com/science/article/pii/S146350031300187X> [Accessed: 28 March 2016].
- Zhou, J. et al. 2014b. Optimization modelling of the impacts of a Severn Barrage for a two-way generation scheme using a Continental Shelf model. *Renewable Energy* 72, pp. 415–427. Available at: <http://dx.doi.org/10.1016/j.renene.2014.07.036>.
- Zhou, J. et al. 2014c. Refinements to the EFDC model for predicting the hydro-environmental impacts of a barrage across the Severn Estuary. *Renewable Energy* 62, pp. 490–505. Available at: <http://dx.doi.org/10.1016/j.renene.2013.08.012>.
- Zienkiewicz, O.C. and Taylor, R.L. 2000. *The finite element method*. 5th ed. Oxford Butterworth-Heinemann. Available at: <http://openlibrary.org/books/OL6900453M>.

Publication list

Journal papers

Čož, N. et al. 2019. Implementation of a Full Momentum Conservative Approach in Modelling Flow Through Tidal Structures. *Water* 11(9), p. 1917. Available at: <https://www.mdpi.com/2073-4441/11/9/1917>.

(Under preparation) Čož, N., Lin, B., Falconer, R.A., Ahmadian, R., Analysis of the velocity field in a flume downstream of a barrage using a 3D hydrostatic model with momentum conservation (working title).

Conference proceedings

Čož, N., 2018. 3D Modelling of Swansea Bay Tidal Lagoon using Delft3D. *5th PRIMaRE Conference*. (poster presentation)

Čož, N., Ahmadian, R., Falconer, R.A., 2017. Modelling the Impacts of Tidal Range Energy Structures in the Severn Estuary and Bristol Channel, UK. *37th IAHR World Congress, Kuala Lumpur*.

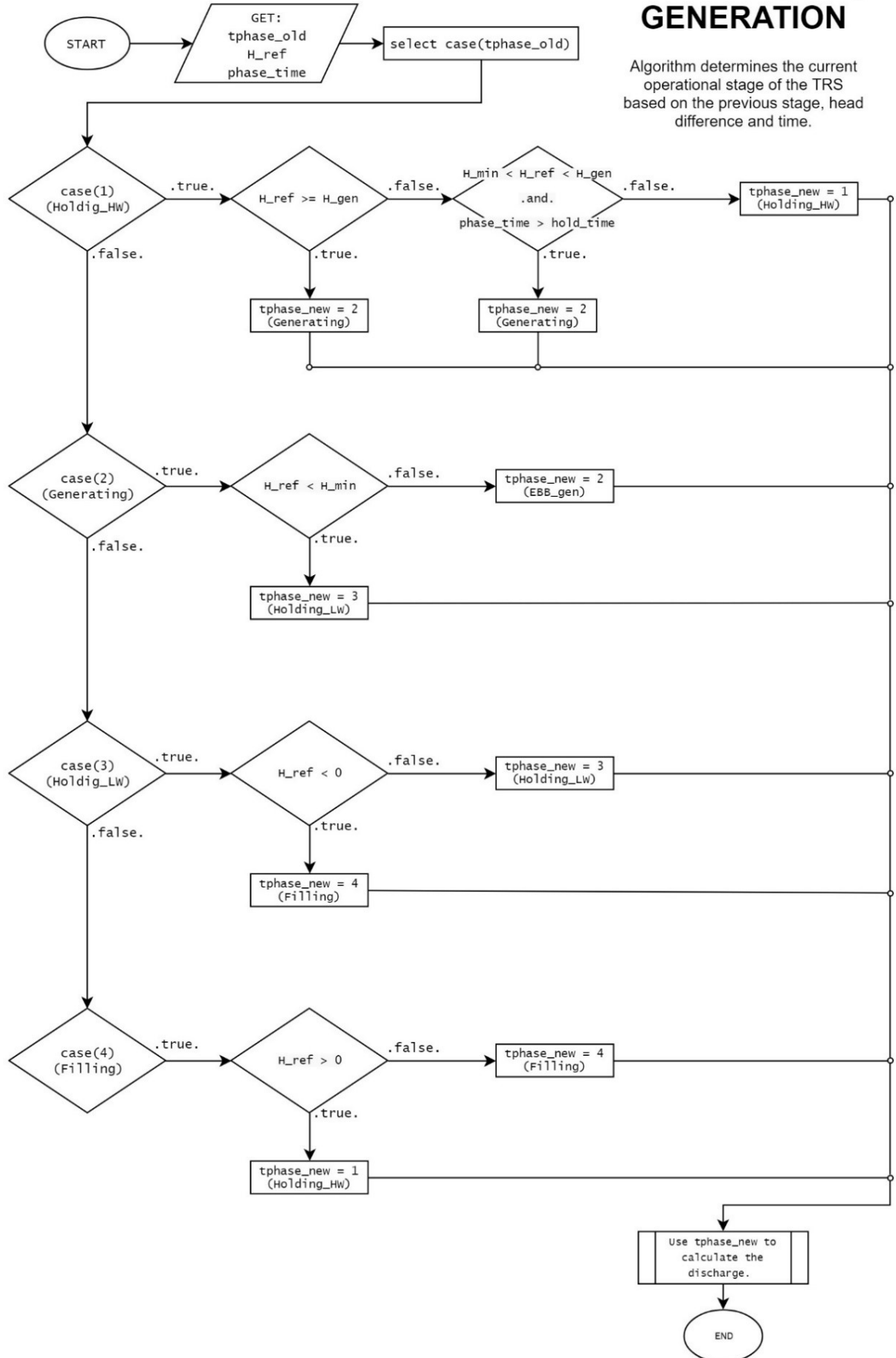
Čož, N., Falconer, R.A., Ahmadian, R., 2017. High-Resolution 3D Modelling of the Swansea Bay Tidal Lagoon. *10th International Conference on Sustainable Energy and Environmental Protection, Bled*.

A Operational sequence flow charts

A.1 One-way ebb generation

ONE-WAY (EBB) GENERATION

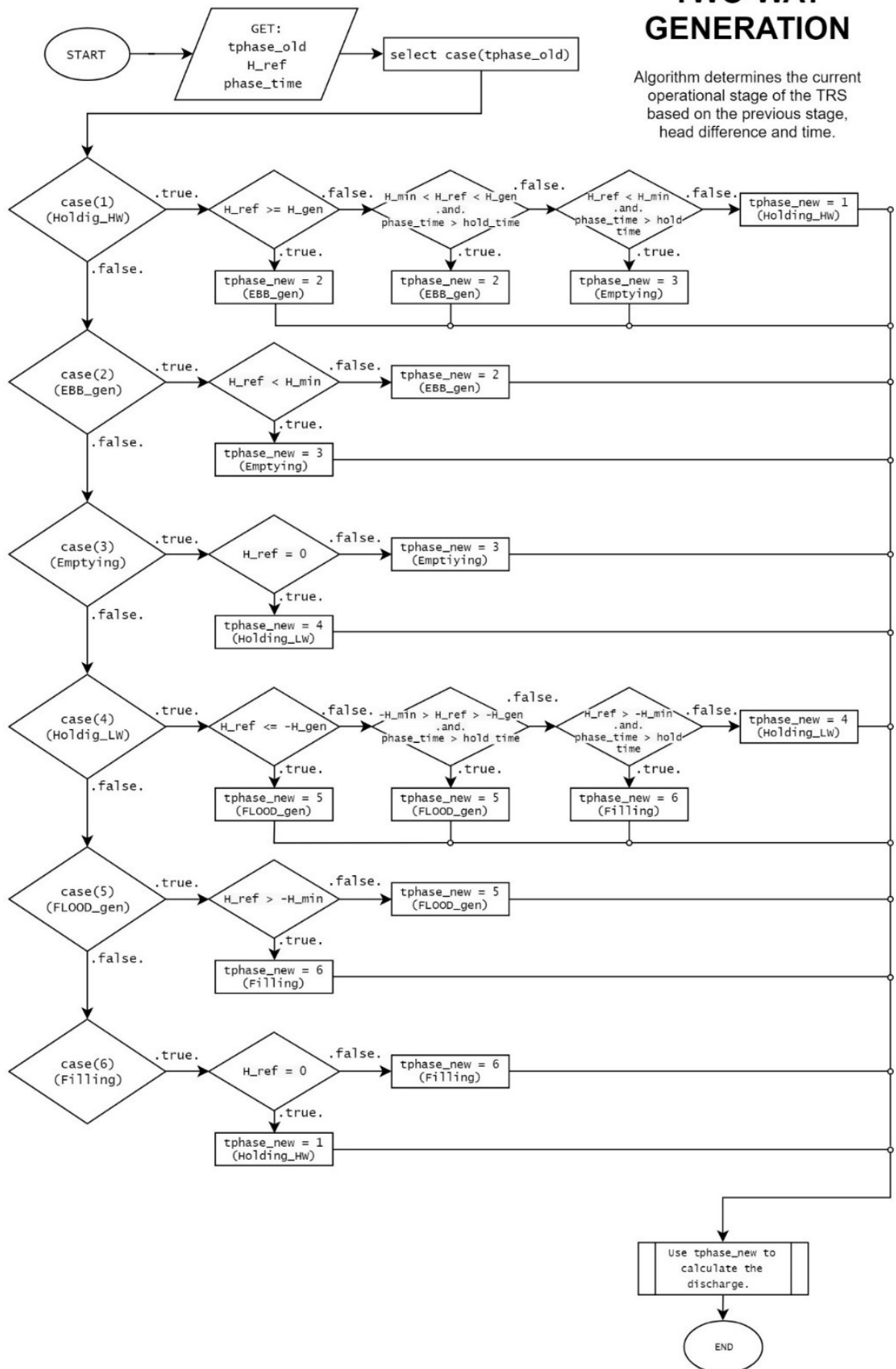
Algorithm determines the current operational stage of the TRS based on the previous stage, head difference and time.



A.2 Two-way generation

TWO-WAY GENERATION

Algorithm determines the current operational stage of the TRS based on the previous stage, head difference and time.

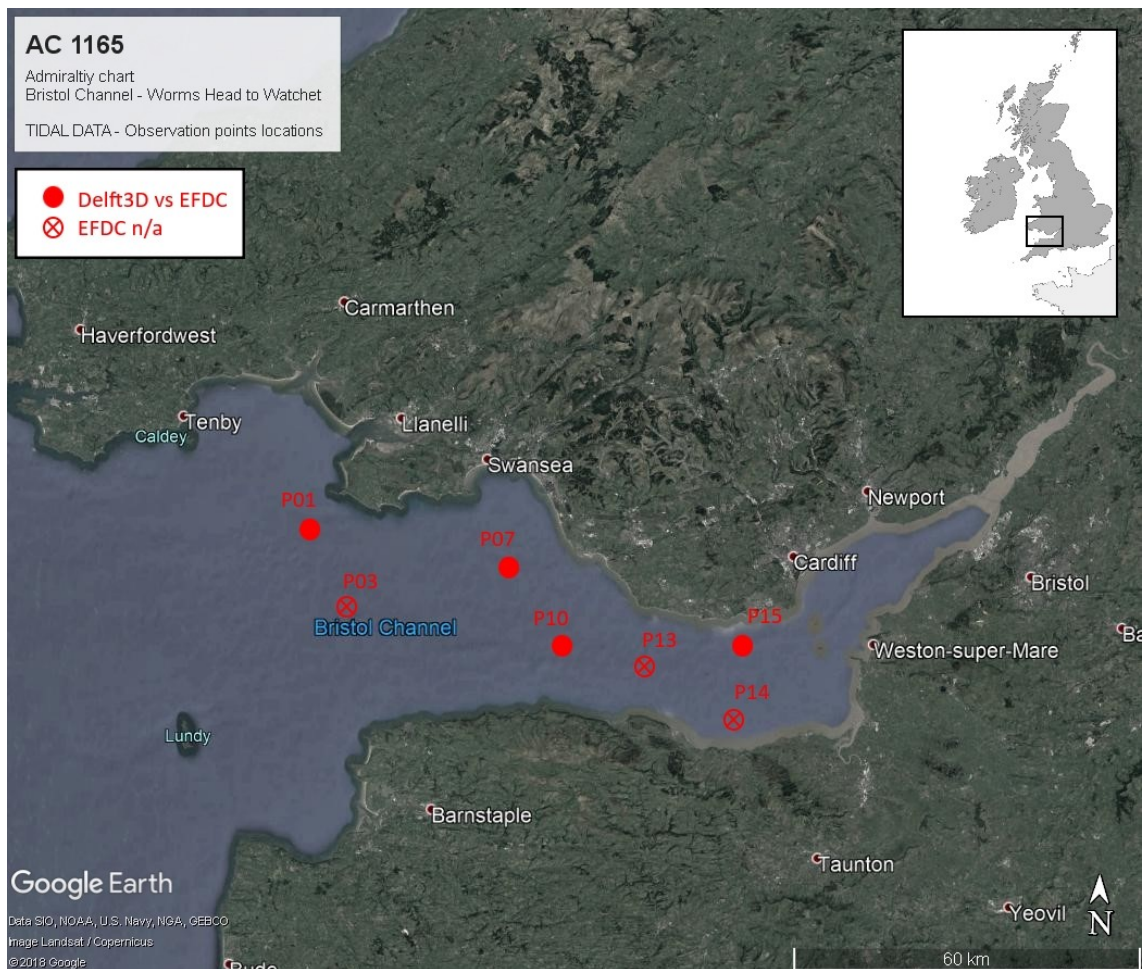


B Additional CSM validation results

B.1 Severn Estuary and Bristol Channel

From Admiralty Chart 1165 Bristol Channel – Worms Head to Watchet

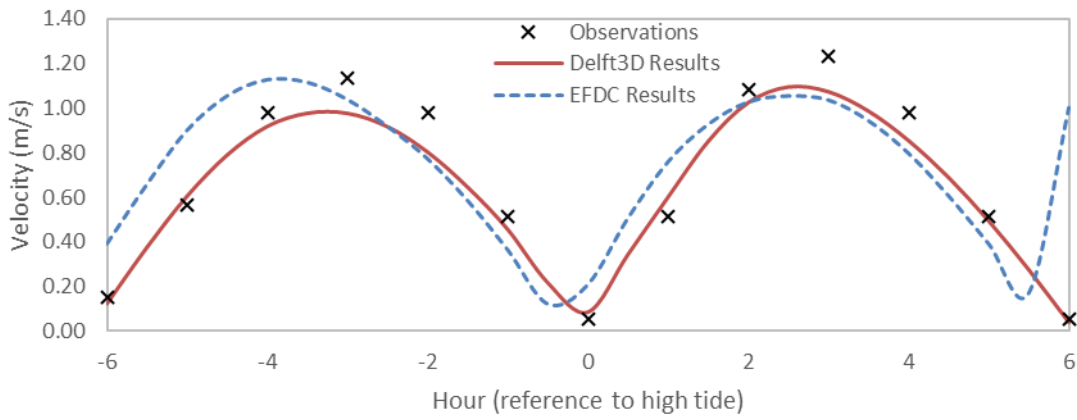
Comparison between simulation results and observation data for locations in the Severn Estuary and Bristol Channel. Showing a time series of velocity magnitude and direction during a 12-hour interval, relative to the occurrence of the high tide, including: (i) Spring tide velocity magnitude; (ii) Neap tide velocity magnitude; and (iii) Velocity direction (clockwise with true north at 0 degrees).



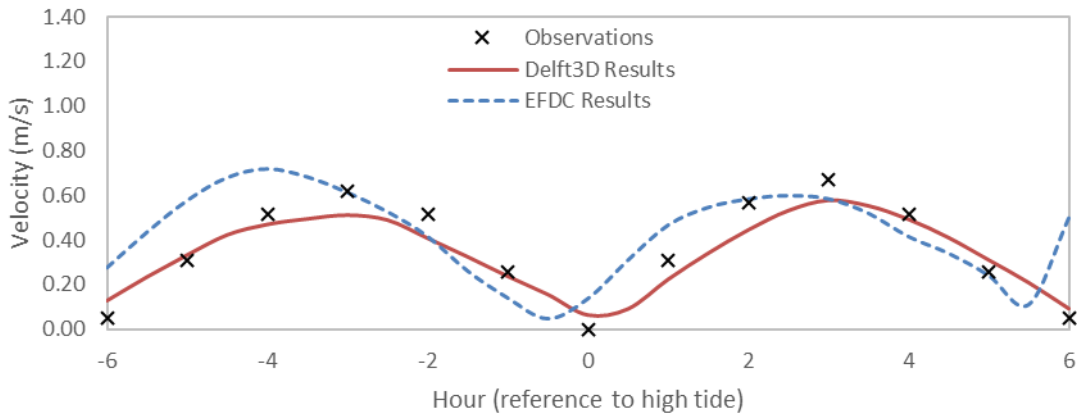
Obs. Station	LAT	LONG	EFDC available
P01 - Gower_01	51.51389	-4.41667	Yes
P03 - BC_01	51.36389	-4.32778	No
P07 - Porthcawl_01	51.45000	-3.93333	Yes
P10 - Lynton	51.33611	-3.84167	Yes
P13 - BarryMinehead_01	51.32500	-3.54444	No
P14 - BarryMinehead_02	51.23889	-3.35278	No
P15 - BarryMinehead_03	51.35000	-3.35000	Yes

P01 - Gower_01

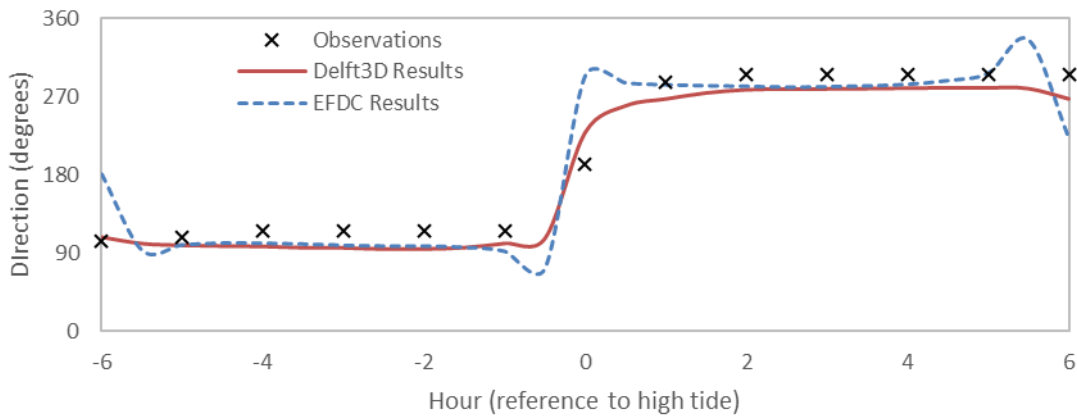
Velocity magnitude – Spring Tide



Velocity magnitude - Neap Tide

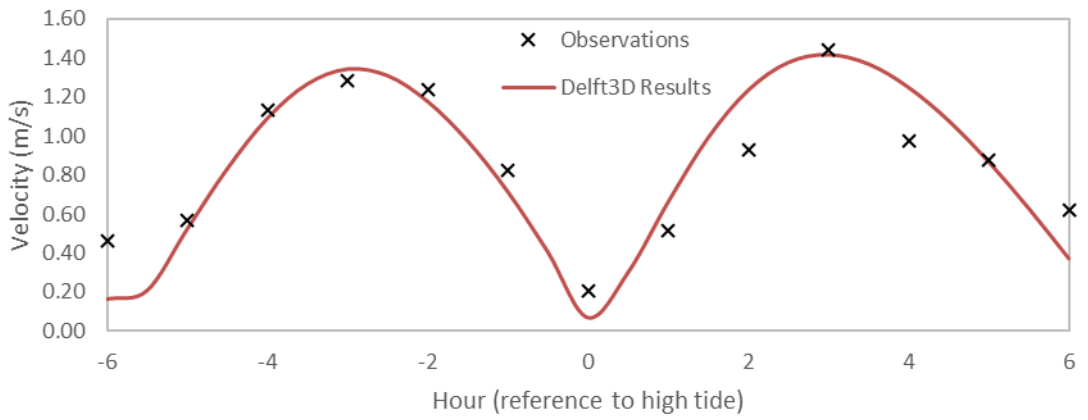


Velocity direction

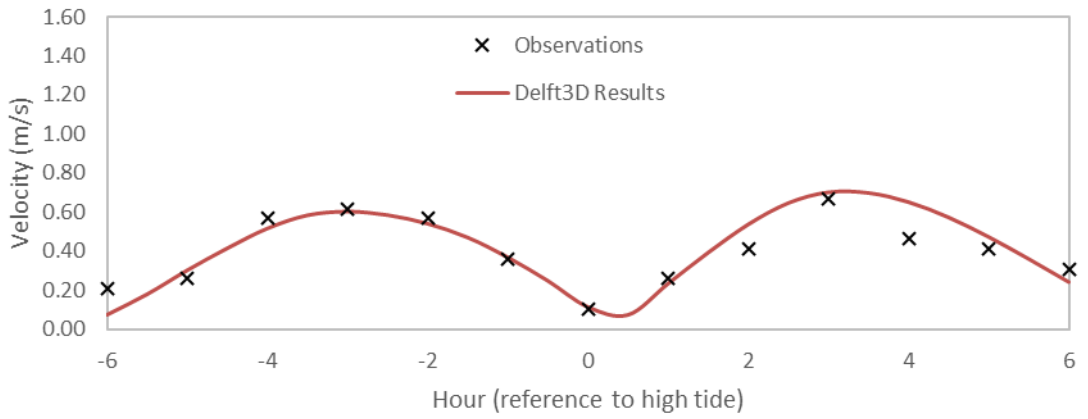


P03 - BC_01

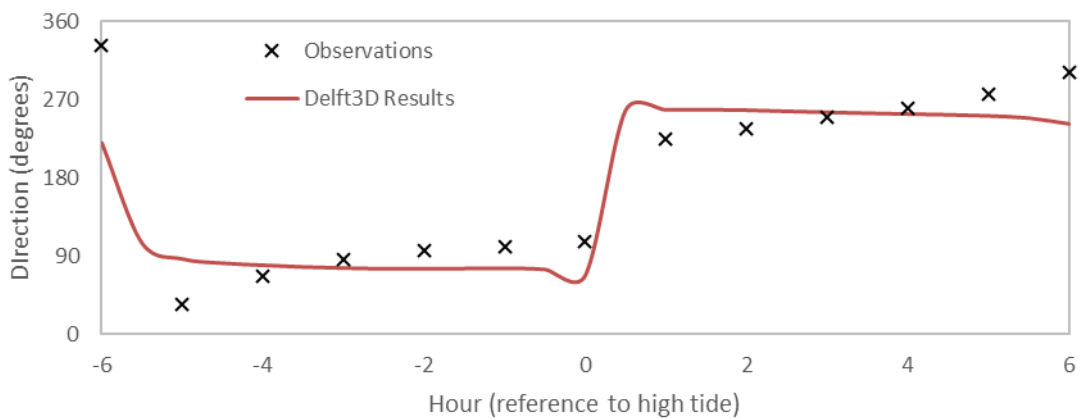
Velocity magnitude – Spring Tide



Velocity magnitude – Neap Tide

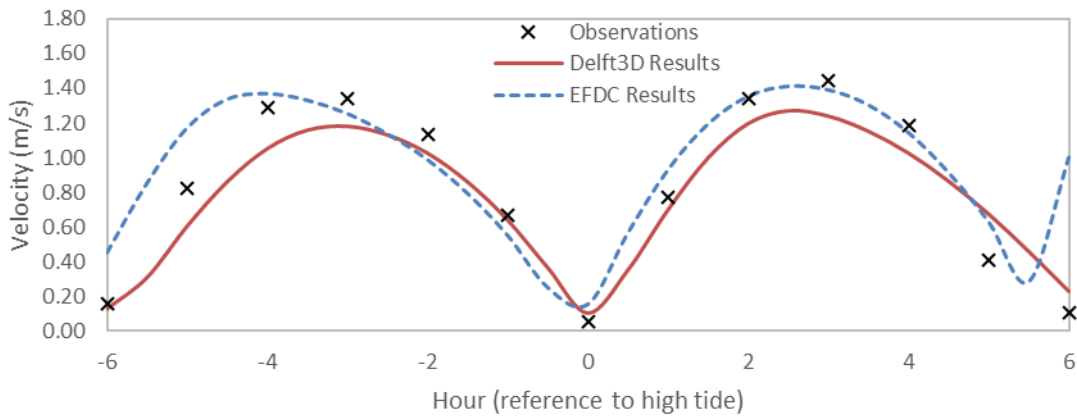


Velocity direction

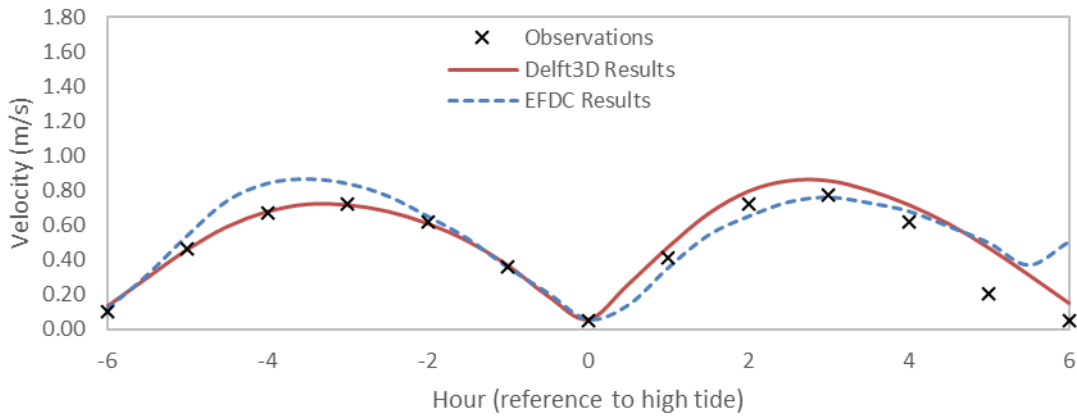


P07 – Porthcawl_01

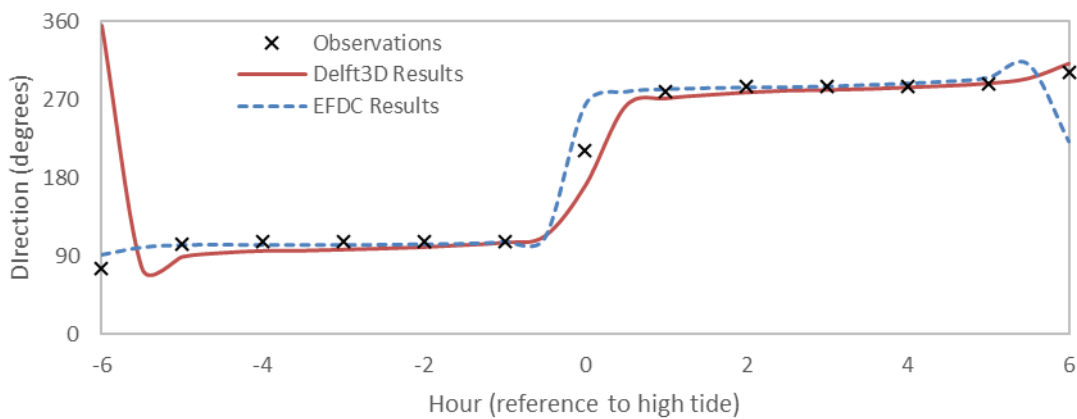
Velocity magnitude – Spring Tide



Velocity magnitude – Neap Tide

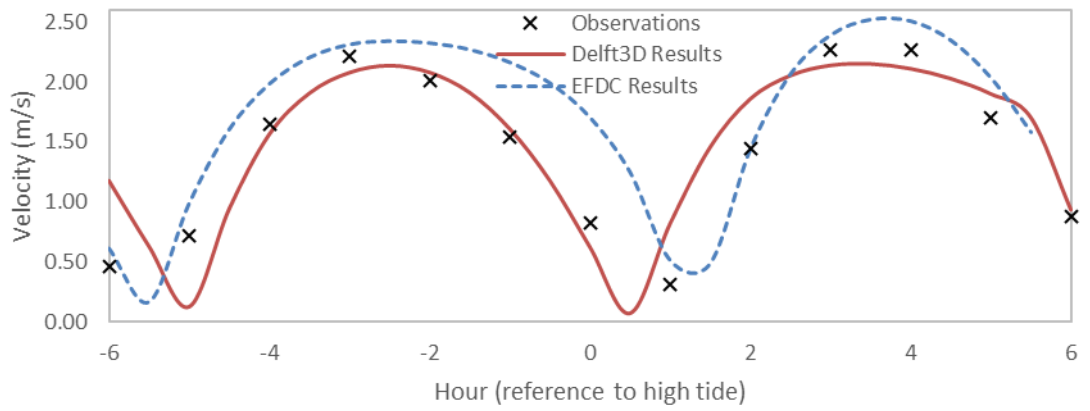


Velocity direction

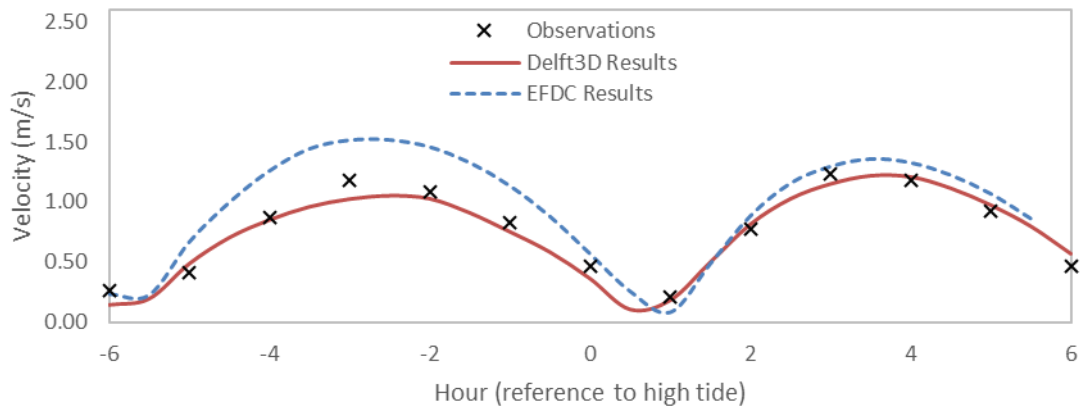


P10 – Lynton

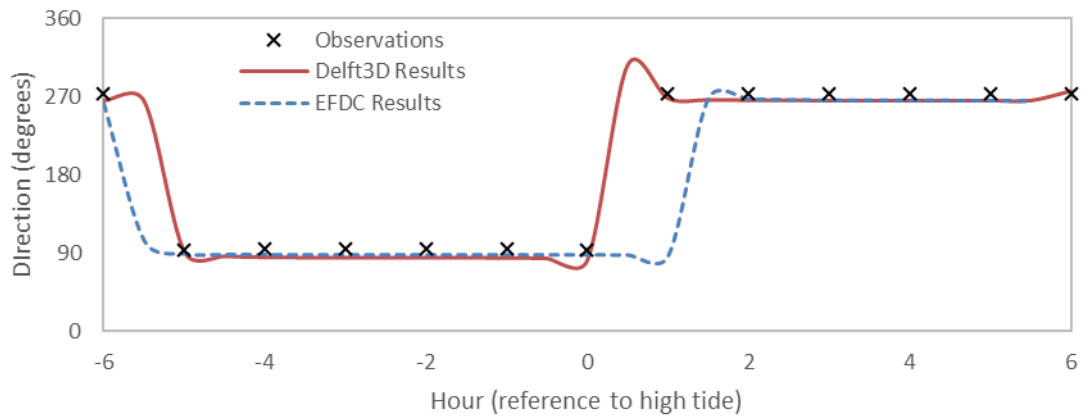
Velocity magnitude – Spring Tide



Velocity magnitude – Neap Tide

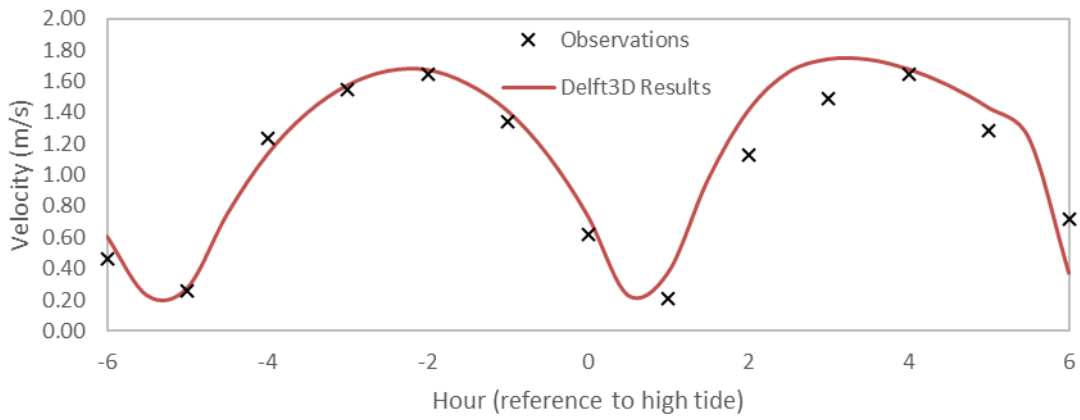


Velocity direction

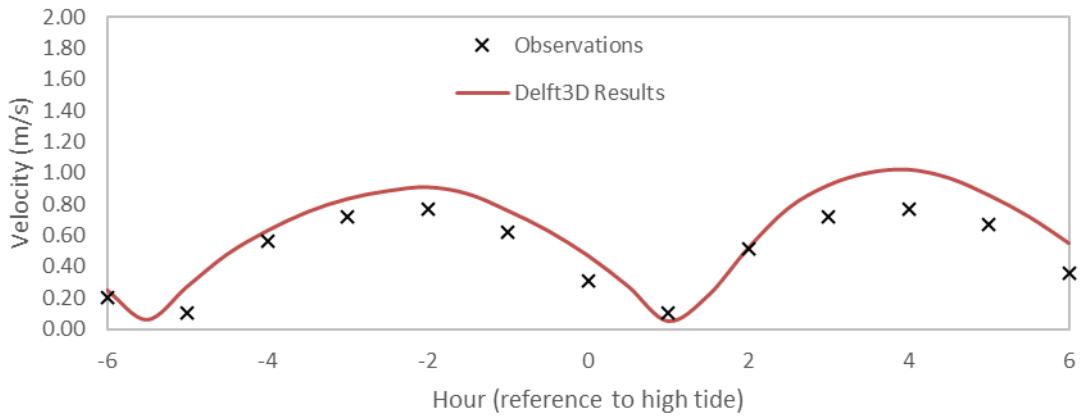


P13 – BarryMinehead_01

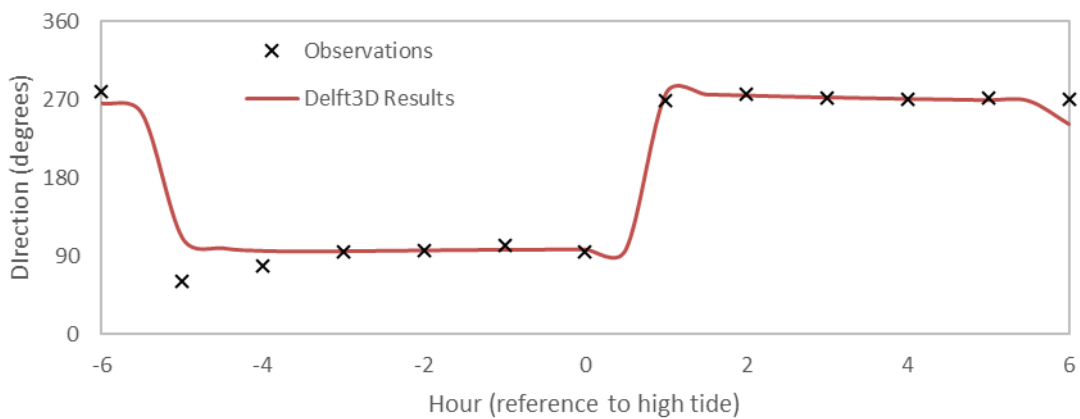
Velocity magnitude – Spring Tide



Velocity magnitude – Neap Tide

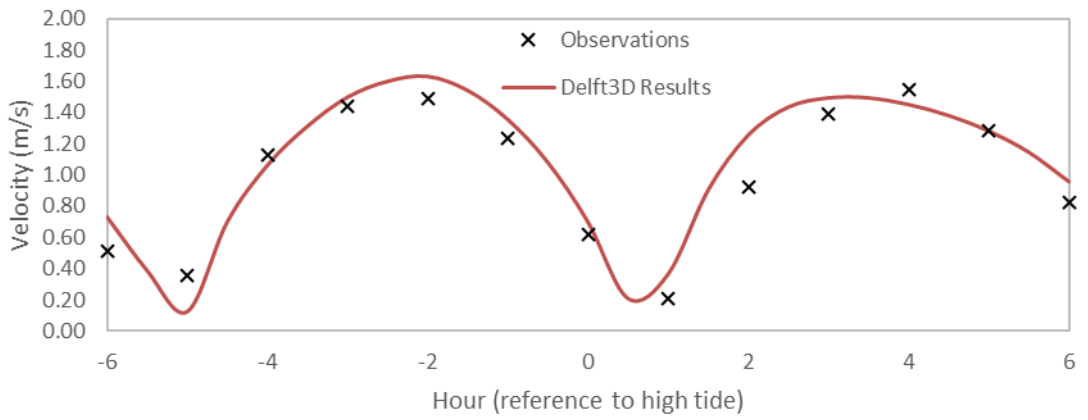


Velocity direction

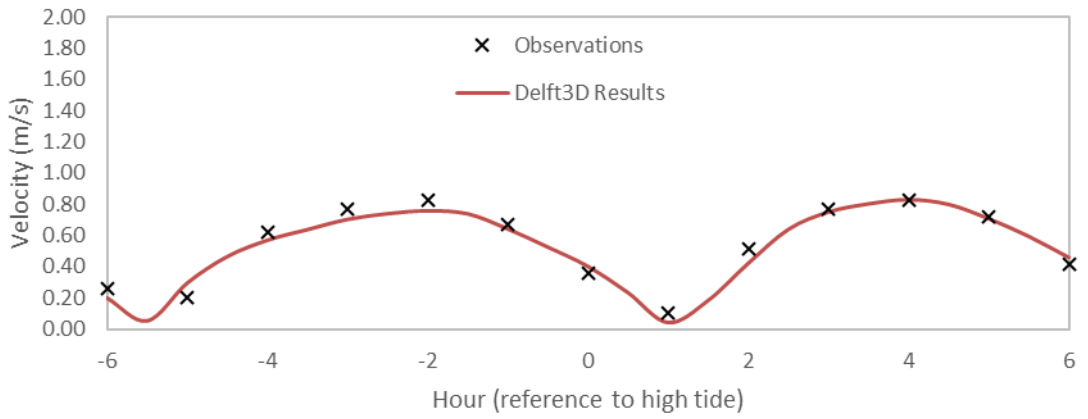


P14 – BarryMinehead_02

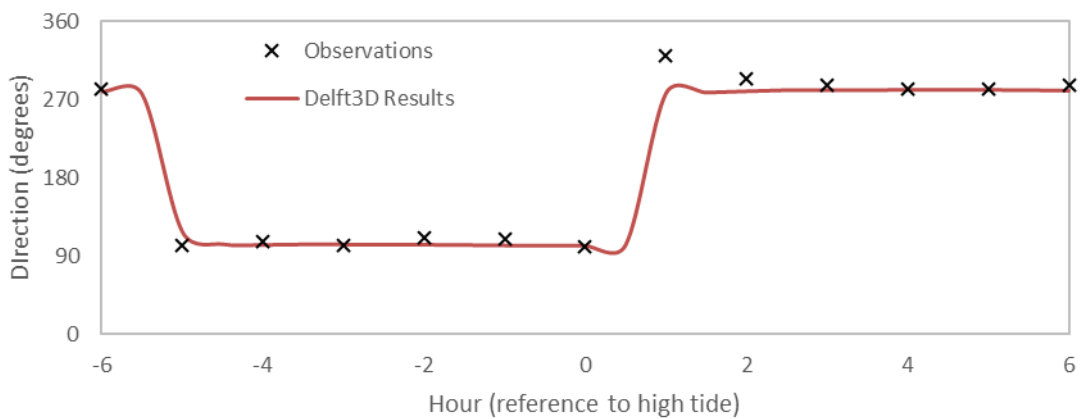
Velocity magnitude – Spring Tide



Velocity magnitude – Neap Tide

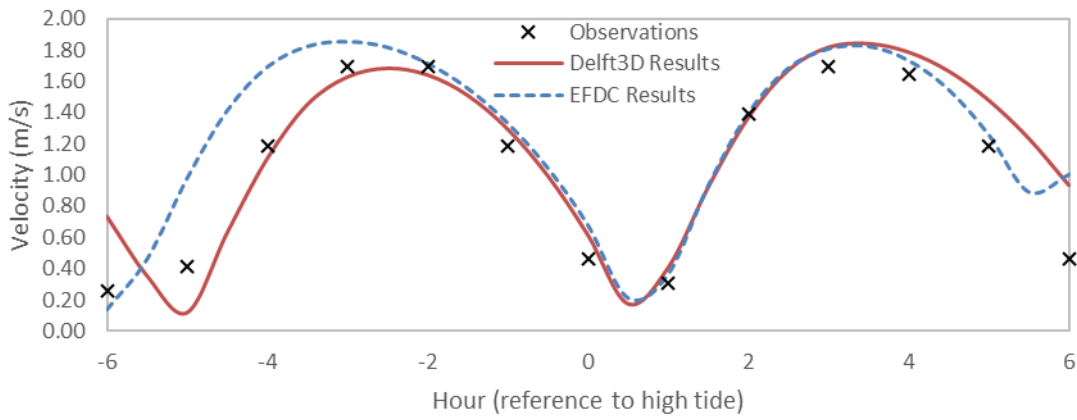


Velocity direction

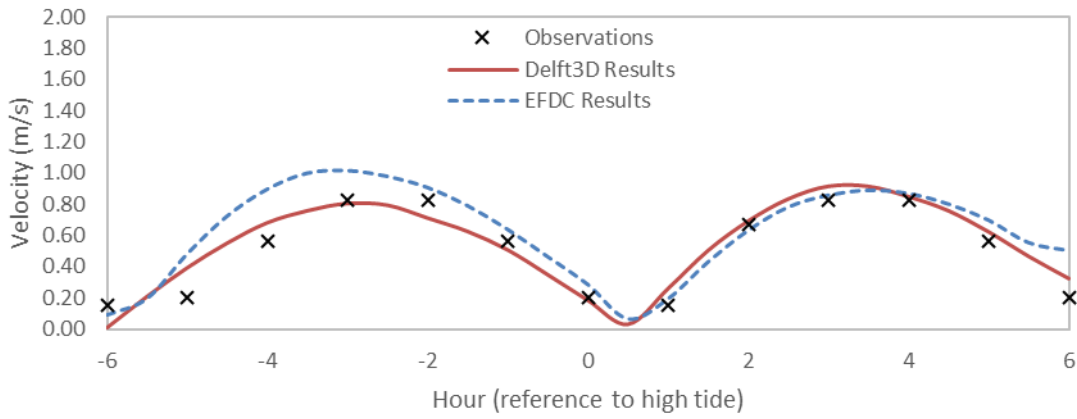


P15 – BarryMinehead_03

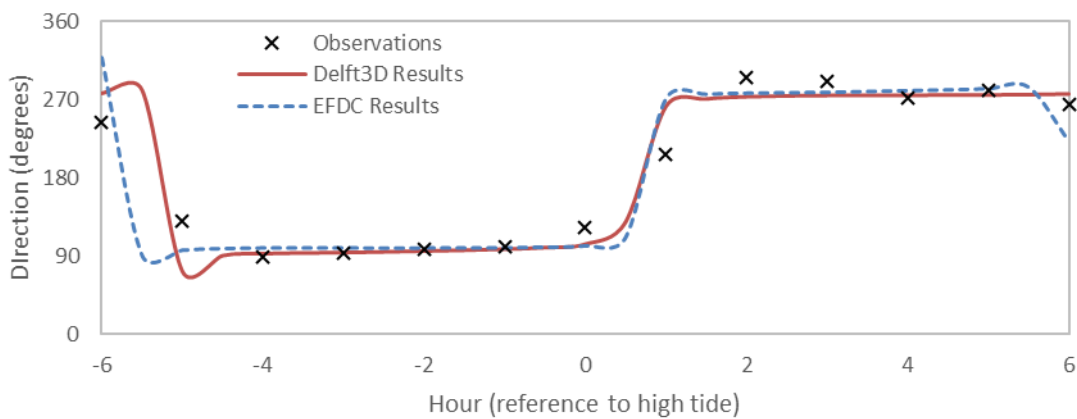
Velocity magnitude – Spring Tide



Velocity magnitude – Neap Tide



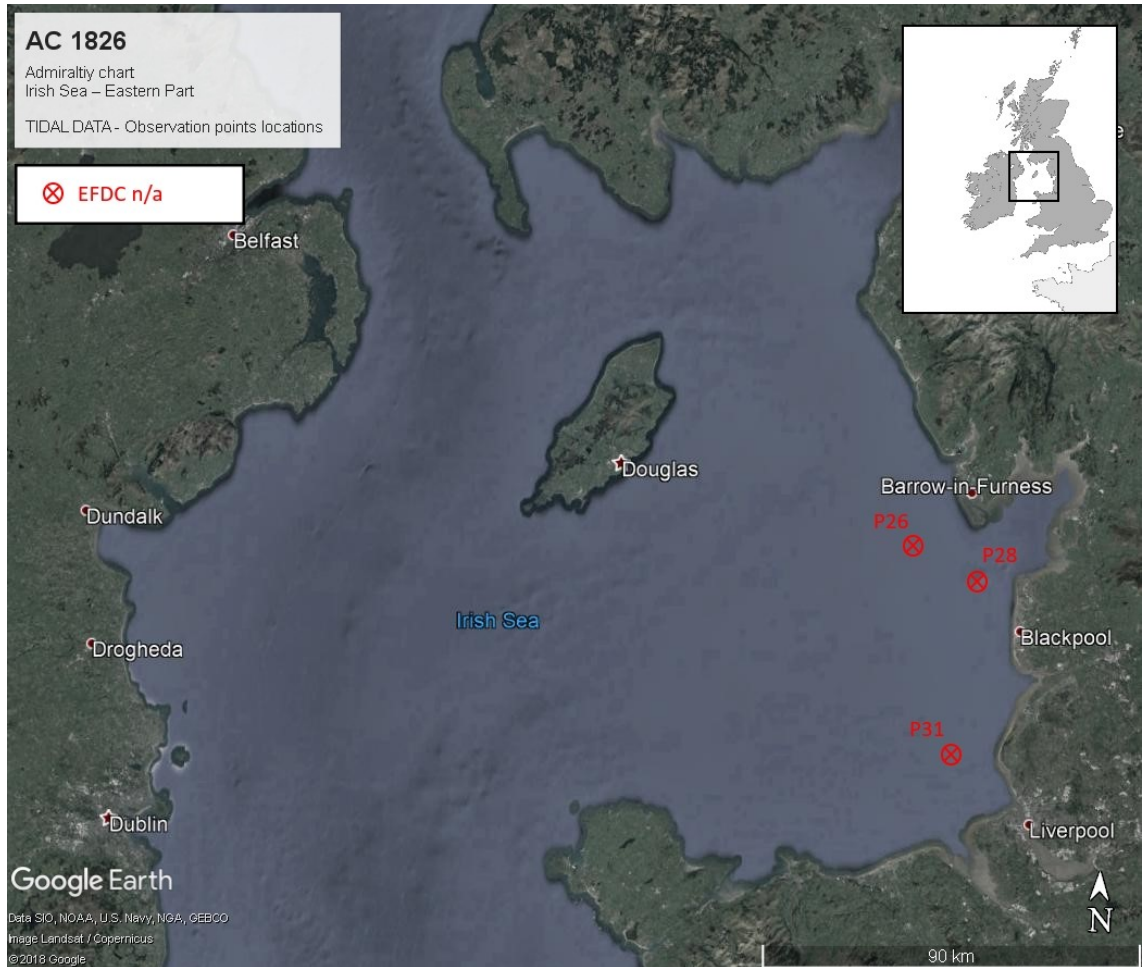
Velocity direction



B.2 Irish Sea

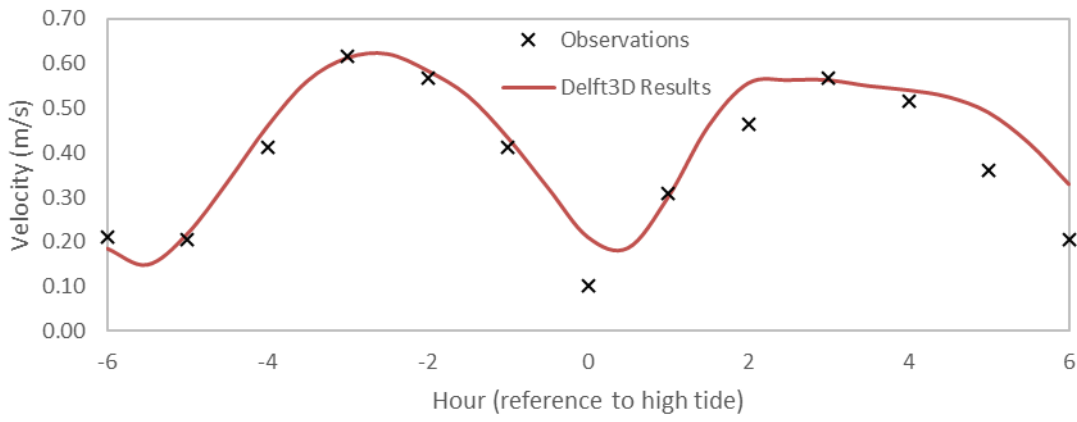
From Admiralty Chart 1826 Irish Sea – Eastern Part

Comparison between simulation results and observation data for locations in the Severn Estuary and Bristol Channel. Showing a time series of velocity magnitude and direction during a 12-hour interval, relative to the occurrence of the high tide, including: (i) Spring tide velocity magnitude; (ii) Neap tide velocity magnitude; and (iii) Velocity direction (clockwise with true north at 0 degrees).

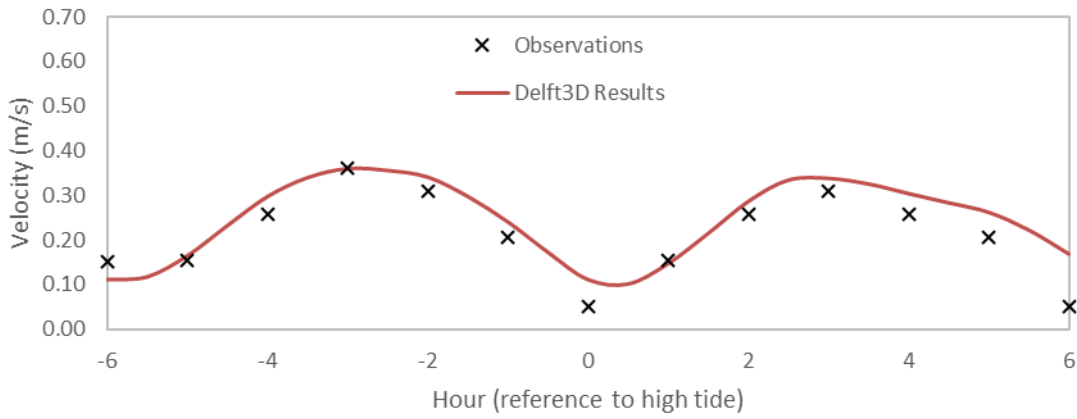


Obs. Station	LAT	LONG	EFDC available
P26 – IrishSea_11	53.99167	-3.48500	No
P28 – IrishSea_13	53.90000	-3.23500	No
P31 – IrishSea_16	53.52500	-3.50167	No

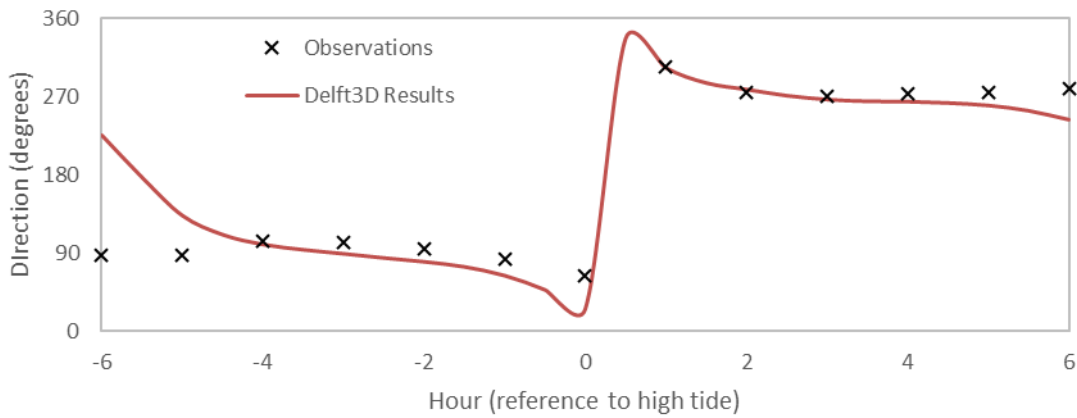
Velocity magnitude – Spring Tide



Velocity magnitude – Neap Tide

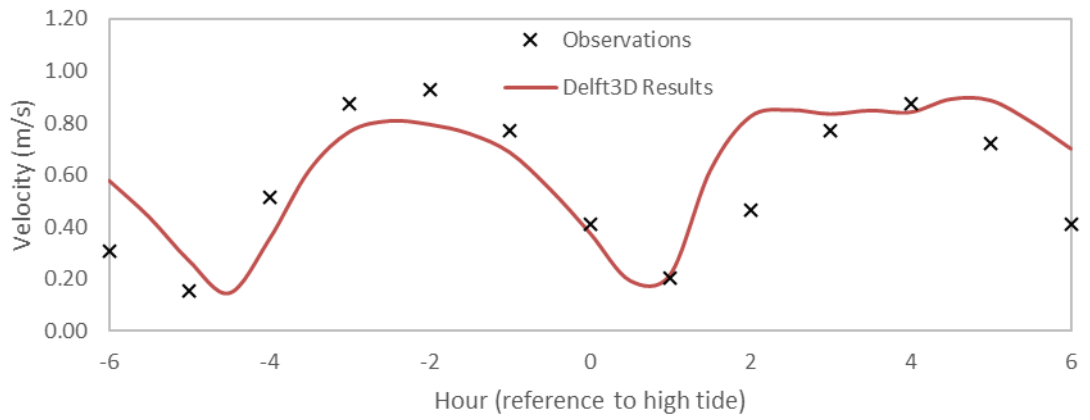


Velocity direction

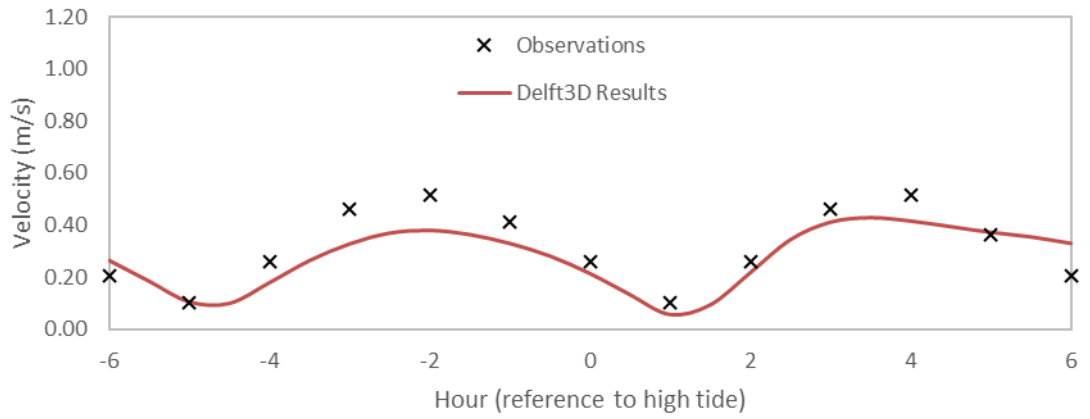


P28 – IrishSea_13

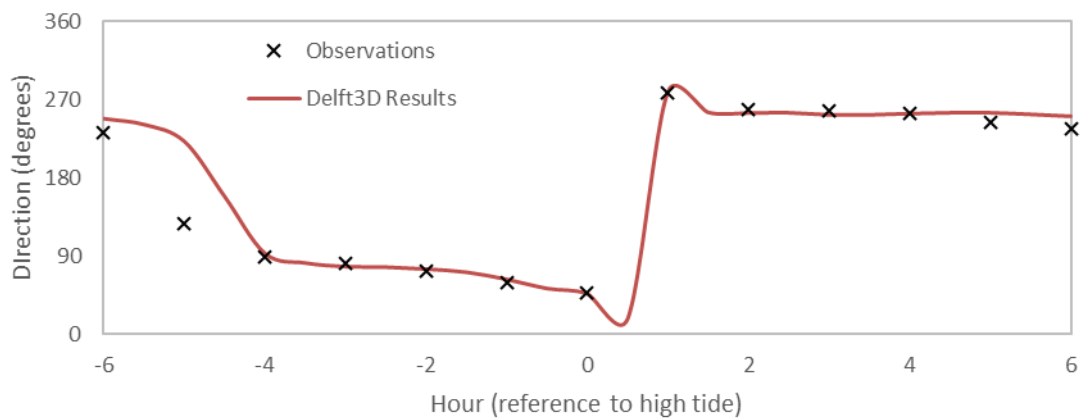
Velocity magnitude – Spring Tide



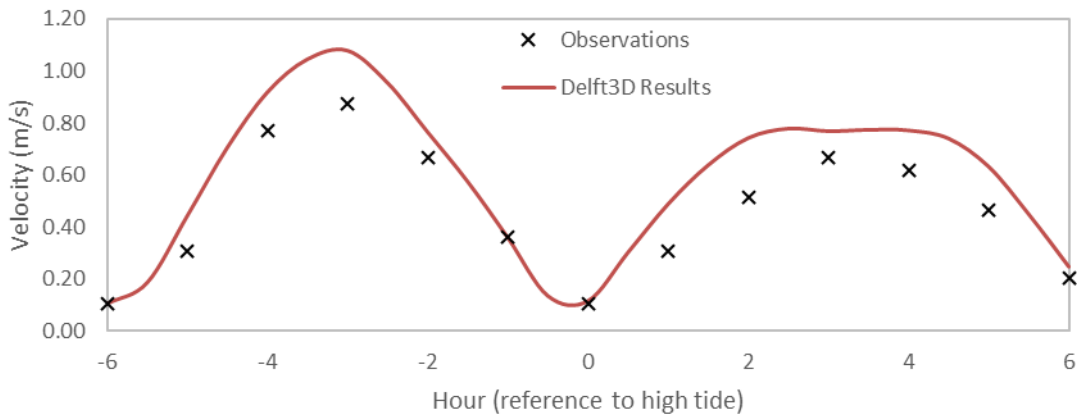
Velocity magnitude – Neap Tide



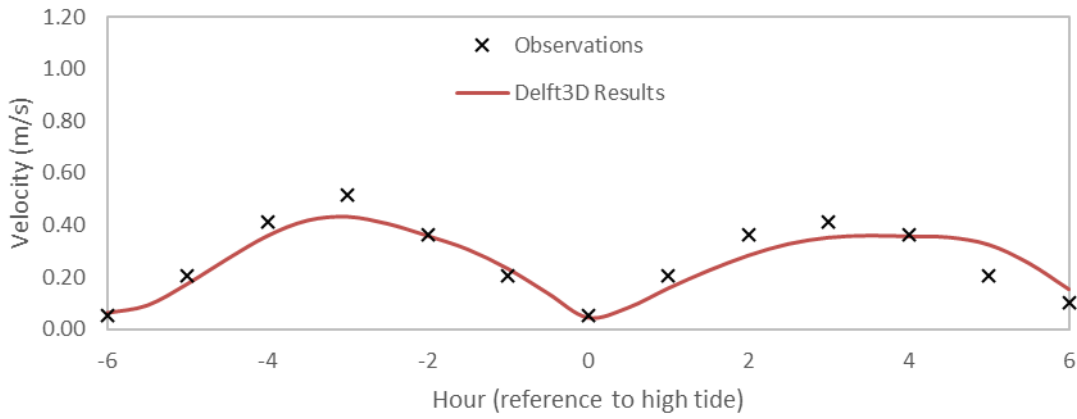
Velocity direction



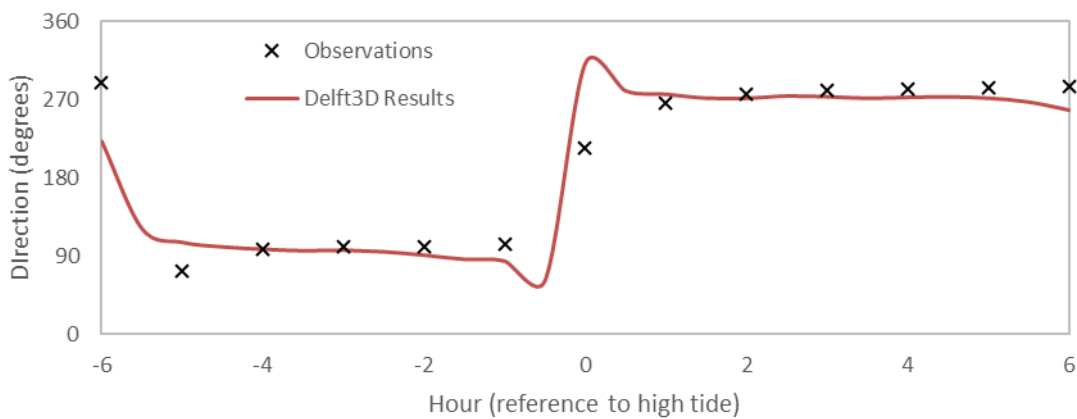
Velocity magnitude – Spring Tide



Velocity magnitude – Neap Tide



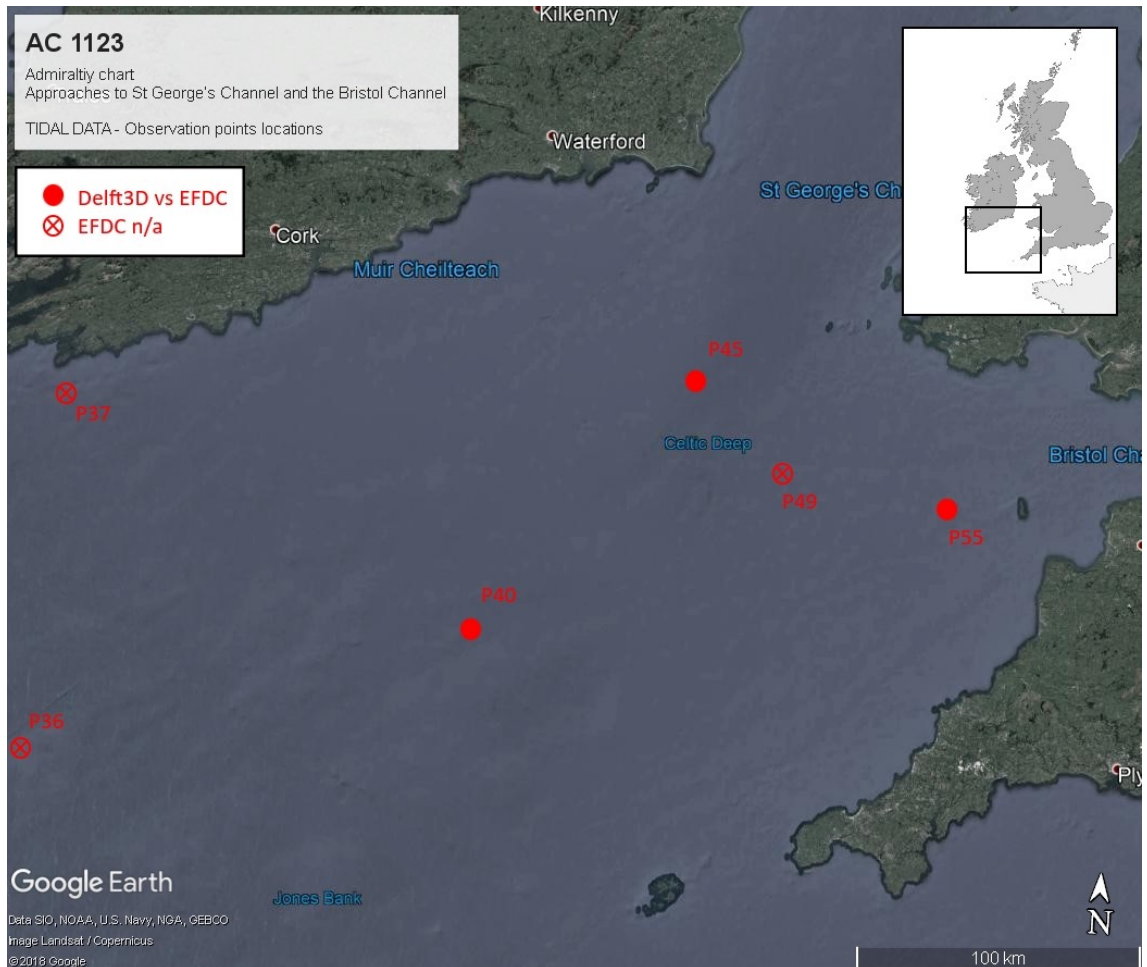
Velocity direction



B.3 Celtic Sea

From Admiralty Chart 1123 Approaches to St George's Channel and the Bristol Channel

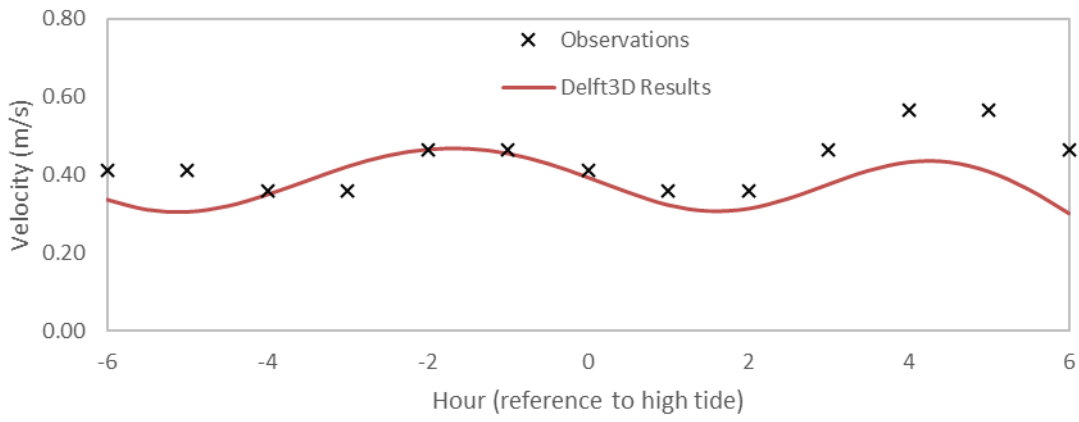
Comparison between simulation results and observation data for locations in the Severn Estuary and Bristol Channel. Showing a time series of velocity magnitude and direction during a 12-hour interval, relative to the occurrence of the high tide, including: (i) Spring tide velocity magnitude; (ii) Neap tide velocity magnitude; and (iii) Velocity direction (clockwise with true north at 0 degrees).



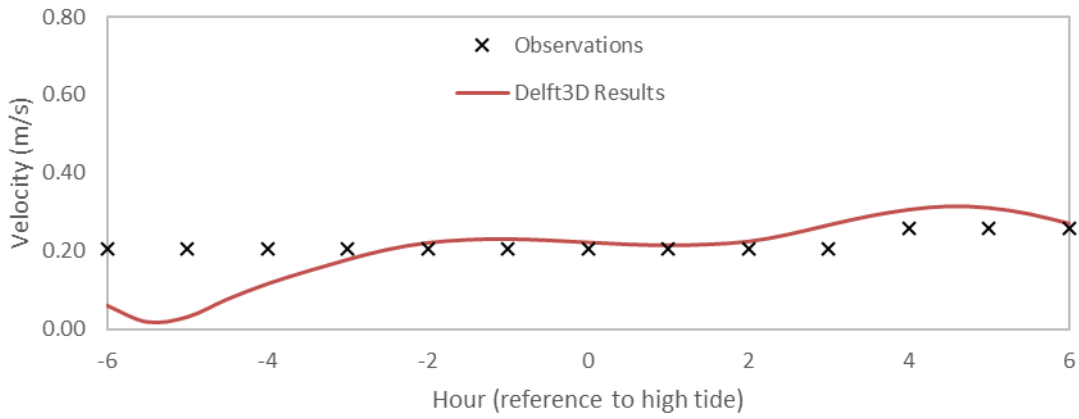
Obs. Station	LAT	LONG	EFDC available
P36 – ContinentalShelf_01	50.61667	-10.26667	No
P37 – ContinentalShelf_02	51.33333	-9.50000	No
P40 – CelticSea_01	50.80000	-7.59167	Yes
P45 – CelticDeep_01	51.56667	-6.38333	Yes
P49 – CelticDeep_02	51.25000	-5.83500	No
P55 – BC_03	51.16667	-5.00167	Yes

P36 – ContinentalShelf_01

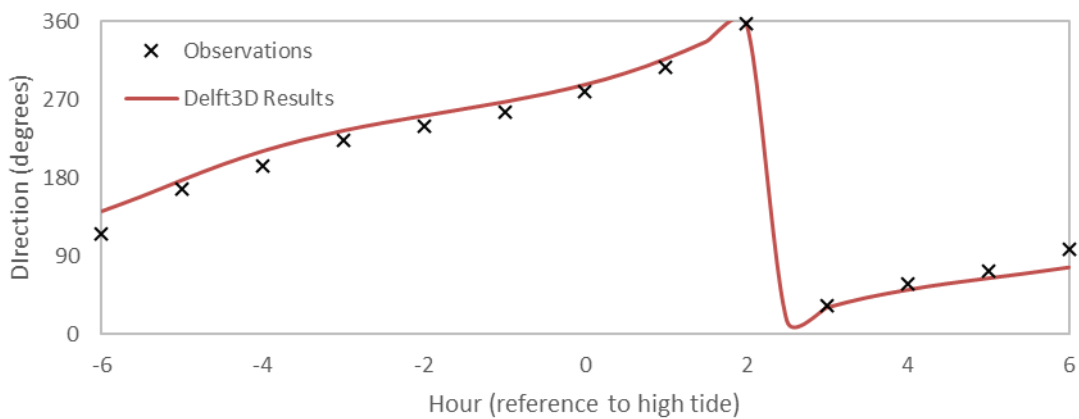
Velocity magnitude – Spring Tide



Velocity magnitude – Neap Tide

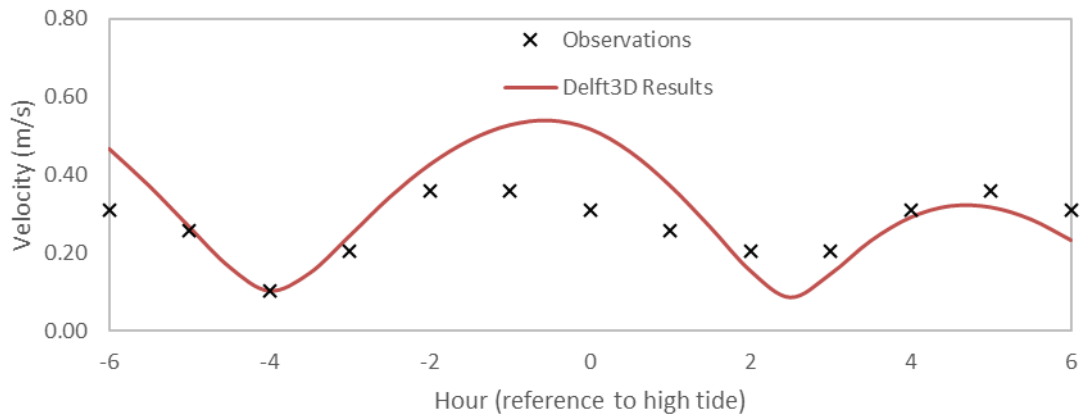


Velocity direction

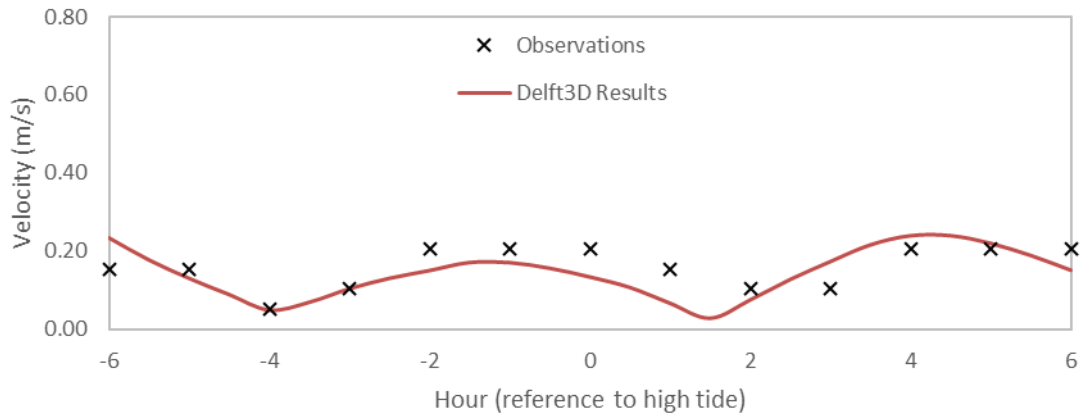


P37 – ContinentalShelf_02

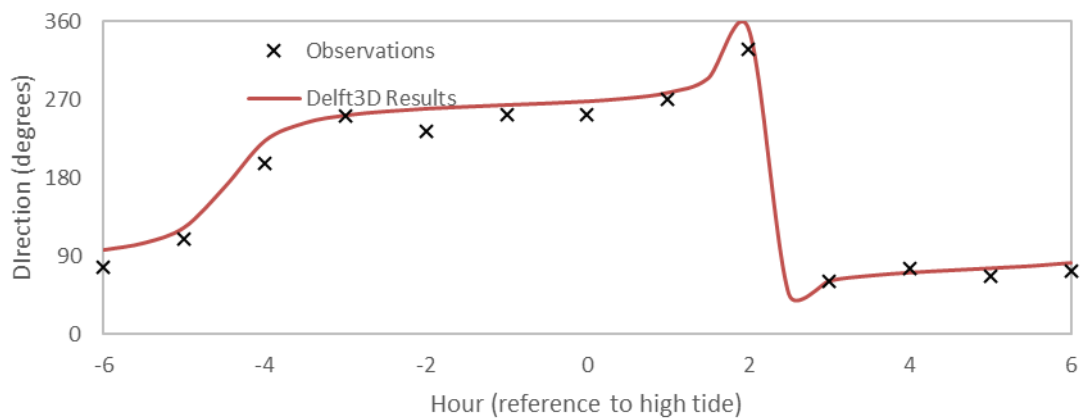
Velocity magnitude – Spring Tide



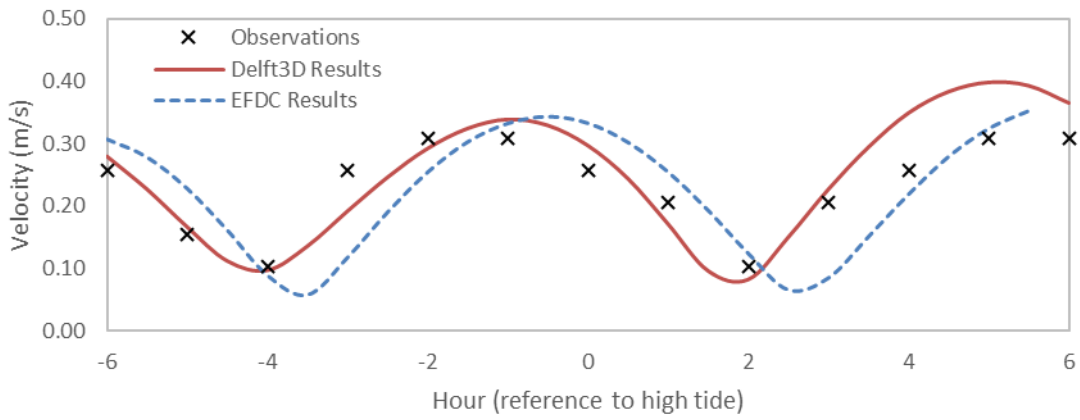
Velocity magnitude – Neap Tide



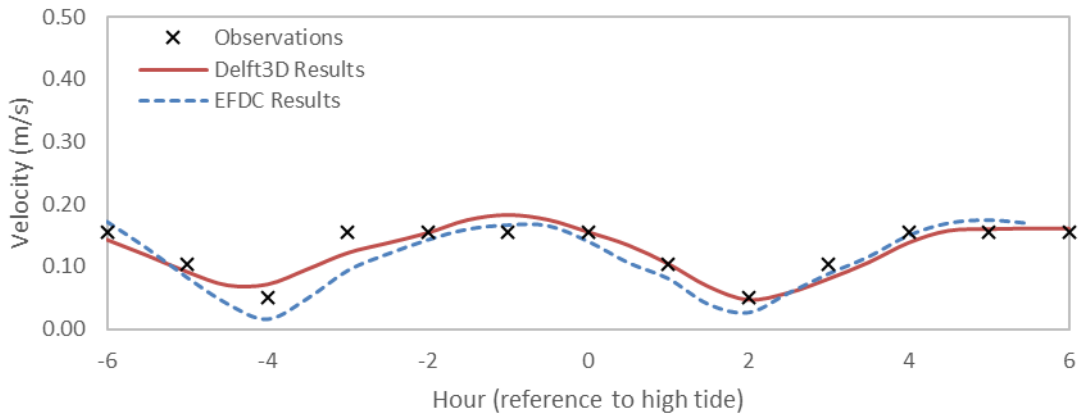
Velocity direction



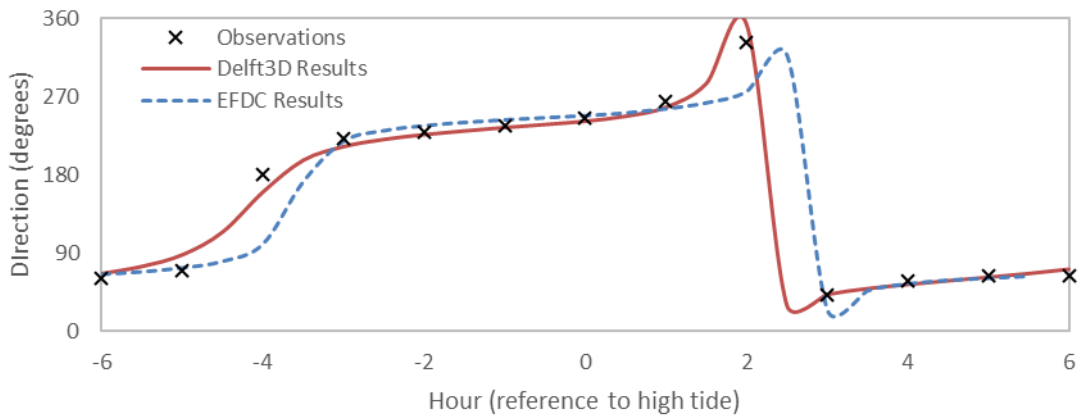
Velocity magnitude – Spring Tide



Velocity magnitude – Neap Tide

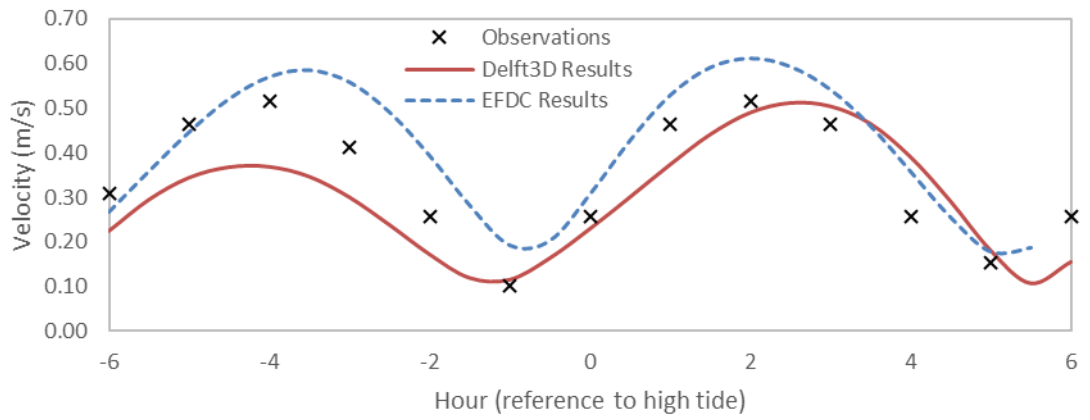


Velocity direction

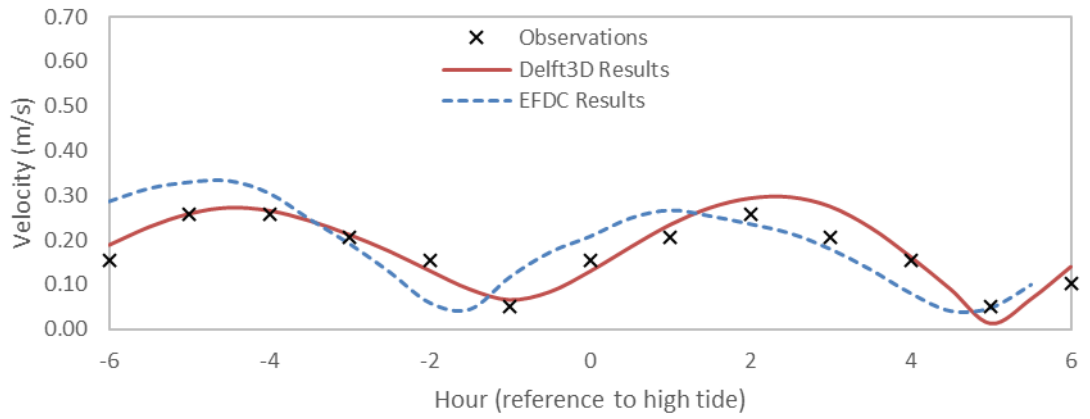


P45 – CelticDeep_01

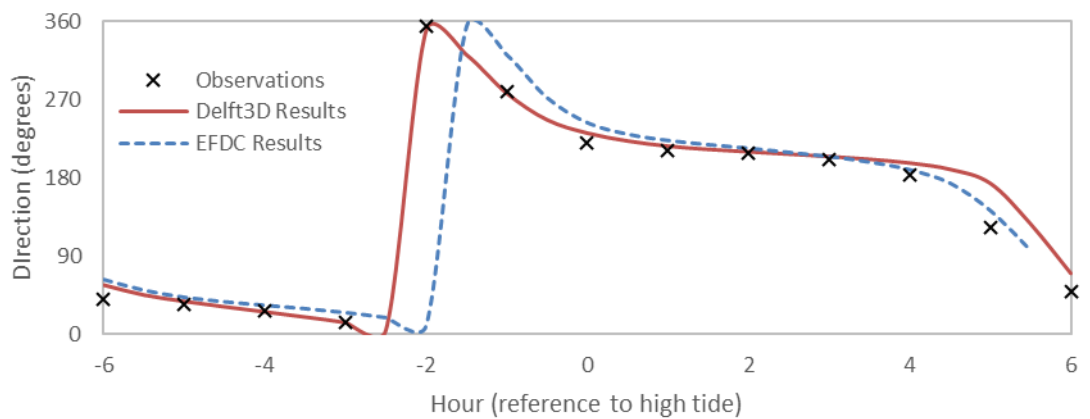
Velocity magnitude – Spring Tide



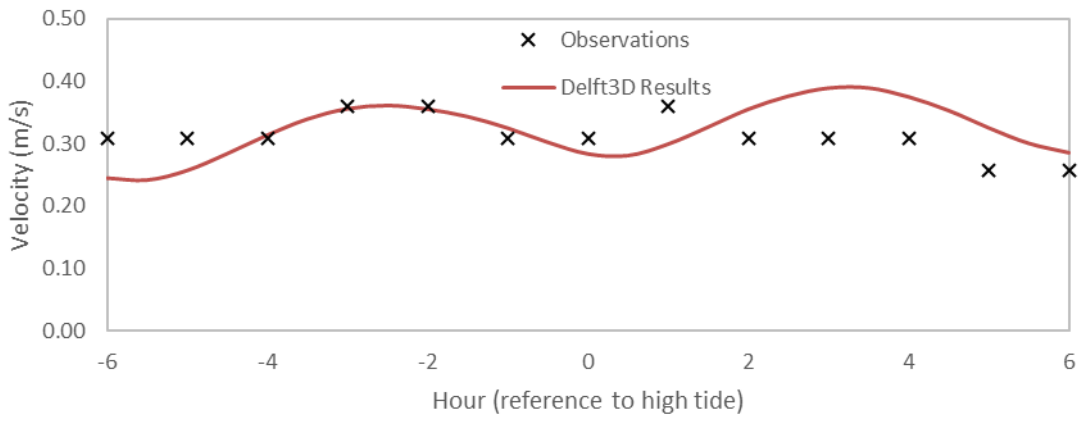
Velocity magnitude – Neap Tide



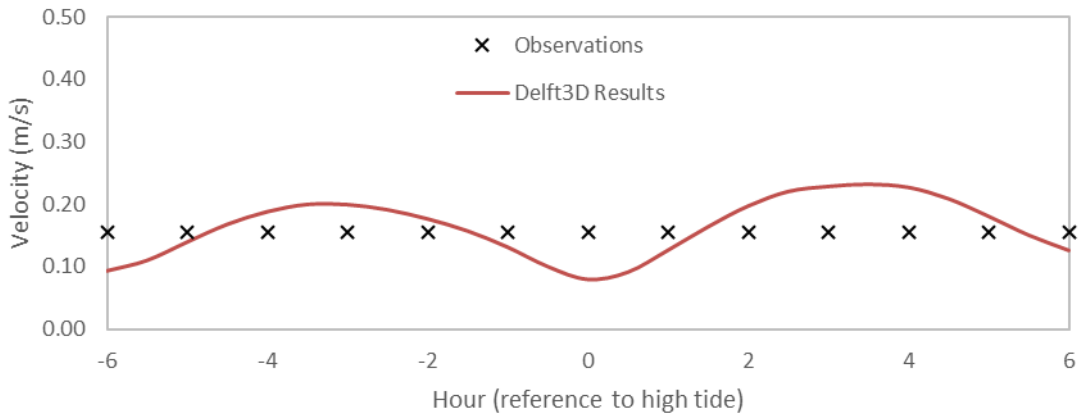
Velocity direction



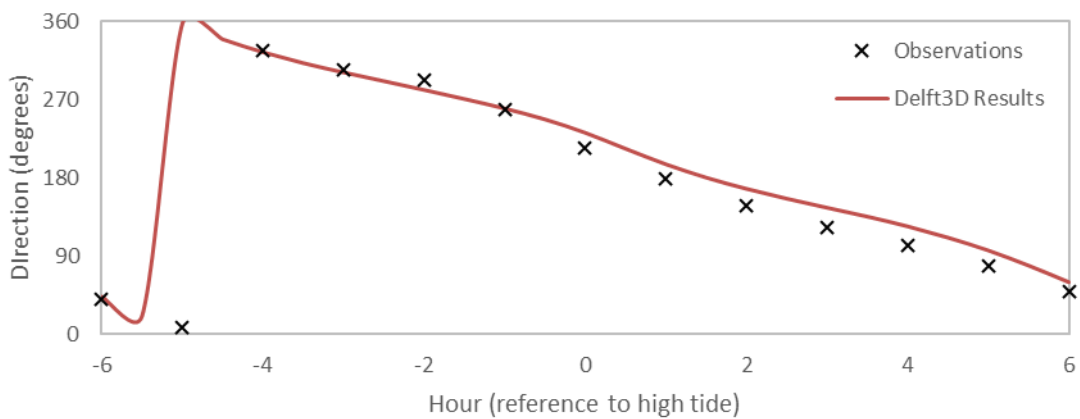
Velocity magnitude – Spring Tide



Velocity magnitude – Neap Tide

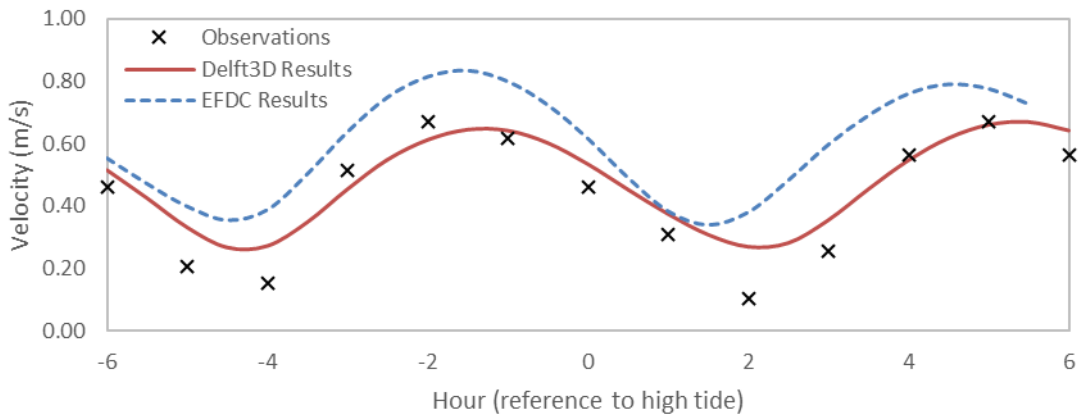


Velocity direction

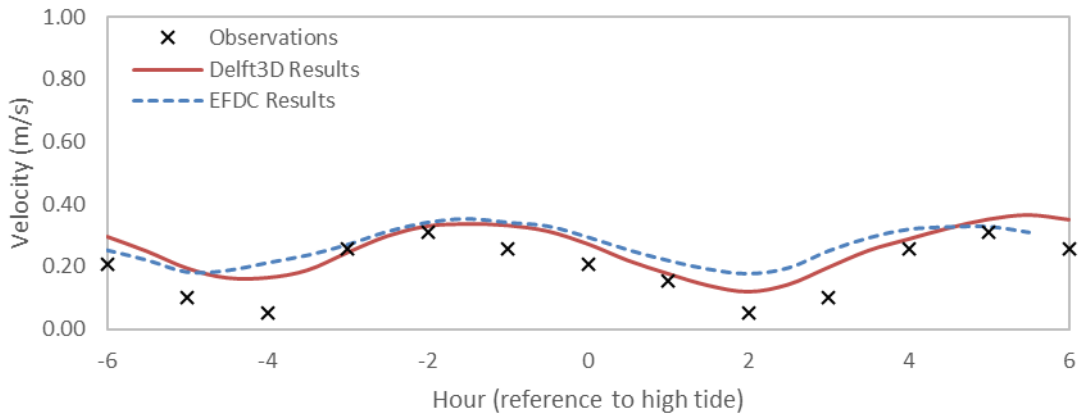


P55 - BC_03

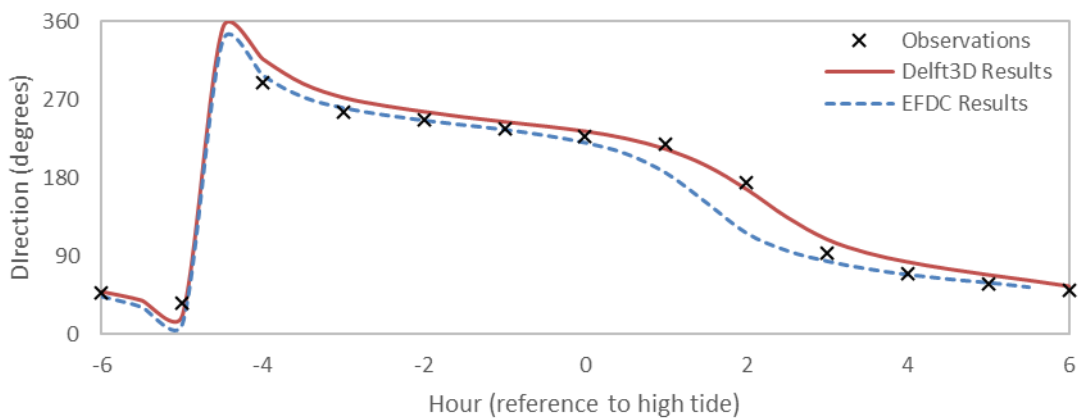
Velocity magnitude – Spring Tide



Velocity magnitude – Neap Tide



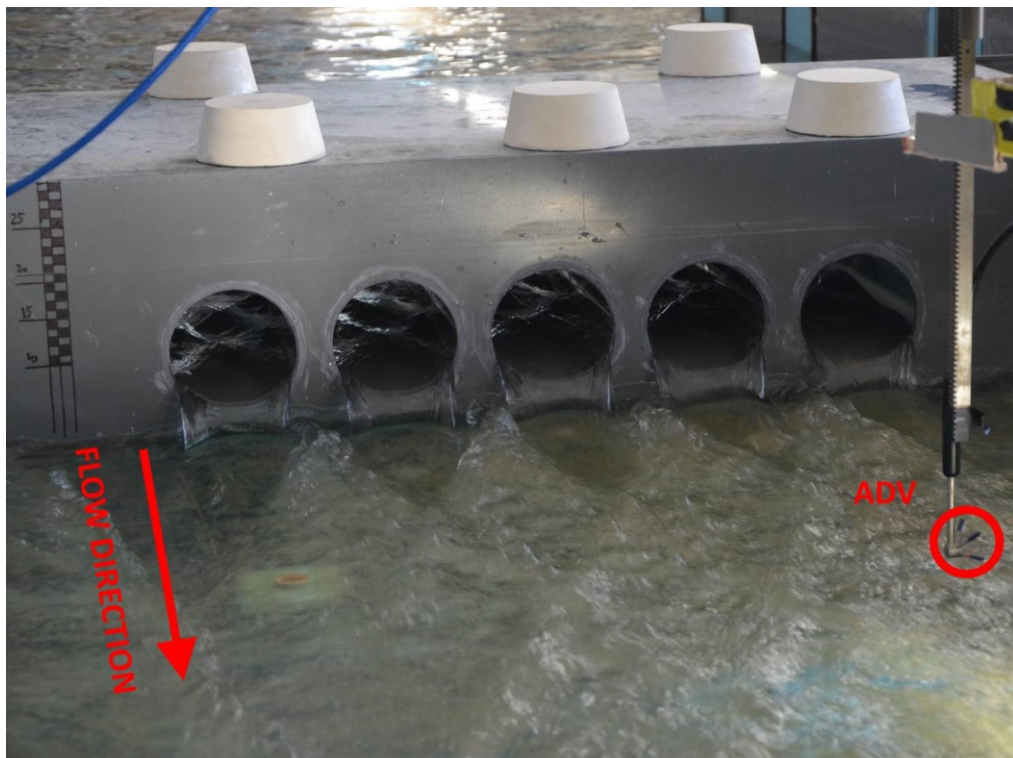
Velocity direction



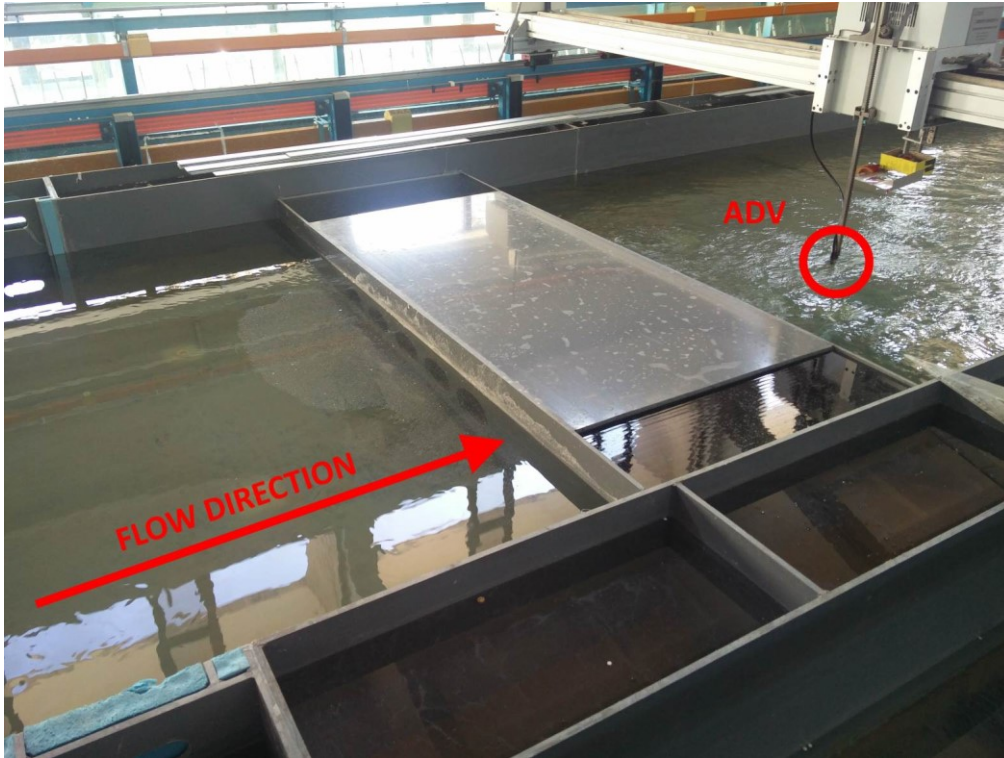
C Photos from Tsinghua hydraulic laboratory



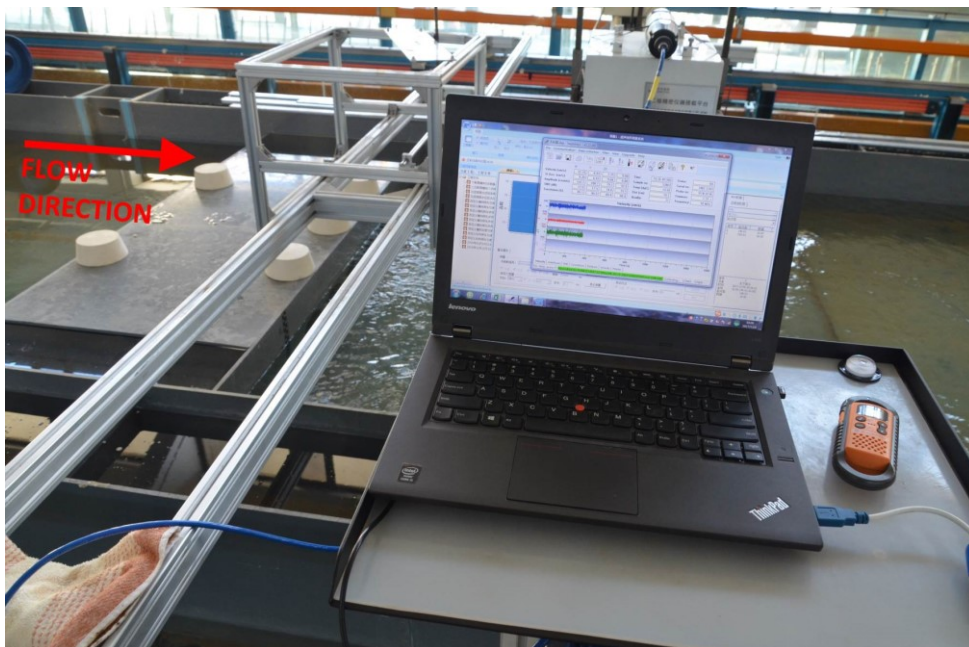
C.1: Bird's-eye view of an empty flume with the barrage already installed.



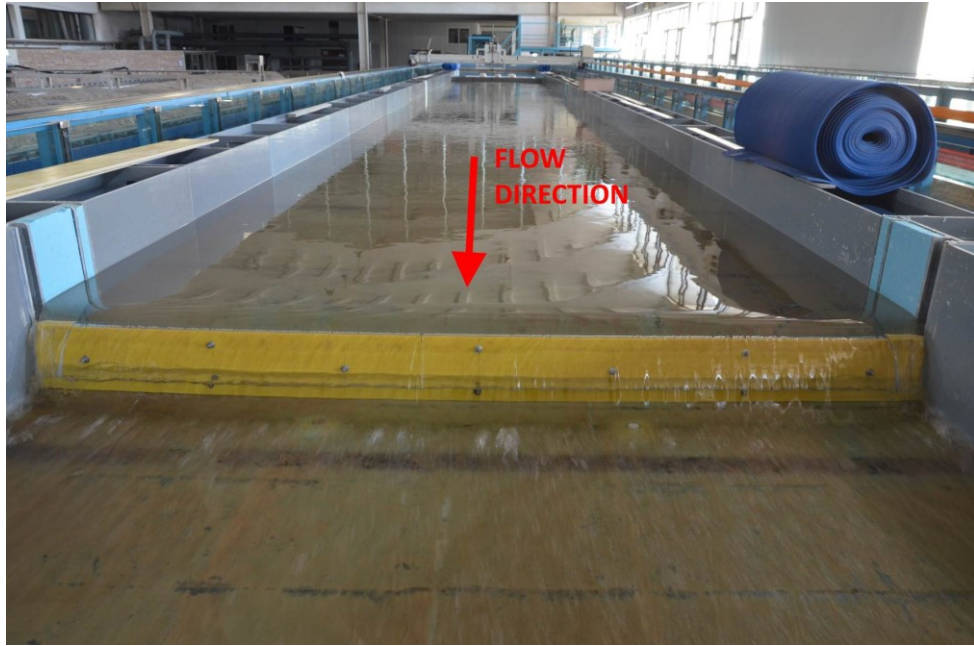
C.2: Flow through the barrage during the filling of the flume. The ADV sensor is seen suspended above the water on the right side of the image.



C.3: Running the experiment with all five ducts open. The head difference between the upstream and downstream water levels is visible. The ADV is mounted on the gantry, with the sensor submerged to record the velocity downstream of the barrage.



C.4: Live recording of the velocity field with the ADV.



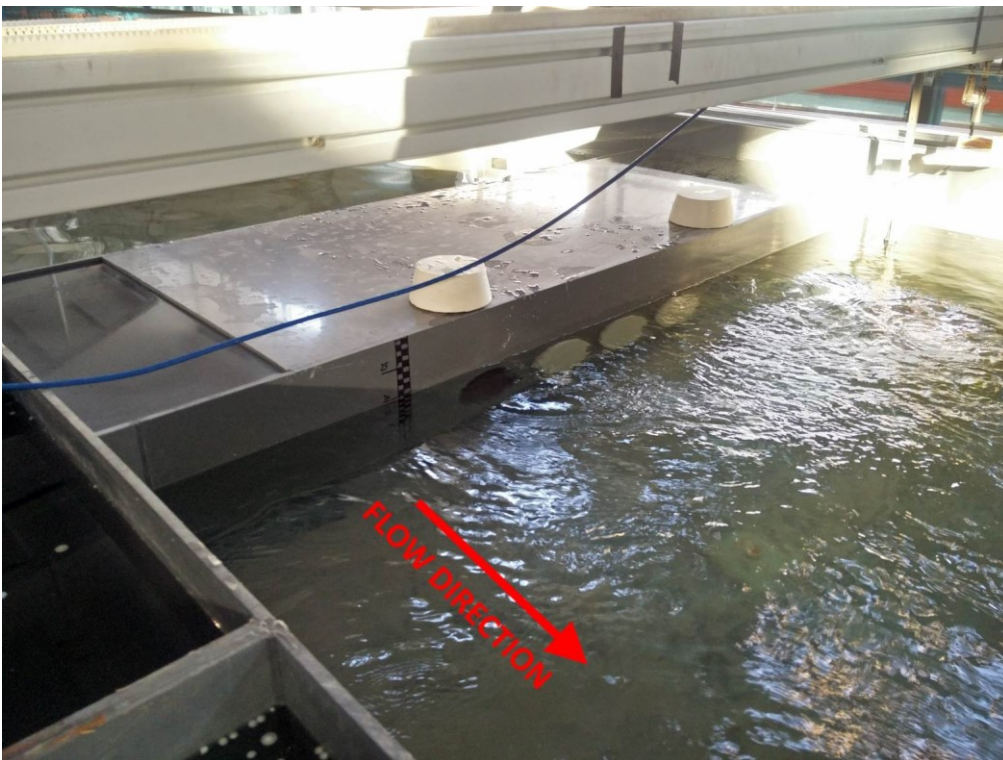
C.5: The weir was installed at the far end of the flume.



C.6: White silicone plugs were used to change the configuration of the open ducts.

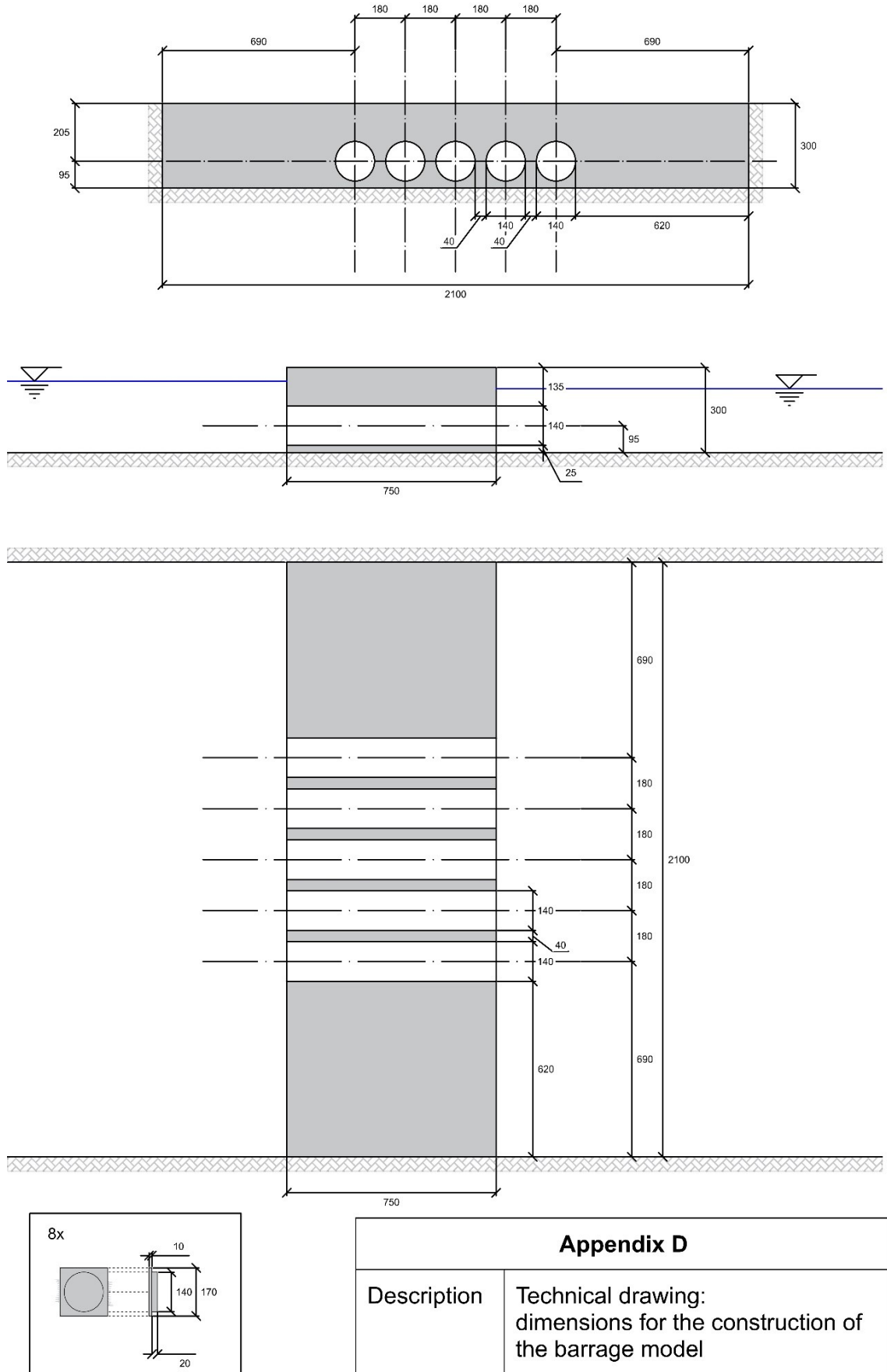


C.7: Running the experiment with two inner ducts open.



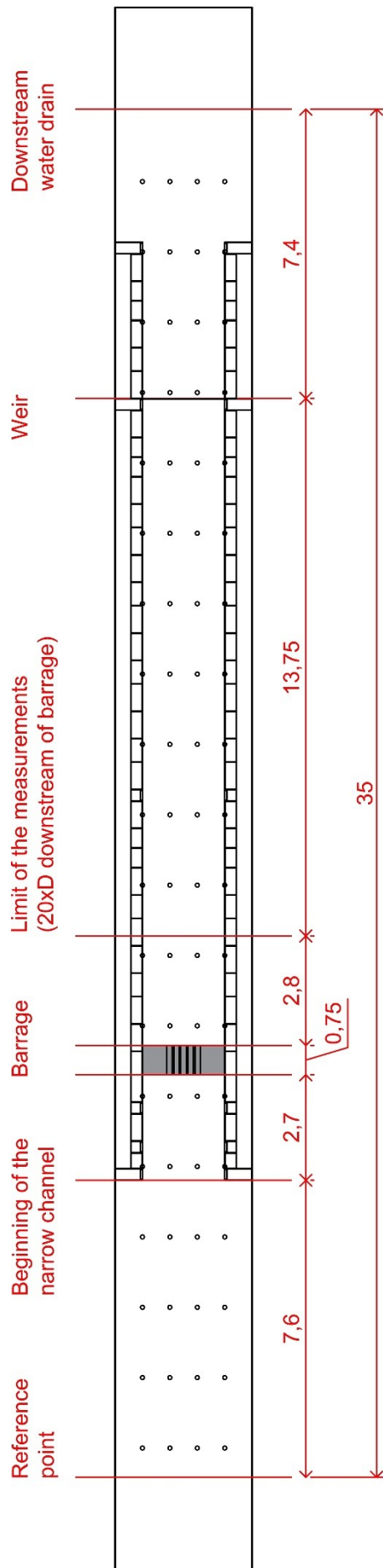
C.8: Running the experiment with two outer ducts open.

D Technical drawing - barrage model



Appendix D	
Description	Technical drawing: dimensions for the construction of the barrage model
Author	Nejc Čož
Date	30/10/2017 at Tsinghua University

E Layout of the experiment - plan view

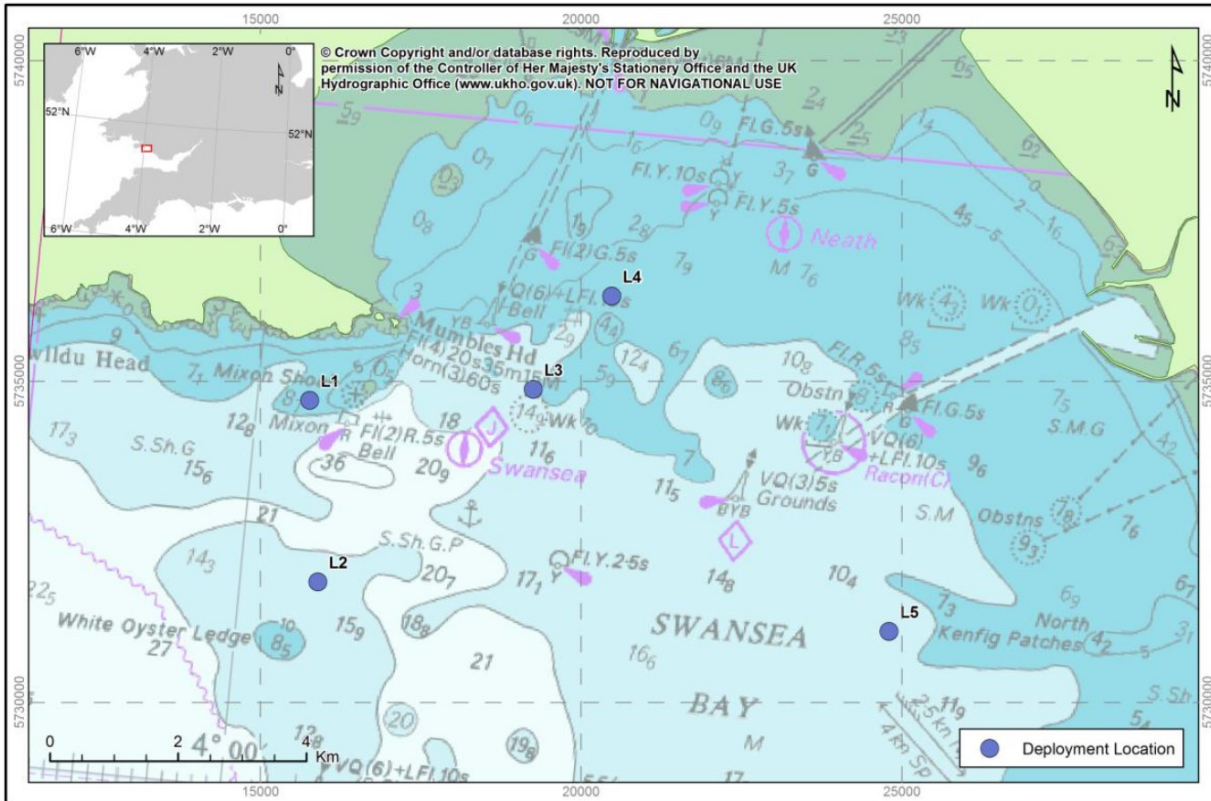


Appendix E	
Description	Diagram of the flume layout, showing streamwise locations of barrage, weir and other elements
Author	Nejc Čož
Date	30/10/2017 at Tsinghua University

F Validation results – Swansea Bay

Validation results of the hydrodynamic conditions in the Swansea Bay for the Swansea Bay lagoon model, before the inclusion of the lagoon. Plots include the location of the selected observation point, a compass plot of the velocity vector and time series plots for water levels, velocity magnitude and velocity direction.

Locations of the observation points:



Map Document: (V:\U1012014_Swansea_Bay_Current_Monitoring\3_Plots\1_SurveyArray\Q2014_Deployment_Locations_RJM_20121024.mxd)
24/10/2012 -- 12:14:39

Validation of the Swansea Bay lagoon model

Data	ADCP (Aberystwyth University, 2012)
Simulation time	
- Start	24/07/2012 21:00:00
- Stop	07/08/2012 00:00:00
Manning's roughness coef.	0.030
Mode	2D – depth-averaged

